Monte Carlo Computing Applied to X-ray Room Design

by

Graham Hugh McVey

Wolfson College

University of Oxford

2002

Thesis submitted in partial fulfilment of the requirements for the degree of Doctor of Philosophy in Clinical Medicine in the Division of Medical Sciences at the University of Oxford.

Approximately 50000 words

MONTE CARLO COMPUTING APPLIED TO X-RAY ROOM DESIGN

by

Graham Hugh McVey

Thesis submitted for the Degree of Doctor of Philosophy
at the University of Oxford

Faculty of Clinical Medicine
Medical Physics Department
The Churchill
Oxford Radcliffe Hospital

Wolfson College
Trinity Term 2002

Abstract

Currently, x-ray rooms are designed by employing measured scatter and transmission data obtained nearly thirty years ago. Subsequently, there is a clear need to re-evaluate this information as the use of modern equipment is becoming increasingly common. For example, x-ray tubes with medium frequency generators are replacing single phase units. Recent literature has re-evaluated transmission data. However, the scatter found in x-ray rooms has not been studied in detail.

Two programs using Monte Carlo techniques have been developed for this purpose. The first program models the x-ray room including a slab phantom simulating the patient, a DAP meter, air and the room walls. The second program implements a realistic model of a patient in the imaging system. The results of the two programs have been validated by comparison with each other and by measurements.

The results confirm that the patient is the primary source of scatter in a x-ray room. However, large variations in the scatter values are observed for different x-ray examinations and when the imaging parameters are changed. The results also show that there is a significant scatter contribution from other materials in the primary x-ray beam including the air, DAP meter and x-ray collimators. The first program has been used to calculate the scatter at a door positioned behind a protective screen at the radiographer's console. It predicts that no shielding in the door is required for the imaging system investigated.

Therefore, a valuable computational tool has been developed which will aid the decision process in the design of clinical x-ray rooms.

Acknowledgements

I would like to thank the following people for their invaluable help and assistance throughout this work:

Henry Weatherburn, Head of the Medical Physics Department, for his support and professional guidance, and his assistance with undertaking the measurements.

My college supervisor, Basil Shepstone, for his advice and his support.

All friends and colleagues at the Medical Physics Department. In particular, Steve Mutch and Jonathan Van Den Broek for introducing me to diagnostic radiology physics and John Fenwick for helping with the early stages of Monte Carlo programming. The radiographers at the Churchill Hospital for allowing after hours access to the x-ray equipment.

David Dance, Gudrun Alm Carlsson, Michael Sandborg and Jan Persliden for sharing their experience of Monte Carlo programming and for useful discussions. I would also like to thank Gudrun and Carl for their hospitality during my visits to Linköping.

Elly Castellano and Claire Skinner at the Royal Marsden Hospital for making comments, suggestions and overall enthusiasm at the end of this work when time was running out. Sonia Lester for helpful discussions. Marcus O'Brien for keeping the computers running smoothly.

My colleagues and friends at Glan Clwyd Hospital for their support and understanding.

All the friends I made during my time at Wolfson College, in Oxford and in London.

My family for their patience, love and understanding.

And last but not least, Alison for love and support, who kept me going during the tough times.

Contents

List of Figures

List of Tables

Chapter 1: Radiation Protection in Diagnostic X-ray Facilities

1.1 Introduction

While it is recognised that doses to staff and visitors in areas surrounding diagnostic radiology x-ray rooms are small, it is assumed that there is no dose threshold for the induction of cancer or genetic effects by x-rays (ICRP, 1991). Following revision of the radiation risk evidence (ICRP, 1991), the legal requirements for annual dose limits for staff and the public were reduced (IRR, 1999). Therefore, it is important to ensure that any potential dose received by staff or the public is as low as reasonably achievable. As this has to be achieved within the context of increasing pressure on health care budgets, it is therefore vital to have a method to predict dose accurately which provides confidence that the design criteria of the diagnostic x-ray facility are fulfilled.

Currently, transmission and scatter data from the literature are used to design a diagnostic x-ray facility. Much of this information is nearly 30 years old although a recent BIR report (Sutton and Williams, 2000) has attempted to update this information. Technological advances during this period have for example seen single phase x-ray generators being replaced by medium frequency x-ray generators. Application of both old and more recent data is limited due to the small number of beam parameters investigated and the lack of agreement between different investigators. Therefore, it is important to consolidate and extend this data set.

In this thesis, two computer programs have been developed for this purpose. Both programs are based on existing Monte Carlo codes which simulate radiation transport. These computer programs have the potential to undertake calculations to a high precision. They have been validated by comparison with calculation and measurement. Different situations affecting the design of x-ray rooms have been studied for a range of beam qualities and scattering materials including a realistic simulation of human anatomy.

The overall aims of this thesis are thus: to provide improved data for use in the design of x-ray rooms and to provide validated programs that may be used to further extend the data set as future needs require. This chapter describes the general principles of radiation protection, reviews the currently available shielding data and discusses the main aims of this thesis in more detail.

1.2 Historical Background

The application of x-rays to medicine was recognised soon after Roentgen's early experiments in 1895. The use of radiation in therapy and diagnosis has led to great improvements in the health of the population. However early investigators, who received severe damage to their skin including erythema and lesions, observed the need for caution in using x-rays. Almond (1993) recounts Elihu Thompson's report, in 'Electrical World' for 28th November 1896, of exposing his fingertip to radiation for half an hour:

"*Eleven days after the exposure, the skin of the back of the finger is red, swollen, and painful to touch and the finger feels somewhat stiff. It has begun to blister*".

Early recommendations for radiation protection were therefore developed to restrict exposures to radiation workers. The quantity of radiation required to produce burning or lesions of the skin over a short period of time is relatively high. This describes the deterministic effect. Radiation damage increases for increasing exposure and if the dose received is high enough then death can occur. The first recommendations were thus designed to keep exposures considerably below that for a deterministic effect (Hendee, 1993).

Evidence that no level of radiation is safe has been gathered over the years. For example, the incidence of leukaemia in Japanese Atomic Bomb survivors exposed to high doses has been studied (Hendee, 1993). This data was extrapolated to low doses to predict the increased incidence of leukaemia in the general population. This work assumed that radiation can cause damage to a single cell or cellular component that will exhibit effects only after a period of time. This describes the stochastic effect which can produce cancer (carcinogenesis) or genetic mutations (mutagenesis). Abnormalities in children may be caused by exposures before birth. Exposures of the foetus or embryo to radiation can produce both stochastic and deterministic effects such as structural anomalies and/or mental retardation (ICRP, 1991).

1.3 Diagnostic X-ray Facilities

1.3.1 Description of an X-ray Room

An x-ray room is the facility where a patient is imaged. The imaging equipment includes the x-ray generator, the x-ray tube, patient support device, grid or air gap, and image receptor. An x-ray room is designed to be large enough to allow easy access of patients to the x-ray equipment.

Patients are assumed to receive a net benefit from x-ray exposures whereas staff and the public only receive a detriment. Staff inside the room position themselves behind protective screens at the radiographer's console for radiographic procedures and staff wear lead aprons for all fluoroscopic procedures. The structure of the x-ray room itself must be designed to provide adequate shielding to the surrounding areas which staff, patients and visiting members of the general public may occupy.

1.3.2 Radiation in an X-ray Room

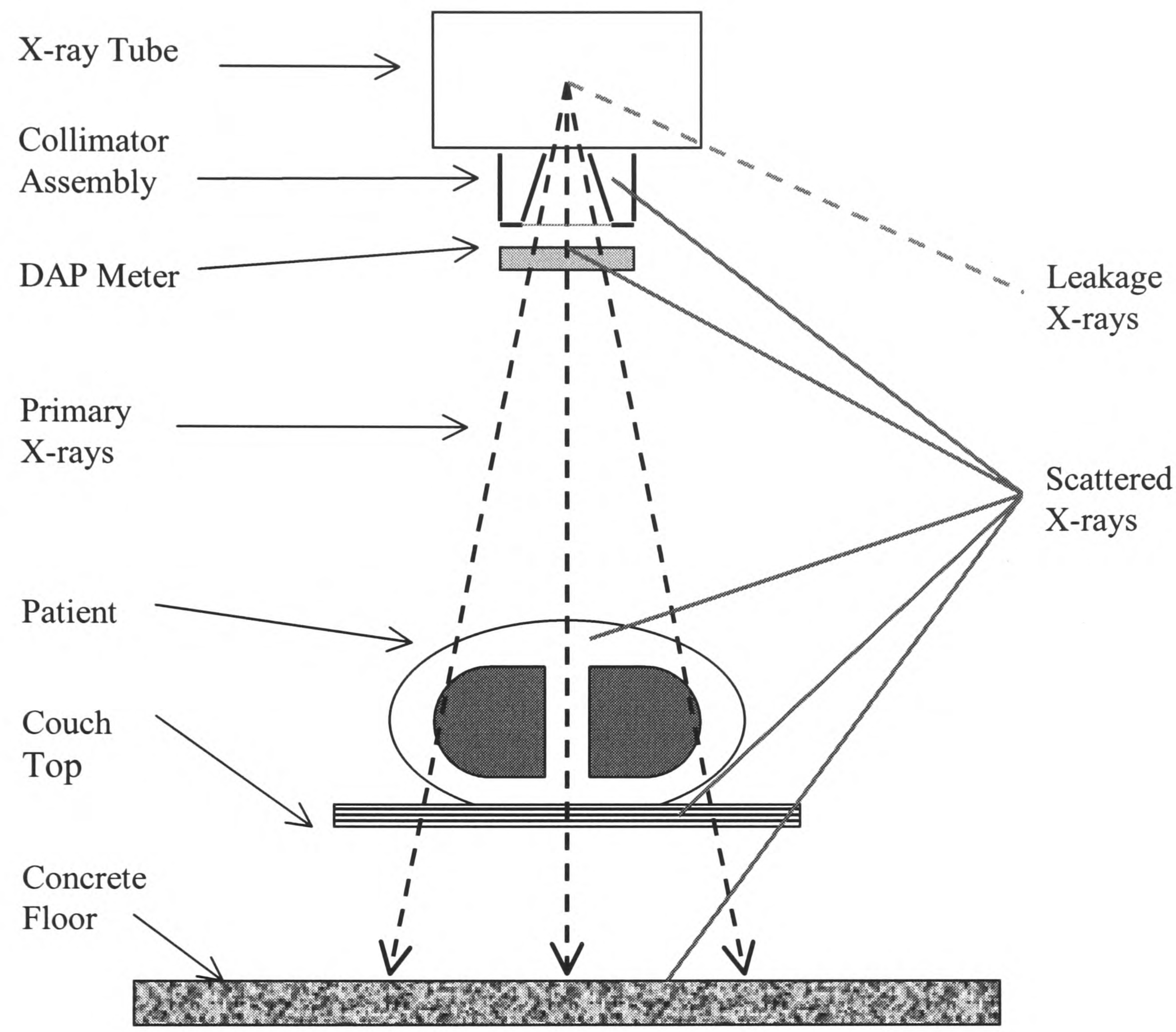

***Figure 1.1**. The different sources of primary, leakage and scatter radiation produced in a x-ray room.*

The x-ray room protection is designed by taking into account the radiation dose produced by the primary, leakage and scattered radiation shown in figure 1.1. They are described in more detail below:

- *Primary* radiation is produced directly from the x-ray tube focus. The dimensions of the radiation beam are defined by the collimator system of the unit. The beam output and quality are determined by the tube voltage, tube current, filtration, anode target material, target angle, voltage rectification, exposure duration, equipment age, etc.

- *Leakage* radiation is also produced directly from the x-ray tube focus. However, it is not determined by the collimator system but by x-rays which are transmitted through the protective tube housing. Therefore, the leakage radiation has been substantially attenuated. The U.K. Guidance Notes (NRPB, 1988) state that the leakage radiation must not exceed an air kerma of 1 mGy in one hour averaged over an area not greater than 100 cm^2 at one metre from the focal spot.
- *Scattered* radiation is produced when either the primary or leakage radiation interacts with material. IPSM Report No. 46 (IPSM, 1986) states the percentage scatter for a primary beam incident on a patient or a shielding barrier is less than 0.2% even at the maximum field size and it will be typically 0.1% of the primary beam at 1 metre.

The dose at a point in or outside the x-ray room is determined by the summation of the primary, leakage and scatter radiation doses where appropriate.

1.3.3 Dose Reduction

A patient receiving a direct x-ray exposure is presumed to gain a net benefit from a radiological examination. The x-ray image will aid the clinician to make a diagnosis. This benefit outweighs the increased risk or detriment from the radiation dose. The dose to the patient must be kept As Low As Reasonably Practicable i.e. the ALARP principle (IR(ME)R, 2000). This means that the dose level should be sufficient that the diagnostic detectability in the image is not compromised.

Staff and the general population however receive only a detriment from radiation. Dose limits for staff and the general population have been set taking into account that the radiation level cannot be reduced to zero and hence, there is always a risk of inducing cancer as it is assumed that there is no threshold dose for stochastic radiation damage. The total dose received by staff and the general population should be reduced by the ALARP principle also. Three concepts should be employed to undertake this and are detailed below:

- *Exposure Time*: the dose imparted is equal to the dose rate multiplied by the duration of the radiation exposure. Therefore if the latter is reduced then so is the dose.
- *Distance*: the dose is reduced by the inverse square law for a point source. The dose or dose rate decreases considerably for large distances from the x-ray source.
- *Shielding*: all materials attenuate x-rays. Radiation barriers use materials that effectively reduce the dose or dose rate with a finite thickness of material. Shielding should be as close as possible to the radiation source.

Two other factors reduce the cumulative dose to staff or the public. The first being the 'occupancy' factor and is the time a person occupies an area adjacent to the x-ray room. The room design therefore has to take into account if this person is occasionally in this area or is undertaking a full time job.

The second factor is the direction in which the x-ray tube is pointed over a period of time. This 'use' factor may also be included in the x-ray room design. For a chest x-ray room, the x-rays may be directed at a wall bucky which would give a use factor of 1.0 for a particular wall. For a general purpose x-ray room, the use factor for a wall may be reduced to 0.25 or less.

All the factors are combined to calculate the dose at a position outside the x-ray room. The amount of shielding is adjusted to achieve the design criterion.

1.3.4 Dose Limits and Constraints

The whole body dose limit for the general population is currently 1 mSv per year (IRR, 1999). This has been reduced from 5 mSv per year (IRR, 1985) following the application of the ICRP Publication No. 60 (1991) recommendations to legislation. The new dose limit takes account of recent data concerning late effects observed in Japanese atomic bomb survivors and the hereditary effects in their progeny. Any further large reductions in the dose limit are unlikely as the average annual exposure from natural background radiation to the UK population is 2.2 mSv (Hughes, 1999).

The NRPB (1993) recommends that the annual dose to the public be no more than $3/10$ of the dose limit, and less when this is readily achievable. Therefore, the maximum dose constraint is 0.3 mSv per year for the public and this is the value which would be used for the design criterion.

1.4 Data for X-ray Room Design

1.4.1 Introduction

In order to design an x-ray room, data are required to determine the shielding against primary, leakage and scattered radiation. These data are obtained from a number of references: 'Handbook of Radiological Protection' (HMSO, 1971), 'Recommendation for Data on Shielding from Ionizing Radiation' (BSI, 1971), ICRP Report No.33 (ICRP, 1982), and NCRP Report No. 49 (NCRP, 1976). It should be noted that the HMSO and BSI reports are very similar. These reports are becoming increasingly obsolete since they refer to measurements of transmission through shielding barriers and scatter from phantoms carried out nearly thirty years ago. Recently, the BIR Report 'Radiation Shielding for Diagnostic X-rays' (Sutton and Williams, 2000) was published to bring together up to date information.

Transmission is defined as the air kerma behind a shielding barrier divided by the air kerma at the same position for the shielding barrier not being present. Scatter is defined as the ratio of air kerma for a position at a scattering angle surrounding a phantom or patient to the incident air kerma (without backscatter). The angle of scatter can be defined from either the surface of the phantom or from the centre of the phantom.

Two Monte Carlo programs have been developed with the aim of providing updated information on the protection of x-ray rooms. Both programs are fully described in Chapter 6 and a brief summary of each is given below. The first program, XYZSCAT, uses the EGS4 Monte Carlo code (Nelson et al., 1985). The program can calculate the percentage scatter at all points in an x-ray room and the transmission behind protective barriers. The computational model for the scatter calculation consists of a slab phantom of tissue equivalent material to represent the patient, a Dose Area Product (DAP) meter, the air and the walls to provide a realistic simulation of an x-ray room. The second program complements the first program as it can provide a more realistic model of the patient but not of the x-ray room. The second program, VOXSCAT, has been modified from a slab phantom code (Sandborg et al., 1994: Dance et al., 1997) to calculate scatter from a voxel phantom (Zubal et al., 1992, 1994) which provides a realistic model of an adult male patient. The results of the calculations with both programs are shown in chapters 7 and 8.

1.4.2 Data for Calculating the Primary Radiation Transmission

When the measurements were undertaken for the early reports, single phase generators for x-ray tubes were common, whereas today there is increasing use of medium frequency generator units. In 1989, the AAPM Task Group No. 9 was set up to research this concern and communicate their findings to the scientific community. This was undertaken in order to prompt the NCRP to revise their reports (Archer, 1995).

Archer et al. (1994) reported the results of x-ray transmission measurements carried out through lead, steel, plate glass, gypsum wallboard, lead acrylic and wood for three phase x-ray tubes. Rossi et al. (1991) measured the transmission and Simpkin (1989) calculated the transmission using the EGS4 code for a similar set of materials including concrete. Simpkin's and Archer's work provides transmission data for a greater number of materials than was presented in the early reports. Simpkin (1995) summaries the studies by Archer and Simpkin and that of Légaré et al. (1977) to provide a comprehensive set of fits for an equation to interpolate transmission data for tube potentials between 25 kV and 150 kV. The interpolation equation was developed by Archer et al. (1983).

The work summarised above applies to the primary x-ray beam being directly incident on the shielding barrier. However, this may be an oversimplification as parts of the patient and imaging system lie between the x-ray tube and the shielding barriers. Dixon (1994) measured the transmission behind a RANDO phantom, the phantom plus grid and the phantom plus grid, cassette and cassette holder. Dixon found that the primary beam is attenuated by 2 to 3 orders of magnitude depending on the number of components in the imaging system. Therefore, the amount of radiation which is incident on the shielding may be considerably lower than is usually used to design x-ray rooms. Sutton and Williams (2000) have also considered accounting for the attenuation of the patient and other parts of the imaging system in designing x-ray rooms.

However, if the x-ray room shielding is designed in this way, then its use may be limited. For example, the room design may be compromised if different equipment was installed or different radiological procedures were undertaken. Therefore, the x-ray room design should be designed with a conservative estimate of the transmitted dose to allow the facility to be used flexibly.

The work in this thesis has concentrated on comparing the recent data of Archer et al. (1994), Simpkin (1989) and Rossi et al. (1991) with calculations using the XYZSCAT code (section 7.3.1.2). The recently published primary beam transmission data (Archer et al., 1994, Simpkin, 1989; and Rossi et al., 1991) provides a thorough re-evaluation and the results of the XYZSCAT calculations have been compared to show that they are consistent with this up to date information.

1.4.3 Data for Calculating the Transmission of Leakage Radiation

Archer's interpolation equation (Archer, 1983) for calculating transmission can be used to obtain the thickness of barriers required to shield against leakage radiation. It can be manipulated to provide the half value layer (HVL) i.e. the thickness required to reduce the intensity by half.

Equation 1.1 shows that the thickness of a shielding material s can be defined by a numbers of HVLs. The value of HVL_i is dependent on the depth in the shielding material. For leakage radiation, which is assumed to be highly penetrating, a high attenuation HVL (usually the 10th HVL) is used to estimate the shielding penetrations.

$$s = \sum_{i=1}^{N} HVL_i \tag{1.1}$$

Leakage radiation data has also been thoroughly revised. Therefore, the work in this thesis has concentrated on showing that the XYZSCAT calculations are consistent with the recent data of Archer et al. (1994), Simpkin (1989) and Rossi et al. (1991) in section 7.3.1.3. Leakage radiation from modern x-ray tubes is low and was measured to be negligible below 100 kV (section 3.2.4) which agrees with the data given in Sutton and Williams (2000). Thus, leakage radiation is assumed not to be a significant problem and is not investigated in depth in this thesis.

1.4.4 Data for Scatter Radiation

1.4.4.1 Magnitude of Percentage Scatter

Table 1.1 compares the percentage scatter for tissue equivalent phantoms irradiated with an incident field size of 400 cm^2 by 100 kV x-rays. The most commonly used scatter values are from NCRP Report No. 49 which were derived from measurements by Trout and Kelley (1972). The NCRP data shown in table 1.1 are the average of Trout's measurements obtained with the x-ray beam incident on the centre and on the edge of a torso shaped masonite phantom. Self-rectified and single phase generators produced the x-rays for tube potentials between 50 and 150 kV. Averaging Trout's scatter values gives the values quoted by the NCRP for all scattering angles except 60° which may be due to a typing error in Trout's paper.

Another source of scatter values is ICRP Report No. 33. These values are reported by Bomford and Burlin (1963) for measurements undertaken using a MixD phantom with 100 kV x-rays. They are thus very limited in scope. Bomford's values shown in table 1.1 have been corrected by a backscatter factor of 1.3 (BIR, 1996) as the incident exposure was measured on the surface of the phantom.

Williams (1996) measured the scatter from a RANDO phantom for 50 to 125 kV x-rays produced by a medium frequency generator. Williams' data is presented in the paper as scattered air kerma relative to DAP. The values in table 1.1 are shown as relative to incident air kerma.

	Percentage Scatter Values described in the Literature				
Field Position	**NCRP Report No. 49 Average of Centre and Edge**	**Trout and Kelley (1972) Phantom Centre**	**Phantom Edge**	**Bomford and Burlin (1963) Phantom Centre**	**Williams (1996) Phantom Centre**
Scattering Angle (°)					
30	0.150	0.127	0.170	0.026	0.108
45	0.120	0.100	0.140	0.039	0.106
60	0.120	0.098	0.270	0.052	0.108
90	0.130	0.110	0.150	0.065	0.163
120	0.200	0.190	0.210	0.156	0.291
135	0.220	0.210	0.220	0.221	0.355

Table 1.1. *Comparison of the percentage scatter from NCRP Report No. 49 (1976), Trout and Kelley (1972), Bomford and Burlin (1963) and Williams (1996).*

The data from the older papers show the best agreement (within ±5%) at a 135° scattering angle. However for decreasing scattering angle, the differences between the older scatter values increase. Trout et al's. values are larger than Bomford and Burlin's by more than a factor of 3 for a 30° scattering angle. These differences may be due to Bomford and Burlin correcting for scatter from the x-ray room walls and the leakage from the x-ray tube whereas Trout's values will include these contributions. Table 1.1 shows that Williams' scatter values are considerably larger in the backward direction than for the other studies. Williams' values are larger than Trout's by a factor of 1.7 for a 135° scattering angle. Williams noted that there was a possible scatter contribution from the collimators and the DAP meter but did not investigate further. Trout and Kelley (1965) measured a significant amount of scatter from the collimator system and the air cone in front of the phantom. Therefore, different potential sources of scatter other than the phantom or patient have been investigated in sections 3.2 and 7.2.3.

Other measurements of scatter have been undertaken by Sanders et al. (1960) for a presswood phantom; by Martin and Muller (1961) for wax, aluminium, iron and lead phantoms; are reported in the 'Handbook of Radiological Protection' (HMSO, 1971) for concrete, barytes concrete, brick and lead; by Faulkner and Moores (1982) for a water phantom; and by Marshall and Faulkner (1992) for a RANDO phantom.

The problems with the percentage scatter reported in the literature can be briefly summarised to be that the values vary greatly between studies, are limited in scope and are strongly influenced by surrounding materials whose contribution is difficult to estimate.

Thus to gain an understanding of the scattering process, the first order Compton scatter was calculated by analytical methods as described in Chapter 5. This was undertaken by studying the variation of the first order percentage scatter with photon energy, tube voltage and the scatter contributions from different depths in a phantom. A limited check of the percentage first order Compton scatter was undertaken by comparison with the values calculated by the Monte Carlo codes (sections 7.2.1.1 and 7.2.1.2). A rigorous validation of the Monte Carlo codes was carried out by the comparison of their total scatter values (sections 7.2.1.3 and 7.2.1.4). A comparison of the Monte Carlo values with measurements showed if the calculated values were representative of the clinical situation (section 7.2.3). This study highlights the difficulty of comparing calculations with measurements due to the scatter contributions from other materials. Figure 1.1 shows the different sources of scattered radiation. The DAP meter and collimator system were shown to produce significant contributions to the total scatter and was further demonstrated with a simulation of the experimental set up used in Williams' (1996) work (section 7.2.4.1).

The variation of scatter from slab phantoms was calculated with the Monte Carlo codes for differing tube potentials, field sizes, focus to surface distances and scattering materials. These variations were then used to verify 'rule of thumb' methods for estimating scatter in different situations for example, for varying field sizes or at varying distances from the phantom. 'Rule of thumb' models are a convenient method for estimating scatter at positions where it is difficult to measure. It is important that these estimates of scatter are reliable as Monte Carlo simulations of x-ray rooms are not in routine use. In section 8.3.2.3, Monte Carlo calculations were compared to 'rule of thumb' estimates of scatter from the ceiling to a position at an x-ray room entrance behind a protective screen at the radiographer's console. From the results, it was possible to decide whether a door at this position was required to be shielded with lead.

In most of the literature, the scatter was measured from homogeneous tissue equivalent phantoms. Therefore, it is not known whether these values are representative of scatter from a patient. The VOXSCAT code includes a voxel phantom (Zubal et al., 1992, 1994) to provide a realistic model of the patient. Thus the scatter from the voxel phantom was systematically compared to the scatter from different slab phantoms (section 8.2.2). Furthermore, the variation of patient scatter for different imaging parameters was studied in sections 8.2.3 and 8.2.4 and was shown to have a different variation with field size from that expected for slab phantoms.

The VOXSCAT code (Dance et al., 2000; Sandborg et al., 2001) was initially developed for a study of image quality and patient dose undertaken for an European Union (EU) funded project entitled 'Predictivity and Optimisation in Medical

Radiation Protection'. The voxel phantom was shown to be representative of a patient (sections 7.4 to 7.6) by comparison of entrance air kerma calculations with measurements made available by Linköping University, Sweden (sections 3.3 and 3.4).

1.4.4.2 Quality of Scattered Radiation

The NCRP Report No. 49 (NCRP, 1976) states that the quality of the scattered radiation is similar to that for the primary radiation. Trout and Kelley (1972) measured the transmission for 90° scatter through lead to be slightly less penetrating than for primary radiation. Marshall et al. (1996) measured the scattered spectra from a 3M pelvic phantom using a Germanium crystal spectrometer. The half value layers and mean energies calculated from the scattered spectra are different from the values for incident x-ray spectra depending on angle of scatter.

It is difficult to measure the quality of scattered radiation and therefore, Monte Carlo calculations are a useful method of gaining this information. Two short studies of scattered radiation quality were carried out as part of the codes' validation. Firstly, the scattered spectra calculated by the XYZSCAT and VOXSCAT codes were compared in section 7.2.1.5. Secondly, the mean photon energies and half value layers for scattered spectra calculated by the VOXSCAT code were compared to the values from Marshall et al. (1996) in section 7.2.4.2.

1.4.5 Simulation of an X-ray Room

Metzger et al. (1993) calculated the dose at different positions surrounding a x-ray room using the MCNP Monte Carlo code. They included a realistic model of a patient by using an anthromorphic phantom to produce scatter. However, there are four problems with this work.

The first problem is that the statistical uncertainty was large in the dose values outside the shielding. The second problem is that values of the percentage scatter and the scatter transmission have not been reported so it is difficult to compare Metzger's results with those of the XYZSCAT and VOXSCAT programs. The third problem is that the model has not been validated but was compared with the dose derived from NCRP (1976) assumptions. The fourth problem is that it is difficult to interpret the results as the dose outside the room is averaged over a distribution of workloads for each tube potential.

Simpkin and Dixon (1998) calculate the dose behind secondary shielding using the percentage scatter from Trout and Kelley (1972) combined with the primary transmission data of Archer et al. (1994) and Légaré et al. (1977). The percentage scatter measured by Trout et al. for single phase equipment was corrected for all angles of scatter by the 90° scatter measurements of Dixon (1994) for modern equipment. It is obviously more accurate to obtain the percentage scatter for all the situations of interest rather than extrapolating the older data.

The XYZSCAT code has not been used to calculate the transmission of scatter radiation due to the excessive calculation time required. Instead, an application of the XYZSCAT code has been to estimate the scatter dose at an x-ray room entrance behind a protective screen at the radiographer's console (section 8.3.2.4).

1.5 Summary of this Thesis

Chapter 1 describes the general principles of radiation protection and the main methods of dose reduction. A critical review of the data available for shielding diagnostic x-ray rooms is given. The main aims and the areas of investigation for the thesis are described.

Chapter 2 describes the interaction processes which are simulated in the Monte Carlo programs to transport photons in an x-ray room and the dosimetric quantities such as air kerma which are calculated by the programs.

Chapter 3 gives the experimental details of the scatter measurements used for comparison with calculations. A short study is made of the different sources of scatter within the x-ray room. The experimental details are given of the collection and analysis of x-ray images and the optical density measurements used to validate that the voxel phantom is representative of a patient.

Chapter 4 describes the model used to determine the x-ray tube spectrum which is an important input parameter for the codes. Different x-ray spectrum programs are used with the different codes and these are compared. A comparison of the calculated and measured half value layers (described in chapter 3) is used to show if the x-ray spectra are representative of the clinical situation.

Chapter 5 describes the analytical calculation of scatter. This chapter provides an insight into the Compton scattering process by studying the contributions of scatter at different depths in the phantom, the variation of scatter with photon energy and tube potential.

Chapter 6 describes an overview of the Monte Carlo method and the reasons for choosing the Monte Carlo codes. The different computational implementations of the of the two Monte Carlo models are described and their input settings are detailed.

Chapter 7 describes the validation of the Monte Carlo codes for the calculation of scatter and shows if the voxel phantom is representative of a patient. The scatter calculations are compared to measurements to show if they are representative of the clinical situation. The variation of scatter from slab phantoms is investigated for different imaging parameters. Scatter and transmission calculations are compared to the values found in the literature.

Chapter 8 describes two applications of the Monte Carlo programs. The first application is the calculation of scatter from the voxel phantom simulating a patient. The scatter from a patient is compared to different slab phantoms before showing the variation of patient scatter for different imaging parameters. The second application is the estimation of the scatter dose at an x-ray room entrance behind a protective screen at the radiographer's console. Measurements are difficult at this position and the only method previously used was a 'rule of thumb' calculation. Monte Carlo calculations are compared to this quick method and the dose is calculated to determine if a door at this position would need to be lead lined.

Chapter 9 summarises the thesis and gives its main conclusions. The scope for future work is also discussed.

Chapter 2: Interaction Processes and Dosimetric Quantities

2.1 Introduction

This chapter describes the interaction processes which are used in computer models of radiation transport. Photons interact with materials by undergoing either photoelectic absorption, incoherent scattering or coherent scattering in the diagnostic x-ray energy range i.e. from 1 to 150 keV. The overall effect of these interactions is to reduce the intensity of the radiation i.e. the attenuation process. Electrons can be produced by both absorption and (incoherent) scattering. However in the energy range from 1 to 150 keV, they are assumed to deposit their energy locally. Electron transport is therefore not included in the VOXSCAT code and is switched off with the EGS4 Monte Carlo code (Nelson et al., 1985) calculations.

This chapter defines the dosimetric quantities used in this thesis. The calculated quantities have to be the same as the measured quantities to allow a comparison to be made. Therefore, conversion factors are employed, for example to convert fluence to air kerma. The methods used to access these conversion factors are discussed.

2.2 Photoelectric Effect

The photoelectric effect occurs when a photon interacts with a bound electron and total absorption of the incident photon takes place. Momentum is conserved in the interaction by the recoil of the residual atom. Electrons in the innermost (K and L) shells have the highest probability of absorbing a photon if the incident photon has enough energy. The energy, T, given to the electron is thus the incident photon energy, E, minus the binding energy of the electron B_e (equation 2.1).

$$T = E - B_e \tag{2.1}$$

After the electron has been ejected, the shells return to equilibrium when an outer electron fills the lower shell vacancy and the excess energy is released as characteristic x-rays and/or Auger electrons.

2.3 Incoherent Scattering

The incoherent scattering process derives from the Compton interaction. Compton scattering involves the interaction of a photon with a free (or loosely bound) electron. Klein and Nishina showed that the differential Compton cross section per unit solid angle (equation 2.2) is given by the product of the Thomson scattering differential cross section, $d\sigma_0 / d\Omega$, and a factor F_{KN} (equation 2.3).

$$\frac{d\sigma}{d\Omega} = \frac{d\sigma_0}{d\Omega} F_{KN} = \frac{r_0^2}{2}(1+\cos^2\theta) F_{KN} \tag{2.2}$$

$$F_{KN} = \left\{\frac{1}{1+\alpha(1-\cos\theta)}\right\}^2 \left\{1+\frac{\alpha^2(1-\cos\theta)^2}{[1+\alpha(1-\cos\theta)](1+\cos^2\theta)}\right\} \tag{2.3}$$

Let r_0 be the classical electron radius and $r_0^2 = 7.94\times10^{-30} m^2$ (Johns and Cunningham, 1983). Let θ be the angle of scatter with respect to the direction of the incident photon. The variable $\alpha = E/511$ where E is the energy of the incident photon in keV and 511 keV is the rest mass energy of the electron. The differential Compton cross section dependence with scattering angle and energy, calculated using equations 2.2 and 2.3, is shown in figure 2.1. It demonstrates that for increasing photon energy the scatter is predominantly directed in the forward direction as well as being substantial in the backward direction.

Incoherent scattering involves the interaction of a photon with an electron bound to the atomic nucleus. The incoherent differential scattering cross section, $d\sigma_{inc}/d\Omega$ (equation 2.4) is derived from the Compton differential cross section $d\sigma/d\Omega$ (equation 2.2) and a factor *S(x,Z)* to correct for electron binding, known as the incoherent scattering function. Hubbell et al. (1975) give tabulated incoherent scattering functions which can be used to calculate the incoherent differential scattering cross section.

$$\frac{d\sigma_{inc}}{d\Omega} = \frac{d\sigma}{d\Omega} S(x,Z) \tag{2.4}$$

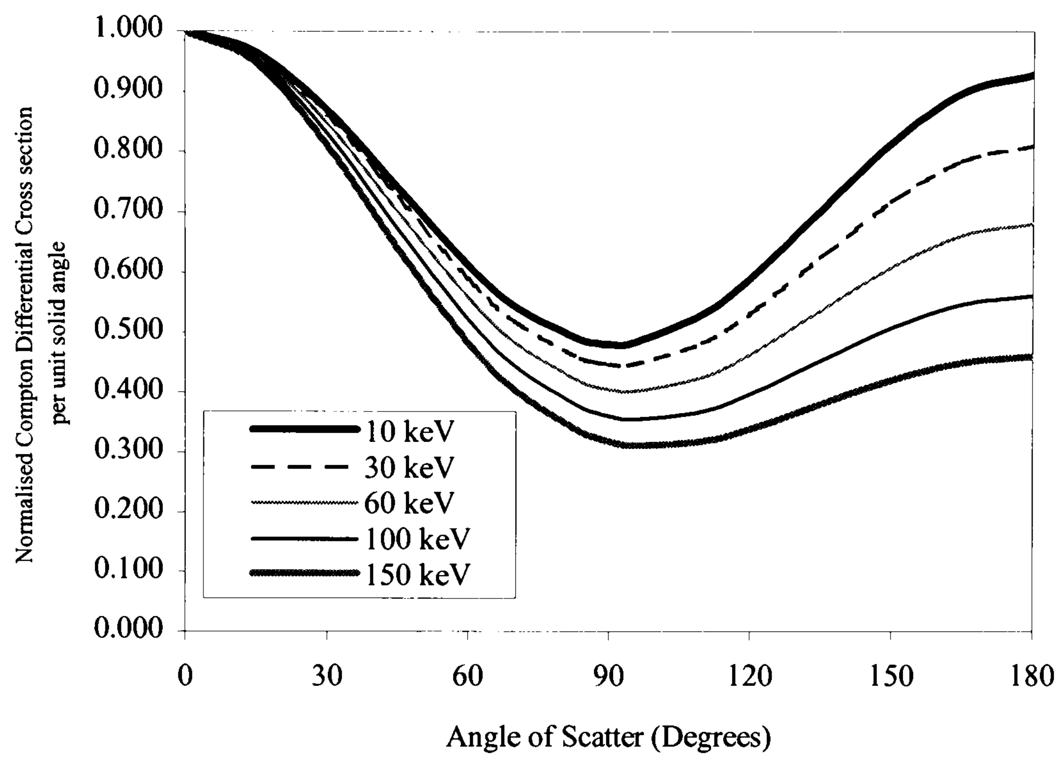

Figure 2.1. *The normalised differential Compton cross section per unit solid angle for various photon energies.*

The incoherent scattering function has a zero value in the forward direction and increases to the atomic number, Z, of the material for increasing x, known as the momentum transfer variable (equation 2.5). It depends on the angle of scatter θ and the wavelength λ (in Ångstroms) of the incident photons.

$$x = \frac{\sin(\theta/2)}{\lambda} \tag{2.5}$$

The total incoherent scattering cross section, σ_{inc}, is obtained from integrating the differential incoherent cross section. Integration of the differential Compton cross section gives the total Compton cross section, σ, shown in equation 2.6.

$$\sigma = \frac{3}{4}\sigma_0\left\{\left(\frac{1+\alpha}{\alpha^2}\right)\left(\frac{2(1+\alpha)}{1+2\alpha} - \frac{\ln(1+2\alpha)}{2\alpha}\right) + \frac{\ln(1+2\alpha)}{2\alpha} - \frac{(1+3\alpha)}{(1+2\alpha)^2}\right\} \quad (2.6)$$

Let σ_0 be the total Thomson cross section given by $\sigma_0 = \frac{8}{3}\pi r_0^2$.

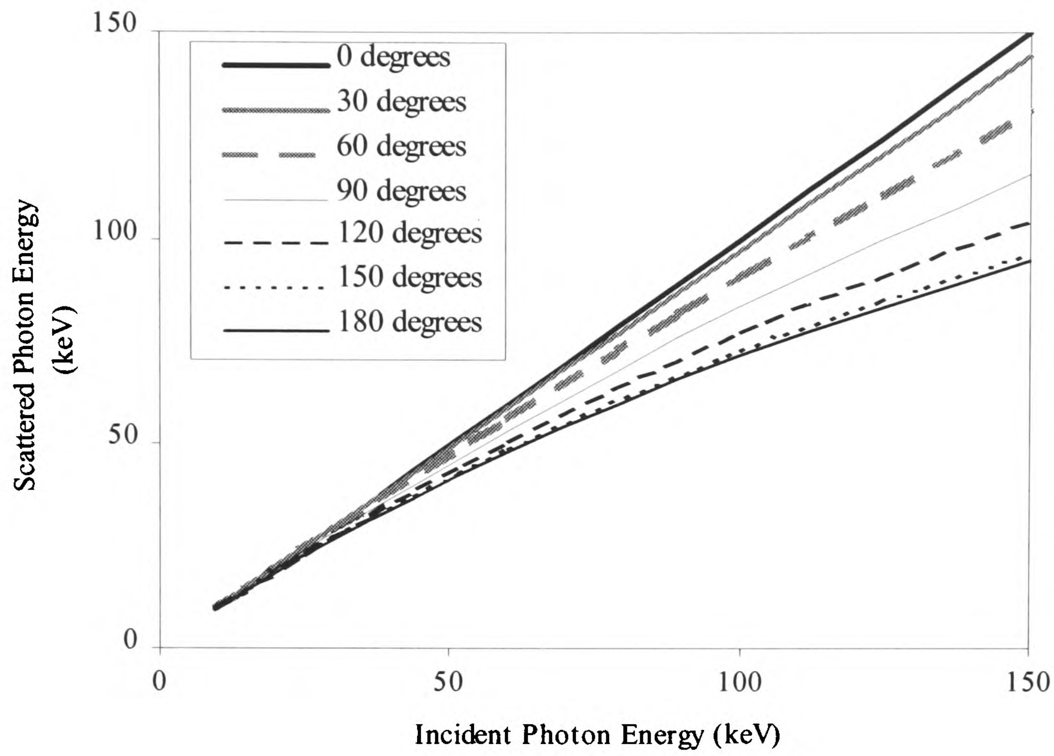

Figure 2.2. *The scattered photon energy for different scattering angles.*

In a Compton interaction, part of the incident photon's energy is transferred to the free electron and the remainder is emitted as a scattered photon of lower energy. Energy is conserved in the collision. The electron is emitted at an angle to the path of the incident photon and travels a very short distance before it is absorbed. Equation 2.7 gives the relationship between the energy of the scattered photon E_s and the energy of the incident photon E.

$$E_s = \frac{E}{1+\alpha(1-\cos\theta)} \quad (2.7)$$

The dependence of the scattered photon energy with incident photon energy and scattering angle is shown in figure 2.2. This figure demonstrates that the energy of a scattered photon is lower in the backward direction and that this effect increases for increasing photon energy.

2.4 Coherent Scattering

When a photon undergoes a coherent interaction with an atom, no energy is lost and all of the energy is transferred to the scattered photon. The differential coherent scattering cross section per atom per solid angle $d\sigma_c/d\Omega$ (equation 2.8) is derived from the Thomson scattering coefficient $d\sigma_0/d\Omega$ and an atomic form factor *F(x,Z)*.

$$\frac{d\sigma_c}{d\Omega} = \frac{d\sigma_0}{d\Omega}[F(x,Z)]^2 \tag{2.8}$$

The atomic form factor depends on the momentum transfer variable x (equation 2.5) and the atomic number of the material Z. Hubbell and Øverbø (1979) give tabulated atomic form factors which can be used to calculate the differential coherent scattering cross section. The differential coherent scattering cross section peaks in the forward direction (Johns and Cunningham, 1983). The total coherent cross section is obtained by integration of the differential coherent cross section.

2.5 Mass Attenuation Coefficients

The linear attenuation coefficient, μ, is defined as the probability per unit pathlength that a photon will interact in a medium (Hubbell, 1969). It is dependent on the photon energy and the atomic number of the material. The mass attenuation coefficient μ/ρ is the linear attenuation coefficient divided by the density of the material ρ (equation 2.9) and is the sum of the attenuation produced by the photoelectric interaction μ_{ph}/ρ, Compton scatter μ_{inc}/ρ and coherent scatter μ_c/ρ in the diagnostic energy range.

$$\frac{\mu}{\rho} = \frac{\mu_{ph}}{\rho} + \frac{\mu_{inc}}{\rho} + \frac{\mu_c}{\rho} \tag{2.9}$$

Attenuation is the reduction in the intensity of a photon beam by a material. The fractional reduction in intensity dI is proportional to the probability of an interaction in an infinitesimal thickness dz (equation 2.10).

$$dI / I = -\mu dz \qquad (2.10)$$

The intensity I transmitted (equation 2.11) through an homogeneous material of thickness Z_t with an intensity I_0 incident on it is:

$$I = I_0 e^{-\mu Z_t} \qquad (2.11)$$

2.6 Mass Energy Absorption and Mass Energy Transfer Coefficients

During the attenuation process part of the photon's energy is radiated as scattered radiation and part is given to electrons as kinetic energy. These electrons will lose energy by coulomb scattering or by emission of Bremsstrahlung depending on the electron energy and the atomic number of the material. The mean energy transferred and the mean energy absorbed can be determined after a large number of electron collisions. The mass energy transfer coefficient μ_{tr}/ρ (equation 2.12) is the combination of the mass attenuation coefficient and the average energy transferred per interaction $\overline{E}_{tr}$.

$$\frac{\mu_{tr}}{\rho} = \frac{\mu}{\rho}\frac{\overline{E}_{tr}}{E} \qquad (2.12)$$

The mass energy absorption coefficient μ_{en} / ρ (equation 2.13) is similarly defined by the combination of the mass attenuation coefficient and the average energy absorbed per interaction $\overline{E}_{ab}$.

$$\frac{\mu_{en}}{\rho} = \frac{\mu}{\rho}\frac{\overline{E}_{ab}}{E} \qquad (2.13)$$

The mass energy absorption coefficient is equal to the mass energy transfer coefficient (equation 2.14) minus the fraction that is lost by Bremsstrahlung production, g.

$$\frac{\mu_{en}}{\rho} = \frac{\mu_{tr}}{\rho}(1-g) \qquad (2.14)$$

Bremsstrahlung losses are negligible in the diagnostic x-ray energy range and therefore in the present case, the mass energy absorption coefficient is equal to the mass energy transfer coefficient.

2.7 Accessing Mass Attenuation Coefficients in the Computer Programs

The computer models require access to mass attenuation and mass energy transfer coefficients for all energies between 1 and 150 keV. Published coefficients (e.g. Hubbell, 1982) have to be interpolated for energies between the tabulated values.

The EGS4 Monte Carlo code (Nelson et al., 1985) uses a pre-processor program called PEGS4 (section 6.4.2.1) to calculate the mass attenuation coefficients and ratios of interaction cross section to the total cross section for elements, compounds or mixtures with atomic numbers between 1 and 100. This data is derived from Storm and Israel (1970) for the photoelectric and coherent cross sections and the Compton cross section without electron binding corrections.

The VOXSCAT Monte Carlo code uses more recent tabulations: Berger and Hubbell (1987) for photoelectric cross sections; Hubbell and Øverbø (1979) for coherent scattering cross sections; and Hubbell et al. (1975) for incoherent scattering cross sections with electron binding corrections.

The analytical calculations undertaken in this thesis use the mass attenuation coefficients from 10 to 150 keV for tissue equivalent (WT1) material (White et al., 1977). The mass attenuation coefficients were calculated by the PEGS4 program and fitted to a fifth order polynomial (equation 2.15) by the general linear least squares method (Press et al., 1992) in order to interpolate the coefficients. This enabled comparison of the analytical and XYZSCAT calculations (sections 7.2.1.1 and 7.2.1.2).

$$\frac{\mu}{\rho} = \alpha E^{-5} + \beta E^{-4} + \delta E^{-3} + \gamma E^{-2} + \varepsilon E^{-1} + \eta \qquad (2.15)$$

In equation 2.15, E is the photon energy (in units of MeV) and α, β, δ, γ, ε, and η are the fitted parameters. The values of the fitted parmeters for WT1 material are shown in table 2.1 and provide the mass attenuation coefficients in units of m^2/kg.

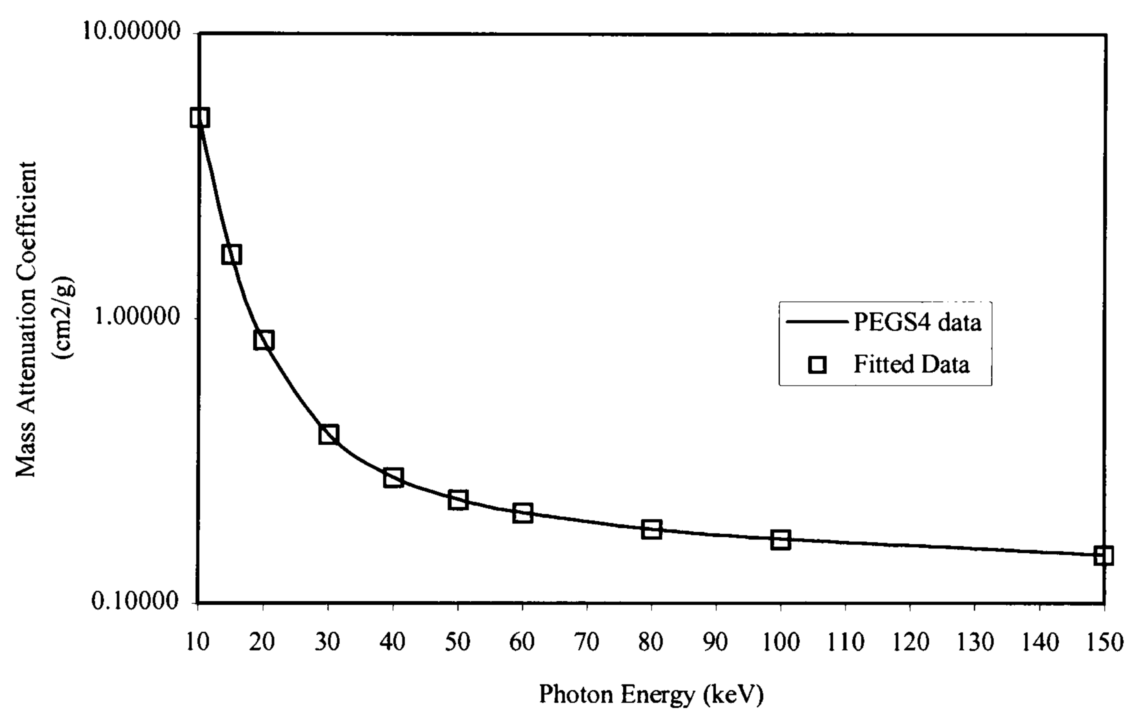

***Figure 2.3**. The comparison of the mass attenuation coefficients for WT1 material calculated by the PEGS4 code and the least squares fitted values.*

Figure 2.3 shows good agreement between the mass attenuation coefficients calculated with the PEGS4 code and the least squares fitted values. The 'goodness of fit' of the fitted coefficients to the coefficients calculated with the PEGS4 code were estimated using the R^2 statistic. The R^2 statistic was calculated by the sum of the squares of the regression divided by the sum of the squares about the mean (Altman, 1991). An adjusted R^2 statistic also estimates the 'goodness of fit' taking into account the number of fitting parameters. The R^2 and the adjusted R^2 statistics are very close to 1 indicating a 'good fit' (Altman, 1991). Further evidence of the good agreement between the tabulated and fitted mass attenuation coefficients is shown in figure 2.4. The differences between the PEGS4 and fitted values are smaller than the differences between the PEGS4 and the ICRU Report No. 44 (1989) coefficients.

	Fitted Parameter Values for WT1 Material
Energy Range Parameter	**10 keV – 150 keV**
α	3.850×10^{-11}
β	-9.942×10^{-9}
δ	1.422×10^{-6}
γ	-4.185×10^{-5}
ε	1.030×10^{-3}
η	9.314×10^{-3}

Table 2.1. *The parameters obtained in this work from least squares fitting a 5th order polynominal to the mass attenuation coefficients for WT1 material calculated by the PEGS4 code.*

2.8 Comparison of the WT1 Material Mass Attenuation Coefficients

Hubbell (1982) states that the mass attenuation coefficients and mass energy absorption coefficients have uncertainties of ±5% for 1 to 5 keV and ±2% for 5 keV to 10.0 MeV. Hubbell (1982) suggests that the uncertainties in the mass attenuation coefficients and the mass energy transfer coefficients reflect:

"differences of measured values among independent experimenters and the magnitudes of ad hoc adjustments, corrections and extrapolations of quantities entering into the computation of cross sections from incomplete available theory".

Figure 2.4 shows the differences of the WT1 material mass attenuation coefficients used with the EGS4, analytical and VOXSCAT codes from those stated in ICRU Report No. 44 (1989). The coefficients used with the VOXSCAT code differ by less than 1% from the ICRU data. The largest difference is 2.9% for comparing the

PEGS4 data with the ICRU data at a photon energy of 50 keV. Hence, there are no significant differences between the sets of mass attenuation coefficients.

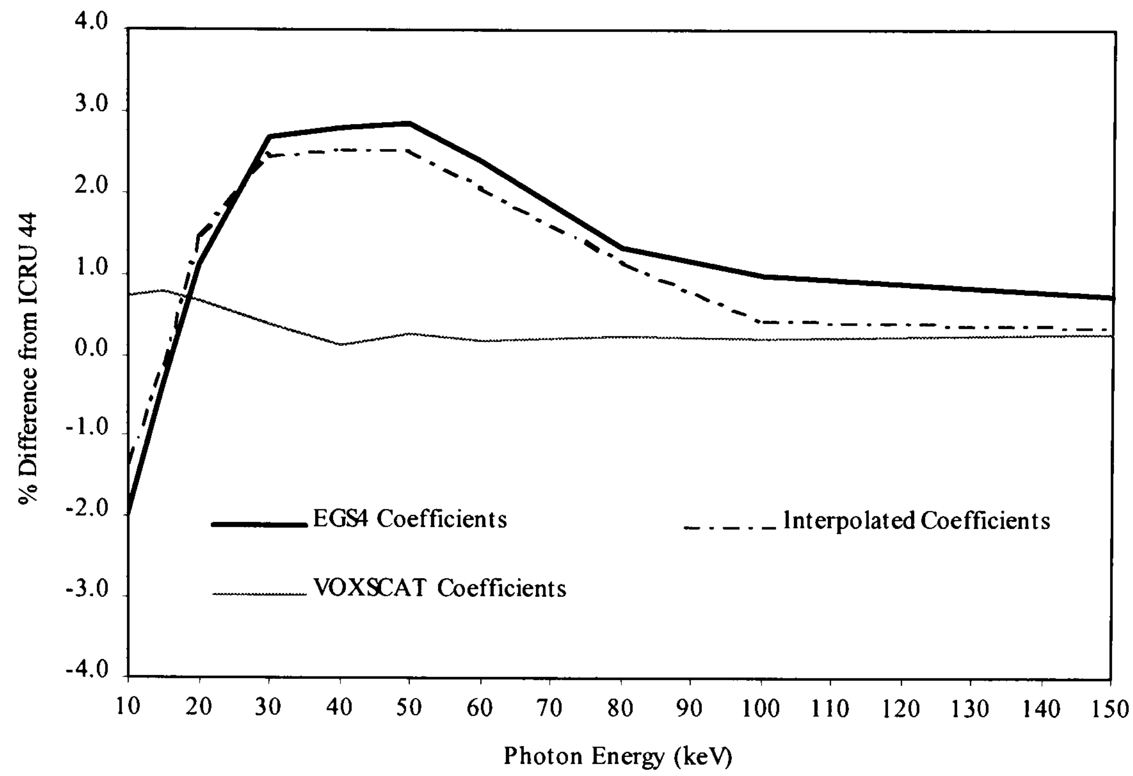

Figure 2.4*. The differences between the mass attenuation coefficients for WT1 material used in the Monte Carlo and analytical codes to those published in ICRU Report No. 44 (ICRU, 1989).*

2.9 Accessing the Mass Energy Transfer Coefficients in the Computer Programs

The mass energy transfer coefficients for air $[\mu_{tr}/\rho]_{air}$ are required for calculating fluence to air kerma conversion factors $C_{K.air}$ from 1 to 150 keV. The VOXSCAT code carries out logarithmic interpolation directly on the tabulated data of Hubbell (1982). The analytical and XYZSCAT codes use equation 2.16 (Rogers, 1984b) to calculate the fluence to air kerma conversion factors. The mass energy transfer coefficients were obtained using a fifth order polynomial (equation 2.15) with the fitted parameters given in table 2.2. These parameters were derived from the tabulated values of Hubbell (1982) by the general linear least squares method (Press et al., 1992). Equation 2.15 calculates the mass energy transfer coefficients in units of m^2/kg.

$$C_{K,air} = 1.602 \times 10^{-10} E \left[\frac{\mu_{tr}}{\rho} \right]_{air} \qquad (2.16)$$

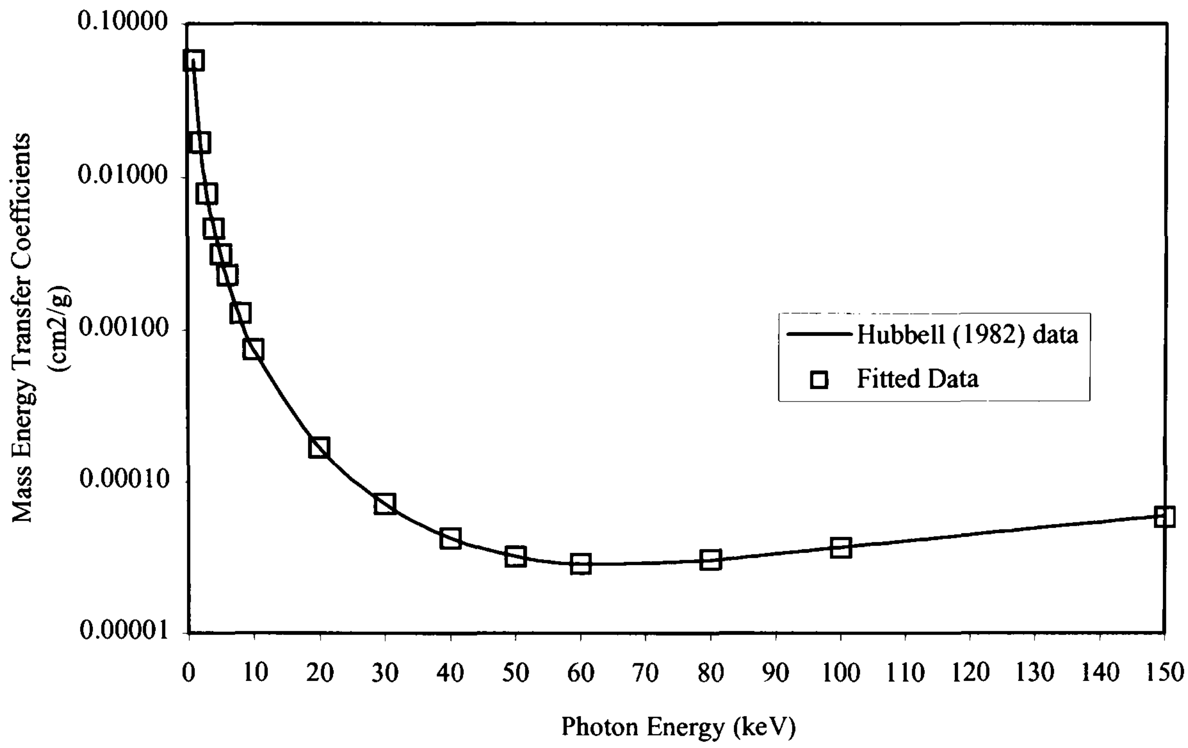

Figure 2.5*. The comparison of the mass energy transfer coefficients for air from Hubbell (1982) and the least squares fitted values.*

Figure 2.5 shows good agreement between the mass energy transfer coefficients tabulated by Hubbell (1982) and the least squares fitted values. The 'goodness of fit' of the values calculated using the parameters in table 2.2 to Hubbell's data were estimated using the R^2 and adjusted R^2 statistics as detailed in section 2.7. For the energy range from 1 to 10 keV, the R^2 and adjusted R^2 statistics are 0.39 and 0.37. This indicates that the fit may not be quite as good as first thought. The largest difference between the fitted and Hubbell's coefficients is 8% at 8 keV. However, these differences are unlikely to introduce significant errors into the calculation of scattered or transmitted air kerma as photons with energies between 1 and 10 keV are very rare and have a short mean free path. It was observed in the calculations of scattered x-ray spectra in section 7.2.1.5 that the lowest photon energy was 13 keV. For the energy range from 10 to 150 keV, there is good agreement between the fitted coefficients and the tabulated values as both R^2 and adjusted R^2 are very close to 1.

	Fitted Parameter Values for Air	
Energy Range Parameter	**1 keV – 10 keV**	**10 keV – 150 keV**
α	8.000×10^{-14}	-3.800×10^{-12}
β	-4.080×10^{-10}	1.203×10^{-9}
δ	8.302×10^{-7}	3.865×10^{-7}
γ	-1.737×10^{-4}	5.283×10^{-7}
ε	3.548×10^{-2}	-1.318×10^{-4}
η	-2.236×10^{0}	3.181×10^{-3}

Table 2.2. *The parameters obtained in this work from least squares fitting a 5th order polynominal to the mass energy transfer coefficients for air tabulated by Hubbell (1982).*

2.10 Dosimetric Quantities

2.10.1 Fluence and Energy Fluence

The radiation field can be characterised by the particle fluence Φ which Attix (1986) states is the expectation value of the number of rays impinging a finite sphere surrounding a point P during a time interval extending from an arbitrary starting time t_0 to a time t. The fluence is then defined in equation 2.17, by reducing the sphere to an infinitesimal point at P, as the quotient of the differential expectation value, dN, with a great circle area, da, such that:

$$\Phi = \frac{dN}{da} \qquad (2.17)$$

Chilton (1978, 1979) provides an alternative definition of fluence:

"the fluence at a point P is numerically equal to the expectation value of the sum of the particle track lengths (assumed to be straight) that occur in an infinitesimal volume of dV at P, divided by dV".

This definition can then be expressed in equation 2.18 as the sum of the particle track lengths $\bar{s}$ travelling through the volume dV.

$$\Phi = \frac{\sum \bar{s}}{dV} \qquad (2.18)$$

The energy fluence Ψ takes into account the energies of individual rays. Let R be the expectation value of the total energy or the radiant energy (ICRU, 1998), exclusive of the rest mass energy, carried by all the N rays striking a sphere surrounding point P. By employing the same assumptions as those for the particle fluence, the energy fluence is the quotient of R with da such that:

$$\Psi = \frac{dR}{da} \tag{2.19}$$

When only a single energy, E, of particles are present, $R = EN$ and the energy fluence is related to the particle fluence by:

$$\Psi = E\Phi \tag{2.20}$$

2.10.2 Kerma

Kerma K (equation 2.21) is defined as the kinetic energy transferred, $d\overline{E}_{tr}$, from photons to electrons in a volume element whose mass is dm. This is expressed in terms of the System Internationale (SI) units of the Gray which is equivalent to Joule per kilogram (J/kg).

$$K = d\overline{E}_{tr} / dm \tag{2.21}$$

The kerma at a point P is related (equation 2.22) to the energy fluence by the mass energy transfer coefficient for air for monoenergetic photons.

$$K = \Psi\left[\frac{\mu_{tr}}{\rho}\right] \tag{2.22}$$

2.10.3 Absorbed Dose

Absorbed dose D is also expressed in Systeme Internationale (SI) units of the Gray. The absorbed dose is defined as the energy absorbed $d\overline{E}_{ab}$ in a mass dm as shown in equation 2.23.

$$D = d\overline{E}_{ab} / dm \tag{2.23}$$

In the diagnostic x-ray energy range where no Bremsstrahlung is produced, the mass energy transfer coefficients equals the mass energy absorption coefficients providing the distance travelled by electrons before being absorbed is negligible. In this case, the absorbed dose equals the kerma and equation 2.24 can be used to express the absorbed dose.

$$D = \Psi\left[\frac{\mu_{en}}{\rho}\right] \tag{2.24}$$

2.11 Summary of Work

This chapter describes the photon interactions: the photoelectric effect, incoherent and coherent scattering which are simulated by the Monte Carlo computer programs. These interactions produce attenuation of the x-rays as they pass through matter. In order for the programs to simulate radiation transport, they must have access to mass attenuation coefficients and fluence to air kerma conversion factors in order to calculate air kerma. The methods for obtaining these coefficients are described. The values obtained have been analysed and shown not to be significantly different from the published values at the energies used in the calculations. Therefore, the coefficients employed should not be a source of error in the calculations.

Chapter 3: Experimental Work for the Validation of the Computational Models

3.1 Introduction

Demonstrating that the calculated values are comparable to the measured values in the clinical situation is an important part of developing computational models. This chapter describes two sets of measurements carried out in the clinic. Firstly, scatter measurements were undertaken for different phantom materials irradiated by an x-ray tube with a modern medium frequency generator. The phantom materials included a block of WT1 material which was used to represent the patient. Other phantom materials used included aluminium, brick, concrete and copper slabs used to represent commonly used building and shielding materials. The details of the experimental arrangements were carefully noted for incorporation in the XYZSCAT code calculations. During the course of the work, it was found that other materials in the x-ray room apart from the phantom influence the measured scatter and therefore, a short study was undertaken.

Secondly, a patient study was undertaken which provided measurements of entrance air kerma and optical density (OD) on chest and lumbar spine radiographs. This work was used to validate the VOXSCAT code and the voxel phantom. The diversity of patients makes it difficult to validate the voxel phantom as being representative of a patient. Therefore, an intermediate step was undertaken to measure the transmission and the OD on films behind PMMA (polymethyl methacrylate) slabs placed in the imaging system. The intermediate step provides data for checking that the imaging system is described properly. This chapter describes the experimental details of the measurements and the results are compared with calculations in sections 7.4 to 7.6.

3.2 Measurements of Scatter from Slab Phantoms

Scatter measurements were undertaken with a Philips X-ray unit in a Fluoroscopy room at the Churchill Hospital, Oxford. An overcouch x-ray tube was operated in radiographic mode for all exposures.

3.2.1 Initial Measurements

3.2.1.1 Quality Control Measurements

Initially, a radiation protection survey was undertaken. The tests were conducted with a *DIGI-X Plus* (RTI Electronics AB, Mölndal, Sweden), using a Keithley 15cc ionisation chamber (Keithley Instruments, Ohio), remote controlled with "oRTIgo" software (RTI Electronics AB, Mölndal, Sweden).

Parameter	Philips X-ray Tube
X-ray Generator	Philips Medio 65 CP-H
Focal Spot Size (mm)	0.6/1.3
Nominal Tube Potentials (kV)	50 – 120
Target Angle (°)	13
Half value layer (mmAl)	3.3 (at 80 kV)
Filtration (mmAl)	3.4 (at 80 kV)
Voltage Ripple (%)	3

Table 3.1. *X-ray tube characteristics.*

Table 3.1 shows the results for the half value layer (HVL), tube filtration and voltage waveform and the x-ray tube characteristics. Additional checks were carried out on incident air kerma, tube potential (kV_p) accuracy and tube current (mA) and exposure time (s) linearity. All tests gave satisfactory results.

3.2.1.2 Half Value Layer Measurements

Additional HVL measurements were carried out. High purity aluminium filters were positioned on the exit side of the DAP meter at a distance of 28.3 cm from the x-ray focus. A Keithley 15cc ionisation chamber, attached to an E.I.L. 37D electrometer, was placed 1 metre from the x-ray focus. The field size was 10 cm × 10 cm at 1 m from the x-ray focus.

Figure 3.1 shows the experimental arrangement which follows the guidelines stated in the literature. IPEM Report No. 32 (Cranley, 1995) states a standard distance between the x-ray focus and the chamber as 1 m. The filters being placed as close as possible to the x-ray focus. The HPA (1976) recommend that the field size is sufficient to cover the chamber with a margin of 2 cm. Thus, the 10 cm × 10 cm field size was used as the diameter of the Keithley 15cc chamber is 6.4 cm.

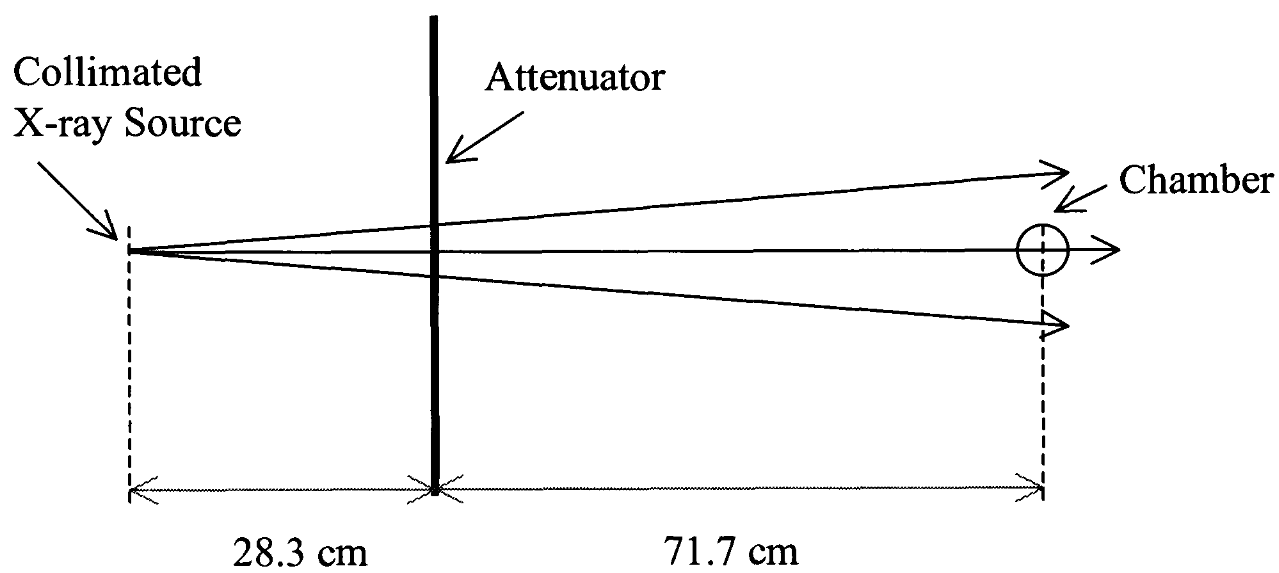

Figure 3.1*. The experimental arrangement for measuring the half value layer.*

Unfiltered air kerma readings were taken at the start and at the end of the sequence of measurements for each tube potential. Air kerma measurements were taken with added filtration in steps of 0.4 mmAl until the output reduced to below 0.5 of the unfiltered value. For transmissions around 0.5, the filtration was added in steps of 0.2 mmAl. Certain measurements were repeated to check their reproducibility. All measurements were then normalised to the average unfiltered air kerma. The thickness required to give a transmission of 0.5, the half value layer, was found by interpolation.

3.2.2 Scattering Materials

Material	Phantom Dimensions
Aluminium	300 mm long, 200 mm wide and 10.8 mm thick
Brick	260 mm long, 430 mm wide and 102.5 mm thick
Concrete	443 mm long, 213 mm wide and 100 mm thick
Copper	300 mm long, 300 mm wide and 2 mm thick
WT1	305 mm long, 305 mm wide and 100 mm thick

Table 3.2*. The materials and their dimensions used in the experiments to measure scatter.*

Table 3.2 shows the five scattering materials and their dimensions. The aluminium and copper slabs are of high purity as they are used as filter materials. The copper slabs were supported on a plywood block of dimensions: 300 mm long, 300 mm wide and 10 mm thick.

A Thermolite aerated concrete block was employed as a scattering material as it is representative of the concrete material used in the construction of x-ray rooms. It should be noted that as thermolite blocks are of low density, they would not be used as protective barriers without using barytes plaster as additional shielding. In section 7.3.2.3, figure 7.25 shows that the backscattered radiation is insensitive to concrete thickness which implies backscatter is also insensitive to concrete density. Therefore, only a small density correction may be applied to the measured scatter to estimate the scatter from concrete blocks of normal density.

Three holed bricks were employed as a scattering material as they are representative of the brick material used in the construction of x-ray rooms. However, three holed bricks should not be used for shielding x-ray rooms without insuring that the holes are filled with mortar (Sutton and Williams, 2000). The measured scatter will be lower than the scatter for a solid brick. Therefore, a density correction may be applied to the measured scatter to estimate the total scatter. Table 3.2 shows the dimensions for two columns of bricks with each column having four bricks.

3.2.3 Scatter Measurements

Scatter measurements were performed in a newly commissioned Fluoroscopy room at the Churchill Hospital, Oxford. The majority of the measurements were carried out over a two month period to ensure that the imaging system parameters did not alter. Some measurements were repeated at a later date. It was found that the tube potential settings had been adjusted by an engineer at this time. Therefore, a nominal tube potential of 117 kV had to be used instead of 120 kV for the repeat measurements. Output and scatter measurements were repeated to check the consistency of the experimental set up on each day the measurements were undertaken.

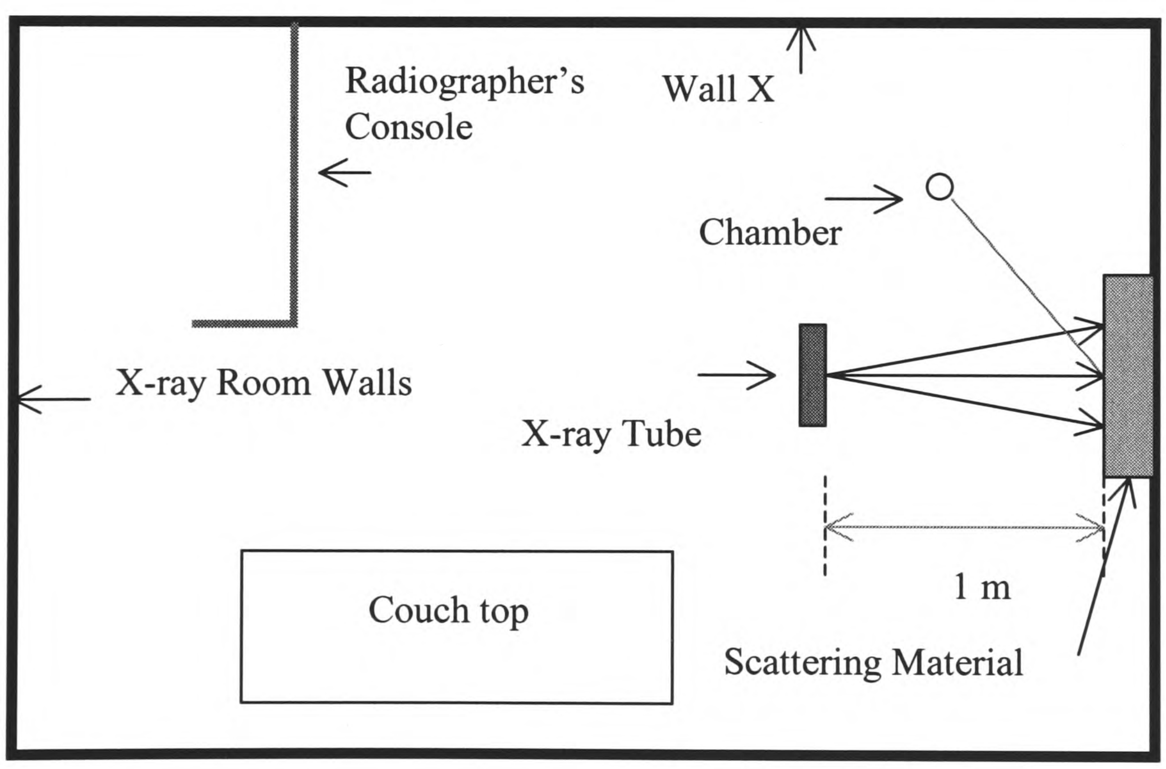

Figure 3.2. *An overhead view of the positions of the x-ray tube and detector in the x-ray room with the scattering material supported against the x-ray room wall.*

Figure 3.2 shows the x-ray tube focus positioned 1 m from the surface of the scattering material. The centre of the field was aligned to the centre of the phantom's incident surface with the aid of the light field. The scatter was measured with a

Pitman 35cc ionisation chamber connected to an E.I.L. 37D electrometer. The centre of the chamber's measuring volume was positioned 1 m from the field centre on the phantom's surface. The chamber was placed at the same height above the floor as the field centre for all angles of scatter.

The scattered air kerma was measured for a range of tube potentials, field sizes, scattering angles and scattering materials. The phantom was placed in the centre of the x-ray room for measuring forward directed scatter. The mAs setting was changed to keep the reading on the same meter scale for increasing tube potential. The different parameters investigated were varied systematically. The percentage scatter was determined by the ratio of the scattered air kerma to the incident air kerma measured by the *DIGI-X* instrument.

3.2.4 Leakage Measurements

Leakage from the head of the x-ray tube was measured with the collimators closed. The detector was placed in the same position as the scatter was measured. It was found that the leakage readings were negligible in most cases. The scatter measurements were corrected if required.

3.2.5 Influence of Scatter from the Walls, Ceiling and Floor of the X-ray Room

An attempt was made to measure the secondary scatter from one of the walls (wall X in figure 3.2) and adjacent sections of wall, ceiling and floor. Lead sheets 2 mm thick were placed in close proximity to the detector to shield out the scatter contributions from the x-ray tube head and the phantom. The ratio of the shielded to the unshielded air kerma was 0.067. This demonstrates that the secondary scatter from the walls, ceiling and floor has only a small contribution to the total scatter.

3.2.6 Influence of X-ray Tube Head Scatter

Figure 3.3 shows that the detector is positioned close to the collimators and DAP meter for measuring scatter from the phantom at an angle of 135°. Williams (1996) suggested that there may be a significant contribution to the measured scatter from the x-ray tube head but did not investigate further. Therefore, a short study was made of this suggestion by placing a mobile shield between the detector and the x-ray tube head as shown in figure 3.4.

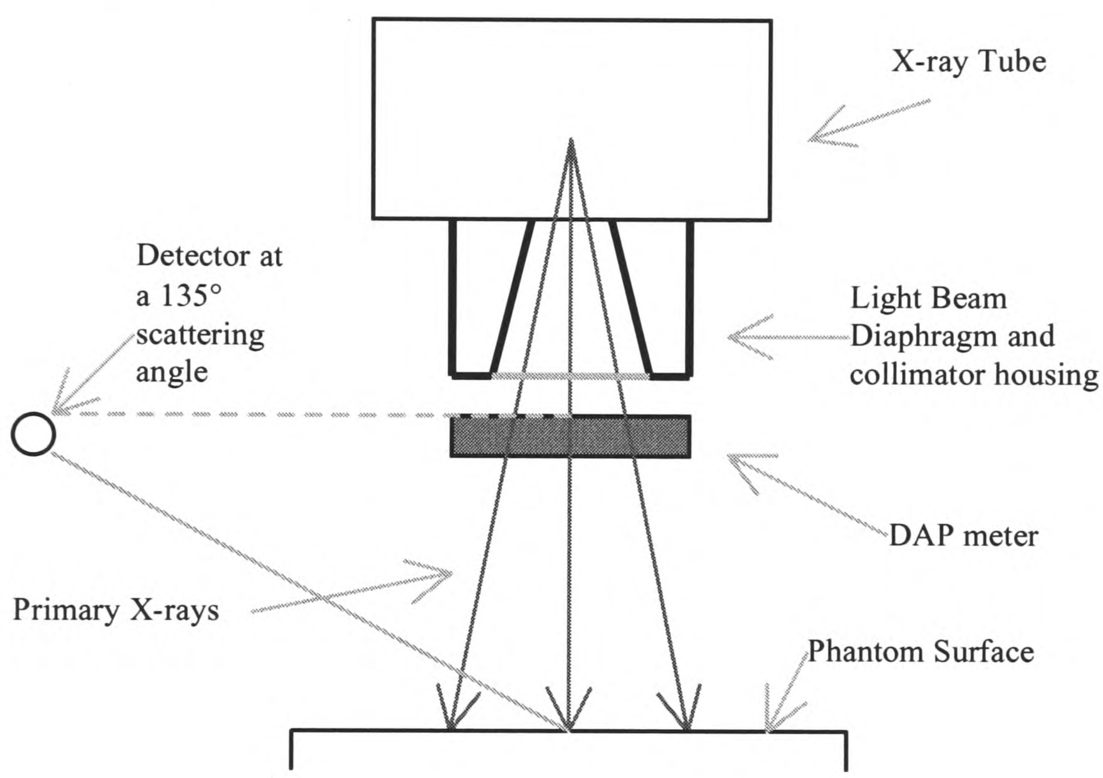

Figure 3.3. *The detector position for measuring scatter at a 135° angle in relation to the DAP meter and the x-ray tube collimators.*

The measurements were carried out with the WT1 block placed in the centre of the x-ray room. Measurements were undertaken for a 135° angle for nominal tube potentials from 50 kV to 117 kV and for 45°, 87°, 120° and 150° angles at 70 kV. Readings were taken with the collimator housing and DAP meter unshielded and shielded. It was assumed that the secondary scatter from the mobile shield itself reaching the detector will be small and was further minimised by positioning the mobile shield as close as possible to the x-ray tube head (figure 3.4).

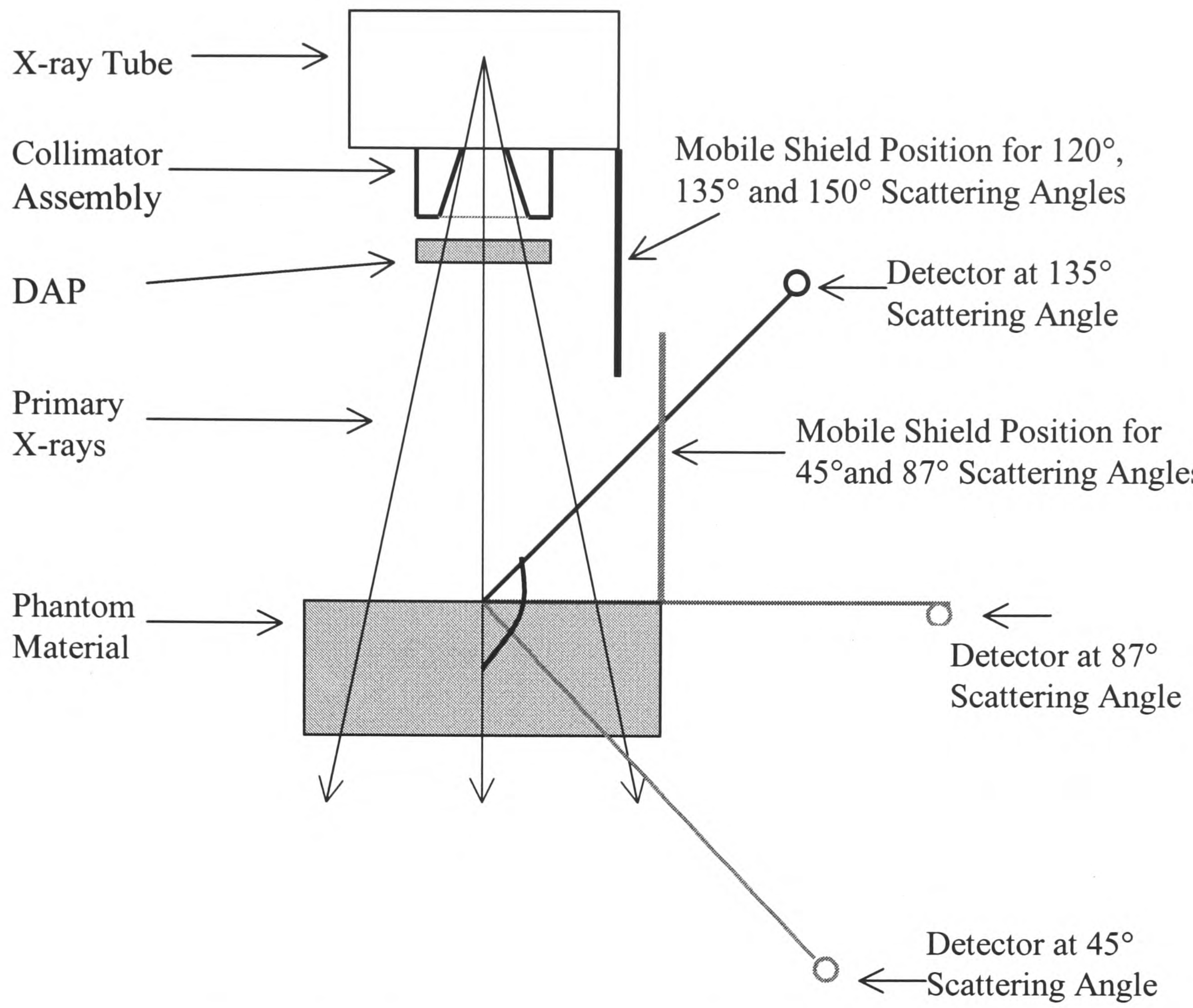

***Figure 3.4**. The detector and mobile shield positions for scatter measurements at angles of 45°, 87° and 135°.*

The transmission through the mobile shield was measured to determine whether the scatter from the x-ray tube head was reduced significantly with the mobile shield in position. Figure 3.5 shows the experimental arrangement for the measurement of the primary beam transmission of the mobile shield using the Pitman 35cc ionisation chamber. It was placed at 1 metre from the x-ray tube focus with a 400 cm^2 field size. The mobile shield has a thickness stated by the manufacturer to be 0.5 mm lead equivalent.

The measured percentage transmissions were 0.62% and 4.2% for 70 kV and 117 kV x-rays. Archer et al. (1994) provides measured values of 0.53% and 5.0% for 70 kV and 117 kV x-rays while Simpkin (1989) provides calculated values of 0.81% and 5.0% for 70 kV and 117 kV x-rays. The measured transmission through the mobile shield is representative of the values given by other investigators. Thus, the mobile shield should reduce the x-ray tube head scatter to a negligible value.

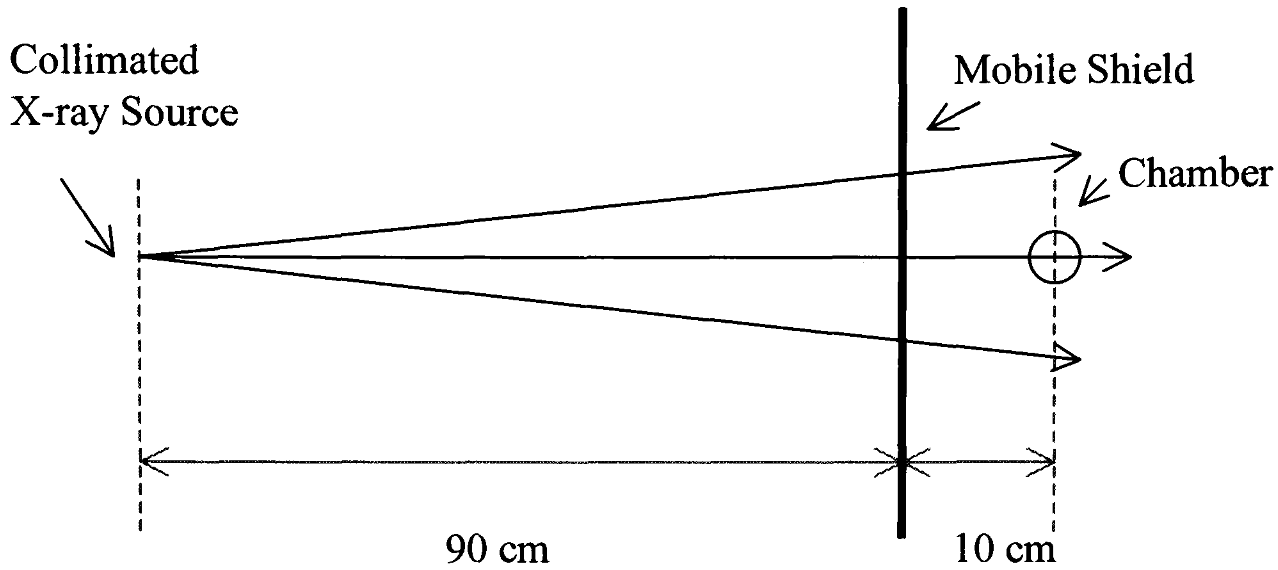

Figure 3.5. *Experimental arrangement for measuring primary beam transmission through the mobile shield.*

Nominal Tube Potential (kV)	Angle of Scatter (°)	Shielded to Unshielded Scatter Measurement Ratio
50	135	0.75
70	45	0.67
70	87	0.34
70	120	0.76
70	135	0.77
70	150	0.91
117	135	0.78

Table 3.3. *The ratio of the scatter measurements with and without the x-ray tube head shielded out.*

Table 3.3 shows the ratios of the measurements with and without the scatter from the x-ray tube head being shielded from the detector. Table 3.3 shows there is significant contribution to the total scatter from the collimator system and DAP meter as the scattered air kerma is reduced by 24% with the mobile shield in place for an 120° scattering angle. The ratios also show that the x-ray tube head scatter contribution is independent of tube potential being 0.75, 0.77 and 0.78 for 50 kV, 70 kV and 117 kV x-rays respectively at a 135° scattering angle.

Trout and Kelley (1965) measured significant scatter contributions from the x-ray tube head by measuring the off-axis dose in a water phantom irradiated by 150 kV x-rays. They used lead to shield their detector from different sources of scattered radiation. The dose was reduced by 27% by shielding the collimator system and its face plate (1.2 mm thick PMMA). A DAP meter was not present in Trout and Kelley's measurements.

3.2.7 Details of the DAP Meter

From the results of the short experimental study, it is therefore necessary to model the DAP meter (Type B 727085, PTW, Freiburg, Germany) in the XYZSCAT code. The collimator system however cannot readily be modeled due to its complicated design. The DAP meter is attached to a tray 6 mm underneath the exit port of the collimator. The distance from the x-ray focus to the top of the DAP meter is 266 mm. The DAP meter has dimensions: 162 mm long, 181 mm wide and 17 mm thick. It is constructed from PMMA with walls 2 mm thick and an air gap between them. The DAP meter was modeled in the calculations as a solid block of PMMA with an average density of 0.319 g/cm^3 found by the mass of Perspex divided by the volume of the DAP meter.

3.2.8 Uncertainty in Output Measurements

The Pitman 35cc chamber was used to check the consistency of the incident air kerma from the x-ray tube on each day the measurements were undertaken. All exposure settings (kV, mAs and field size) were noted for each measurement. All measurements were corrected for ambient conditions of temperature and pressure. The difference between the measured output with the Pitman 35cc and the *DIGI-X* was within ±5%. This is within the measuring uncertainty (given below) of the Pitman chamber.

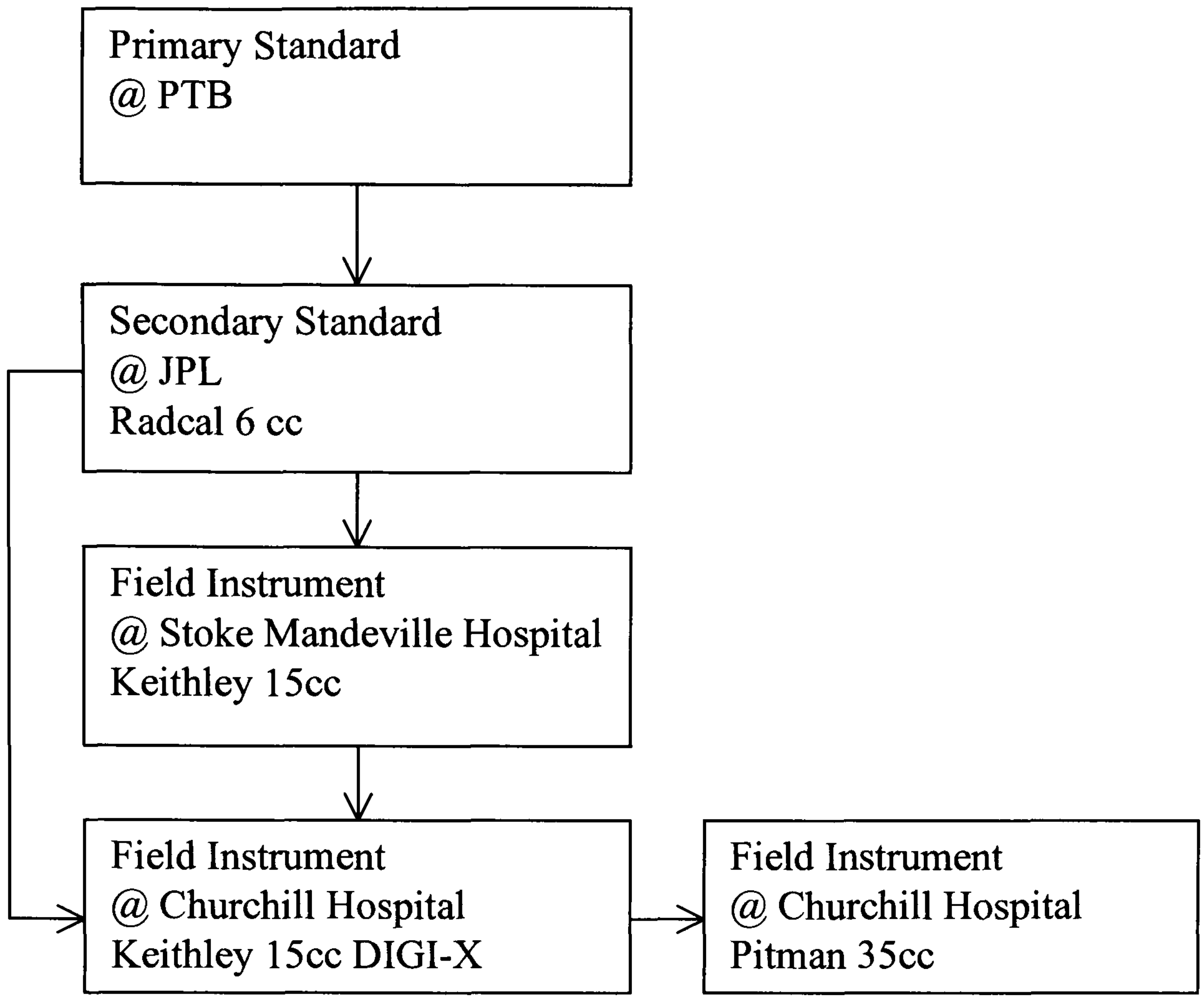

Figure 3.6*. The calibration chain for the DIGI-X and Pitman chambers.*

Figure 3.6 shows the calibration chain of the Keithley 15cc *DIGI-X* and the Pitman 35cc ionisation chambers traceable to a primary standard at PTB (Physikalisch-Technische Bundesanstalt), Germany. The *DIGI-X* is calibrated directly to the secondary standard at JPL (John Perry Laboratory), St. George's Hospital, London in one year and with another Keithley 15cc ionisation chamber the following year.

The *DIGI-X* calibration uncertainty was ±3.0% in both cases. The calibration uncertainty of the Pitman chamber was ±3.8%. The reproducibility of the output measurements were ±3.4% and ±7.0% for the *DIGI-X* and the Pitman chambers. This provides overall uncertainties of ±4.5% and ±8.1%. The *DIGI-X* output measurements were used to give the percentage scatter as the overall uncertainty of the *DIGI-X* readings was less than the uncertainty in the reproducibility of the Pitman chamber readings.

3.2.9 Uncertainty in Tube Potential

The *DIGI-X* tube potential calibration uncertainty was ±2.4% between 50 kV and 150 kV. This gives an uncertainty between ±1 kV and ±3 kV for nominal tube potentials between 50 kV and 120 kV.

3.2.10 Uncertainty in Half Value Layer Measurements

The overall uncertainty in the HVL measurement takes account of the reproducibility in the air kerma measurement (±3.4%), the energy response of the chamber (±2%) and the uncertainty in the interpolation of the readings (±2%). A conservative estimate of the interpolation uncertainty was obtained from the difference in the HVLs found by linear interpolation and quadratic interpolation for transmissions above and below 0.5.

Section 3.2.1.2 describes the experimental arrangement used to minimise scatter from the attenuators as much as possible. However, there will still be a scatter contribution present. This error in the HVL can be estimated from data presented by Knight (1996). Figure 3.7 shows Knight's data for the variation in HVL (in terms of mm Cu) with field size and attenuator to chamber distance. The error in the HVL is estimated as ±8% for a field size incident on the attenuators of 8 cm^2 (equivalent to 3.2 cm field diameter) and the 1 m distance between the x-ray focus and the chamber. Therefore, the uncertainty in the HVL was found to be ±9.1% or between ±0.1 mmAl and ±0.4 mmAl depending on the tube potential.

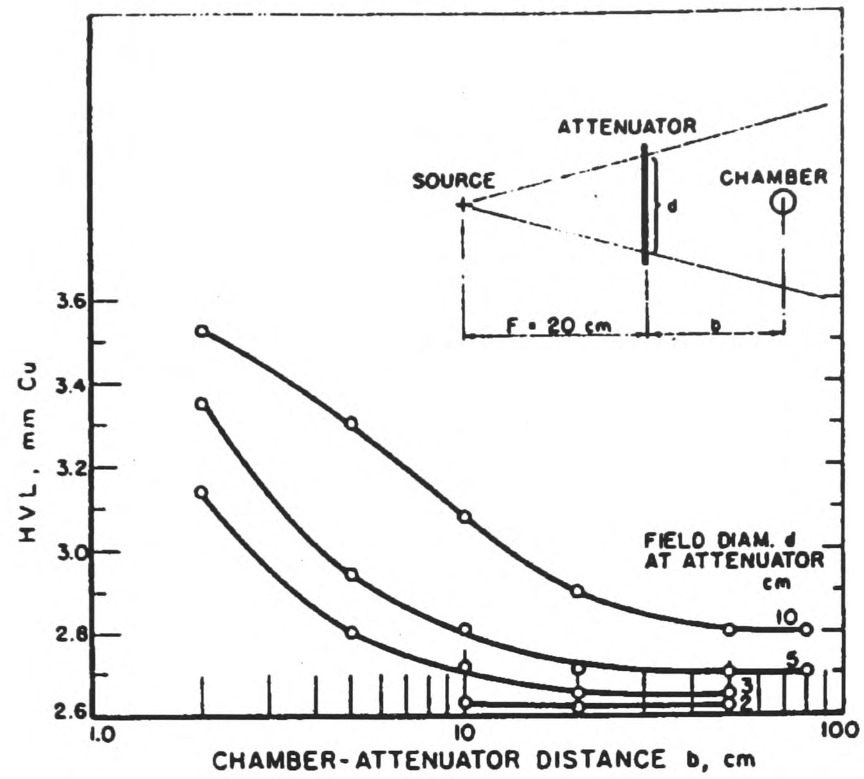

***Figure** 3.7. The variation of HVL with field size at the attenuator and the distance between the attenuator and chamber.*

3.2.11 Uncertainty in the X-ray Tube Filtration

The method of Gilmore and Cranley (1990) can be used to estimate the uncertainty in the x-ray tube filtration. It uses the combined uncertainties of the tube potential (±2 kV at 80 kV), the voltage ripple (±3%), the HVL (±0.30 mmAl at 80 kV) and the target angle (±1°).

The uncertainty in the filtration of the Philips x-ray tube was calculated to be ±18.6% by Gilmore and Cranley's method at 80 kV. Gilmore and Cranley achieved an uncertainty of ±10% at best whereas Nagel (1988) achieved an uncertainty of ±17%. The main difference between this work and that of Gilmore and Cranley is that Gilmore and Cranley have an uncertainty of ±0.06 mmAl for the HVL compared to an uncertainty of ±0.30 mmAl for the HVL measured in this work.

3.2.12 Uncertainties in the Scatter Measurements

The scatter measurements undertaken with the Pitman chamber were reproducible to within ±7%. This large uncertainty was due to the rapid variation of scatter for small changes in scattering angle and distance from the scattering material. The overall uncertainty in the scatter measurements was ±9.4% including the calibration uncertainty (±3.8%) and the energy response of ±5%. This produces an uncertainty in the measured percentage scatter of ±10.4%.

3.3 Collection and Analysis of Patient Images

Patient images were collected and the patient entrance doses were measured. Sandborg and Persliden (private communication) obtained this data at Linköping University, Sweden, as part of an EU funded project entitled 'Optimisation and Predictivity in Medical Radiation Protection'. This data was made available to validate the VOXSCAT code and to check that the voxel phantom was representative of a patient. The patient images were digitised and transferred to the UK via the internet. Approximately half the images were analysed at the Royal Marsden Hospital, London and the other half analysed in Linköping. A brief summary of this work is described below. The comparison of measurements with calculations is described in sections 7.4 to 7.6.

3.3.1 Image Acquisition and Digitisation

A total of 58 chest radiographs in a mixture of posterior-anterior (PA) and lateral (LAT) projections were acquired from Norrköping Hospital. A total of 35 lumbar spine (LS) films, in a mixture of frontal (posterior-anterior or anterior-posterior (AP)) and lateral projections, were acquired from Linköping University Hospital.

All films were digitised with a Vidar VRX-12 digitiser at Malmö University Hospital. The relationship between the grey level in the digitised image and optical density was obtained using a calibrated film step-wedge. The relationship between optical density and air kerma at the film (H and D curve), was derived from carefully controlled measurements some distance behind a block of aluminium for each screen-film combination used. This arrangement is described in detail in section 3.4.

3.3.2 Entrance Dose Measurements

The entrance surface dose for each patient exposure was measured using thermoluminescent dosimeters (TLDs) of LiF (discs with 45 mm diameter and 0.9 mm thick). The TLDs were individually calibrated at 75 kV for lumbar spine imaging and at 140 kV for chest imaging (Sandborg et al., 1997).

3.3.3 Image Analysis

Dynamic range provides a method for investigating the influence of patient anatomy on the radiographs produced. It has been determined for comparison with the dynamic range of the voxel phantom, representing the patient, used in the voxel Monte Carlo model.

Measurements of dynamic range were carried out with ANALYZE software in London and IMAGE TOOL software in Linköping. The software was used to outline regions of interest including the lungs, heart and mediastinum in both the chest examinations. The regions of interest extended across the whole field size in both lumbar spine examinations. Pixel value frequency distributions (histograms) of the incident air kerma at the screen were obtained for these regions of interest and were used to investigate the dynamic range. For comparison purposes, the positions of the 10%, 20%, 30%, 70%, 80% and 90% points of the cumulative frequency distribution were found and the ratios of P90:P10, P80:P20 and P70:P30 obtained. The results from both centres were collated.

The 50% point in the cumulative optical density distribution (median OD value) was also obtained. This point is used to normalise the Monte Carlo estimates of incident air kerma (section 6.5.3.1).

3.4 Measurements of Transmission and Optical Density behind Slab Phantoms

Direct comparison of the VOXSCAT code calculations with the patient measurements is difficult. Therefore, an intermediate step was to compare measurements of transmission and optical density behind PMMA blocks with calculations. The measurements were undertaken by Sandborg and Persliden (private communication) and were made available to provide a validation of the computational method and the image system specifications. Therefore, a concise summary is given of the experimental arrangements.

Measurements were undertaken for three imaging systems: the Linköping Physics laboratory, the Linköping lumbar spine (LS) laboratory and the Norrköping chest laboratory. Table 3.4 shows details of the chest and lumbar spine imaging systems which were used to obtain the patient x-ray films. Following the collection of patient images and the measurement of the H and D curve in the chest laboratory, 0.1 mmCu was added to the filtration. The Physics laboratory was used to obtain measurements under rigorously controlled conditions away from the clinical environment.

A Solidose instrument (RTI Electronics AB) was used for the measurements of air kerma and was cross calibrated with a Shonka ionisation chamber. The Shonka ionisation chamber (Exradin Ltd) was calibrated at the SSI calibration laboratory in Stockholm.

Parameter Type	Norrköping Chest Imaging System	Linköping Lumbar Spine Imaging System
X-ray Tube		
Tube Potential (kV)	140 (PA and LAT)	72 (PA) and 77 (LAT)
Filtration (mmAl)	1.5	3.1
Target Angle (°)	13.5	12
Voltage Ripple (%)	0.0	0.0
Imaging Geometry		
Focus Film Distance (cm)	143.6	110.0
Focus Chest Support/Couch Top Distance (cm)	141.5	97.9
Air Gap (cm)	1.8	11.6
Chest Stand/Couch Top	4mm PMMA	1.947 g/cm^2 PMMA
Anti-scatter Grid	$N=40cm^{-1}$, r=12, d=50μm, D=200μm, 2t=0.3mmAl	$N=70cm^{-1}$ ($N=79cm^{-1}$ actual) r=16, d=36μm, D=90μm, 2t=0.4mmAl
Cassette Front Material and Thickness	1.74 mmAl	1.74 mmAl
Screen	Agfa Curix Medium (120mg/cm^2)	Kodak Lanex Medium (118.4mg/cm^2)
Film	Fuji Super HRL	Fuji HRE

***Table 3.4**. Imaging system characteristics.*

3.4.1 Experimental Arrangement for the Linköping Physics Laboratory

In the Physics laboratory, measurements were made of (1) the transmission through blocks of PMMA, using an ionisation chamber as monitor and (2) the optical density on a film exposed beneath slabs of PMMA, for known exposure conditions. Each set of measurements was made at a range of tube potentials, and two series of measurements were made at different times.

Table 3.5 details the geometry used in both experiments. In the imaging geometry, the screen/film combination was Lanex regular / Fuji Super HRE. The regular screen has a thickness of 133.4 mg/cm^2 Gd_2O_2S. A Kodak X-omatic cassette was used with front face thickness equivalent to 1.74 mm aluminium. The grid was manufactured by Lysholm with parameters: strip density N=70 cm^{-1}, grid ratio r=12, strip width d=36 μm, interspace width D=90 μm, aluminium interspace and grid covers of 2 × 0.2 mm thick aluminium.

	Transmission Geometry		Imaging Geometry
Tube Potentials Used (kV)	50, 70, and 100	70 and 100	60 and 100
Field Size @ FSD (cm^2)	7.5 × 7.5	8.0 × 8.0	22.89 × 22.89
FFD (cm)	150	150	110
FSD (cm)	100	100	94.3
Phantom Area (cm^2)	35 × 35	35 × 35	35 × 35
Phantom Thickness (cm)	3.93 and 11.77	3.93 and 11.77	15.7

Table 3.5. *The transmission and imaging geometries employed in the Linköping Physics Laboratory.*

3.4.2 Experimental Arrangement in the Norrköping Chest Laboratory

In the Chest Laboratory, measurements were made of the optical density on a film exposed beneath slabs of PMMA, for known exposure conditions. The measurements were made both with and without the grid and chest stand, and at two tube potentials. Table 3.6 details the geometry used in the measurements of optical density.

	Phantom+Receptor	Phantom+Chest stand+ Grid+Receptor
Tube Potentials Used (kV)	90 and 140	90 and 140
Field Size @ FSD (cm^2)	28.7 × 29.8	28.7 × 29.8
FFD (cm)	139.0	143.6
FSD (cm)	126.7	126.7
Phantom Area (cm^2)	35 × 35	35 × 35
Phantom Thickness	11.77	11.77

Table 3.6. *The imaging geometries used in the experiments in the chest laboratory.*

3.4.3 Experimental Arrangement in the Linköping Lumbar Spine Laboratory

In the Lumbar Spine Laboratory, measurements were made of (1) the transmission through the table top and table top plus grid using an ionisation chamber as monitor and (2) the optical density on a film exposed beneath slabs of PMMA, for known exposure conditions. The measurements for (2) were made both with and without the grid and table top. This was carried out by placing the screen-film combination in front of and behind the table top and grid system. Each set of measurements was made at a range of tube potentials, and two series of measurements were made at different times. Table 3.7 details the geometry used in the measurements of optical density.

	Phantom+Receptor			**Phantom+Couch Top+Grid+ Receptor**		
Tube Potentials Used (kV)	50 and 70	90	70 and 99	50 and 70	90	70 and 99
Field Size @ FSD (cm^2)	27.5 × 27.4	26.2 × 26.2	16.1 × 16.2	26.8 × 26.8	25.6 × 25.6	16.1 × 16.2
FFD (cm)	99.97	99.97	96.9	110	110	109.2
FSD (cm)	88.2	84.4	77.7	86	83	77.7
Phantom Area (cm^2)	35 × 35	35 × 35	35 × 35	35 × 35	35 × 35	35 × 35
Phantom Thickness (cm)	11.77	15.7	18.22	11.77	15.7	18.22

Table 3.7. *The imaging geometries used in the experiments in the lumbar spine laboratory.*

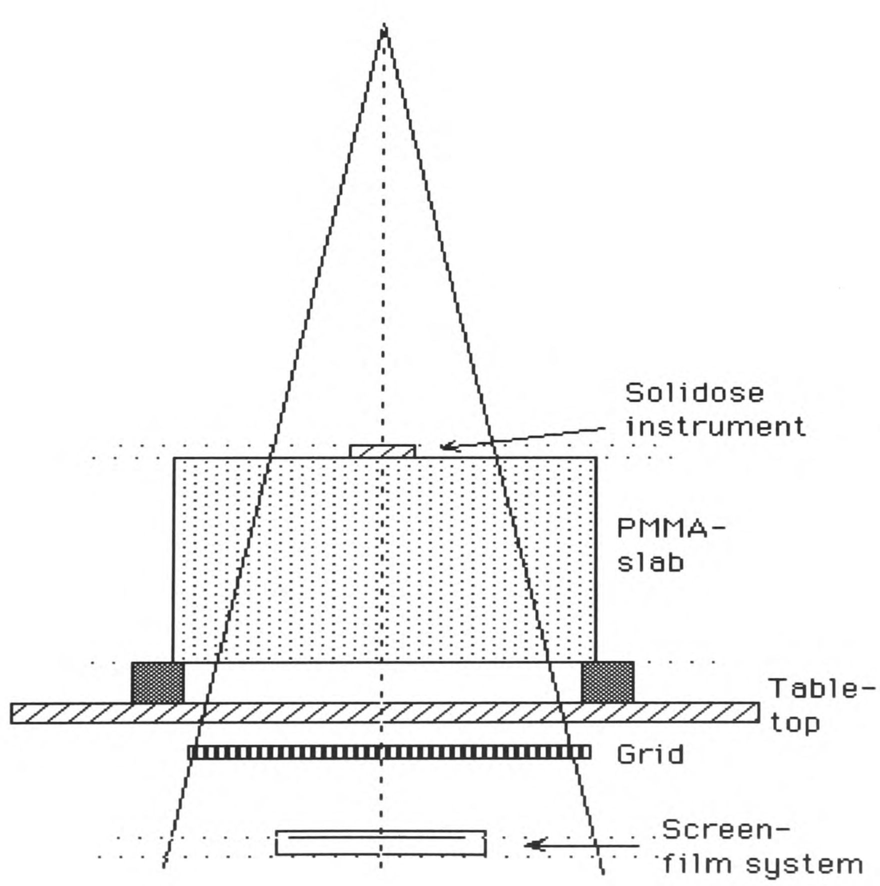

Figure 3.8. *Experimental arrangement for optical density measurements behind PMMA blocks.*

Figure 3.8 shows a typical arrangement used to expose the films in the three laboratories. The experimental conditions in each series of measurements were carefully monitored with readings being taken as appropriate of tube potentials and exposures. The HVLs of each tube were also measured.

3.4.4 Measurement of H and D Curves

In order to estimate the optical density, it is necessary to know the H and D curve for each screen-film combination used. These curves were measured in a controlled system using aluminium to harden the beam and substitute for the patient. To reduce the effects of scatter, a large air-gap was used between the aluminium block and the screen-film combination. The measured H and D curves are expressed in terms of the incident air kerma without backscatter at the entrance to the x-ray cassette.

The H and D curve was measured at 90 kV using a 13 mm thick aluminium block for the optical density measurements in the lumbar spine laboratory. It is assumed that this H and D curve could be used for the optical density measurements in the Linköping Physics laboratory. Both systems use the same film and have similar screen thicknesses. This seems reasonable as the incident air kerma at the entrance to the x-ray cassette used in the H and D curve is proportional to the energy imparted to the screen. The H and D curve was measured at 140 kV using a 20 mm thick aluminium block for the optical density measurements in the chest laboratory. In both cases, the measurements were undertaken at a distance of 3 m from the x-ray focus.

3.5 Summary of Work

This chapter describes the measurements undertaken for comparison with the XYZSCAT and VOXSCAT code calculations. The experimental data to validate the VOXSCAT code was provided by Linköping University.

3.5.1 Scatter Measurements

Initially, it was thought that the scatter measurements could be used to validate the Monte Carlo calculations. However, it was found that the percentage scatter was difficult to measure which is shown in the large uncertainty of ±10.4%. This means that the measurement uncertainty is too large to provide an accurate validation of the calculations but it is still important to show that the calculations are representative of the amount of scatter found in the clinic. The Monte Carlo codes have therefore been rigorously validated by cross comparison of their scatter values.

Further uncertainties were found in the parameters which describe the beam quality. Their values are between ±1 kV and ±3 kV for tube potential, between ±0.1 mmAl and ±0.4 mmAl for half value layer and ±18.6% for tube filtration. All of these parameters are used to determine the x-ray spectra which are employed in the Monte Carlo calculations. The effect of these uncertainties on the beam quality of the calculated spectra and the corresponding effect on the percentage scatter calculations are described in sections 4.4 and 7.2.3 respectively.

One of the reasons that the percentage scatter is difficult to measure is due to the scatter contributions from materials other than the phantom in the x-ray room. In this work, it was found that typically 25% of the total scatter was produced by scatter from the x-ray tube head which compares well with the 27% contribution measured by Trout and Kelley (1965). A smaller contribution of approximately 6% was found in this work from the x-ray room walls, ceiling and floor.

Therefore, the XYZSCAT code needs to include the DAP meter and the x-ray room walls, ceiling and floor in the calculation model. However, the complicated design of the collimator assembly means that it cannot readily be included in the model. The scatter from the collimator system was instead estimated from the measured and calculated scatter values.

3.5.2 Transmission and Optical Density Measurements

Patient images were collected and entrance air kerma measurements were collated to validate the voxel phantom as representative as a patient. Measurements of entrance air kerma and optical density on films behind PMMA phantoms were undertaken to validate the VOXSCAT code and ensure that the imaging systems are correctly described.

Chapter 4: Modeling the Diagnostic X-ray Tube Spectrum

4.1 Introduction

The x-ray spectrum is an important component of the Monte Carlo simulations. Diagnostic x-ray spectra may be obtained from reports such as Birch et al. (1979) and Fewell et al. (1981). These spectra have been tabulated for selected parameters and thus, may not be appropriate for an x-ray tube in clinical use. The ideal method for obtaining clinical x-ray spectra would have been to measure them. However, direct measurements are difficult due to the high dose rate of the primary beam (Marshall et al., 1996). An alternative method may be to use indirect measurements but these require specialised equipment such as a Compton spectrometer (Matscheko and Ribberfors, 1987) which is not in general use. Another alternative is to reconstruct x-ray spectra from transmission measurements through blocks of copper (Archer and Wagner, 1982) or other materials. The problem with this method is that a wrong x-ray spectrum can be reconstructed due to the fitting procedure becoming trapped in local minima.

Therefore, it is very advantageous to have a method for calculating the x-ray spectra using the parameters which influence the production of the x-ray spectra. These are the tube potential, tube filtration, target angle and voltage ripple. The commonly used Birch and Marshall (1979) model has thus been employed to reproduce the beam qualities of the Philips x-ray tube determined by the HVL measurements described in chapter 3.

4.2 Current Models

Semi-empirical models combine theory and measured spectral distributions to provide a convenient method of calculating tungsten target x-ray spectra. One of the most common models is Birch and Marshall (1979) which calculates Bremsstrahlung and characteristic radiation.

Birch and Marshall (BM) calculations employ theoretical spectra adjusted using polynomial fits to the Bremsstrahlung component of measured spectra for tube potentials between 30 kV and 150 kV. Birch et al. (1979) indicate that the BM model is representative of an x-ray unit with a target angle of 17°.

The size of the target angle differs between x-ray tubes depending on the use of the machine (Buchmann et al, 1990). For example, a 7° target angle may be used for imaging the skull whereas a 15° target angle may be used for imaging the chest. Therefore, as the target angles in the x-ray tubes used for radiodiagnosis are typically less than 17°, the x-ray spectra are calculated with the tube filtration adjusted to give good agreement with the measured beam quality. This work is described in section 4.5.

4.2.1 Comparison between the programs: XSPECW and SPECTRA

	Half Value Layers (mmAl)		
Tube Potential (kV)	**Cranley et al. Values**	**SPECTRA Code Values**	**XSPECW Code Values**
55	2.30	2.29	2.33
60	2.51	2.49	2.54
65	2.71	2.69	2.74
70	2.92	2.90	2.94
75	3.14	3.12	3.16
80	3.35	3.35	3.38
85	3.59	3.58	3.60
90	3.83	3.82	3.83

Table 4.1*. Comparison of the HVLs from IPSM Report No. 64 (Cranley et al., 1991) with BM calculations with the SPECTRA and XSPECW codes for 3.4 mmAl total filtration and a 13° target angle.*

Two computer programs have been used to calculate x-ray spectra both employing the BM model. The first program, SPECTRA, was developed by Birch and Marshall (private communication). The second program, XSPECW, was obtained from Newcastle General Hospital (N. Marshall, private communcation). The beam qualities calculated with both programs are compared as the spectra produced with the SPECTRA program have been used with the VOXSCAT code and the spectra produced with the XSPECW program have been used with the XYZSCAT code.

Table 4.1 compares the HVLs for the tube potentials between 55 kV and 90 kV with 3.4 mmAl filtration and a 13° target angle for the Philips x-ray tube (section 3.2.1). The calculated HVLs are compared with those from Cranley et al. (1991) which are the average of the data for 12° and 14° target angles. It is assumed at present that constant potential generators are employed.

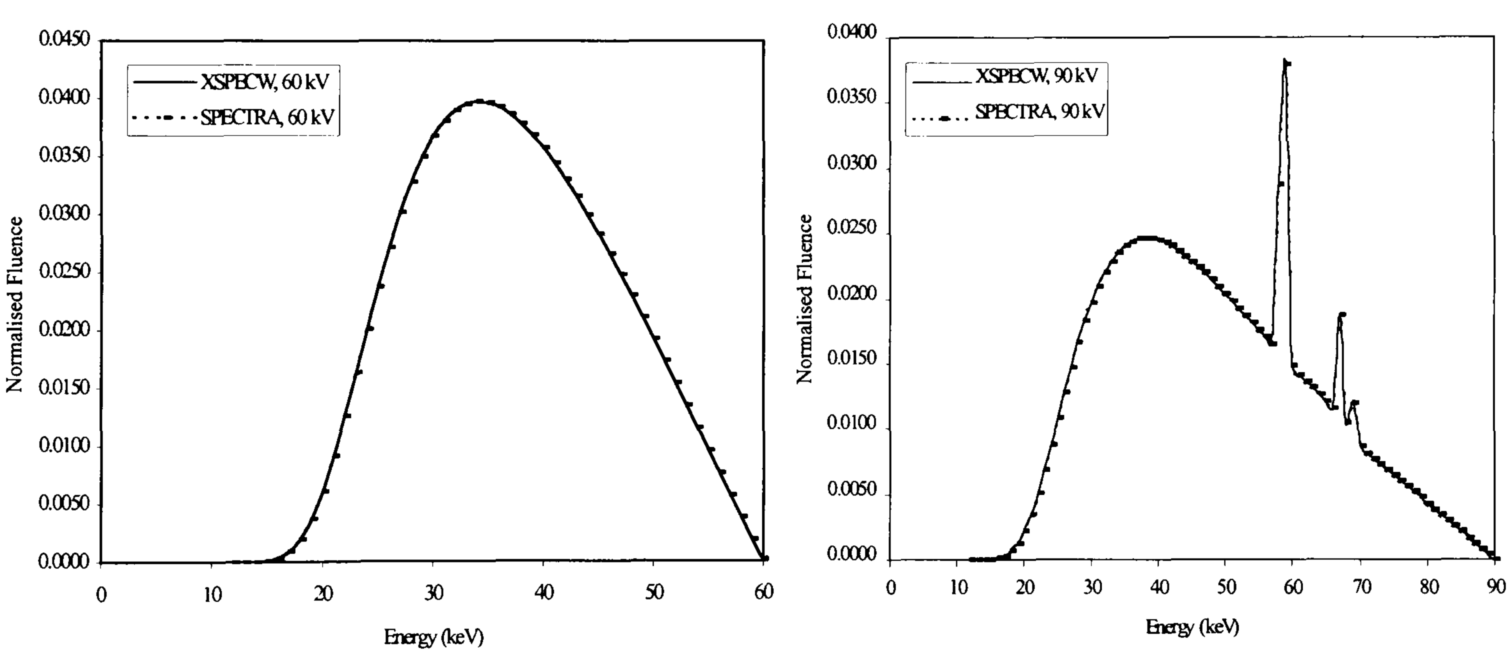

(a) *(b)*

Figure 4.1*. Comparison of the x-ray spectra produced by the BM Models for (a) 60 kV and (b) 90 kV.*

Table 4.1 shows good agreement within ±1% between the values from the two codes and Cranley et al.. Figure 4.1 shows excellent agreement between the spectra calculated with the XSPECW and SPECTRA programs for 60 kV and 90 kV x-rays.

4.3 Inclusion of Voltage Ripple in the X-ray Spectrum Calculation

The spectra calculated so far have been assumed to be produced by x-ray tubes with constant potential generators. The BM model was updated for this work to include voltage ripple so that comparisons can be made with HVL measurements undertaken in the clinical environment.

Generally, the tube potential applied across the anode and cathode varies sinusoidally due to the alternating power source. The degree of voltage variation depends on the amount of rectification in the circuit and the use of three phase power lines. This variation is therefore difficult to parameterise. Matsumoto et al. (1991) incorporated measured waveforms into the BM model. For our work, the size of the voltage variation is assumed to have a greater effect than the shape of the waveform on the resultant spectrum. Thus, the voltage variation has been modeled as a sine function.

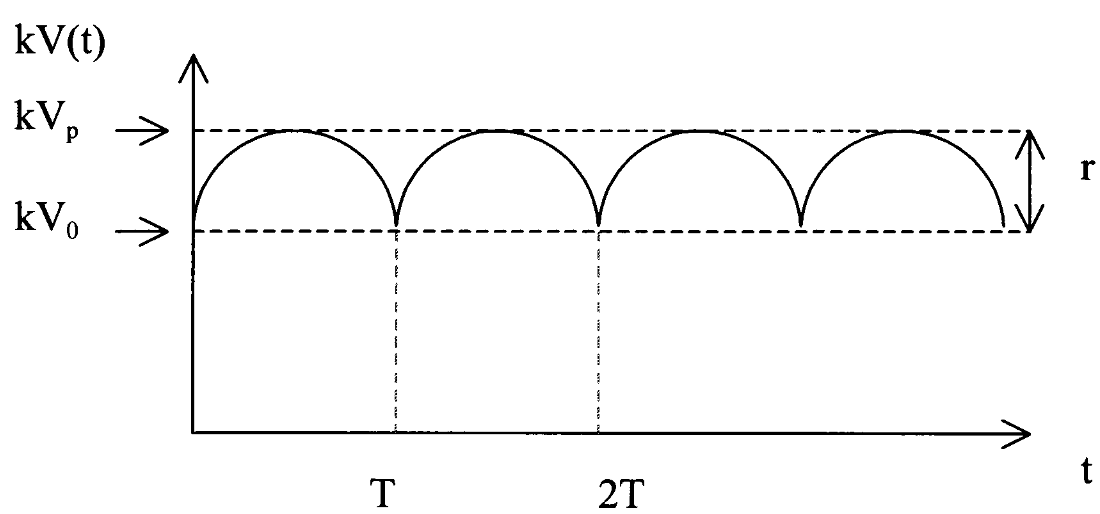

***Figure 4.2**. The sinusoidal variation of the voltage applied across the anode and cathode.*

The waveform amplitude is specified by using the percentage voltage ripple, r, which relates the peak tube potential, kV_p, with the minimum tube potential, kV_0, in the cycle as shown in equation 4.1.

$$kV_0 = kV_p(1 - r/100) \tag{4.1}$$

Figure 4.2 shows the sinusoidal variation of the tube potential, $kV(t)$, with time, t. Equation 4.2 is based on the model given by Boone and Seibert (1997). The time taken for the tube potential to return to its starting value is T.

$$kV(t) = kV_0 + \left(kV_p - kV_0\right) | \sin\left(\pi t/T\right) | \qquad (4.2)$$

The BM model calculates the x-ray spectra $\Phi(E,t)$ for each tube potential, $kV(t)$, in 101 increments from $t = 0$ to $t = T$. The final spectrum, $\Phi(E)$, is obtained by integrating each spectra $\Phi(E,t)$ and weighting with the normalised waveform $w(t)$ (equation 4.3) at each time increment in the cycle as shown in equation 4.4.

$$w(t) = kV(t) \Big/ \int_{t=0}^{T} kV(t)dt \qquad (4.3)$$

$$\Phi(E) = \int_{t=0}^{T} \Phi(E,t)w(t)dt \qquad (4.4)$$

This application of sinusoidal waveforms assumes that the time taken to reach kV_0 at the start of the exposure and the time to fall to zero at the end of the exposure is very small compared to the length of the exposure. The voltage ripple, r, can now be used as an input parameter with the BM model.

4.4 Uncertainties in the Calculation of Spectra

The uncertainty in the spectra calculated by the BM model was determined by the uncertainty in the input parameters: tube potential, tube filtration, target angle and percentage voltage ripple. The uncertainty in the calculated spectra can thus be determined for the Philips x-ray tube.

The uncertainty in the measured tube potentials is between ±1 kV for 49 kV and ±3 kV for 121 kV (or ±2.4% for both tube potentials) and the uncertainty in the measured tube filtration is ±0.63 mmAl (or ±18.6%) for 80 kV x-rays. The target angle is specified by the manufacturer and their tolerance for the tube is unknown. Therefore, it seems reasonable to assume an uncertainty of ±1° in the target angle. The voltage ripple for medium frequency units varies between 0% and 25% (Gilmore and Cranley, 1990) and its uncertainty is assumed to be ±3% (Nagel, 1988).

The BM model was used to calculate the spectra and compute their HVLs with the input parameters adjusted by decreasing the tube potential by 2.4%, increasing the target angle by 1°, decreasing the tube filtration by 18.6% and increasing the percentage voltage ripple by 3% and vice versa for all the parameters. An average difference of ±13% between the HVLs, calculated with and without the input parameters adjusted, was found for tube potentials of 49, 69, 100 and 121 kV.

4.5 Comparison of the Philips X-ray Tube Beam Qualities

A further change was implemented in the BM model to calculate spectra for this thesis. This implementation being similar to the work of Boone (1988). The tube filtration in the XSPECW code was iterated in 0.05 mmAl steps until the calculated HVL gave good agreement with the measured HVL. The iterations were undertaken for different tube potentials in turn. The average filtration over the range of tube potentials was then found and this average filtration used to calculate the x-ray spectra along with the measured tube potential, measured voltage ripple and target angle of the x-ray tube. This procedure was followed if the measured HVLs were available and the normal implementation of the BM model undertaken otherwise.

Table 4.2 shows the comparison of the measured HVLs for the Philips x-ray tube (section 3.2.1) and the values calculated with the BM Model with an average filtration of 2.85 mmAl. The x-ray tube has a target angle of 13° and a voltage ripple of 3%.

Tube Potential (kV)	Half Value Layers (mmAl) Measured Values	BM Model Values with Average Filtration
49	1.83	1.87
69	2.75	2.61
100	4.05	3.88
121	4.80	4.78

Table 4.2. *Comparison of the measured and calculated HVLs, using the BM Model, for the Philips x-ray tube.*

Table 4.2 shows that the HVLs for spectra calculated with the average filtration agrees within ±5% of the measured HVLs. The HVLs calculated for the average filtrations are not statistically different from the measured HVLs. Both the uncertainty in the measured and calculated HVLs are large being ±9.1% and ±13%. The values of measured HVLs would decrease slightly if the scatter from the attenuators could be reduced to zero as shown by the trends in figure 3.7. However, the reduction would still not make the differences statistically significant.

4.6 Summary of Work

The BM model was employed to calculate x-ray spectra for our work. It was used in two programs which were shown to provide very similar x-ray spectra. The BM model was implemented by iterating the tube filtration until there was good agreement between the measured and calculated HVLs. An average filtration was found and the x-ray spectra calculated. The calculated x-ray spectra should thus have the same or similar penetrating power as the clinical x-rays. However, there is a large uncertainty in the measured tube filtration used as an input parameter to the BM model. Therefore, this will have an effect on the uncertainty on the results of scatter calculations for the Philips x-ray tube as detailed in section 7.2.3.

Chapter 5: An Analytical Model for the Calculation of Scatter

5.1 Introduction

This chapter describes the development of an analytical model to calculate first order Compton scatter. The analytical model has been employed as its computational methods are more straightforward to follow than those used in the Monte Carlo codes. Therefore, an understanding of the Compton scattering process has been gained by studying the variation of the first order Compton scatter with incident photon energy and tube potential and by studying the scatter contributions from different depths in a block of WT1 material.

However, four limitations to the analytical model were found in the course of its development. The first limitation is that only the first order scatter was calculated with the analytical model. A calculation involving two or more orders of scatter is difficult. The calculation time becomes excessive without determining more information about the total scatter. The second limitation is that coherent scatter has not been included in the analytical model. This means that the analytical model does not calculate the total first order scatter. Compton scattering has only been modeled as it is the dominant interaction for photon energies between 30 and 150 keV in WT1 material. The contributions of different orders of Compton scatter and coherent scatter to the total scatter are investigated in Chapter 7.

The third limitation is that electron binding correction factors to model incoherent scattering have not been employed. The fourth limitation is that calculations have only been carried out for normally incident photons. It is possible to calculate the first order Compton scatter for different angles of incidence but this has not been implemented in the current model. Calculations with normally incident photons are close enough to the real situation of collimated x-ray beams to provide an understanding of the scattering process. A limited comparison of the analytical calculations with the XYZSCAT and VOXSCAT Monte Carlo codes has thus been carried out in sections 7.2.1.1 and 7.2.1.2.

The computational method used in the analytical model is based on the formalism of Wong et al. (1981a). Their work involved both first and second order computations of scatter to obtain the absorbed dose to water at depths on and off the central axis in a semi-infinite phantom. Wong et al. (1981b) extended the technique to calculate the effect on the dose distributions of small inhomogenities in the phantom. Cunningham et. al. (1984) implemented a similar method to Wong et al. for the calculation of first order scattered spectra at depth in various phantoms. Other investigators have used analytical methods including Ahnesjö (1995) to calculate the scatter from the collimators of a medical linear accelerator and Patrocino et al. (1996) to calculate backscatter factors for low energy radiotherapy between 30 and 150 kV.

5.2 Overview of the Analytical Calculation

Figure 5.1 demonstrates the basis of the analytical approach for the calculation of scatter. The incident beam is assumed to be of finite size with the x-ray focus to surface distance at infinity i.e. a parallel beam. The incident photon is assumed to be monoenergetic for the time being. A field of 200 mm × 200 mm is modeled to be incident on a block of WT1 material with dimensions: 305 mm long, 305 mm wide and 100 mm thick. This block has the same dimensions as the block used for the scatter measurements in the Philips x-ray room (section 3.2.2). The phantom thickness Z_t was divided into n layers of equal thickness, Δz. The position at depth in the phantom, z_i, was set to be at the centre of each layer.

The magnitude of the scatter is calculated for a fluence detector with a small surface area ΔA. The normal perpendicular to the detector's incident surface is aligned with the direction from the centre of the field on the phantom's incident surface to the detector. This is shown in figure 5.2. The distance from the field centre on the phantom's surface to the detector is 1 metre.

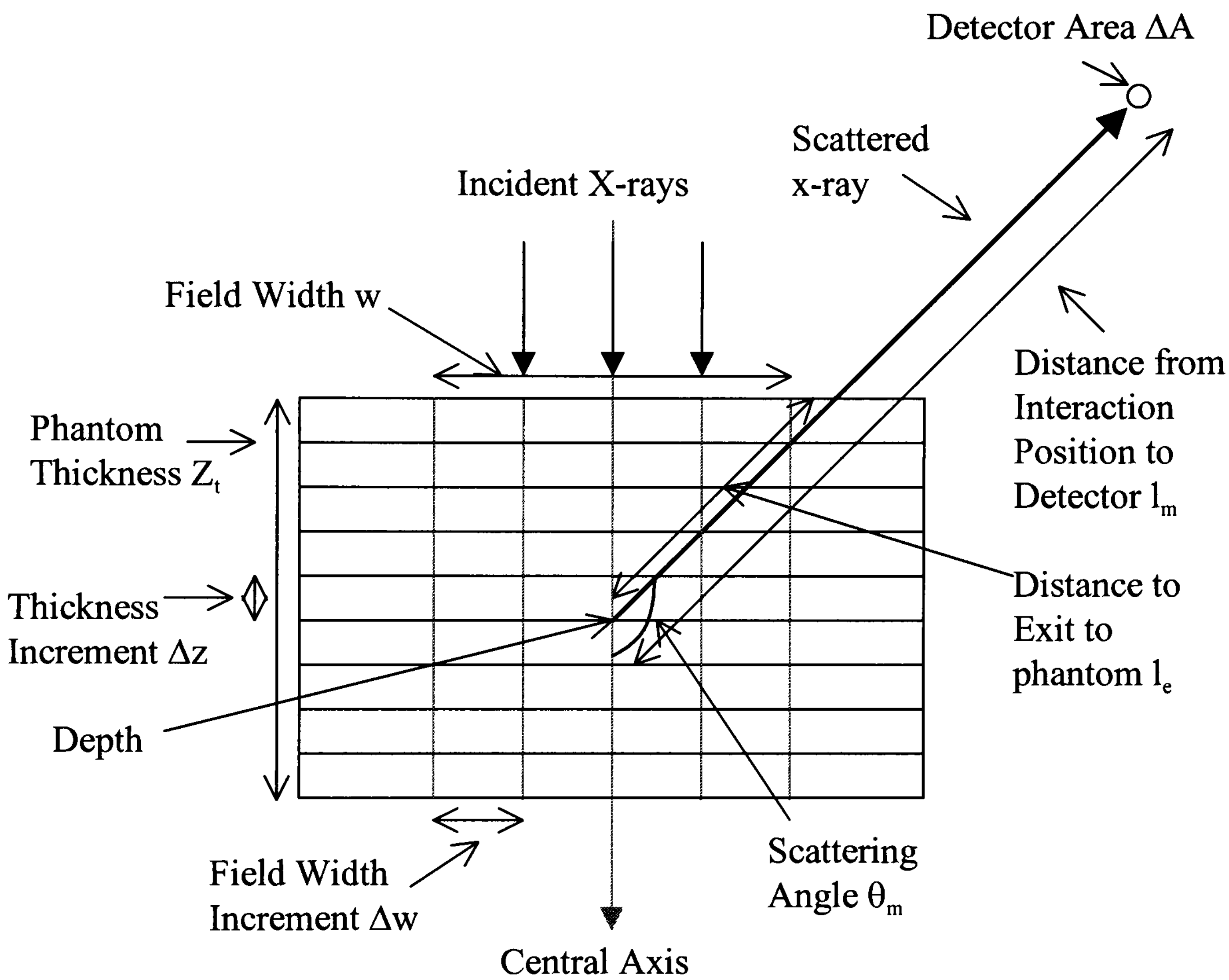

***Figure 5.1**. The model for the analytical calculation of scatter.*

It is useful to formulate the analytical model in terms of probabilities since radiation transport is a stochastic process. The scatter fluence, Φ_s, at the detector for a specified depth in the phantom is the multiplication of the incident fluence, Φ_0, with: the probability of interaction p_{int}; the probability of a Compton interaction p_{Com}; the probability that the Compton scatter will be directed towards the detector p_{sct}; and the probability that the scattered photon will reach the measurement position without interacting p_{esc}. This is shown in equation 5.1.

$$\Phi_s = \Phi_0 p_{\mathrm{int}} p_{Com} p_{sct} p_{esc} \tag{5.1}$$

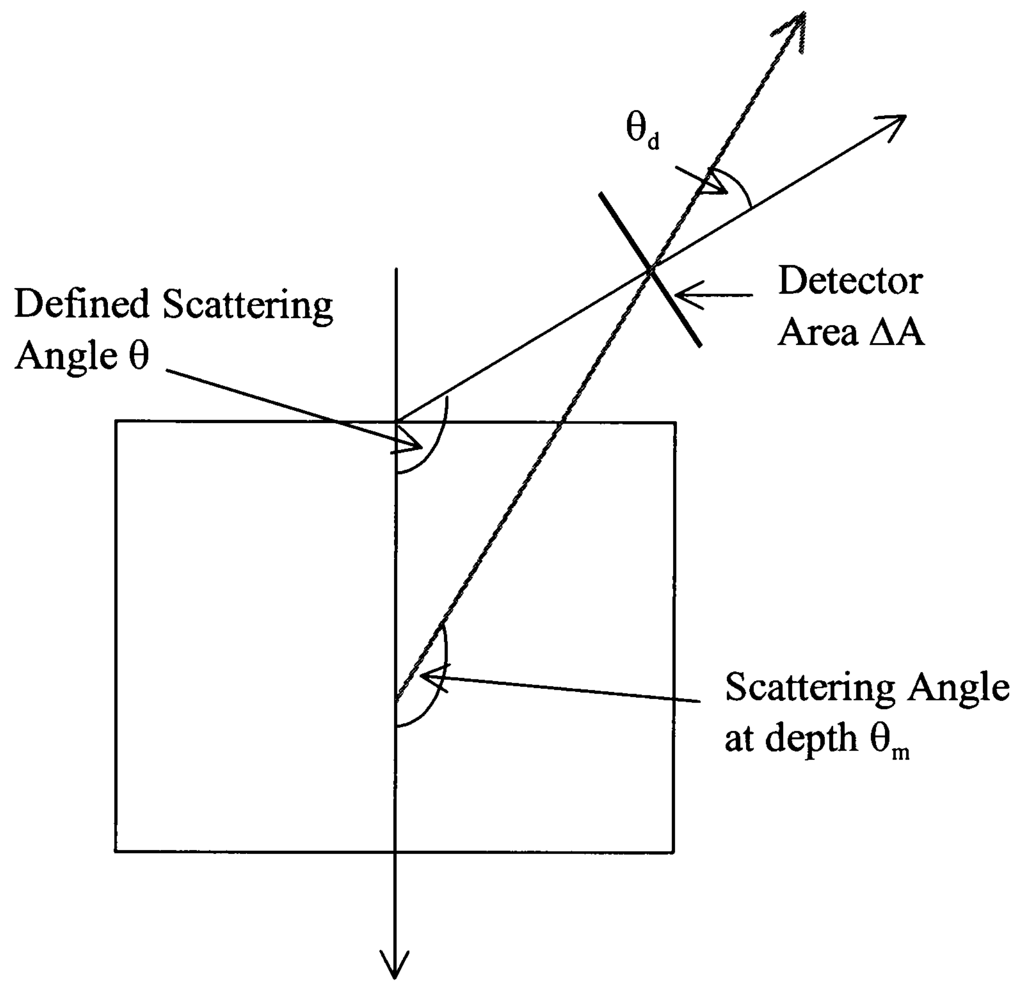

***Figure 5.2**. The orientation of the fluence detector in relation to the phantom.*

5.3 Probability of Interaction

The mass attenuation coefficients for WT1 material, μ/ρ, are the same as those used with the XYZSCAT Monte Carlo code. The mass attenuation coefficients were fitted to a polynomial (equation 2.15) to allow interpolation between 10 and 150 keV. A density of 1.015 gcm^{-3} for WT1 material (White et al., 1977) was used to obtain the linear attenuation coefficients, μ..

Hubbell (1969) states the definition of the linear attenuation coefficient as the probability per unit pathlength that a photon will interact. The interaction probability is $\mu\Delta z$ if the thickness is infinitesimally small. The interaction probability p_{int} at a depth z_i in a thick phantom, composed of infinitesimally small layers, is the combination of $\mu\Delta z$ for the layer at depth with the probability of reaching the depth without interaction. Thus, the interaction probability for a photon of energy E_0 is shown in equation 5.2.

$$p_{\text{int}} = \mu(E_0)e^{-\mu(E_0)z_i}\Delta z \tag{5.2}$$

The probability of interaction, p_{int}, for the whole phantom thickness Z_t is given by the integration of equation 5.2 as follows:

$$p_{\text{int}} = \int_0^{Z_t} \mu(E_0)e^{-\mu(E_0)z}dz \tag{5.3}$$

5.4 Probability of Compton Scatter

At each depth, z_i, in the phantom, the probability that a Compton scatter, p_{Com}, will occur is calculated using equation 5.4. The probability is the ratio of the Compton cross section σ, calculated using equation 2.6, to the linear attenuation coefficient μ for an incident photon energy E_0. The density of WT1 material, ρ, and the electron density of WT1 material, ρ_m, (number of electrons per unit mass) are used to correct the Compton cross section (m^2/electron) to be in the same units as the linear attenuation coefficient (1/m).

$$p_{Com} = \frac{\rho\rho_m\sigma(E_0)}{\mu(E_0)} \tag{5.4}$$

5.5 Probability of Scatter to the Detector

At each depth, z_i, in the phantom, the photon produced by the Compton interaction is scattered in the direction of the detector. The probability of scatter, p_{sct}, to this position is calculated by equation 5.5. It is the ratio of the differential Compton cross section, $d\sigma/d\Omega$ (equation 2.2), and the solid angle between the scattering point and the detector area $\Delta\Omega$, to the total Compton cross section, σ (equation 2.6).

$$p_{sct} = \frac{\frac{d\sigma}{d\Omega}\Delta\Omega}{\sigma} \tag{5.5}$$

The distance, l_m, and the angle of scatter, θ_m, from the scattering point in the phantom to the detector (figure 5.1) are found from straightforward trigonometric formulae. This is a 'ray tracing' technique.

The solid angle takes into account the detector area, $\Delta A \cos\theta_d$, which the scattered photon intersects. Let θ_d be the angle between the direction of the scattered photons reaching the detector and the alignment of the detector as shown in figure 5.2. The angle, θ_d, is also used to take into account the scatter fluence reaching the detector. Therefore, the probability of scatter to the detector area is the multiplication of these factors as shown by equation 5.6.

$$p_{sct} = \frac{\frac{d\sigma(E_0,\theta_m)}{d\Omega}\frac{\Delta A \cos\theta_d}{l_m^2}\frac{1}{\cos\theta_d}}{\sigma(E_0)} \tag{5.6}$$

5.6 Probability of Escape from the Phantom

At each depth, z_i, the scattered photon is transported towards the detector and will exit the WT1 material as the phantom has finite dimensions. The photon will travel the rest of the distance through air. The attenuation by air has been ignored in the analytical model. The air will produce scatter as well as undergoing infrequent photoelectric interactions. The effect of the total volume of air in a x-ray room has been studied using the XYZSCAT code in section 7.2.2.7.

The probability of escaping the phantom, p_{esc}, is calculated by equation 5.7. It is the amount of attenuation encountered by scattered photons of energy, E_s, travelling a distance, l_e, to exit the phantom. The scattered photon energy is dependent on the incident photon energy and the angle of scatter, θ_m. It is calculated using equation 2.7. The linear attenuation coefficient was found by interpolation of equation 2.15 for this energy. The distance to escape the phantom, l_e, was also calculated using the 'ray tracing' technique.

$$p_{esc} = e^{-\mu(E_s)l_e} \tag{5.7}$$

5.7 First Order Scatter Model

5.7.1 Calculation of Scattered Fluence

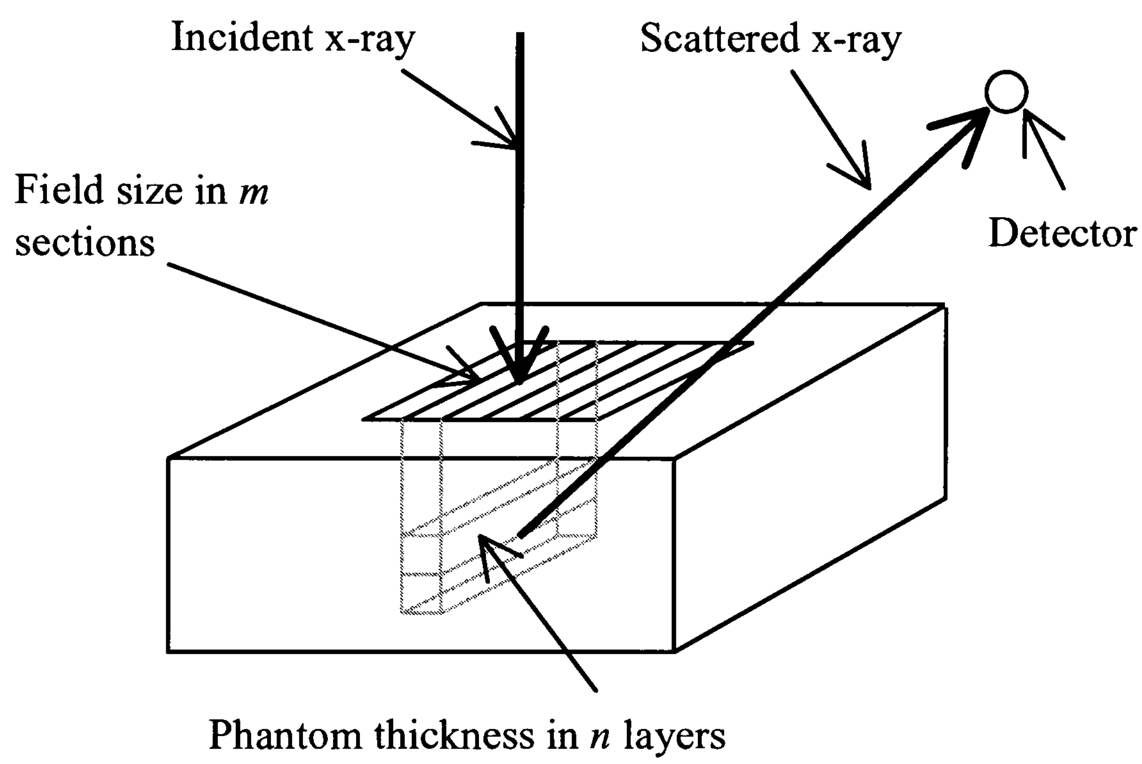

Figure 5.3. The voxels created by dividing the thickness into n layers and the field width into m sections.

The square field incident on the phantom surface is defined by its length l and width w. Figure 5.3 shows that the field width is divided into m sections each of width Δw. The field length is not divided into sections as this increases the calculaton time without changing the scatter values. Thus, the scattering points in the phantom are defined at the centre of voxels with dimensions: l long, Δw wide and Δz thick. The scattering angle θ_m, the angle of incidence on the detector θ_d, the distances l_m and l_e are calculated for all scattering points. Equation 5.6 shows that the angle of incidence

θ_d terms cancel out in the probability of a scatter to the detector. Therefore, the first order scatter fluence is shown by equation 5.8.

The first order scatter fluence, Φ_s, is calculated by the multiplication of probabilities and the incident fluence, Φ_0, normalised to the incident field area, *lw*. This was initially specified by equation 5.1 and is fully described by equation 5.8.

$$\Phi_s = \frac{\Phi_0}{lw} \rho \rho_m \int_0^{Z_t} \mu(E_0) e^{-\mu(E_0)z} \frac{\sigma(E_0)}{\mu(E_0)} \int_{-w/2}^{w/2} \frac{\frac{d\sigma(E_0,\theta_m)}{d\Omega} \frac{\Delta A}{l_m^2}}{\sigma(E_0)} e^{-\mu(E_s)l_e} \, l dw dz \qquad (5.8)$$

5.7.2 Calculation of Scattered Air Kerma

Equation 5.8 calculates the first order scatter fluence for incident photons with energy, E_0. This formula is expanded to calculate the scattered fluence for the Philips x-ray tube spectra obtained in Chapter 4. The scattered fluence is calculated for each photon energy in 2 keV steps between the minimum energy, E_{min}, and the maximum energy, E_{max}, of an x-ray spectrum. The scattered fluence is then averaged using the spectral distribution.

The incident fluence distribution, $\Phi'(E)$, can be thought of as the probability of a photon of an energy, *E*, being incident on the phantom. Equation 5.9 shows the incident fluence distribution normalised so that its sum is equal to one.

$$\int_{E_{\min}}^{E_{\max}} \Phi'(E) dE = 1 \qquad (5.9)$$

Equation 5.10 shows the calculation of the first order scattered air kerma, K_s. It is found by integrating the scattered fluence, $\Phi_s(E)$, with the incident x-ray spectrum for each incident energy *E*, the scattered energy E_s and the mass energy transfer coefficient of air (μ_{tr}/ρ) found by interpolating equation 2.15 for E_s.

$$K_s = \int_{E_{\min}}^{E_{\max}} \Phi'(E)\Phi_s(E)E_s\left(\frac{\mu_{tr}}{\rho}\right)dE \qquad (5.10)$$

The incident air kerma is also obtained. Thus, the analytical model calculates the percentage first order Compton scatter as the scattered air kerma relative to the incident air kerma unless stated otherwise.

5.7.3 Determination of Calculation Parameters for the Analytical Model

The parameters n, the number of layers at depth, and m, the number of field width sections, determine the accuracy and the calculation time of the analytical model. Hence, the effect of these parameters on the percentage first order Compton scatter was studied and their optimal values determined. It was found that the values $n = 100$ and $m = 100$ provided a stable value of the percentage scatter for all photon energies and scattering angles. Thus, all analytical calculations use these values unless otherwise stated.

It was also found that other parameter values can be employed depending on the scattering angle. For scattering angles of 30° and 150°, the number of field width sections m made little difference to the percentage scatter. The distance to escape the phantom does not vary considerably with lateral displacement from the central axis for these scattering angles. It was then possible to use $m = 1$ in the analytical model which produced less than a 1% difference from the percentage scatter calculated for $m = 100$. This difference is not significant as it is less than or equal to the calculation uncertainty shown in section 5.7.4.

5.7.4 Uncertainties in the Analytical Calculation

A method to estimate the uncertainty in the analytical calculations has been developed. This takes into account the uncertainties in the various factors used in the model. The percentage scatter is strongly dependent on the linear attenuation coefficients as they appear in both the exponential components of the interaction and escape probabilites (equations 5.2 and 5.7). Hubbell (1969) states that the uncertainty of linear attenuation coefficients is ±2% in the energy range between 5 to 150 keV and may drop to ±1% where the Compton cross section dominates. Therefore, an uncertainty of ±2% in the linear attenuation coefficients is employed. The differential Compton cross section appears in the probability of scatter and is assumed to have an uncertainty of ±1%.

The uncertainty in the analytical model is calculated as follows. The linear attenuation coefficients, μ, are increased by 2% and the differential Compton cross sections, $d\sigma/d\Omega$, are increased by 1%. The percentage scatter is then re-calculated with the new coefficients. The procedure is repeated by decreasing the coefficients by the same amounts. The estimated uncertainty is then the average difference between the percentage scatter calculated with and without changes to the coefficients. Thus, the uncertainties have been calculated for photon energies between 20 and 150 keV and for nominal tube potentials between 50 and 120 kV.

For monoenergetic photons between 20 and 150 keV, the uncertainty varies between ±17% and ±3% for percentage scatter calculated at a scattering angle of 87°. The uncertainty was ±1% for all photon energies for percentage scatter calculated in the backward direction.

For tube potentials between 50 and 120 kV, the uncertainty varies between ±6% and ±5% for percentage scatter calculated at a scattering angle of 87°. The uncertainty was ±1% for all tube potentials for percentage scatter calculated in the backward direction.

The uncertainty is largest in the forward direction (for scattering angles less than or equal to 87°). Figure 5.5 shows that most of photons interact close to the incident surface of the phantom. The forward directed photons then have a large distance to travel before they escape the phantom whereas the backward directed photons are close to the incident surface. Therefore, as the analytical calculation integrates with depth, the uncertainties added to the attenuation coefficients and the scattering cross sections will have the largest effect on the forward directed photons which travel the furthest.

The uncertainty in the forward directed scatter, calculated with the analytical model, is larger than the statistical uncertainty of ±1% which can be attained with Monte Carlo calculations (section 6.4.2.8). This highlights a further limitation in employing an analytical model to calculate scatter.

5.8 Results of Analytical Calculations

The geometry used in the analytical calculations (section 5.2) is the same as used for the Monte Carlo calculations which enables the comparison of the percentage first order Compton scatter values in sections 7.2.1.1 and 7.2.1.2.

5.8.1 Contribution to the Percentage Scatter from Different Depths in the Phantom

Figure 5.4 shows the percentage contributions to the first order Compton scatter for different depths defined by their range of n layers. The analytical calculations have been undertaken for 60 keV photons. The contributions from different depths in the phantom are shown to vary with scattering angle and this can be explained by examining the variation of the calculated probabilities with depth as shown in figure 5.5.

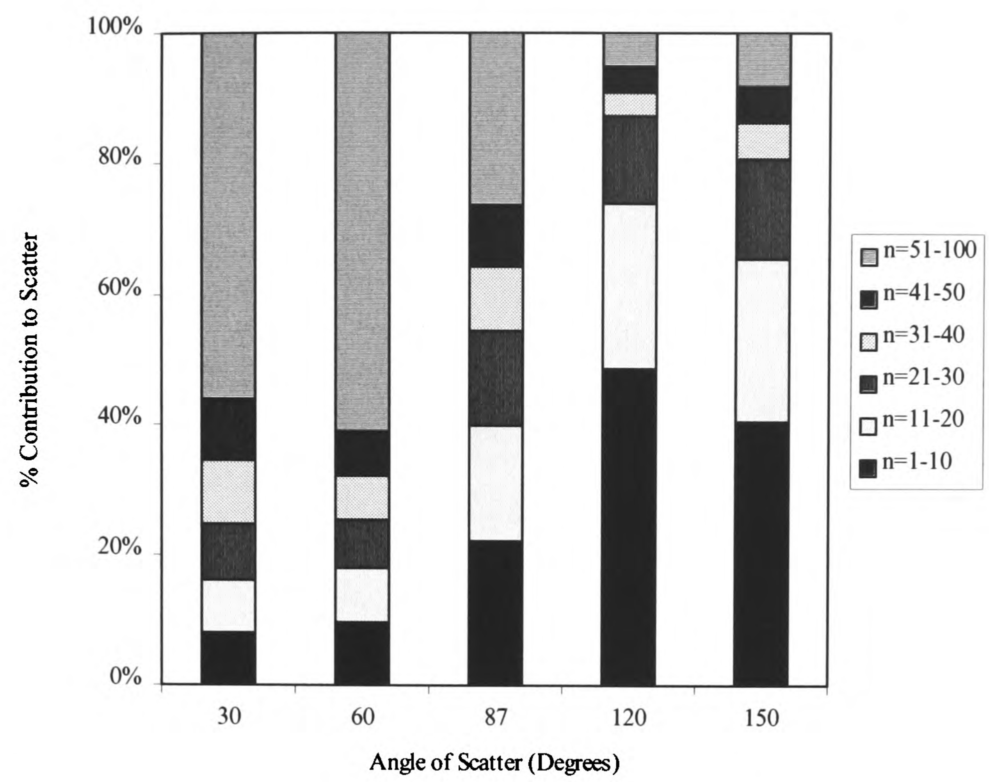

***Figure 5.4**. The percentage scatter contributions of different layers to the first order Compton scatter for 60 keV photons.*

The probability of interaction (equation 5.2) is high at shallow depths. For forward directed scatter, the probability of escape (equation 5.7) is low and for backward directed scatter, it is high. This results in a 8% contribution for 30° scatter and a 48% contribution for 120° scatter from the first 20 layers (within 2 cm) of the phantom. Even the first layer (within 1 mm) produces a relatively large contribution of 6.3% to the first order Compton scatter at the 120° scattering angle.

Figure 5.6 shows the percentage first order Compton scatter produced at different depths in the phantom. The highest percentage scatter values is at 99.5 mm deep for 30° and 60° scattering angles and 0.5 mm deep for 87°, 120° and 150° scattering angles. These depths are close to the surface which is nearest the detector position for the respective angle of scatter with the escape probability being high at these depths. The percentage scatter at depth for backscattered photons is high at shallow depths as both the interaction and escape probabilities are high.

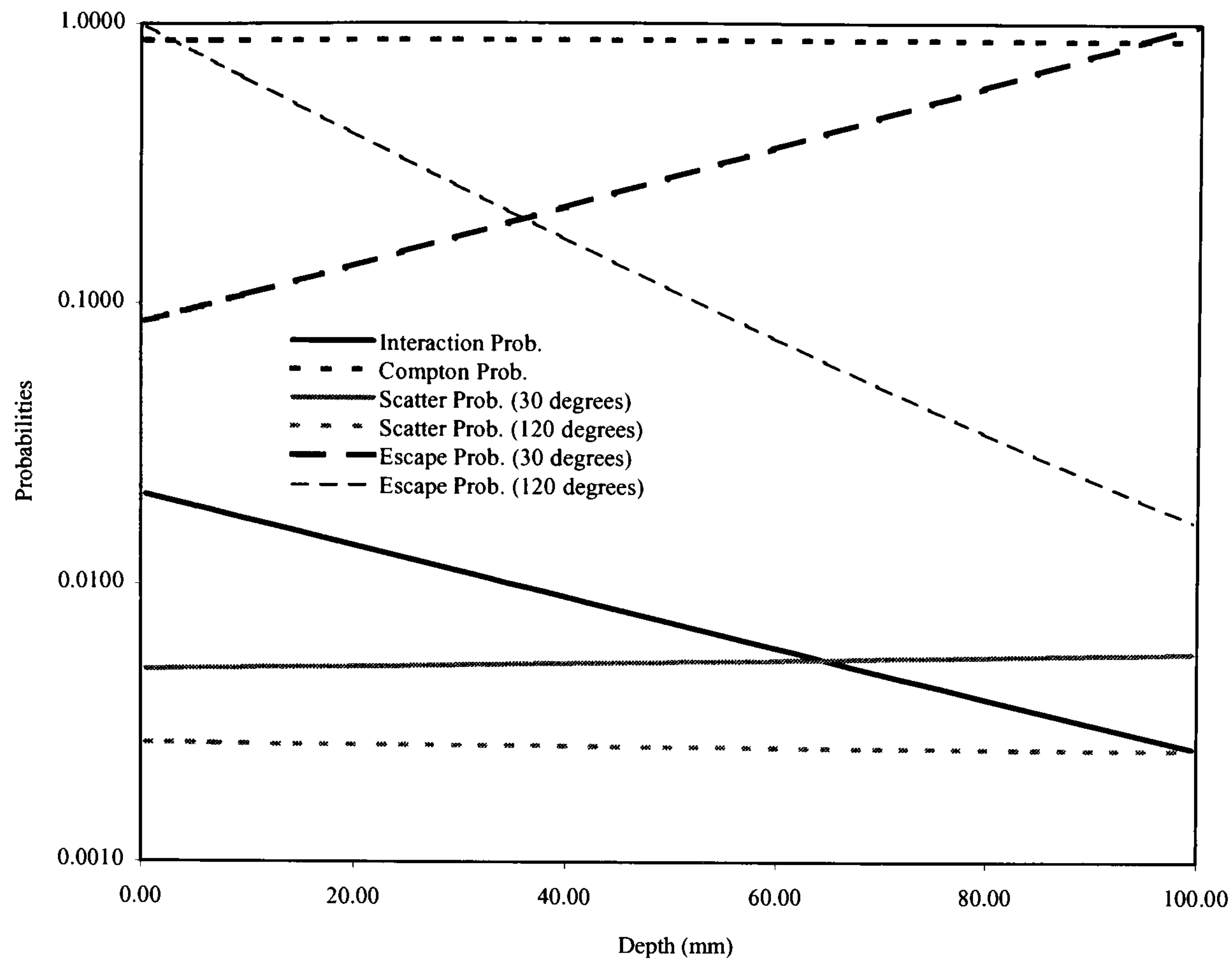

***Figure** 5.5. The probabilities calculated in the analytical model at depth in the phantom for 60 keV photons for different angles of scatter.*

The phantom depth has less of an effect on the percentage scatter at depth in the forward direction than in the backward direction. The mean free path of the scattered photons (4.70 cm) is similar to that of the incident photons (4.75 cm). Therefore, the probability of interaction almost balances the probability of escape. It is demonstrated by the small increase in percentage scatter with increasing depth for the 30° scattering angle. The variation of the probabilities accounts for the forward directed scatter being lower than the backward directed scatter for both low energy photons and x-ray spectra. They also account for the backward directed scatter increasing slowly with increasing phantom thickness while the forward directed scatter decreases rapidly.

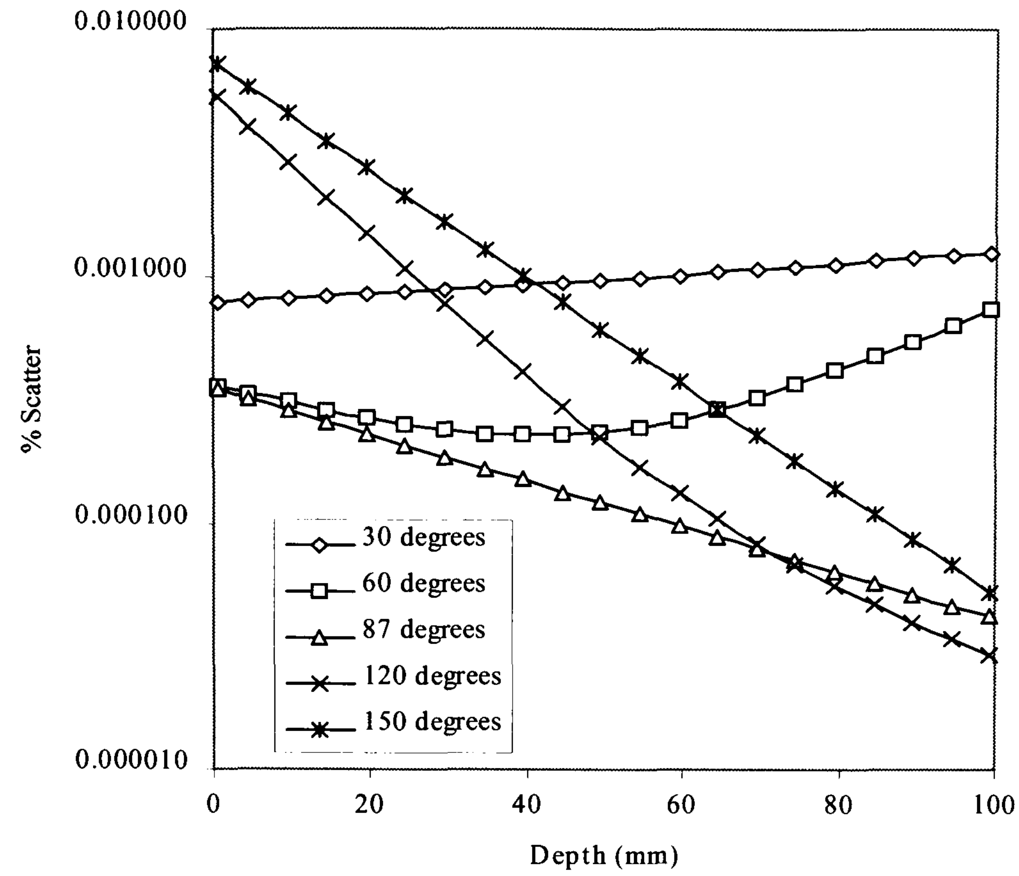

Figure 5.6. *The percentage scatter at depth in the phantom for 60 keV photons for different angles of scatter.*

5.8.2 Effect of Incident Photon Energy

The analytical model has been used to calculate the percentage first order Compton scatter for photon energies between 20 and 150 keV. Figure 5.7 shows the angular distributions of the percentage scatter for 40 keV, 60 keV and 150 keV photons.

For forward scatter, the percentage scatter increases with increasing energy due to the greater penetration of the photons. For backward scatter however, the percentage scatter for 150 keV photons is lower than for 40 keV photons.

Figure 5.8 compares the percentage scatter calculated as scattered fluence relative to incident fluence, scattered energy fluence relative to incident energy fluence and scattered air kerma relative to incident air kerma for a 150° scattering angle. The results shows that the quantity used to calculate the percentage scatter has an effect on the variation of percentage scatter with photon energy. The energies for which the maximum scatter values are reached are: 80 keV for relative fluence; 60 keV for relative energy fluence; and 50 keV for relative air kerma.

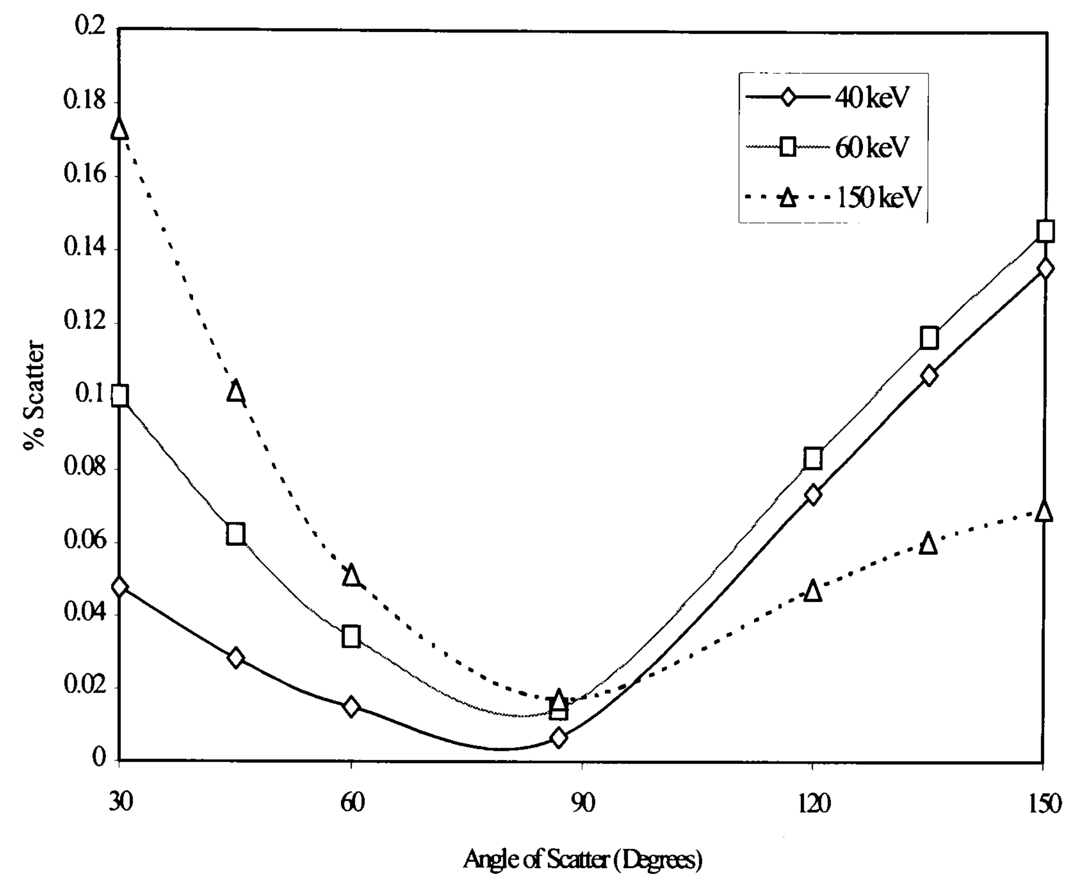

Figure 5.7. *The percentage scatter for 40 keV, 60 keV and 150 keV photons.*

The maximum value of the relative energy fluence Ψ_s/Ψ_0 is lower than the maximum value of the relative fluence value Φ_s/Φ_0. This is due to the scattered photon energy E_s being lower than the incident photon energy E_0. Thus, the relationship between the quantities is the ratio E_s/E_0 which is less than 1.0.

The relative air kerma K_s/K_0 values are higher than the relative fluence and relative energy fluence values for photon energies lower than 60 keV. There is a large increase in the mass energy transfer coefficients μ_{tr}/ρ with decreasing photon energy. Thus, the relationship between Ψ_s/Ψ_0 and K_s/K_0 is the ratio of mass energy transfer coefficients for the scattered and incident photons $\left[\frac{\mu_{tr}(E_s)/\rho}{\mu_{tr}(E_0)/\rho}\right]$ is greater than 1.0. For photon energies greater than 120 keV, K_s/K_0 is lower than Ψ_s/Ψ_0. The mass energy transfer coefficients decrease until 60 keV and then start increasing. For example at 150 keV, the mass energy transfer coefficients for incident photons are larger than for the scattered photons. Thus, the ratio $\left[\frac{\mu_{tr}(E_s)/\rho}{\mu_{tr}(E_0)/\rho}\right]$ is less than 1.0.

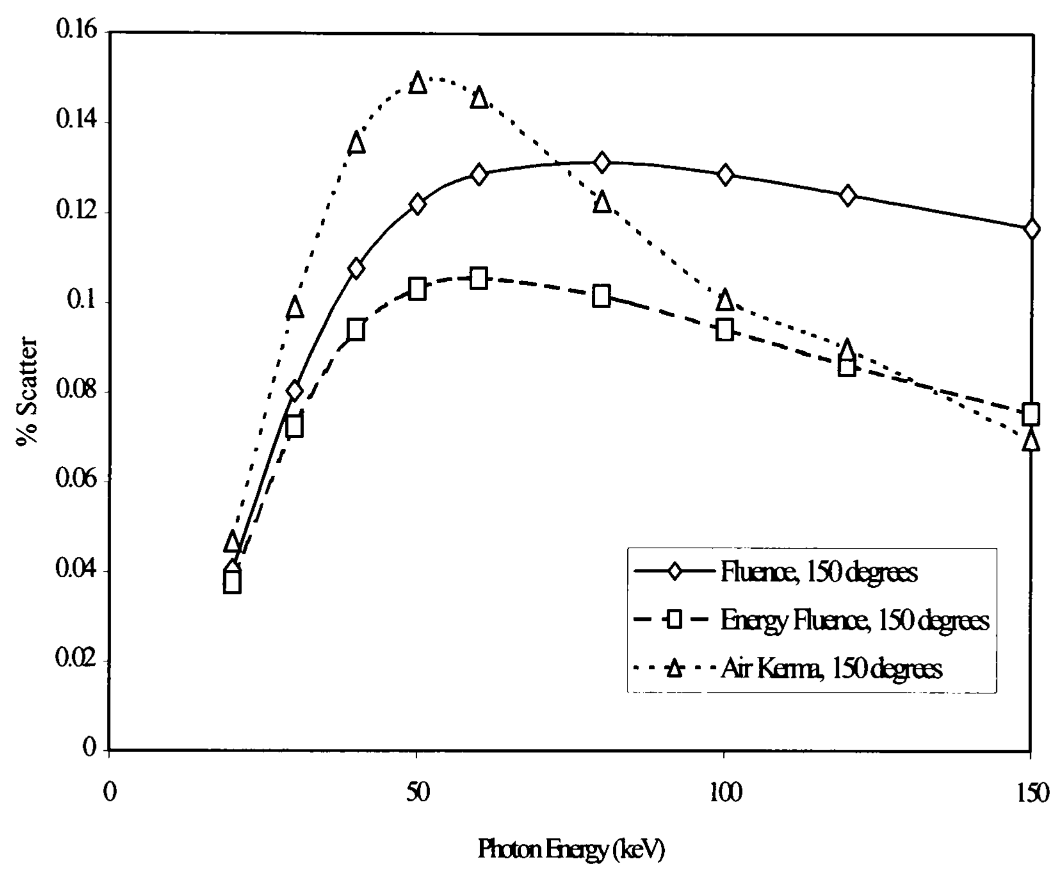

Figure 5.8*. The percentage scatter in terms of relative fluence, relative energy fluence and relative air kerma.*

Therefore, it is possible for the percentage scatter in terms of air kerma to have a lower value at 150 keV than at 40 keV. This is due to the scattered energy being lower than the incident energy and the rapid increase in the mass energy transfer coefficients for decreasing energy. The variation of the percentage scatter in terms of fluence is due to the variation of the analytical probabilities with energy.

5.8.3 Effect of X-ray Spectra

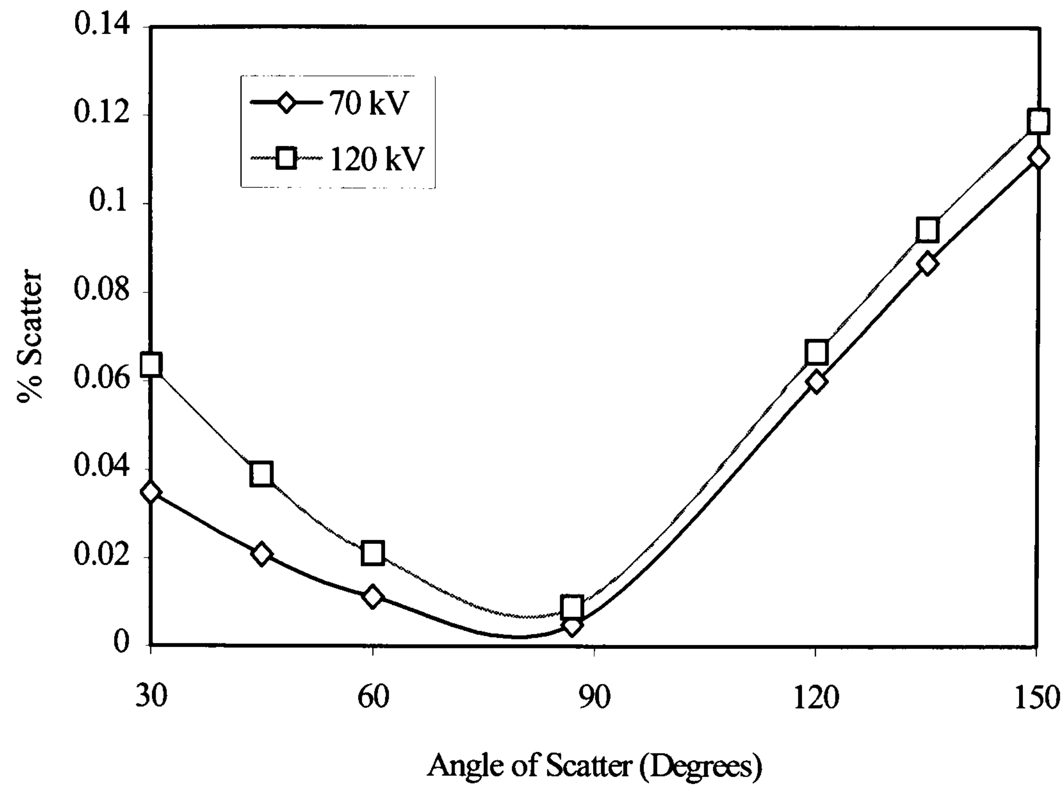

***Figure 5.9**. The percentage scatter for 70 kV and 120 kV x-rays.*

Figure 5.9 shows the percentage scatter in terms of air kerma for tube potentials of 70 kV and 120 kV. The x-ray spectra used in the calculation were for the Philips X-ray tube. Figures 5.9 and 5.10 show that the variation of percentage scatter is greater in the forward direction than in the backward direction for increasing tube potential. This is due to the greater penetration of the scattered x-rays in the forward direction. The percentage scatter for the x-ray spectra is calculated by averaging the percentage scatter distribution for monoenergetic photons with an x-ray spectrum. For increasing tube potential, the combination of the x-ray spectra with the shape of the percentage scatter distribution for backscattered photons (figure 5.8) results in the slower rate of increase for the 150° scatter than for the 30° scatter (figure 5.10).

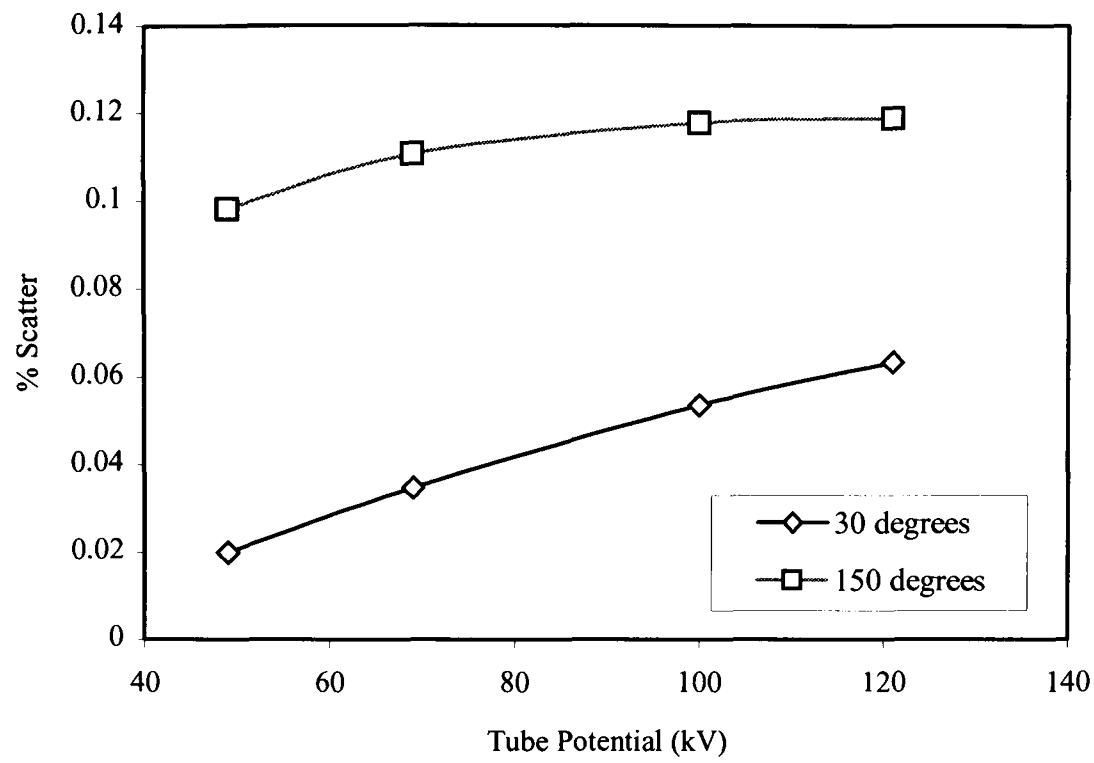

Figure 5.10. *The 30° and 150° percentage scatter in terms of air kerma for tube potentials between 50 and 120 kV.*

5.9 Summary of Work

An analytical model has been developed which calculates the percentage first order Compton scatter. Despite there being a number of limitations to the analytical approach, a greater understanding of Compton scattering has been achieved than if these calculations had not been undertaken.

The studies using the analytical model showed that:

- The largest contribution of the percentage scatter originates from layers close to the incident surface of the phantom for back scattered photons and from close to the exit surface of the phantom for forward scattered photons.
- The backscattered photons are less dependent on phantom or patient thickness than the forward scattered photons.
- The percentage scatter increases for increasing photon energy in the forward direction. The percentage scatter increases between 20 keV and 50 keV and decreases between 50 keV and 150 keV in the backward direction.

- The quantity used to calculate the percentage scatter affects the variation of scatter with photon energy.
- The averaging of the x-ray spectra means that the variation of percentage scatter with tube potential is less than that for the monoenergetic photons.

Good agreement with Monte Carlo calculated values of percentage first order Compton scatter was found as demonstrated in tables 7.1 and 7.2. These comparisons give confidence that the effects observed with the analytical model are real.

Chapter 6: Monte Carlo Techniques

6.1 Introduction

This chapter describes the Monte Carlo technique to realistically model the stochastic nature of photon transport. Two Monte Carlo programs have been developed and are summarised below. The first program described is an EGS4 user code, XYZSCAT. It models a diagnostic x-ray room using voxels to simulate a slab phantom, representing the patient, and the x-ray room walls. The XYZSCAT code calculates scatter at all positions within and outside the x-ray room. The second program described is a voxel phantom based Monte Carlo code, VOXSCAT. It employs a voxel phantom reconstructed from CT data to provide an heterogeneous model of the patient. Hence, the code provides a method of calculating the scatter from a patient. A rigorous validation of both computer programs has been undertaken by intercomparing scatter calculations for a slab phantom geometry (sections 7.2.1.1 to 7.2.1.4).

In order to have confidence that the voxel phantom is representative of a patient, the VOXSCAT code is employed to simulate the complete x-ray imaging chain (Dance et al, 1999; Sandborg et al., 2000). Therefore, calculations of entrance air kerma and dynamic range are compared with measured values from a patient survey (section 7.6.2).

6.2 Overview of the Monte Carlo Method for Photon Transport

Monte Carlo techniques are employed since there are no exact analytical solutions to radiation transport problems (section 5.1). The Monte Carlo method (Morin, 1988) enables calculations involving heterogeneous media and multiple scattering of photons to be undertaken. This is achieved by using machine-generated pseudo-random numbers. These are used to sample the probability distributions of the physical processes describing the radiation transport. The basic use of sampling random numbers is described below with more complicated methods described later.

6.2.1 Distance to Interaction Point

If a photon is being transported through an infinite medium (with linear attenuation coefficient μ) then the probability for an interaction, p, after a distance traveled between s' and $s'+\Delta s'$ is given by equation 6.1.

$$p = \mu e^{-\mu s'} \Delta s' \tag{6.1}$$

A cumulative probability distribution (CPD) is derived and integrated by equation 6.2.

$$CPD = \int_0^s \mu e^{-\mu s'} ds' = 1 - e^{-\mu s} \tag{6.2}$$

Equation 6.3 is found by inverting the CPD. A uniformly distributed random number R between 0 and 1 ($0 < R < 1$) is equivalent to the probability. Then, the distance s to the next interaction is:

$$s = -\frac{1}{\mu}\ln(1-R) \tag{6.3}$$

If R is uniformly distributed between 0 and 1 then this also applies to ($1-R$). Therefore, the distance to the interaction point is found by equation 6.4 where $R \neq 0$.

$$s = -\frac{1}{\mu}\ln R \tag{6.4}$$

6.2.2 Selection of Interaction Type

The interaction type is found by selecting another random number R. The linear attenuation coefficient, μ, is the addition of the linear attenuation coefficients for the photoelectric effect μ_{PE}, coherent scattering μ_{coh} and incoherent scattering μ_{inc}.

The ratios of these linear attenuation coefficients are used to produce a probability distribution. If R lies between 0 and μ_{PE}/μ then a photoelectric interaction is selected. If R lies between μ_{PE}/μ and $(\mu_{PE}+\mu_{inc})/\mu$ then an incoherent scattering is selected. If R lies between $(\mu_{PE}+\mu_{inc})/\mu$ and $(\mu_{PE}+\mu_{inc}+\mu_{coh})/\mu$ then a coherent scattering is selected. The interaction selected is then simulated.

If a photoelectric interaction is selected, the photon transport is stopped. The photoelectron can either be transported or its energy deposited locally. This is the same for the electron produced by the incoherent interaction.

If a coherent or an incoherent scatter is selected, the photon's direction is changed and the photon's energy reduced (for incoherent scatter only). The photon is then transported to the next interaction point.

6.2.3 Selection of Next Interaction Point

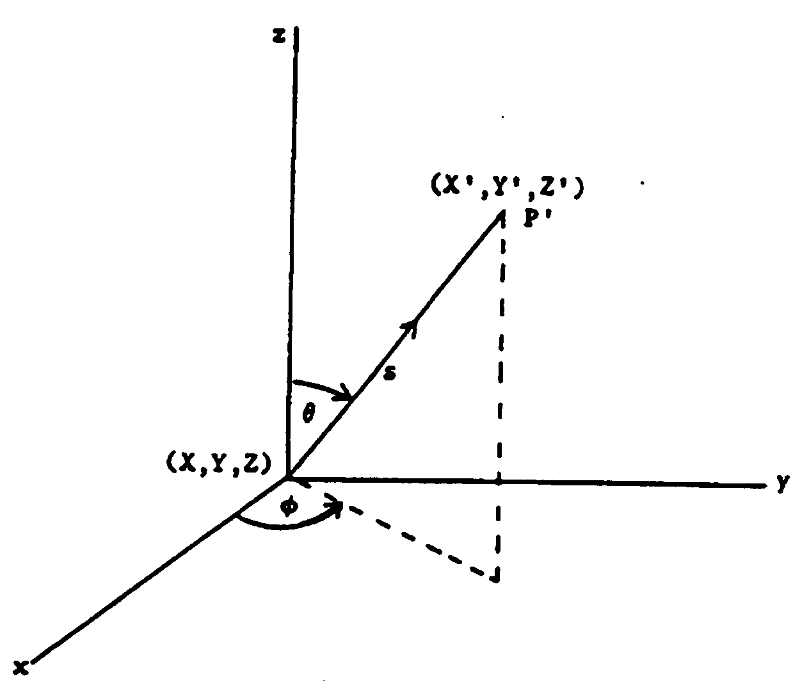

***Figure 6.1**. The spatial displacement of the photon to the next interaction point.*

Figure 6.1 shows that the coordinates of the next interaction point P′ (x',y',z') are found by combining the distance to the interaction point, s, and the direction (u,v,w)

(equation 6.5) with the original coordinates (x,y,z) given by equation 6.6. The photon has scattered through a polar angle θ and an azimuthal angle ϕ.

$$u = \sin\theta\cos\phi$$

$$v = \sin\theta\sin\phi$$

$$w = \cos\theta \qquad (6.5)$$

$$x' = x + us$$

$$y' = y + vs$$

$$z' = z + ws \qquad (6.6)$$

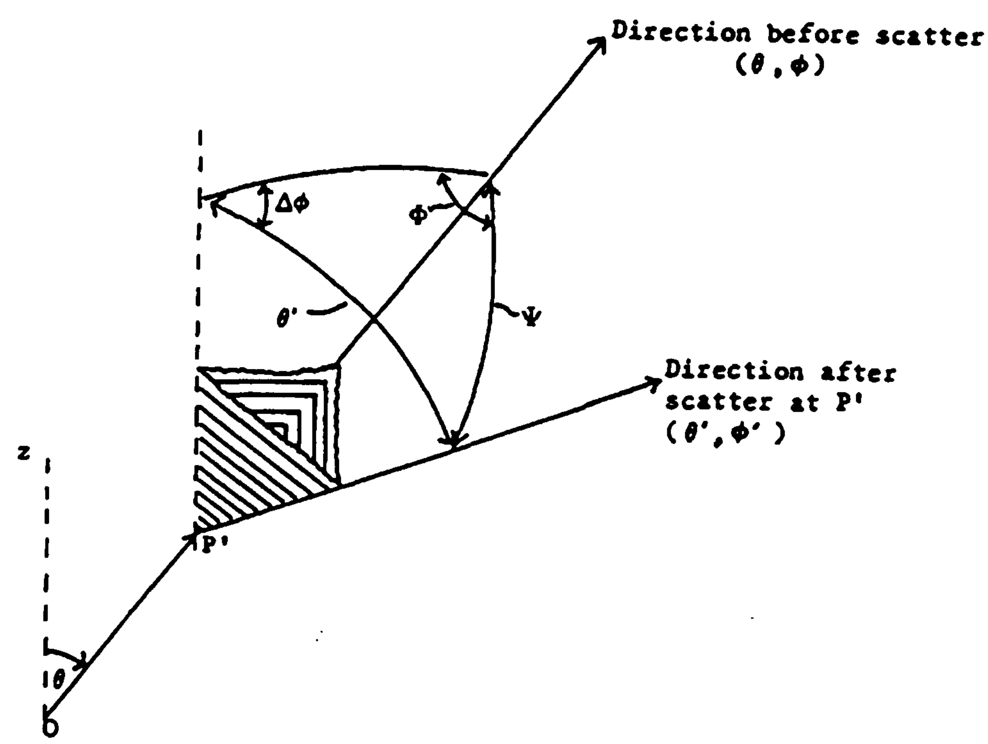

Figure 6.2. *The angular deflection of the photon at the next interaction point.*

Figure 6.2 shows the direction of the photon if it undergoes a further scatter through a polar angle Ψ and an azimuthal angle Φ. The EGS4 code calculates the new direction (u',v',w') in the original coordinate system by equations 6.7 to 6.9 (NPL, 1993) which correspond to those given by Alm Carlsson (1981). The polar angle θ' in the original coordinate system is determined by equation 6.9 The azimuthal angle ϕ' in the original coordinate system is determined by either equations 6.7 or 6.8. However, the azimuthal angle can be more easily found by equation 6.10 (Alm Carlsson, 1981; NPL, 1993) which is used in the VOXSCAT code. If the polar angle after the deflection is small such that $\theta' \to 0$ then $\phi' = \phi$. If the polar and azimuthal angles are both 0° before the deflection, then the new direction is found by the scattering angles Ψ and Φ.

$$u' = \sin\theta' \cos\phi' = \sin\Psi\cos\Phi\cos\theta\cos\phi - \sin\Psi\sin\Phi\sin\phi + \sin\theta\cos\phi\cos\Psi \quad (6.7)$$

$$v' = \sin\theta' \sin\phi' = \sin\Psi\cos\Phi\cos\theta\sin\phi + \sin\Psi\sin\Phi\cos\phi + \sin\theta\sin\phi\cos\Psi \quad (6.8)$$

$$w' = \cos\theta' = \cos\theta\cos\Psi - \sin\theta\sin\Psi\cos\Phi \quad (6.9)$$

$$\sin(\phi' - \phi) = \frac{\sin\Psi\sin\Phi}{\sin\theta'} \quad (6.10)$$

If the photon is being transported through a phantom of finite dimensions, then the photon may leave the volume to be simulated. In this case, the photon may be discarded and its energy scored if required. If the photon has not left the volume, then the transport is continued.

6.3 Selection of Monte Carlo Codes

Andreo (1991) provides a review of the Monte Carlo method and the Monte Carlo codes which are in the public domain. These include EGS, ETRAN, ITS and MCNP. The EGS4 (Electron Gamma Shower) Monte Carlo code (Nelson et al., 1985) and the MCNP (Monte Carlo Neutron Particle) code (Briesmeister, 1994) have become the two public domain codes which are predominately used by the Medical Physics scientific community.

Only photon transport is required for modelling diagnostic x-ray rooms. Therefore, the differences between the codes for transporting electrons are not discussed. The photon transport methods used by the EGS4 and MCNP codes are not considerably different. The major difference is that the incoherent scattering option is used as standard in the MCNP code but not in the EGS4 code. The MCNP code uses Hubbell et al. (1975) cross sections which include incoherent scatter cross sections whereas the EGS4 code uses Storm and Israel (1970) cross sections with Compton scatter cross sections without electron binding corrections. The effect on the percentage scatter calculations of different tabulations of cross sections is small as shown in section 7.2.2.3.

The EGS4 user code, XYZDOS (Bielajew and Rogers, 1992), was chosen as the basis to model diagnostic x-ray rooms because it would be possible to modify the code to calculate 3D distributions of percentage scatter. These iso-scatter distributions can be obtained in one calculation from the rectilinear grid of voxels defining the XYZSCAT model geometry. Love et al. (1998) has shown that an advantage of the EGS4 code is that it is 50% more efficient than the MCNP code when using photon calculations only. However, a disadvantage of the XYZSCAT code is that it has a very rigid geometry and therefore an advantage of the MCNP code is that it is capable of modeling very complex situations. In retrospect, using the MCNP code may have been a more appropriate choice as more realistic x-ray rooms could have been modeled. The benefits of obtaining iso-scatter distributions with the XYZSCAT code have not been fully utilised as yet. Further considerations in choosing the EGS4 code was its availiability in the department and there was experience of using it within the department.

6.4 XYZSCAT: An EGS4 Monte Carlo User Code

6.4.1 Overview of the EGS4 Monte Carlo Code

Figure 6.3 shows the structure of the EGS4 code with the routines above the line provided by the user. This user code then accesses the other routines in the EGS4 code. The HATCH subroutine reads the cross section data produced by the PEGS4 program. The user code includes the HOWFAR subroutine to model the simulation geometry and the AUSGAB subroutine to score the quantities required e.g. energy deposited or photon tracklength. The SHOWER subroutine is used to transport the photons with the appropriate subroutines called depending on which interaction occurs.

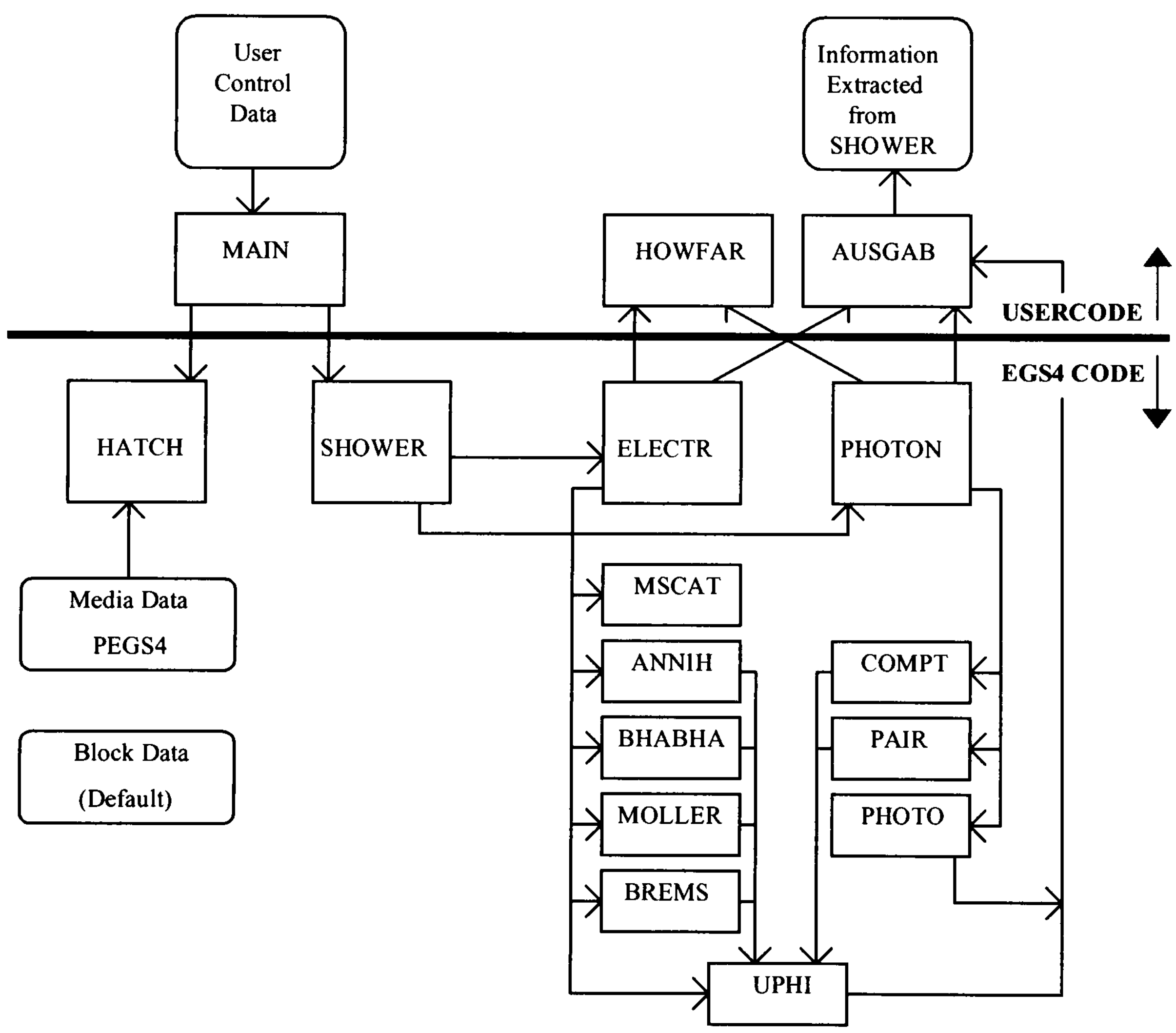

Figure 6.3. The structure of the EGS4 Monte Carlo code.

6.4.2 Description of the User Code

XYZSCAT is a general purpose EGS4 user code developed to simulate radiation transport in a diagnostic x-ray room. It is based on the NRCC (National Research

Council of Canada) XYZDOS user code (Bielajew and Rogers, 1992) for calculating depth doses in a rectangular phantom. Therefore, a number of alterations were made to the XYZDOS code in order to calculate scatter and transmission in x-ray rooms for this thesis. These are discussed below.

6.4.2.1 Preparation of Cross Sections

The PEGS4 program has been used to prepare the cross sections for this work including: the five scattering materials mentioned in table 3.2; the air in the x-ray room; the wood to support the copper slabs; and lead in order to carry out transmission calculations.

Table 6.1 shows the compositions and densities for air (NPL, 1993), WT1 material (White et al., 1977), (Thermolite aerated) concrete (Simpkin, 1989) with a density specified by the manufacturer of 480 kg/m^3 and wood (NPL, 1993). The concrete density is comparable to that for Ytong aerated concrete blocks of 510 kg/m^3 density (Tsalafoutas et al., 1998). The standard densities of aluminium, copper and lead are used: 2702 kg/m^3, 8930 kg/m^3 and 11340 kg/m^3.

Material	Density	Elemental Composition (Percentage by mass)													
	(kg/m^3)	H	C	N	O	Na	Mg	Al	Si	S	Cl	Ar	K	Ca	Fe
Air	1.205	0	0	78.03	21.03	0	0	0	0	0	0	0.94	0	0	0
WT1	1015	8.09	67.22	2.4	19.84	0	0	0	0	0	0.13	0	0	2.32	0
Concrete	480	0.56	0	0	49.83	1.71	0.24	4.56	31.58	0.12	0	0	1.92	8.26	1.22
Wood	500	6.22	44.44	0	49.34	0	0	0	0	0	0	0	0	0	0

***Table 6.1**. Compositions and densities of materials used with the XYZSCAT code.*

Lead has a high atomic number of 82 and therefore, a large proportion of photoelectric interactions will occur for photons travelling through it. Its K shell electron binding energy is 88 keV (Storm and Israel, 1970) and fluorescent photons will be produced for incident photons whose energies are above this value. The

EDGSET subroutine and an alternative photoelectric subroutine PHOTO are used to transport the fluorescent photons.

Photon cross sections were prepared by PEGS4 for the energy range between 1 keV (which equals the lower photon energy cutoffs AP in PEGS4 and PCUT in EGS4) and 200 keV (which equals the upper photon energy cutoff UP in PEGS4). The coherent cross sections were prepared so that coherent scattering is included in the simulations. The EGS4 code models free electron Compton cross sections for incoherent scattering. The effect of electron binding corrections for incoherent scattering was investigated in section 7.2.2.3 using the VOXSCAT Monte Carlo code. The electron transport was switched off in the XYZSCAT calculations. This is due to electrons at these energies producing negligible Bremsstrahlung. Thus, transporting electrons would unnecessarily slow the calculation down.

6.4.2.2 Sampling Photon Energy

The x-ray spectra were prepared by the method described in section 4.5. The method of sampling the spectral distribution to obtain the photon energy was taken from the NRCC INHOM user code (Rogers, 1984a and 1984b).

A cumulative probability distribution (CPD_i) is calculated from the fluence distribution for each energy E_i. Two random numbers R_1 and R_2, uniformly distributed between 0 and 1, are sampled. An energy range (E_{i-1} to E_i) is found such that $CPD_{i-1} \leq R_1 < CPD_i$. The photon energy E (equation 6.11) is obtained by using the random number R_2 to uniformly sample between the energies E_{i-1} and E_i.

$$E = E_{i-1} + R_2(E_i - E_{i-1}) \tag{6.11}$$

6.4.2.3 Geometry Model

Figure 6.4 shows the geometry for the XYZSCAT code which is defined by a 3D grid of voxels. Each voxel is labeled by indices *I*, *J* and *K* which correspond to the x, y and z directions and is associated with a material and density. The figure shows a diagnostic x-ray room constructed with voxels specified as either air, WT1 material for the phantom and concrete for the walls. The total volume is determined by the number of voxels and the voxel size. The size of the voxel sides can vary in all 3 dimensions. However, only a small number of voxels (approximately 40×40×40) can be used to construct a volume as the number of voxels define the size of the program's variable arrays which are in turn limited by the compiler. The size of the voxel sides are therefore large, typically 10 cm, in order to model the dimensions of an x-ray room. For modelling small geometries, some voxels are reduced to the appropriate size and the size of other voxels in the model are increased to compensate. An investigation of the effect of voxel size on scoring the percentage scatter was undertaken in section 6.4.2.8.

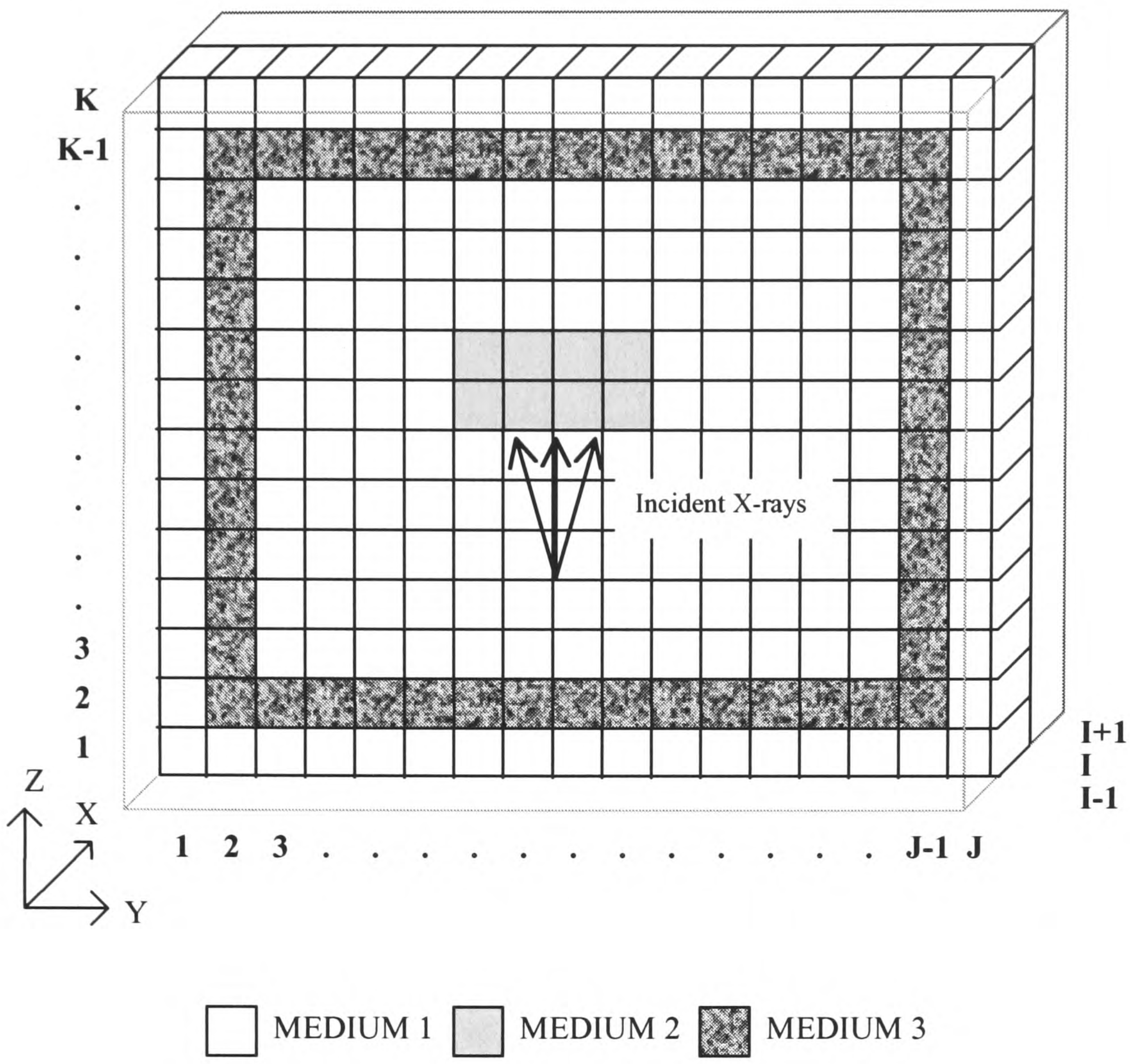

Figure 6.4*. The voxels defining the XYZSCAT model of a diagnostic x-ray room (Media 1, 2 and 3 are the air, WT1 phantom and concrete walls respectively).*

6.4.2.4 Initial Photon Direction

The XYZSCAT code models the x-ray source inside the volume as shown in figure 6.4. For this work, modifications were made to the XYZDOS code which modeled a plane parallel beam outside the volume. In the XYZSCAT code, the photons are modeled as either normally incident or as a divergent beam incident on the phantom's surface. The x-ray source position is specified by the *FSD* (focus surface distance).

The incident position of the photon on the phantom surface is determined following the method described by Morin (1988). Two random numbers R_1 and R_2, uniformly distributed between 0 and 1, are used to sample an isotropic angular distribution. Figure 6.5 shows the x-ray source at position (x,y,z) producing a field of area $2X \times 2Y$ on the phantom's incident surface. The z direction cosine, w, is defined as the cosine of the polar angle θ, and is determined using R_1 in equation 6.12 (NPL, 1993). A parallel beam will be simulated if $\theta_{max} \to 0$.

$$w = \cos\theta = 1 - R_1(1 - \cos\theta_{max}) \qquad (6.12)$$

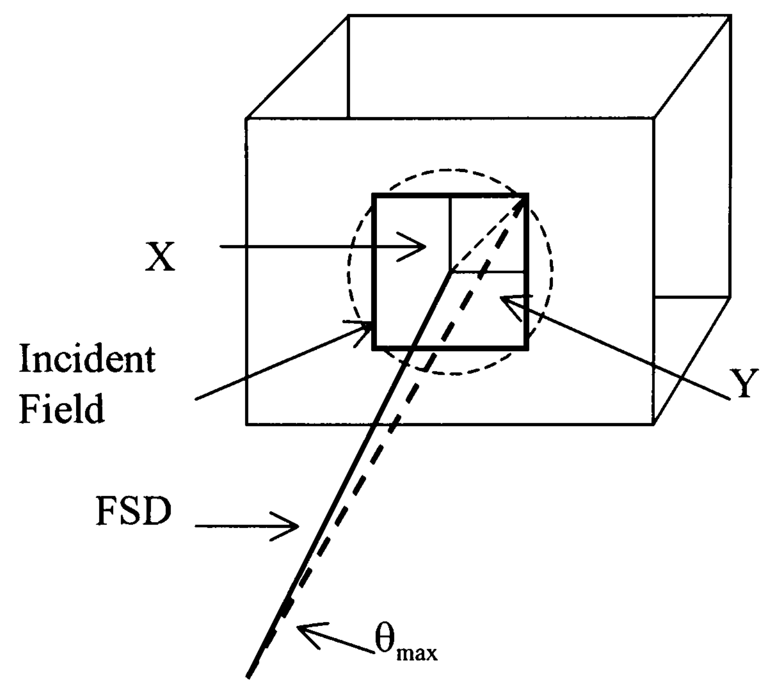

Figure 6.5*. The divergent x-ray beam incident on the phantom.*

The maximum polar angle θ_{max} (figure 6.5) determines that the photons incident on the phantom surface are within a circle circumscribing the rectangular field. Equation 6.13 calculates the cosine of θ_{max} as the ratio of the distance from the x-ray source to the field centre by the distance from the x-ray source to the edge of the circle.

$$\cos\theta_{max} = \frac{FSD}{\sqrt{FSD^2 + X^2 + Y^2}} \qquad (6.13)$$

The azimuthal angle ϕ is determined using R_2 in equation 6.14.

$$\phi = 2\pi R_2 \qquad (6.14)$$

The direction cosine w is accepted if the photon's position (x',y') (equation 6.15) on the phantom's surface ($z' = z + FSD$) is within the field edges. If the incident position is outside the field edges then the random numbers are re-sampled and the procedure repeated until the position is within the field boundaries.

$$x' = x + \frac{\sin\theta\cos\phi}{w} FSD$$

$$y' = y + \frac{\sin\theta\sin\phi}{w} FSD \qquad (6.15)$$

6.4.2.5 Calculated Quantities

The XYZDOS code calculates the energy absorbed in all voxels to obtain the absorbed dose normalised to the incident fluence. For this work, modifications were undertaken to the XYZSCAT code to calculate the quantities described below. The same quantities were calculated with the VOXSCAT code.

The *incident air kerma* (without backscatter) was calculated at the surface of the scattering material as the incident fluence times the fluence to air kerma conversion factor (equation 2.16). Equation 6.16 calculates the incident fluence per photon, Φ_{inc}, using the field area, A, and the polar angle θ between incident photon direction and the normal to the phantom surface.

$$\Phi_{inc} = \frac{1}{A\cos\theta} \qquad (6.16)$$

The *scattered air kerma* was calculated in all voxels containing air as the scattered fluence times the fluence to air kerma conversion factor (equation 2.16) for the scattered photon energy and was given in terms of the scattered air kerma per unit incident fluence. The scattered fluence was calculated by the photon tracklengths (using the EGS4 variable, TVSTEP) across the voxel divided by the voxel's volume as shown in equation 2.18. The *percentage scatter* was calculated in all voxels containing air as the ratio of the scattered air kerma (the normalised scattered air kerma times the incident fluence) to the incident air kerma.

The *percentage first order Compton scatter* was calculated in all voxels containing air as the ratio of the first order scattered air kerma to the incident air kerma. An EGS4 flag called LATCH was used to follow a photon history during a calculation. It was initially set to zero. Everytime a Compton scatter occurred in the phantom the flag was incremented. The Compton scatters produced by an initial coherent scatter were not scored. Therefore, the first order scattered air kerma was scored when LATCH = 1.

The *percentage scatter from different materials* was scored in order to study different sources of scatter in an x-ray room. Everytime a Compton scatter or coherent scatter occurred in a material the LATCH flag was increased by a factor associated with the index of the medium (using the EGS4 variable, MED()).

The *scattered fluence distribution* was found by scoring the fluence in 2 keV energy bins such that the scattered photon energy lies in the energy range E_{i-1} to E_i. The half value layer (HVL) and the mean energy were calculated from the scattered fluence distribution.

The *percentage transmission* was calculated as the ratio of the transmitted air kerma behind the phantom or barrier to the incident air kerma. For divergent beams, the incident air kerma was corrected by an inverse square law factor to give the air kerma at the position where the transmitted air kerma was scored behind the phantom or barrier. The transmitted air kerma was scored for both primary and scattered photons for the central axis voxels behind the phantom or barrier.

6.4.2.6 Estimation of the Calculation Uncertainty

The XYZSCAT code estimates an uncertainty for all air kerma quantities. The calculations are undertaken with N photons and are divided into n batches. Ten batches are commonly used with EGS4. The scored quantity, q_i, is summed for N/n photon histories for each batch. The mean quantity, $\bar{q}$, is found for the 10 batches. The uncertainty is reported as the standard deviation of the mean, $\sigma_{\bar{q}}$ as shown in equation 6.17.

$$\sigma_{\bar{q}} = \left[\frac{\sum_{i=1}^{n=10} (q_i - \bar{q})^2}{n(n-1)} \right]^{1/2} \tag{6.17}$$

6.4.2.7 Random Number Generators

Angle of Scatter (°)	RAN6 RNG Values Percentage Scatter (%)	RAN6 RNG Values Uncertainty (1 S. D.) (%)	RANMAR RNG Values Percentage Scatter (%)	RANMAR RNG Values Uncertainty (1 S. D.) (%)
30	0.100	0.003	0.100	0.003
45	0.080	0.003	0.082	0.004
60	0.060	0.002	0.064	0.003
87	0.050	0.002	0.052	0.003
120	0.164	0.005	0.154	0.007
135	0.233	0.005	0.254	0.004
150	0.294	0.006	0.294	0.004

Table 6.2*. The percentage scatter calculated with the XYZSCAT code using the RAN6 and RANMAR random number generators.*

The *RAN6 linear congruential random number generator* is used with the XYZDOS code and has a period of 10^9. Pseudo-random number generators (RNGs) are heavily used in Monte Carlo codes. They can be sampled between 20 and 1000 times for each photon history depending on the calculation carried out. The number of photons used in scatter calculations approach 10^8 when high precision (less than ±2%) is required. Therefore, the sequence length of the RAN6 random number generator may not be long enough. Instead, the *RANMAR lagged-Fibonacci pseudo-random number generator* is used with the XYZSCAT code and has a period of 2×10^{43} (NPL, 1993).

It is important to test that the new random number generator gives the same results as the old one. The percentage scatter was calculated for 120 kV x-rays with a 400 cm^2 field size incident on a block of WT1 material.

Table 6.2 shows the comparison of the percentage scatter calculated with 10^6 photons with the RAN6 and RANMAR random number generators. The statistical uncertainty in the percentage scatter is shown as one standard deviation of the mean. A paired t-test (Altman, 1991) was used to test whether there is a difference between the scatter values calculated with the RAN6 and RANMAR random number generators. The t-test can be used in this way to determine any differences between the mean values of scatter and to quantify the variability of individual scatter estimates. The t-test shows that the mean scatter calculated with the two RNGs are not significantly different (P=0.47). The difference in the mean scatter values is very small (1.9%) and similar to the uncertainty in the individual scatter estimates. The limits of agreement as derived for the t-test at the 95% confidence level for individual scatter estimates are –0.021% to 0.015%. This corresponds to good agreement between the calculations using the different RNGs (Bland and Altman, 1986).

6.4.2.8 Effect of the Voxel Size

The percentage scatter is scored in all voxels containing air. However, only a relatively small number of voxels are of interest when comparing the calculated percentage scatter with measured values or with values from the literature. Figure 6.6 shows the positions of these voxels for scattering angles of 30°, 45°, 60°, 87°, 120°, 135° and 150° with the centre of the voxel being 1 metre from the centre of the field on the phantom surface.

If the scoring voxel size is small, then the calculation uncertainty will be large. However, if the scoring voxel size is too large then the scoring volume may no longer be representative of the detector volume used in the measurements. The air kerma scored will be averaged over too large a volume and thus a systematic error may be introduced. The effect of the voxel dimensions on the scatter values is investigated in order to determine which voxel size to use in subsequent calculations. The voxel dimensions, equal in the x, y and z directions, were varied between 1 and 10 cm. The phantom thickness of 10 cm limited the size of the largest voxel investigated in this short study. The percentage scatter was calculated for a 60 keV photon beam with a field size of 400 cm^2 incident on a block of WT1 material. The calculation used 120 $\times$ 10^6 photons to keep the statistical uncertainty relatively low for the voxel size of 1 cm.

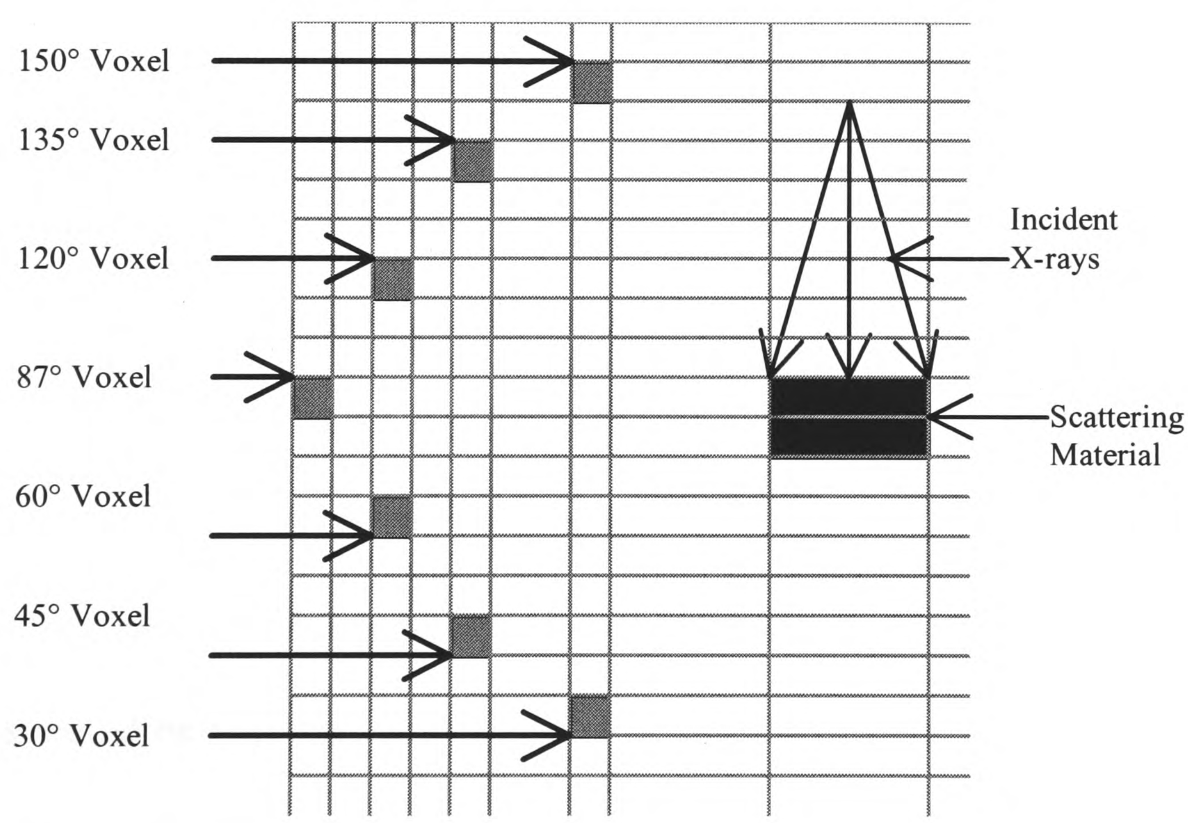

Figure 6.6. *The scoring voxel positions relative to the scattering material.*

Table 6.3 shows the variation of the percentage scatter, for a scoring voxel at a scattering angle of 87°, with changing the voxel size between 1 and 10 cm. A single sample t-test (Altman, 1991) was used to compare the percentage scatter calculated for different voxel sizes (1 to 8 cm) with the scatter value for a 10 cm long voxel. The t-test showed that the mean scatter estimate of the 6 voxel sizes is not significantly different from the value for the 10 cm voxel size (P=0.11). The difference between the mean estimate and the scatter value for 10 cm was small (2.5%). Thus, there is good agreement between the scatter calculated using the different voxel sizes.

Voxel Size	**Percentage Scatter (%)**	**Uncertainty (1 S.D.) (%)**	**Percentage Uncertainty (1 S.D.) (%)**
1cm×1cm×1cm	0.0776	0.0064	8.2
2cm×2cm×2cm	0.0737	0.0030	4.1
3cm×3cm×3cm	0.0736	0.0020	2.7
4cm×4cm×4cm	0.0750	0.0015	2.0
6cm×6cm×6cm	0.0728	0.0010	1.4
8cm×8cm×8cm	0.0727	0.0007	1.0
10cm×10cm×10cm	0.0727	0.0006	0.8

***Table 6.3**. The percentage scatter and their uncertainties calculated for voxel sizes between 1 and 10 cm for an 87° scattering angle.*

Figure 6.7 shows the percentage uncertainties are largest for the voxel at the 87° scattering angle due to the scattered photons having the largest distance to travel to exit the phantom. The percentage uncertainties are similar for the other scattering angles. The uncertainty at the 87° scattering angle then determines the number of photons to be used and therefore, the calculation time. The 10^3 cm^3 voxel size gives a percentage uncertainty of ±0.8% for calculations using 120×10^6 photons. In order to achieve the same uncertainty for the 1^3 cm^3 voxel size then 100 times the number of photons would be required. In this case, the calculation time would be weeks rather than hours which would be unsatisfactory. Therefore, the 10^3 cm^3 voxel size has been used in subsequent calculations as the uncertainty is small which is in turn keeps the calculation time relatively small without affecting the scatter values.

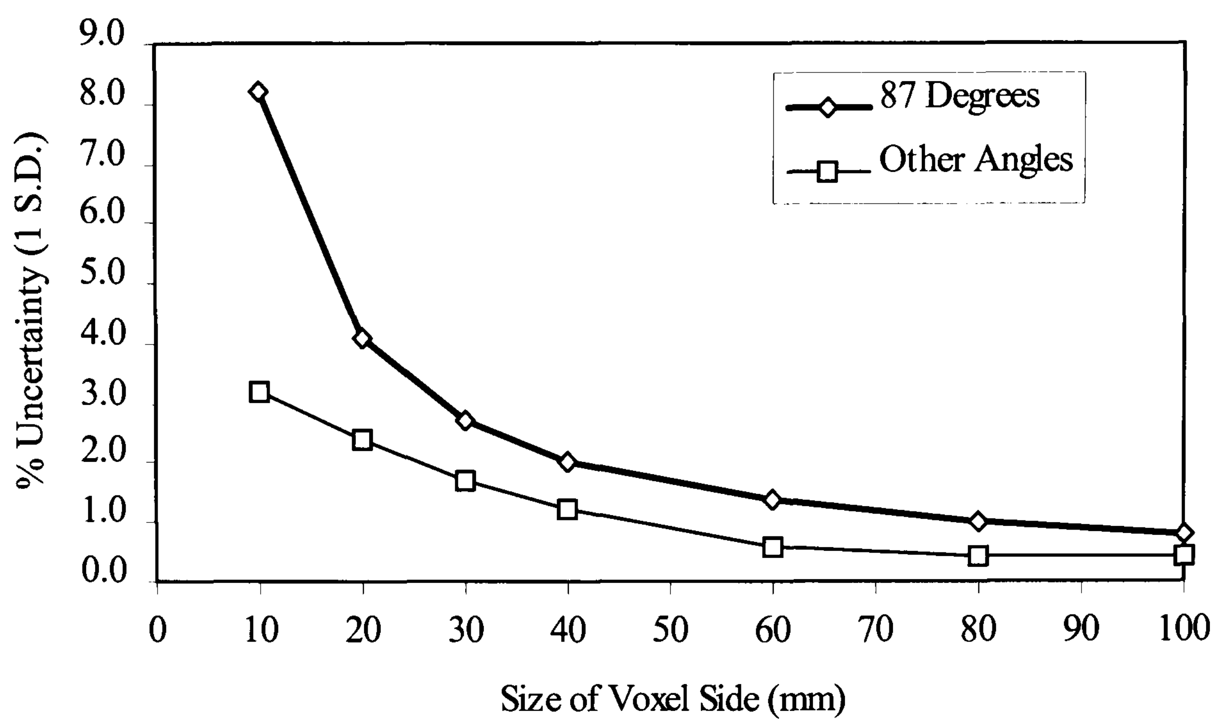

Figure 6.7*. The dependence of the percentage uncertainty on the voxel size.*

6.5 VOXSCAT: A Voxel Monte Carlo Code

The VOXSCAT Monte Carlo code has been developed from a homogeneous phantom model (Sandborg et al. 1994, Dance et al. 1997) by the addition of a voxelised phantom (Zubal et al., 1992, 1994) to realistically simulate the patient. The VOXSCAT code has been used for two purposes in this thesis.

The first purpose is to show that the voxel phantom is representative of a patient. Calculations have been compared to measurements of entrance air kerma from a patient survey to undertake this validation. Figure 6.8 shows that the VOXSCAT code models the complete imaging system which includes the couch top or chest stand to support the patient, a grid or an air-gap as the scatter rejection technique, and the imaging system comprising the cassette front, fluorescent screen and film with characteristic H and D curve. Table 3.4 shows the details of the Norrköping (chest) and Linköping (lumbar spine) imaging systems used in the validation.

The second purpose is to use the VOXSCAT code to model scatter from a patient. The code calculates the scatter from the voxel phantom. As the voxel phantom includes the patient and the patient support device, this means that the scatter from the couch top or the chest stand is included in the calculation depending on the examination simulated.

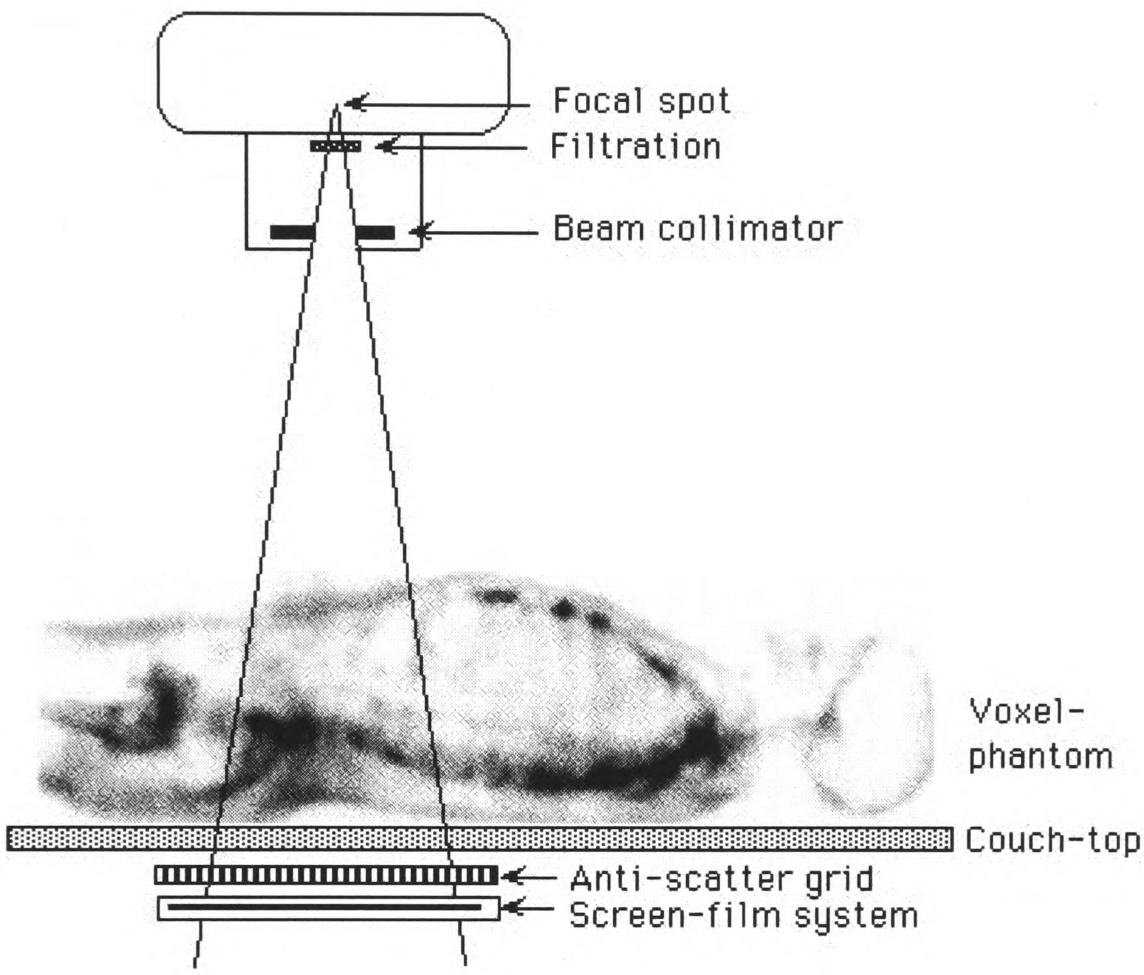

***Figure 6.8**. The Monte Carlo model used in the VOXSCAT code.*

6.5.1 Voxel Phantom

Figure 6.8 shows the voxel phantom developed by Zubal et al. (1992, 1994) at Yale University. It has been derived from three-dimensional CT data of an adult male, which has been segmented into the human anatomy. It is 238 voxels long, although the first voxel and last voxel are outside the body surface (x-direction), 128 voxels wide (y-direction) and 72 voxels thick (z-direction).

A slab phantom is modeled for the first part of the validation procedure. All voxels are set to have the composition and density of PMMA (ICRU, 1989) for the comparison of calculations with measurements of transmission and optical density (section 3.4). The voxel sizes were adjusted to match the dimensions of the software phantom to those of the physical phantom.

The primary purpose of the voxel phantom is to model the patient. Each voxel belongs to one of 52 organs (excluding outside the body surface). Each organ is identified with one of four tissue types: average soft tissue, healthy lung, bone or bone spongiosa. The tissue densities and compositions (Table 6.4) are taken from ICRU Report No. 46 (ICRU, 1992a) except for bone which is taken from work at GSF (Kramer, 1979). An extra layer of voxels is added to the voxel phantom to model the couch top or chest stand if required.

Tissue Type	**Density**	**Elemental Composition (Percentage by mass)**							
	(kg/m^3)	**H**	**C**	**N**	**O**	**Mg**	**S**	**Cl**	**Ca**
Average Soft Tissue	1030	10.5	25.6	2.7	60.2	-	0.3	0.2	-
Healthy Lung	260	10.3	10.5	3.1	74.9	-	0.3	0.3	-
Bone	1486	7.0	22.8	3.9	48.6	0.11	0.17	0.14	9.91
Bone Spongiosa	1180	8.5	40.4	2.8	36.7	0.1	0.2	0.2	7.4

Table 6.4*. Tissue compositions and densities.*

Zubal indicates that the voxel dimensions should be 4 mm × 4 mm × 4 mm in the x, y and z directions. The corresponding dimensions of the phantom would then be 952 mm long, 512 mm wide and 288 mm thick with a mass of approximately 66kg for the tissue densities shown in table 6.4. The mass of the voxel phantom can be compared with the ICRP Reference Man weight of 70 kg (ICRP, 1975) and the GSF ADAM anthromorphic phantom weight of 70.5 kg. However, the Yale voxel phantom does not have the lower limbs present. A very large patient would thus be modeled if the phantom were implemented with this voxel size.

If the voxel size is reduced to make the dimensions of the phantom equivalent to an average European Male (ICRU, 1992b) then: the length of the voxel phantom should be set to the sitting height (899 mm), as the lower limbs are not present; the thickness of the phantom should be set to the chest thickness (221mm); and the width of the phantom should be set to the bi-acrominal (shoulder) width (390 mm). The voxel size required to give these dimensions is 3.809 mm × 3.047 mm × 3.069 mm in the x, y and z directions. The voxel dimensions in the y direction (phantom width) and z direction (phantom thickness) are thus very similar for this situation.

Initially, it was uncertain whether the dimensions mentioned above should be chosen. Therefore, calculations were carried out for thicknesses of both 200 mm and 260 mm and compared to measurements for the patient study (section 7.6.1.1). The voxel sizes in the y and z directions were assumed to be equal. These were 2.778 mm for a 200 mm phantom thickness and 3.611 mm for a 260 mm phantom thickness. This gave shoulder widths of 356 mm and 462 mm for the two phantoms.

6.5.1.1 Incident Field Size on the Voxel Phantom

Four examinations have been investigated in order to validate the patient model. These are the chest and lumbar spine in both the frontal and lateral projections. Initially, experiments were carried out to decide on the size and position of the field incident on the voxel phantom by calculating their effect on the entrance air kerma and dynamic range. This was undertaken most extensively for the chest PA projection but also for the lumbar spine PA projection (section 7.6.1.2).

For the chest PA projection, three field sizes were considered with different values of field length (x direction) but with field width (y direction) fixed to cover the lateral extent of the ribs. For the small field size, the superior border of the rib cage and the inferior border of the lungs set the length. For the intermediate field size, the same superior border and the inferior border of the stomach set the length. For the large field size, the same superior border and the inferior borders of both the rib cage and the liver set the length. For the chest LAT projection, the field length was the same as the largest length used for the PA projection. The field width was set to cover the posterior-anterior extent of the ribs.

For the lumbar spine PA projection, the field length was defined at its superior border by the head of the eleventh rib and at its inferior border by midway down the sacrum. The field width was defined half way along the iliac crests. For the lumbar spine LAT projection, the field length was the same as that used for the PA projection. The field width was defined by its borders being close to the anterior border of the spine and the posterior edge of the spinous processes.

6.5.2 Development of the VOXSCAT Monte Carlo Code

The main modification from previous versions of the Monte Carlo code (Sandborg et al., 1994; Dance et al., 1997) was the inclusion of a voxel phantom. Several alterations were made to the code and are described by Lester (1998) in order to include the GSF paediatric voxel phantoms (Veit et al., 1989). For this thesis, further alterations were made which included: implementing the Zubal adult voxel phantom (Dance et al., 1999; Sandborg et al., 2000); simulating x-ray images by using approximately 200 calculation points in the image plane; and implementing incident air kerma, scattered air kerma and transmitted air kerma calculations.

The VOXSCAT code makes use of variance reduction techniques to improve the efficiency of its calculations. This means that the VOXSCAT photon transport model is different from that described in section 6.2 and that used in the EGS4 Monte Carlo code. Therefore, these features of the VOXSCAT code are described below.

6.5.2.1 Distance to Interaction Point using the Coleman Algorithm

The VOXSCAT code samples the distance to the interaction point using the method described by Coleman (1968). In an homogeneous medium, equation 6.4 selects the distance the photon travels before undergoing an interaction. In an heterogeneous medium such as a voxel phantom, the distance to the interaction site is significantly larger than the voxel size and the photon has to be transported through many voxels. This results in a long calculation time if the conventional method is used. The distance to the interaction point can be calculated more efficiently by using the Coleman algorithm.

The minimum distance to the interaction is calculated using equation 6.4 by finding the material with the highest linear attenuation coefficient, $\mu_{\max}$. The coordinates of the interaction point are found. If this position is within the voxel phantom then the material and the linear attenuation coefficient, μ, are known. This position is accepted as the interaction site if for a sampled random number R that $R \leq \mu/\mu_{\max}$. If this potential interaction site is rejected then the procedure is repeated from this position until a new interaction site is accepted.

6.5.2.2 Interaction Forcing

All photons are forced to undergo scattering at each interaction position (Sandborg et al., 1994). One purpose of the VOXSCAT code is to calculate the percentage scatter at positions surrounding the phantom. Therefore, modeling photons undergoing photoelectric interactions would reduce the efficiency of the calculation.

The photoelectric interaction is taken into account by applying a weight, w_{n+1}, to the scattered photon produced in the nth interaction. Equation 6.18 shows this weight is calculated by the weight of the photon before interaction, w_n, and correcting by the ratio of the photoelectric linear attenuation coefficient, μ_{PE}, to the total linear attenuation coefficient, μ. The linear attenuation coefficients are selected for the appropriate energy.

$$w_{n+1} = w_n \left(1 - \frac{\mu_{PE}}{\mu}\right) \tag{6.18}$$

Russian roulette is 'played' if the weight of the photon, w_{n+1}, is below 0.05. A photon with this weight or below has low 'importance'. This means that its contribution to the score will be low. A random number, R, is sampled and if $R < 0.95$ then the photon transport is stopped. Otherwise, the photon transport continues with the weight increased 20 times.

6.5.2.3 Collision Density Estimator

The collision density estimator (Persliden and Alm Carlsson, 1986) is an efficient method of calculating the scatter with the VOXSCAT code. The collision density estimator forces a contribution from the point of interaction to be scored at the detector for all interactions in the phantom. This is used in two ways in the VOXSCAT code as described below.

The first use is to estimate the energy imparted to the image receptor per unit area. This quantity, normalised to the incident air kerma at the voxel phantom surface, is used to calculate the entrance air kerma as described in section 6.5.3.1. The contribution to the collision density estimator following each interaction in the phantom is the probability, p_{CD}. This is the probability of a photon reaching the scoring position without undergoing further interaction.

$$p_{CD} = \frac{1}{\sigma_T} \frac{d\sigma}{d\Omega} \frac{\Delta A \cos\theta}{l_m^2} e^{-d} t_{grid} \tag{6.19}$$

Equation 6.19 takes into account the total cross section σ_T; the differential scattering cross section $d\sigma/d\Omega$ for either Compton or coherent scatter; and the probability in the radiological pathlength d traveled of no further interactions. The pathlength is found using the Siddon algorithm (section 6.5.2.4). The solid angle is defined by the angle θ between the normal to the detector surface area ΔA and the photon's direction. The distance between the interaction point and the detector is l_m. The transmission through the grid and cassette front is given by t_{grid}.

Equation 6.20 calculates the energy imparted to the image receptor per unit area, $\bar{\varepsilon}$. This calculation uses the mean energy imparted for each interaction, ε_{coh} and ε_{incoh}, and their probabilities, $p_{CD,coh}$ and $p_{CD,incoh}$. This is summed for all N interactions. A separate calculation accounts for the energy imparted to the image receptor per unit area produced by photons scattered in the grid (Sandborg et al., 1994).

$$\bar{\varepsilon} = \sum_{i=1}^{N} w_i \left(p_{CD,coh}\varepsilon_{coh} + p_{CD,incoh}\varepsilon_{incoh}\right)_i \qquad (6.20)$$

The second use is to estimate the scattered air kerma at a fluence detector. This quantity, normalised to the incident air kerma, is used to obtain the percentage scatter at different scattering angles. The contribution to the collision density estimator again uses equation 6.19 but with t_{grid} set equal to 1 as the transmission through the grid and cassette is not required for this calculation.

Equation 6.21 calculates the air kerma per unit area at the fluence detector, $\bar{K}$. The contribution to the fluence per unit area incident on the detector equals $1/\cos\theta$ and is calculated for both Compton and coherent scatter. The air kerma for each interaction type, K_{coh} and K_{incoh}, is calculated with the appropriate fluence contribution, scattered photon energy and mass energy transfer coefficient (Hubbell, 1982). The estimated air kerma is then summed for all interactions to obtain the scatter from the voxel phantom.

$$\overline{K} = \sum_{i=1}^{N} w_i \left(p_{CD,coh} K_{coh} + p_{CD,incoh} K_{incoh} \right)_i \tag{6.21}$$

6.5.2.4 Siddon Algorithm

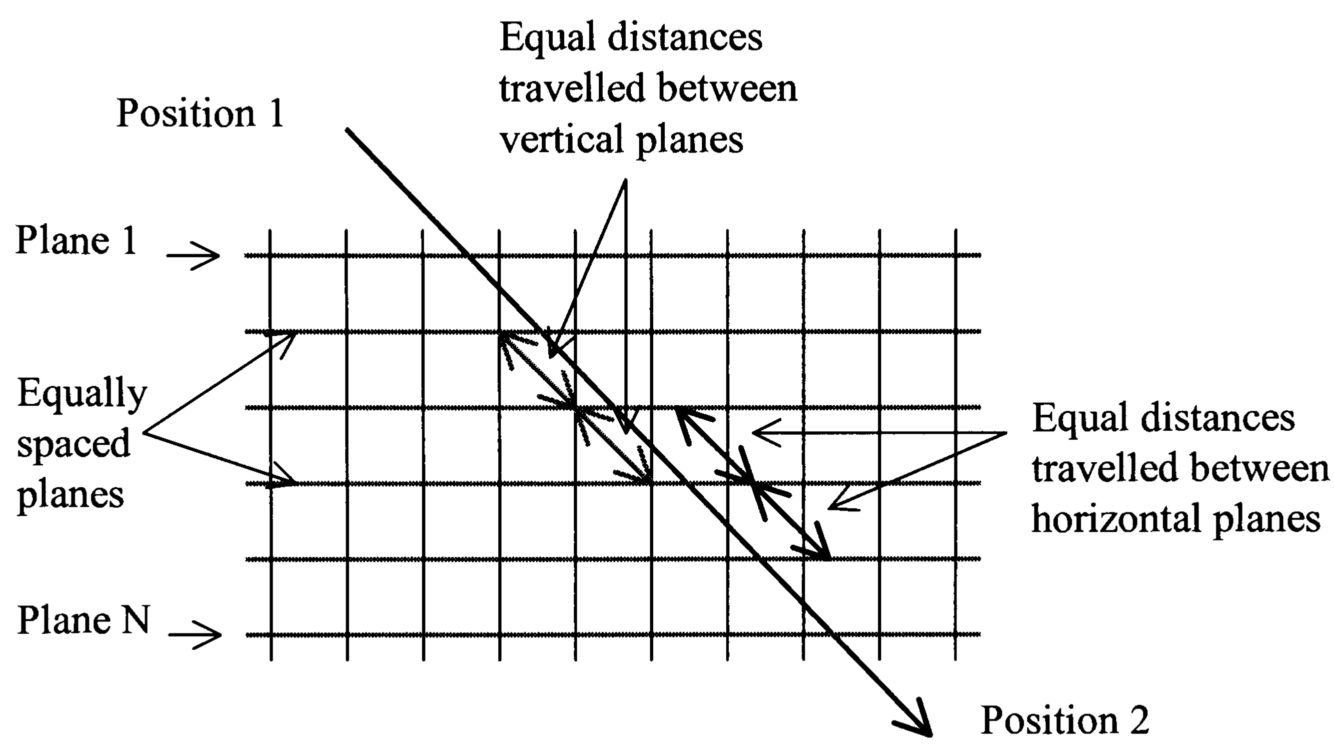

***Figure 6.9**. A photon travelling through equally spaced planes in the x and y directions.*

All voxels in the Zubal phantom have the same dimensions. Therefore, a voxel is defined by the intersection of equally spaced planes in the x, y and z directions. The distance between the x, y and z planes (d_x, d_y and d_z respectively) can be different in each direction such that $d_x \neq d_y \neq d_z$. Figure 6.9 shows that a photon traverses the same distance between planes for example, in the x and y direction. The Siddon algorithm (Siddon, 1985) takes advantage of this to efficiently calculate the radiological pathlength, d. The radiological pathlength is used by the collision density estimator as detailed in the previous section. It is calculated by equation 6.22 using the linear attenuation coefficent of a particular voxel, $\mu(i,j,k)$, and the distance across it, $l(i,j,k)$.

$$d = \sum_i \sum_j \sum_k \mu(i,j,k) l(i,j,k) \tag{6.22}$$

The phantom is defined by $N_x - 1 \times N_y - 1 \times N_z - 1$ voxels where N_x, N_y and N_z are the number of planes in each direction. Figure 6.9 shows the photon travelling along the ray traced from position 1 (X_1,Y_1,Z_1) to position 2 (X_2,Y_2,Z_2) can be parameterised by finding the parameters α_x, α_y and α_z for every plane $X(i)$, $Y(j)$ and $Z(k)$ intersected where i = 1 to N_x, j = 1 to N_y and k = 1 to N_z. The parameters, α_y and α_z, have the same form as α_x for intersecting the ith plane as shown by equation 6.23 if $X_2 - X_1 \neq 0$.

$$\alpha_x(i) = [X(i) - X_1]/[X_2 - X_1] \tag{6.23}$$

Sets of this parameter are calculated for all planes in each direction. The minimum and maximum parameters, α_{min} and α_{max}, are calculated for the range of planes with indices $\{i_{min}, i_{max}\}$, etc. However, not all planes will intersect the ray traced between the coordinates. Therefore, each set of parameters $\{\alpha_x\}$ are re-calculated between the i_{min} and i_{max} indices using equation 6.24 if $X_2 - X_1 \neq 0$.

$$\alpha_x(i) = \alpha_x(i-1) + d_x/(X_2 - X_1) \tag{6.24}$$

Each set for the planes in the x, y and z directions are merged and sorted so that they represent the ray traced from beginning to end. The parameters then lie between α_{min} and α_{max} and the mth parameter lies between 1 and n. Thus, the distance, $l(m)$, travelled by a photon intersecting any planes m-1 and m is shown in equation 6.25.

$$l(m) = [\alpha(m) - \alpha(m-1)]\left[(X_2 - X_1)^2 + (Y_2 - Y_1)^2 + (Z_2 - Z_1)^2\right]^{1/2} \tag{6.25}$$

Equation 6.26 shows that the photon's total radiological pathlength d from position 1 to 2 is calculated by summing all the distances, $l(m)$, for the n intersections with the linear attenuation coefficients for each voxel traversed.

$$d = \sum_{m=1}^{n} \mu(m) l(m) \tag{6.26}$$

6.5.2.5 Estimation of the Calculation Uncertainty

The uncertainty in the quantity, Q, at each specified point is calculated by the VOXSCAT code. This is obtained using the contribution to the quantity, q_i, calculated by the collision density estimator (section 6.5.2.3).

Equation 6.17 shows the calculation of the standard deviation of the mean. Equation 6.27 estimates the relative uncertainty $R_{\bar{Q}}$ as the standard deviation of the mean divided by the mean. A full description of estimating relative errors is given by Breismeister (1994). Equation 6.27 holds if N is large. In the case where all $q_i = 0$ then $R_{\bar{Q}} = 0$.

$$R_{\bar{Q}} = \left[\frac{\sum_{i=1}^{N} q_i^2}{\left(\sum_{i=1}^{N} q_i \right)^2} - \frac{1}{N} \right]^{1/2} \tag{6.27}$$

An advantage of using equation 6.27 is that the VOXSCAT code can monitor the uncertainty in the quantities calculated during the simulation. Therefore, the calculation can be terminated if the desired uncertainty is reached. All VOXSCAT calculations of scatter are stopped after a percentage uncertainty of ±1% is reached.

6.5.3 Quantities Derived from Monte Carlo Calculations

6.5.3.1 Calculation of Entrance Air Kerma and Optical Density

The VOXSCAT code calculates incident air kerma (without backscatter), air kerma in front of the cassette and the energy imparted to the image receptor per unit area. Knowledge of these three quantities, combined with the H and D curve, allows the computation of entrance air kerma for a fixed optical density on the film or optical density for a fixed entrance air kerma. This is implemented in three stages.

In the first stage, the geometry used for the measurement of the H and D curve is simulated. A calibration factor, r_1, is obtained in equation 6.28 as the ratio of the energy imparted to the image receptor per unit area, $\varepsilon_{c,1}$, and the air kerma in front of the cassette, K_{cass}.

$$r_1 = \varepsilon_{c,1} / K_{cass} \tag{6.28}$$

Equation 6.29 shows that the factor r_1 is used to scale the air kerma values in the measured H and D curve, $K_{H\&D}$.

$$\varepsilon_{H\&D} = r_1 K_{H\&D} \tag{6.29}$$

Figure 6.10 shows that a new H and D curve is produced which relates the energy imparted to the image receptor per unit area, $\varepsilon_{H\&D}$, to optical density.

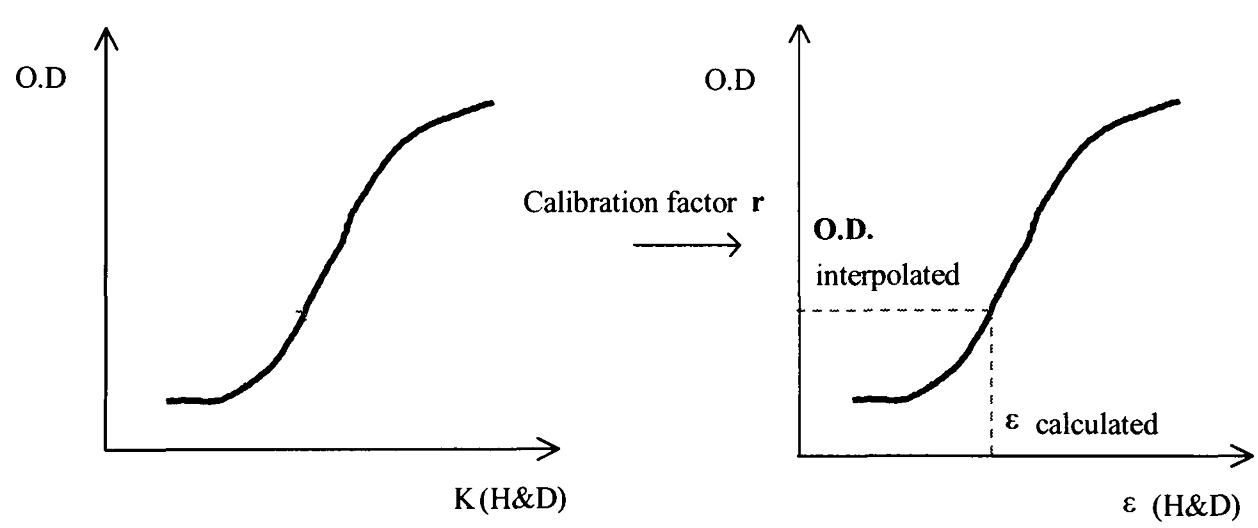

***Figure 6.10**. Calculation of the H and D curve which relates energy imparted to the screen per unit area to the optical density.*

The second stage is to model the imaging systems using the VOXSCAT code for comparison with the patient measurements. A further factor, r_2, is calculated. Equation 6.30 shows the ratio of the energy imparted to the screen per unit area, $\varepsilon_{c,2}$, to the incident air kerma without backscatter, K_{inc}.

$$r_2 = \varepsilon_{c,2} / K_{inc} \tag{6.30}$$

The factor r_2 is calculated for a large number of points behind the voxel phantom to simulate a patient image. Representative regions of interest were selected. A frequency distribution (histogram) of the values of r_2 is produced and the median factor $r_{2,50}$ obtained. The selection of points of interest was achieved by creating a regular grid across the image and retaining all points which lay within a region of interest chosen to match that outlined earlier on the real patient images (section 3.3). For the chest projections this region included the lungs, heart and mediastinum and for the lumbar spine projections it included the whole field.

Examination	**Range in Number of Points used in Simulations**
Chest PA	54 – 1054
Chest LAT	54 – 507
Lumbar Spine AP	54 – 898
Lumbar Spine LAT	56 – 457

***Table 6.5**. The number of points used in simulating x-ray images.*

The precision of $r_{2,50}$ is dependent on the number of points in the simulated image and the Monte Carlo statistical uncertainty for each point. Table 6.5 shows the number of points investigated for each examination with the results shown in section 7.6.1.3. The statistical uncertainty on an individual point was 8% or better. Because a large number of points was used in the estimation of the median value, the statistical error on an individual point could be quite large, and this helped to reduce the computation time required.

In the third stage, the measured median optical density on a particular patient image is used to find the corresponding value of the energy imparted to the screen per unit area, $\varepsilon_{m,50}$, by interpolating the values in the calibrated H and D curve. The calculated value of the entrance air kerma (without backscatter), K_{cal}, is then obtained using equation 6.31.

$$K_{cal} = \varepsilon_{m,50} / r_{2,50} \tag{6.31}$$

The entrance air kerma for the chest PA projection was also obtained by normalisation to the measured optical density at one position in the central right lung and the optical density at one position in the left lung apex. This also followed the procedure described above. The patient TLD measurements (section 3.3.2) were converted to incident air kerma without backscatter using backscatter factors tabulated by Jones and Wall (1985) to facilitate the comparison with the Monte Carlo calculations.

Only one value of factor r_2 is required for the PMMA phantom calculations. It is applied to the measured entrance air kerma (without backscatter), $K_{c,air}$, to obtain the energy imparted to the screen per unit area, ε (equation 6.32).

$$\varepsilon = r_2 K_{c,air} \tag{6.32}$$

The optical density behind the slab phantom is found from ε by interpolating the $\varepsilon_{H\&D}$ values in the calibrated H and D curve. The calculated optical density can thus be compared to the measured optical density behind the slab phantoms in the three x-ray rooms described in section 3.4.

6.5.3.2 Calculation of Dynamic Range

As stated in the previous section, the r_2 factor has been calculated for a large number of points of interest in the simulated image and a frequency distribution (histogram) obtained. In order to compare with the dynamic range measured on patient images, the positions of the 10%, 20%, 30%, 70%, 80% and 90% points of the cumulative frequency distribution were found and the ratios P90:P10, P80:P20 and P70:P30 calculated.

6.6 Summary of Work

The XYZSCAT and VOXSCAT Monte Carlo codes have been developed to calculate the same quantities including percentage scatter. Both codes implement the calculations in significantly different ways and their methods have therefore been discussed in depth. The VOXSCAT code employs a voxel phantom to model the patient which therefore also needs validation. This involves a separate calculation of entrance air kerma for a fixed optical density which can be compared to measurements carried out in a patient survey.

6.6.1 XYZSCAT Code

The EGS4 code was chosen for its greater efficiency over the MCNP code (Love et al., 1998) and for its ability to undertake calculations at many positions at the same time. The XYZSCAT code was developed from the XYZDOS code and modified for this work to include the x-ray spectra from x-ray tubes, with a divergent beam incident on a homogeneous block in an x-ray room. The RANMAR RNG replaced the RAN6 RNG which did not have a long enough sequence length to produce the number of photon histories needed to calculate the scatter with a low uncertainty. The percentage scatter is scored in large voxels of size 10cm×10cm×10cm to ensure low uncertainty and relatively short calculation times whilst maintaining the same scatter values as smaller voxels would give.

6.6.2 VOXSCAT Code

The VOXSCAT code models the patient within the complete imaging system. The patient is simulated with the Zubal voxel phantom of an adult male. In order to validate that the voxel phantom is representative of a patient, comparisons were made of entrance air kerma and dynamic range from patient survey measurements (section

7.6.2). A calibration procedure was undertaken in order to obtain appropriate phantom thickness, field size, field positions and the number of points to simulate an x-ray image to be used in the calculations (section 7.6.1). The VOXSCAT code employs efficient methods to calculate entrance air kerma and percentage scatter from the voxel phantom. The Coleman algorithm selects the interaction points in a heterogeneous medium. Interaction forcing and the collision density estimator are used to efficiently calculate scatter.

Chapter 7: Validation of the Monte Carlo Codes and the Results of Scatter and Transmission Calculations

7.1 Introduction

7.1.1 Code Validation

This chapter describes the validation of the VOXSCAT and XYZSCAT Monte Carlo codes and shows a limited check of the analytical calculation. The validation has been undertaken in seven parts and is briefly summarised below:

Part 1 of the Validation: involves the comparison of the percentage scatter calculated with the XYZSCAT code, the VOXSCAT code and the analytical code (sections 7.2.1.1 to 7.2.1.4) and the comparison of the scattered x-ray spectra calculated with the XYZSCAT and the VOXSCAT codes (section 7.2.1.5). All three codes use the same input parameters.

Part 2 of the Validation: involves the comparison of the measured and calculated percentage scatter for a variety of materials including WT1 (section 7.2.3). The measurements were carried out in the Philips Fluoroscopy Room (section 3.2).

Part 3 of the Validation: involves the comparison of calculations with measurements reported in the literature (section 7.2.4). The percentage scatter (Williams, 1996) and the quality of scattered radiation (Marshall et al., 1996) for human torso shaped phantoms have been studied.

Part 4 of the Validation: involves the comparison of percentage transmission calculated with the XYZSCAT code to that reported in the literature for lead and concrete barriers (section 7.3.1). These materials are commonly used in shielding x-ray rooms.

Part 5 of the Validation: involves the comparison of the transmission calculated with the VOXSCAT code to the transmission measured behind PMMA blocks (section 7.4).

Part 6 of the Validation: involves the comparison of the optical density calculated with the VOXSCAT code to the optical density measured behind PMMA blocks (section 7.5). The comparisons in parts 5 and 6 are used to validate the VOXSCAT code and show that the imaging systems are modeled correctly.

Part 7 of the Validation: involves the comparison of the entrance air kerma calculated with the VOXSCAT code to the measured values obtained for chest and lumbar spine patient radiographs (section 7.6.2.1). This comparison shows if the voxel phantom is representative of patient anatomy.

7.1.2 Initial Investigations

Results have been obtained from five investigations and are summarised below:

Initial Study 1: The VOXSCAT code was used to study the effect of different physical factors on the percentage scatter. The contribution from different orders of Compton and coherent scatter to the total scatter was studied (sections 7.2.2.1 and 7.2.2.2). The variation of the percentage scatter with different tabulations of interaction coefficients, including Compton cross sections with and without electron binding corrections, was also studied (section 7.2.2.3).

Initial Study 2: The VOXSCAT code was used to calculate the percentage scatter for different FSDs and different distances between the phantom and detector (sections 7.2.2.4 to 7.2.2.6) as both distances are typically 100 cm.

Initial Study 3: The XYZSCAT code was used to calculate the contribution to the total scatter from different materials in an x-ray room: for the WT1 phantom and air only (section 7.2.2.7) and for the WT1 phantom, air, ceiling, floor, walls and DAP meter (section 7.2.3.3).

Initial Study 4: The XYZSCAT code was used to study the variation of the percentage scatter with field size for small field areas incident on slab phantoms (section 7.2.3.2) to large field areas incident on x-ray room walls (section 7.3.2.2). The variation of the percentage scatter is compared to the expected values from 'rule of thumb' calculations.

Initial Study 5: The variation of entrance air kerma with voxel phantom thickness, field size, tissue density and the number of points used to simulate an x-ray image has been studied with the VOXSCAT code (section 7.6.1).

7.2 Calculation of Scatter

7.2.1 Comparison of the Codes

The percentage scatter calculated with the XYZSCAT code, the VOXSCAT code and the analytical code (only for first order Compton scatter) are compared in this section. There are significant differences in the implementation of the Monte Carlo models as described in Chapter 6. The percentage scatter is calculated with high precision using both Monte Carlo codes. Therefore, this comparison provides a rigorous validation.

The same geometry has been used in all the calculations described in sections 7.2.1.1 to 7.2.1.5 and sections 7.2.2.1 to 7.2.2.7 except where noted. The geometry consists of a plane parallel beam with a field size of 400 cm^2 incident on a block of WT1 material with dimensions 305 mm × 305 mm × 100 mm. This geometry simulates x-rays incident on a patient in an upright position. All codes use Storm and Israel (1970) cross sections except for incoherent scattering which employs Compton cross sections without electron binding corrections. Both the VOXSCAT and analytical codes do not include air outside the phantom. Therefore, the density of air used with XYZSCAT code has been reduced from 1.205 kg/m^3 to 1.205×10^{-6} kg/m^3 to ensure that no interactions occur in the air.

7.2.1.1 First Order Compton Scatter for Monoenergetic Photons

Table 7.1 compares the percentage first order Compton scatter calculated with the XYZSCAT, the VOXSCAT and the analytical codes for monoenergetic photons between 20 and 150 keV. The XYZSCAT calculations use between 400×10^6 and 120×10^6 photons for energies between 30 and 150 keV. This achieves a percentage uncertainty of less than ±2% which is comparable to that obtained with the VOXSCAT code. However, using 400×10^6 photons with an energy of 20 keV produces a percentage uncertainty of between ±8% and ±23% for scattering angles between 30° and 87°. This reflects the small number of Compton interactions that occur at this energy. Better statistics require a larger number of photons but the calculation time would then become excessive. It was therefore decided to accept the results as they are.

Angle (°)	Percentage First Order Compton Scatter for Monoenergetic Photons					
	20 keV Photons			30 keV Photons		
	XYZSCAT Values	VOXSCAT Values	Analytical Values	XYZSCAT Values	VOXSCAT Values	Analytical Values
30	0.00009	0.00010	0.00010	0.0134	0.0134	0.0135
45	0.00004	0.00004	0.00004	0.0072	0.0073	0.0072
60	0.00003	0.00003	0.00003	0.0036	0.0038	0.0037
87	0.00004	0.00003	0.00003	0.0018	0.0018	0.0018
120	0.02440	0.02423	0.02461	0.0517	0.0518	0.0530
135	0.03546	0.03559	0.03634	0.0753	0.0756	0.0774
150	0.04565	0.04599	0.04698	0.0966	0.0971	0.0994

Angle (°)	40 keV Photons			50 keV Photons		
	XYZSCAT Values	VOXSCAT Values	Analytical Values	XYZSCAT Values	VOXSCAT Values	Analytical Values
30	0.0467	0.0469	0.0478	0.077	0.078	0.078
45	0.0280	0.0280	0.0284	0.047	0.048	0.048
60	0.0152	0.0151	0.0152	0.026	0.026	0.026
87	0.0066	0.0068	0.0068	0.012	0.012	0.011
120	0.0723	0.0742	0.0740	0.082	0.083	0.083
135	0.1037	0.1065	0.1068	0.115	0.118	0.118
150	0.1324	0.1352	0.1361	0.146	0.148	0.149

Angle (°)	60 keV Photons			80 keV Photons		
	XYZSCAT Values	VOXSCAT Values	Analytical Values	XYZSCAT Values	VOXSCAT Values	Analytical Values
30	0.099	0.099	0.100	0.127	0.127	0.128
45	0.061	0.063	0.062	0.078	0.080	0.080
60	0.034	0.035	0.034	0.043	0.044	0.043
87	0.014	0.015	0.015	0.017	0.018	0.017
120	0.082	0.082	0.084	0.074	0.075	0.075
135	0.113	0.115	0.117	0.099	0.101	0.101
150	0.143	0.144	0.146	0.121	0.122	0.123

Angle (°)	100 keV Photons			120 keV Photons			150 keV Photons		
	Xyzscat Values	Voxscat Values	Analy-tical Values	Xyzscat Values	Voxscat Values	Analy-tical Values	Xyzscat values	Voxscat Values	Analy-tical Values
30	0.142	0.144	0.145	0.156	0.158	0.158	0.169	0.170	0.173
45	0.087	0.089	0.089	0.094	0.096	0.095	0.100	0.102	0.102
60	0.047	0.048	0.048	0.050	0.050	0.050	0.051	0.052	0.052
87	0.017	0.018	0.018	0.019	0.018	0.019	0.017	0.018	0.017
120	0.064	0.065	0.065	0.059	0.056	0.060	0.047	0.048	0.048
135	0.084	0.085	0.085	0.075	0.072	0.077	0.059	0.059	0.061
150	0.099	0.102	0.101	0.087	0.084	0.090	0.068	0.068	0.070

Table 7.1*. The comparison of the percentage first order Compton scatter calculated with the XYZSCAT code, the VOXSCAT code and the analytical code for monoenergetic photons.*

The values of the percentage first order Compton scatter calculated with the XYZSCAT, VOXSCAT and analytical codes were compared using three paired t-tests (Altman, 1991) by the method described in section 6.4.2.7. The t-tests show that the mean scatter estimates calculated by the three codes are significantly different ($P < 0.001$) with the analytical values being larger than the VOXSCAT values which in turn are larger than the XYZSCAT values. However, the differences in the mean scatter estimates are very small (less than 2%) which is similar to the uncertainty in individual scatter estimates. It is also reassuring that the limits of agreement, as derived from the t-tests, at the 95% confidence level for individual scatter estimates are small being: -0.003% to 0.002% between the XYZSCAT and VOXSCAT codes; -0.003% to 0.001% between the XYZSCAT and analytical codes; and -0.003% to 0.002% between the VOXSCAT and analytical codes. This corresponds to good agreement between the three calculation methods (Bland and Altman, 1986).

7.2.1.2 First Order Compton Scatter for Clinical X-ray Beams

Table 7.2 compares the percentage first order Compton scatter calculated with the XYZSCAT, the VOXSCAT and the analytical codes for x-rays produced by the Philips Unit (table 3.1) with measured tube potentials between 49 and 121 kV. The XYZSCAT calculations use between 240×10^6 and 180×10^6 photons to achieve a percentage uncertainty of, for the most part, less than ±1.1% which is comparable to that used with the VOXSCAT code. The largest uncertainty for the XYZSCAT code calculations is ±2.2% for the 87° scattering angle due to the scattered photons being more attenuated at this angle than at other scattering angles.

The values of the percentage first order Compton scatter calculated with the XYZSCAT, VOXSCAT and analytical codes were compared using three paired t-tests (Altman, 1991) by the method described in section 6.4.2.7. The t-tests show that the mean scatter estimates calculated by the XYZSCAT and VOXSCAT codes are not significantly different ($P=0.86$) but the mean scatter calculated with the analytical code is significantly different (P < 0.001). The values calculated with the analytical code are larger than the values calculated with the other two codes. However, the differences in the mean scatter estimates are small (less than 3.3%) which is similar to the uncertainty in individual scatter estimates calculated with the analytical code (section 5.7.4). It is also reassuring that the limits of agreement, as derived from the t-tests, at the 95% confidence level for individual scatter estimates are small being: -0.001% to 0.001% between the XYZSCAT and VOXSCAT codes; -0.005% to 0.002% between the XYZSCAT and analytical codes; and –0.005% to 0.001% between the VOXSCAT and analytical codes. This corresponds to good agreement between the three calculation methods (Bland and Altman, 1986).

	Percentage First Order Compton Scatter for Clinical X-ray Beams					
Angle	**49 kV X-rays**			**69 kV X-rays**		
(°)	**XYZSCAT Values**	**VOXSCAT Values**	**Analytical Values**	**XYZSCAT Values**	**VOXSCAT Values**	**Analytical Values**
30	0.0193	0.0187	0.0200	0.0338	0.0331	0.0349
45	0.0111	0.0109	0.0115	0.0205	0.0199	0.0209
60	0.0063	0.0061	0.0061	0.0115	0.0112	0.0113
87	0.0030	0.0029	0.0028	0.0052	0.0052	0.0050
120	0.0509	0.0506	0.0527	0.0581	0.0583	0.0604
135	0.0741	0.0737	0.0767	0.0839	0.0837	0.0871
150	0.0951	0.0945	0.0983	0.1064	0.1066	0.1110

Angle	**100 kV X-rays**			**121 kV X-rays**		
(°)	**XYZSCAT Values**	**VOXSCAT Values**	**Analytical Values**	**XYZSCAT Values**	**VOXSCAT Values**	**Analytical Values**
30	0.0517	0.0520	0.0538	0.0612	0.0616	0.0636
45	0.0320	0.0321	0.0328	0.0379	0.0382	0.0390
60	0.0179	0.0180	0.0178	0.0212	0.0213	0.0211
87	0.0081	0.0080	0.0076	0.0094	0.0093	0.0089
120	0.0639	0.0635	0.0656	0.0647	0.0651	0.0670
135	0.0898	0.0901	0.0934	0.0910	0.0916	0.0946
150	0.1132	0.1142	0.1180	0.1141	0.1154	0.1191

***Table 7.2**. The comparison of the percentage first order Compton scatter calculated with the XYZSCAT code, the VOXSCAT code and the analytical code for clinical x-rays.*

7.2.1.3 Total Scatter for Monoenergetic Photons

Angle (°)	Percentage Scatter for Monoenergetic Photons					
	20 keV Photons		30 keV Photons		40 keV Photons	
	XYZSCAT Values	VOXSCAT Values	XYZSCAT Values	VOXSCAT Values	XYZSCAT Values	VOXSCAT Values
30	0.00033	0.00034	0.0405	0.0409	0.147	0.147
45	0.00014	0.00014	0.0238	0.0240	0.096	0.097
60	0.00010	0.00009	0.0133	0.0137	0.060	0.060
87	0.00010	0.00009	0.0063	0.0063	0.027	0.027
120	0.03480	0.03471	0.0901	0.0906	0.157	0.161
135	0.04945	0.04935	0.1264	0.1269	0.213	0.217
150	0.06183	0.06202	0.1554	0.1569	0.256	0.261

Angle (°)	50 keV Photons		60 keV Photons		80 keV Photons	
	XYZSCAT Values	VOXSCAT Values	XYZSCAT Values	VOXSCAT Values	XYZSCAT Values	VOXSCAT Values
30	0.243	0.246	0.300	0.305	0.333	0.340
45	0.168	0.171	0.212	0.217	0.243	0.248
60	0.110	0.110	0.142	0.143	0.161	0.165
87	0.052	0.051	0.068	0.069	0.078	0.080
120	0.207	0.209	0.227	0.229	0.215	0.220
135	0.273	0.276	0.292	0.296	0.270	0.275
150	0.322	0.326	0.344	0.348	0.309	0.314

Angle (°)	100 keV Photons		120 keV Photons		150 keV Photons	
	XYZSCAT Values	VOXSCAT Values	XYZSCAT Values	VOXSCAT Values	XYZSCAT Values	VOXSCAT Values
30	0.326	0.331	0.325	0.325	0.310	0.314
45	0.236	0.240	0.231	0.232	0.216	0.221
60	0.155	0.160	0.152	0.151	0.136	0.142
87	0.074	0.076	0.074	0.070	0.062	0.065
120	0.184	0.189	0.165	0.159	0.130	0.133
135	0.228	0.233	0.202	0.191	0.154	0.156
150	0.254	0.263	0.224	0.214	0.170	0.173

***Table** 7.3. The comparison of the total percentage scatter calculated with the XYZSCAT code and the VOXSCAT code for monoenergetic photons.*

Table 7.3 compares the total percentage scatter calculated with the XYZSCAT and the VOXSCAT codes for monoenergetic photons between 20 and 150 keV. The XYZSCAT calculations use between 400×10^6 and 120×10^6 photons for energies between 30 and 150 keV. This achieves a percentage uncertainty of less than ±1% which is comparable to that obtained with the VOXSCAT code. The percentage uncertainty for using 400×10^6 photons with an energy of 20 keV is between ±5% and ±13% for scattering angles between 30° and 87°. Again, it was decided to accept the results as they are.

The values of the percentage scatter calculated with the XYZSCAT and the VOXSCAT codes were compared using a paired t-test (Altman, 1991) by the method described in section 6.4.2.7. The t-test shows that the mean scatter estimates calculated by the two codes are significantly different ($P < 0.001$) with the VOXSCAT values being larger than the XYZSCAT values. However, the difference in the mean scatter estimates is very small (1.1%) which is similar to the uncertainty in individual scatter estimates. It is also reassuring that the limits of agreement, as derived from the t-tests, at the 95% confidence level for individual scatter estimates are small being -0.009% to 0.005%. This corresponds to good agreement between the two calculation methods (Bland and Altman, 1986).

7.2.1.4 Total Scatter for Clinical X-ray Beams

Angle (°)	Percentage Scatter for Clinical X-ray Beams							
	49 kV X-rays		69 kV X-rays		100 kV X-rays		121 kV X-rays	
	XYZSCAT Values	VOXSCAT Values	XYZSCAT Values	VOXSCAT Values	XYZSCAT Values	VOXSCAT Values	XYZSCAT Values	VOXSCAT Values
30	0.060	0.058	0.105	0.103	0.155	0.155	0.177	0.177
45	0.038	0.037	0.070	0.069	0.107	0.108	0.123	0.124
60	0.024	0.023	0.045	0.044	0.071	0.070	0.082	0.081
87	0.012	0.011	0.022	0.021	0.035	0.035	0.040	0.041
120	0.096	0.095	0.123	0.123	0.148	0.148	0.155	0.156
135	0.132	0.131	0.166	0.166	0.194	0.195	0.202	0.205
150	0.162	0.161	0.200	0.200	0.231	0.233	0.240	0.242

***Table 7.4**. The comparison of the total percentage scatter calculated with the XYZSCAT code and the VOXSCAT code for clinical x-rays.*

Table 7.4 compares the total percentage scatter calculated with the XYZSCAT and VOXSCAT codes for x-rays produced by the Philips Unit with measured tube potentials between 49 and 121 kV. The XYZSCAT calculations use between 240×10^6

and 180×10^6 photons to achieve a percentage uncertainty of less than ±0.6% which is comparable to that obtained the VOXSCAT code.

The values of the percentage scatter calculated with the XYZSCAT and the VOXSCAT codes were compared using a paired t-test (Altman, 1991) by the method described in section 6.4.2.7. The t-test shows that the mean scatter estimates calculated by the two codes are not significantly different (P = 0.76) and the difference in the mean scatter estimates is very small (0.1%). It is also reassuring that the limits of agreement, as derived from the t-tests, at the 95% confidence level for individual scatter estimates are small being -0.002% to 0.002%. This corresponds to good agreement between the two calculation methods (Bland and Altman, 1986).

	Percentage Scatter							
	50 kV X-rays		**70 kV X-rays**		**100 kV X-rays**		**120 kV X-rays**	
Mean Energy Angle (°)	**kV Values**	**$\overline{E}$ Values 33.7 keV**	**kV Values**	**$\overline{E}$ Values 41.1 keV**	**kV Values**	**$\overline{E}$ Values 50.6 keV**	**kV Values**	**$\overline{E}$ Values 55.6 keV**
30	0.060	0.080	0.105	0.158	0.155	0.251	0.177	0.281
45	0.038	0.050	0.070	0.106	0.107	0.175	0.123	0.198
60	0.024	0.029	0.045	0.065	0.071	0.113	0.081	0.131
87	0.012	0.013	0.022	0.029	0.035	0.054	0.040	0.064
120	0.096	0.117	0.123	0.163	0.148	0.211	0.155	0.223
135	0.132	0.162	0.166	0.220	0.194	0.276	0.202	0.287
150	0.162	0.197	0.200	0.265	0.231	0.326	0.240	0.341

Table 7.5. *The comparison of the percentage scatter calculated using x-ray spectra and using monoenergetic photons with the mean energies of the spectral distributions.*

Table 7.5 compares the XYZSCAT calculations of percentage scatter using spectral distributions and using monoenergetic photons with the mean energies of the spectral distributions. These values show that the scatter values calculated for monoenergetic photons considerably overestimate the scatter produced by clinical x-ray beams with the average difference being 42%. If accurate values of percentage scatter are required then the results of calculations using x-ray spectra should be employed.

7.2.1.5 Quality of Scattered Radiation

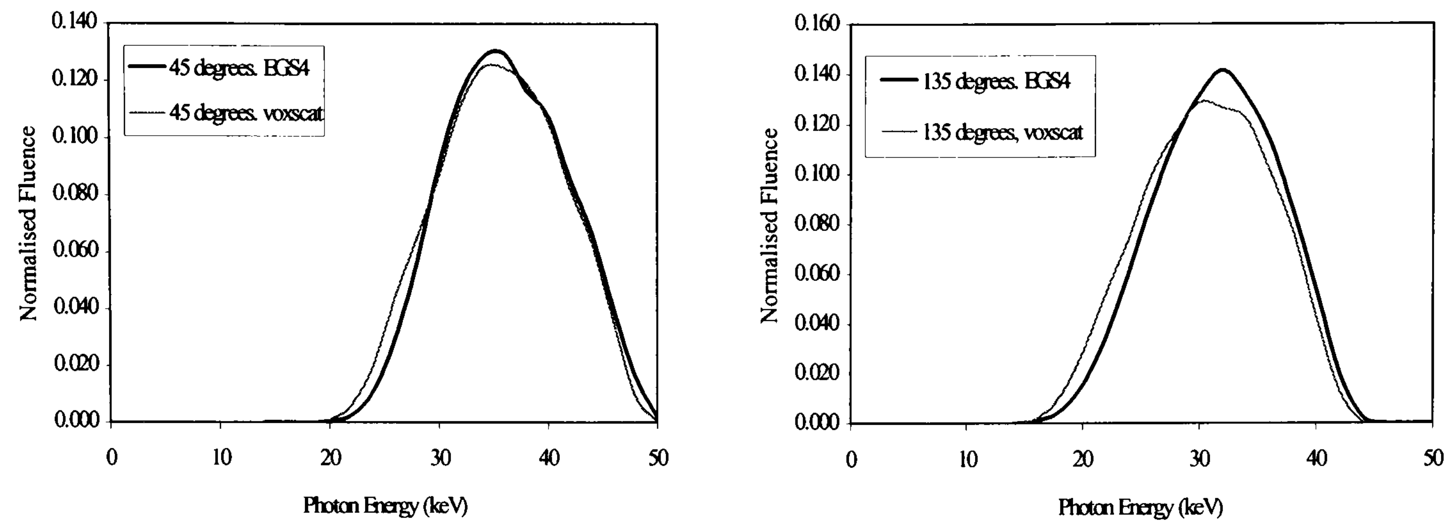

(a) *(b)*

Figure 7.1. *The XYZSCAT and VOXSCAT calculated scattered spectra for 49 kV x-rays at scattering angles of (a) 45° and (b) 135°.*

Figures 7.1 and 7.2 show example comparisons of the scattered spectra calculated with the XYZSCAT and VOXSCAT codes. Figure 7.1 compares the scatter fluence distribution (normalised to the total scatter fluence) at 45° and 135° scattering angles for 49 kV x-rays produced by the Philips Unit. Figure 7.2 compares the scatter fluence distribution (normalised to the total scatter fluence) at 45° and 135° scattering angles for 121 kV x-rays produced by the Philips Unit. The scattered spectra are shown in the figures with an energy bin size of 2 keV. The XYZSCAT calculations used between 240×10^6 and 180×10^6 photons. The precision is determined for the highest fluence contribution in the distribution. The percentage uncertainty is thus ±2% for all scattering angles except 87° which is ±4%. The calculation uncertainties are comparable for the two codes.

Figures 7.1 and 7.2 show that there is reasonably good agreement between the scattered spectra calculated with the XYZSCAT and VOXSCAT codes. The scattered spectra calculated with the VOXSCAT code are of slightly lower quality for the 49 kV x-rays but the differences between the spectra are not significant. The mean energies for the scattered spectra calculated by the VOXSCAT code are less than 1 keV lower than the mean energies calculated by the XYZSCAT code. The greatest changes are between the incident and scattered spectral distributions for high tube potentials and large scattering angles (section 7.2.4.2).

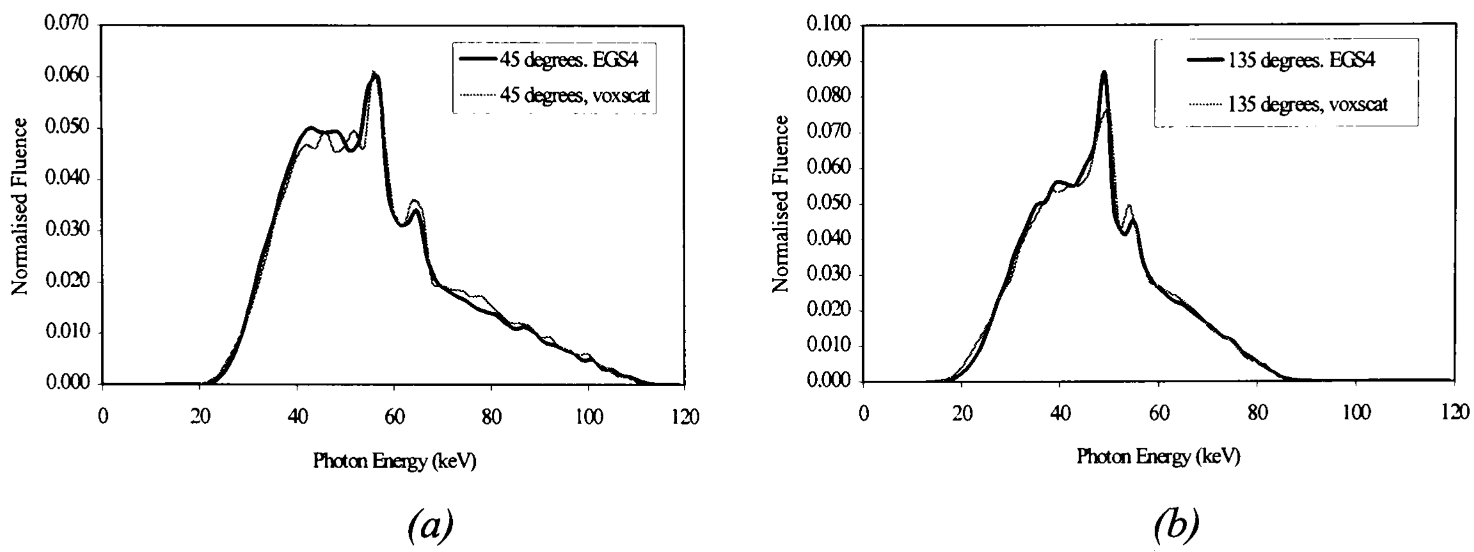

***Figure** 7.2. The XYZSCAT and VOXSCAT calculated scattered spectra for 121 kV x-rays at scattering angles of (a) 45 ° and (b) 135 °.*

7.2.2 Initial Investigations of Scatter

7.2.2.1 The Contributions from Different Orders of Compton Scatter

Sections 7.2.1.2 and 7.2.1.4 have shown the percentage scatter for the first order Compton scatter and for all interactions. This section therefore investigates the contributions of different orders of Compton scatter to the total scatter calculated using the VOXSCAT code.

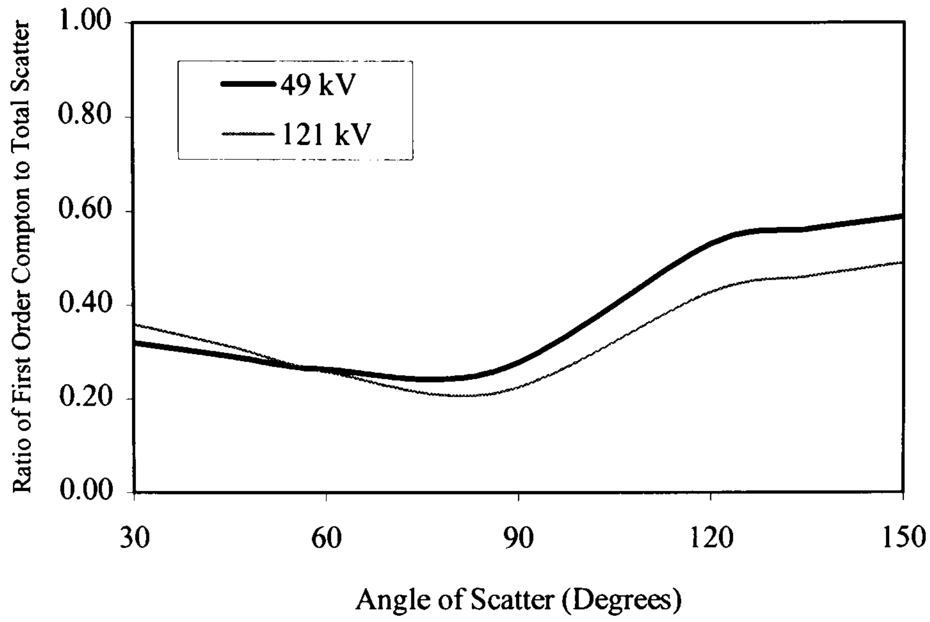

***Figure 7.3**. The ratio of the first order Compton scatter to the total scatter for 49 kV and 121 kV x-rays.*

Figure 7.3 shows the ratio of the first order Compton scatter to the total scatter for 49 kV and 121 kV x-rays. It can be seen that the first order Compton scatter is not a good estimate of the total scatter. The ratio is 32% and 59% at scattering angles of 30° and 150° for 49 kV x-rays. The ratio is 36% and 49% at scattering angles of 30° and 150° for 121 kV x-rays. The ratio then varies with angle of scatter and beam quality. Thus, it is difficult to predict the value of the total scatter using the values of the first order Compton scatter.

Figure 7.4 shows the percentage contributions from all orders of Compton scatter to the total Compton scatter for 49 kV and 121 kV x-rays. The first four orders of Compton scatter are shown to produce the majority of the total Compton scatter with their smallest contribution being 82% at a scattering angle of 87° for 121 kV x-rays. The contributions from orders of scatter greater than 4 increases for increasing tube potential due to the greater penetration of the scattered photons. The results show the importance of including all orders of Compton scatter to provide an accurate calculation of the total scatter.

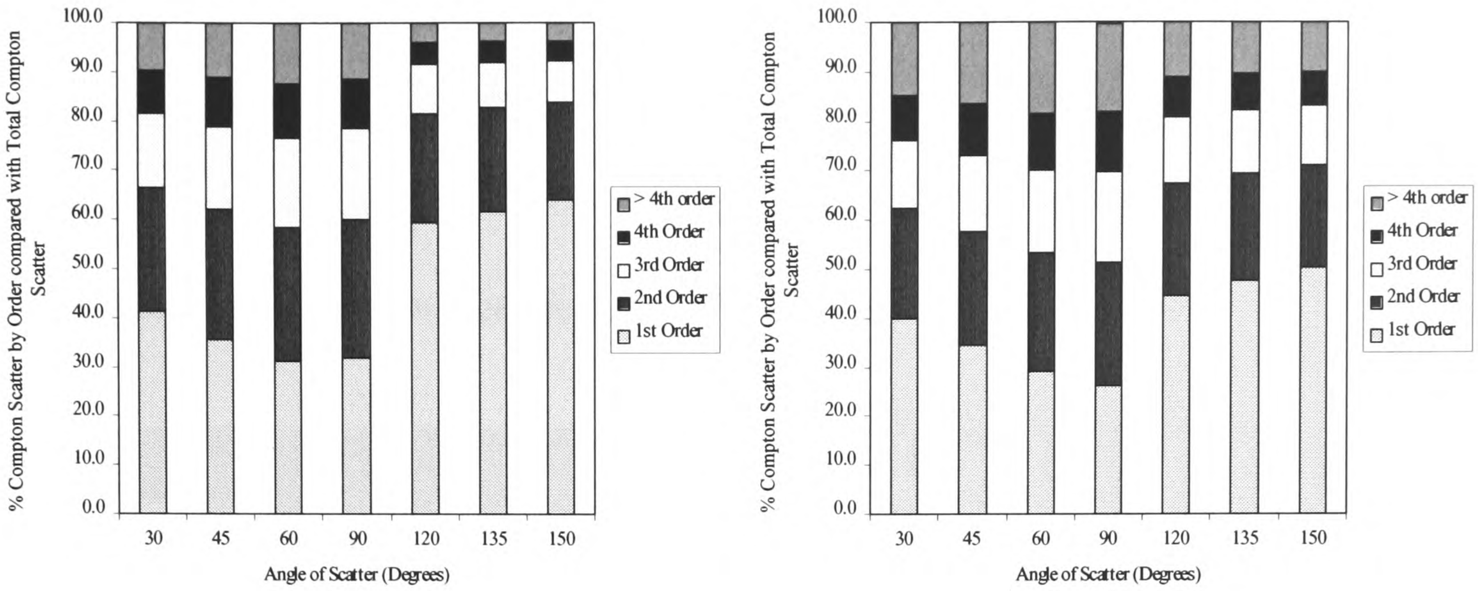

(a) *(b)*

***Figure 7.4**. The percentage contributions from different orders of Compton scatter to the total Compton scatter for (a) 49 kV and (b) 121 kV x-rays.*

7.2.2.2 The Contributions from Different Orders of Coherent Scatter

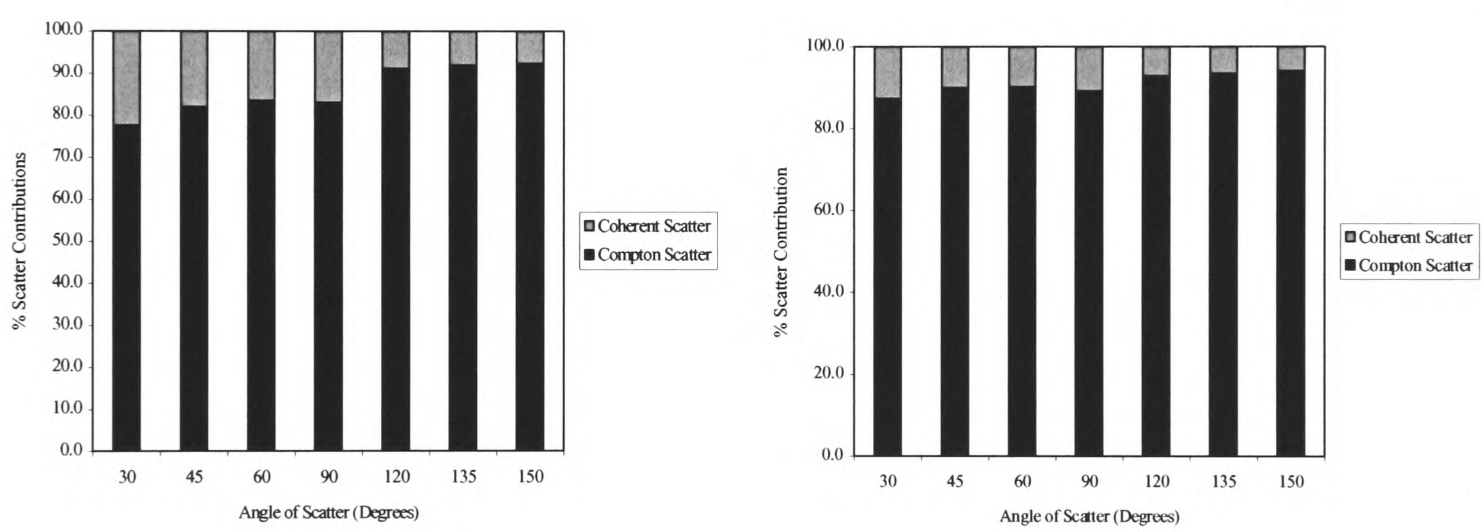

(a) *(b)*

***Figure 7.5**. The percentage contributions of Compton and coherent scatter to the total scatter for (a) 49 kV and (b) 121 kV x-rays.*

This section investigates the contribution of coherent scatter to the total scatter. Figure 7.5 shows the contributions of all Compton and coherent interactions to the total scatter calculated using the VOXSCAT code. The largest coherent scatter contributions are in the forward direction with a 22% contribution at a 30° scattering angle compared to an 8% contribution at a 150° scattering angle for 49 kV x-rays.

This is due to the differential coherent cross section peaking for small scattering angles (maximum value at 0°). The coherent scatter contribution decreases with increasing photon energy for all angles of scatter due to the total coherent cross section decreasing with increasing photon energy.

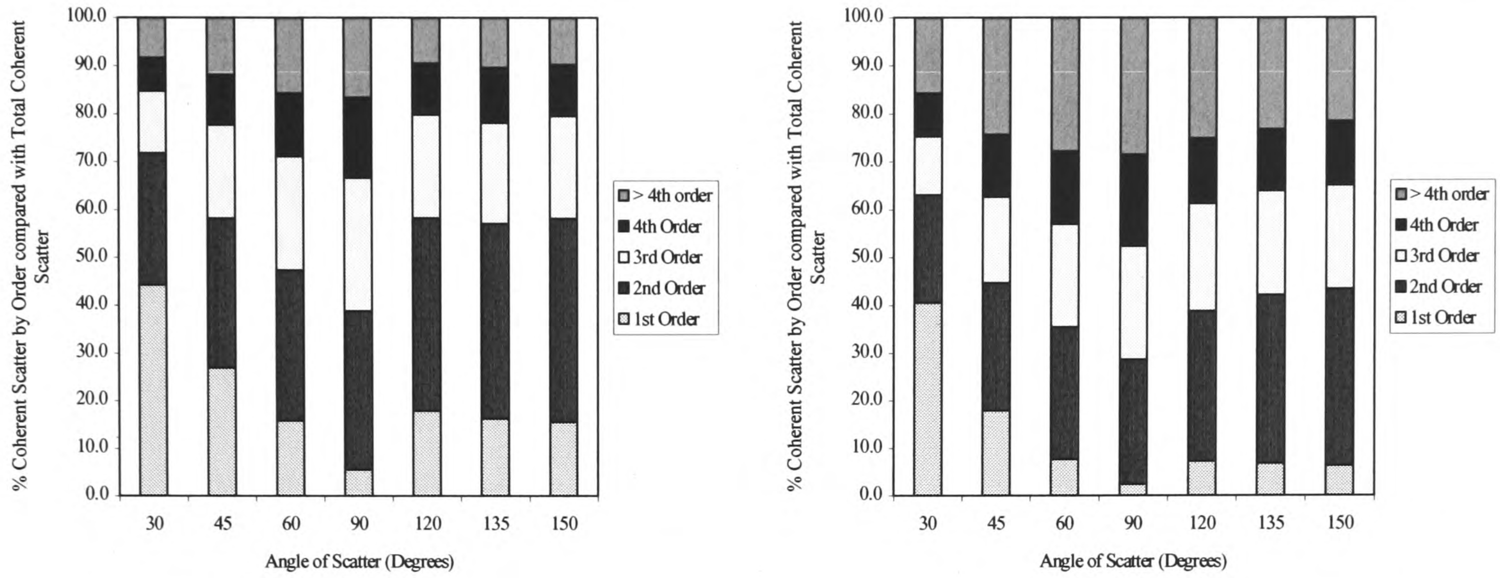

(a) *(b)*

Figure 7.6*. The percentage contributions from different orders of coherent scatter to the total coherent scatter for (a) 49 kV and (b) 121 kV x-rays.*

Figure 7.6 shows the percentage contributions from all coherent interactions to the total coherent scatter for 49 kV and 121 kV. It shows that the first four coherent scatters produce the majority of the total coherent scatter with their smallest contribution being 71% at a scattering angle of 87° for 121 kV x-rays. The second order coherent scatter has the largest contributions for all scattering angles except 30° being 31% and 43% at scattering angles of 45° and 150° for 49 kV x-rays. The large coherent contributions at the 150° scattering angle are from the photons that initally Compton scattered through a large angle. The results show that coherent scatter has a significant contribution to the total scatter. Therefore, it is important to include all coherent scatters to provide an accurate calculation of the total scatter.

7.2.2.3 Effect of Attenuation Coefficients and Incoherent Scatter Form Factors on the Percentage Scatter Calculations

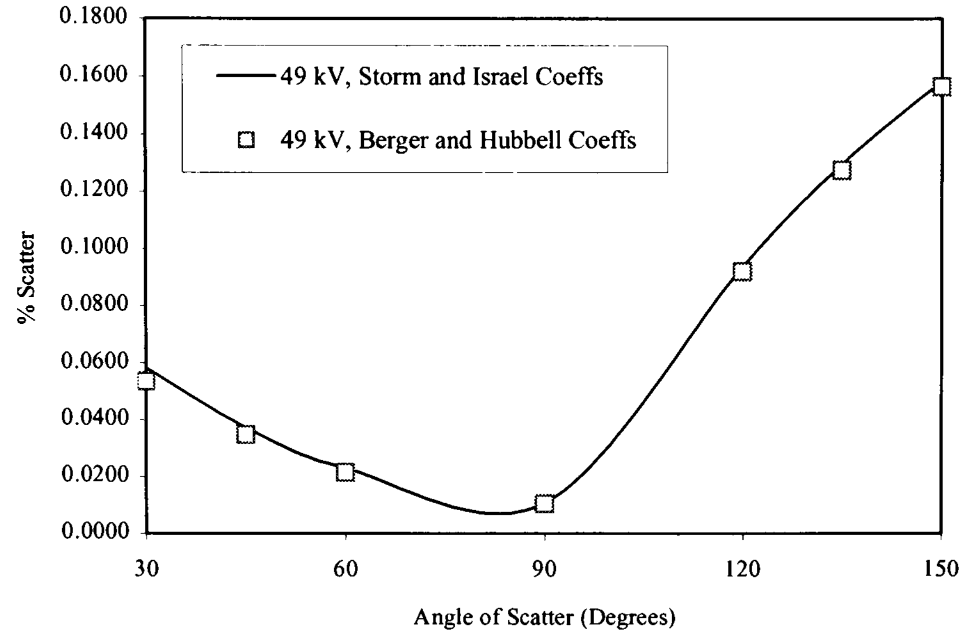

***Figure** 7.7. The percentage scatter calculated using the VOXSCAT code with Storm and Israel (1970) cross sections (including Compton scattering cross sections) and with Berger and Hubbell (1987) cross sections (including incoherent scattering cross sections) for 49 kV x-rays.*

The percentage scatter calculations have so far used Storm and Israel (1970) cross sections and Compton scattering without electron binding corrections. However, there are a number of revisions to these cross sections available for example, Berger and Hubbell (1987) which includes incoherent cross sections with electron binding corrections. Therefore, the effect of the Berger and Hubbell cross sections on the calculation of percentage scatter has been investigated using the VOXSCAT code for tube potentials between 49 and 121 kV. Two intermediate steps have also been studied. The first step involved calculations using the incoherent scattering cross sections from Storm and Israel (1970) instead of the Compton scattering cross sections. The second step involved calculations using the incoherent scatter form factors (Hubbell et al., 1975) to correct the differential Compton cross sections for electron binding.

Figure 7.7 shows the percentage scatter calculated for the Storm and Israel (1970) cross sections (with Compton scattering) and the Berger and Hubbell (1987) cross sections (with incoherent scattering) with 49 kV x-rays. Changing the attenuation coefficients and form factors had the greatest effect for this tube potential as the differences between the two sets of linear attenuation coefficients and differential cross sections decrease for increasing tube potential. It was also observed that the differences in scatter are largest in the forward direction for all tube potentials. The figure shows that the scatter values calculated with Berger and Hubbell coefficients are 8% and 1.5% lower than the values for the Storm and Israel coefficients at scattering angles of 30° and 150°. For the 30° scattering angle, the overall decrease of 8% is given by: a 12% decrease for using the incoherent scatter form factors; a 9% increase for using the Storm and Israel incoherent cross sections; and a 5% decrease for using the Berger and Hubbell cross sections.

Therefore, if the cross section data used by the EGS4 code was changed to that used by the VOXSCAT code (for Berger and Hubbell data) then the largest difference would be 8% for forward directed scatter and no significant difference for backward directed scatter. In conclusion, there is little overall effect of using different tabulations of cross section data.

7.2.2.4 Effect of Focus to Surface Distance on the Percentage Scatter Calculations

This section examines the effect of changing the FSD on the percentage scatter calculated using the VOXSCAT code. The FSD was varied between 0.5 and 40 m. The FSD of 40 m simulates a plane parallel beam (the beam divergence is less than 0.2°). The percentage scatter was calculated for 49 kV x-rays with an incident square field area of 400 cm^2.

Figure 7.8 shows the percentage scatter for FSDs of 0.5 m and 40 m. Figure 7.9 shows the variation of percentage scatter for FSDs between 0.5 and 1 m for scattering angles of 30° and 87°. Both figures show that the FSD has little effect on the percentage scatter calculated. The largest differences from the scatter values for 1 m FSD are 5%. This is for a change in FSD from 1 to 0.5 m for the 30° and 150° scatter values and for a change in FSD from 1 to 40 m for the 87° scatter values. In conclusion, the variation of FSD has little effect on the percentage scatter calculated. This result agrees with the work of Marshall and Faulkner (1992) who observed no variation of measured scatter with changing FSD.

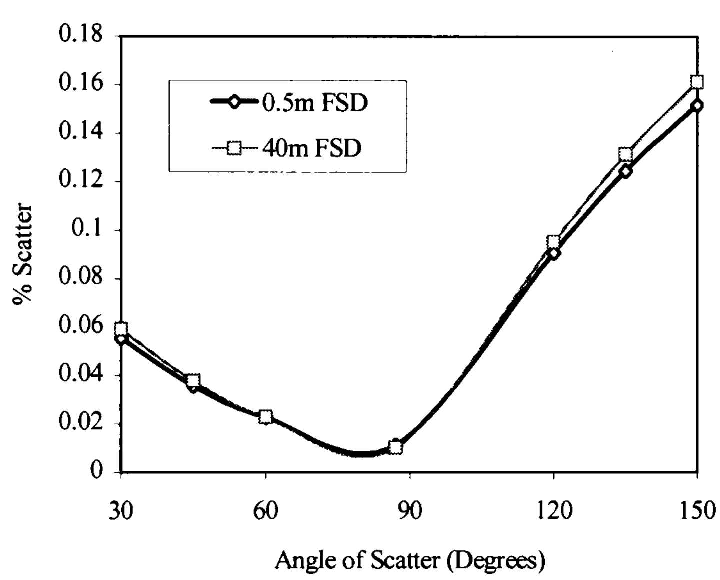

Figure 7.8. *The variation of percentage scatter with scattering angle for FSDs of 0.5 m and 40 m for 49 kV x-rays.*

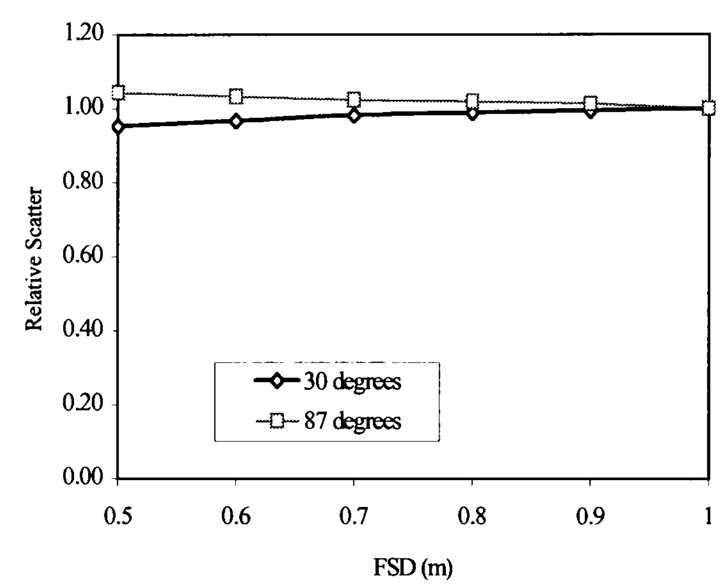

Figure 7.9. *The variation of percentage scatter with FSD at 30° and 87° scattering angles for 49 kV x-rays.*

7.2.2.5 Effect of Distance from Scattering Phantom to Detector on the Percentage Scatter Calculations

The percentage scatter is conventionally measured at 1 m from the phantom for all scattering angles. A 'rule of thumb' calculation used by NCRP Report No. 49 (NCRP, 1976) assumes that the percentage scatter varies with distance from the phantom by the inverse square law. Therefore, the VOXSCAT code has been used to calculate the percentage scatter at positions between 0.5 and 5 m from the phantom surface. The percentage scatter was calculated for 49 kV and 121 kV x-rays. The percentage scatter at 1 m from the phantom surface is then scaled to different distances using the inverse square law factor and compared to the percentage scatter calculated by the VOXSCAT code at these distances.

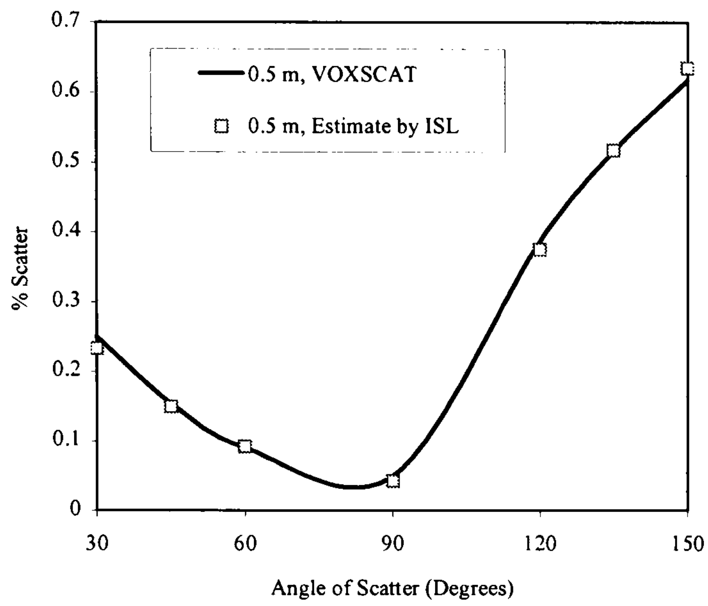

Figure 7.10. The comparison of the percentage scatter calculated at 0.5 m from the phantom and the percentage scatter estimated by the inverse square law (ISL). The calculations were carried out for 49 kV x-rays.

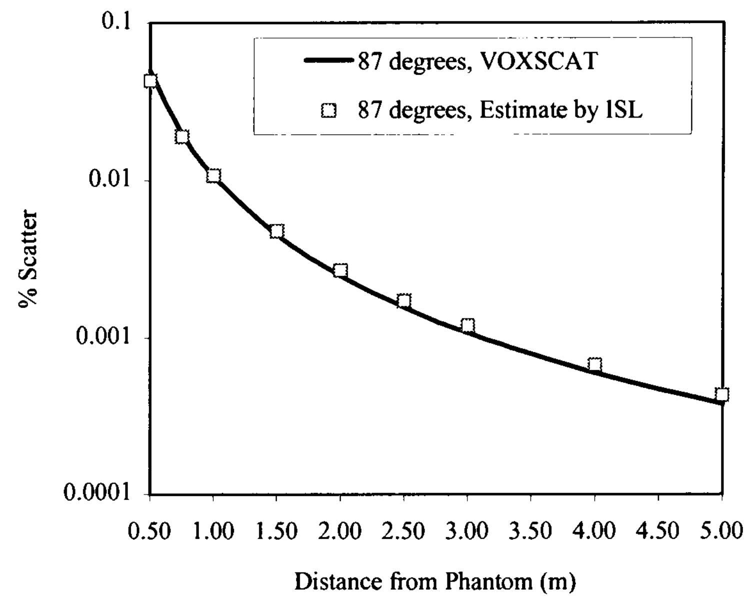

Figure 7.11. The comparison of the percentage scatter calculated for an 87° scattering angle and the percentage scatter estimated by the inverse square law (ISL). The calculations were carried out for 49 kV x-rays.

Figure 7.10 compares the percentage scatter calculated by the VOXSCAT code at 0.5 m from the phantom to the percentage scatter estimated using the inverse square law correction factor at this distance from the phantom. The estimated values are 7% and 14% lower than the calculated values at 30° and 87° scattering angles. There are no significant differences for the other angles of scatter.

Figure 7.11 compares the percentage scatter calculated by the VOXSCAT code at different distances from the phantom at a scattering angle of 87° to the percentage scatter estimated by the inverse square law correction factor for these distances. The estimated value is lower than the calculated value by 14% at 0.5 m and greater than the calculated by 13% at 5 m. A similar difference of 11% can be observed between measured and estimated values from Sanders et al. (1960) data for percentage scatter at 0.5 m from a compressed wood phantom at a 90° scattering angle.

In conclusion, the percentage scatter at 1 m can be used to estimate the percentage scatter at different distances using the inverse square law correction factor. Between distances of 0.5 m and 5 m, using the correction factor will result in at most a ±14% difference from the actual percentage scatter.

7.2.2.6 Scatter Distribution Parallel to the Direction of the X-ray Beam

The percentage scatter has thus far been calculated for specified positions 1 m from the centre of the x-ray field incident on the phantom's front surface. These calculation points produce a radial distribution of percentage scatter. However, it is of interest to observe the distribution of percentage scatter in a plane parallel to the x-ray beam direction (figure 7.12). This is the distribution that will be incident on shielding barriers and/or members of staff standing in the x-ray room. Hence, the VOXSCAT code has been used to calculate the percentage scatter at distances of 2 m for 30° and 150° scattering angles, 1.41 m for 45° and 135° scattering angles, 1.155 m for 60° and 120° scattering angles and 1.001 m for an 87° scattering angle for tube potentials beween 49 and 121 kV.

Figure 7.13 shows the percentage scatter calculated at positions on a radius of 1 m and in a plane at 1 m from the phantom surface for 49 kV x-rays. There are two maximum values of percentage scatter for the positions on the plane. One maximum is between 45° and 60° and the other is between 120° and 135°. The maximum values occur because the values at 30° and 150° scattering angles are reduced due to their scoring positions being 2 m instead of 1 m away from the phantom's incident surface. The ratio of the percentage scatter at 120° to the percentage scatter at 45° is 3.8 for 49 kV x-rays i.e. approximately the ratio of the maximum values. This ratio decreases for increasing tube potential being 2.4 at 69 kV, 1.8 at 100 kV and 1.7 at 121 kV. This is because the scattered photons in the forward direction become more penetrating with increasing tube potential.

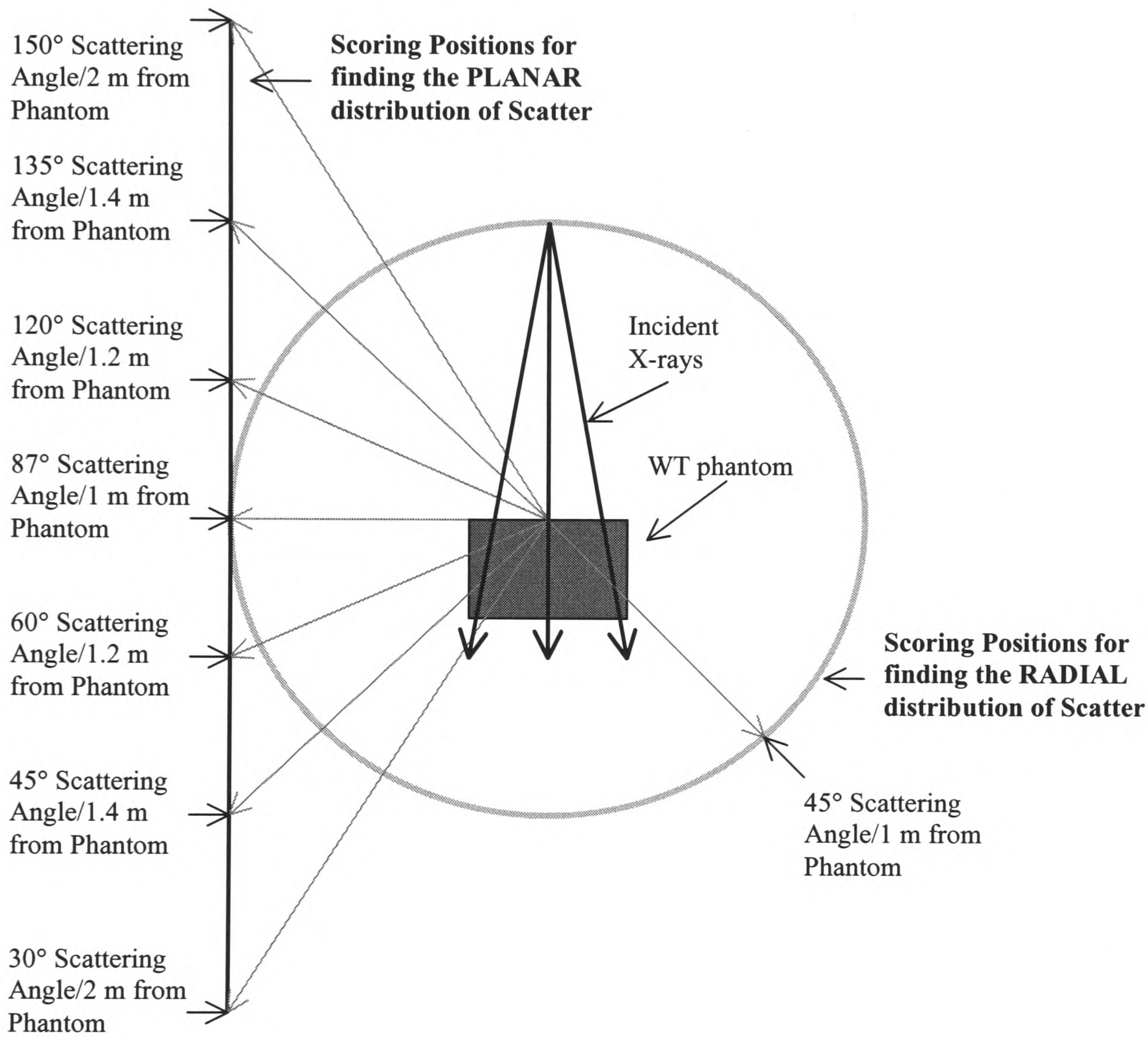

***Figure** 7.12. The scoring positions in a plane parallel to the x-ray beam direction.*

The largest percentage scatter values are between scattering angles of 120° and 135°. These positions are below a person's waist for an under couch tube and above a person's waist for an over couch tube. ICRP Report No. 60 (ICRP, 1991) states that there are many radiosensitive organs in the abdominal region of the human body. Therefore, staff effective doses will be greatly reduced if an under couch tube is employed in fluoroscopic procedures.

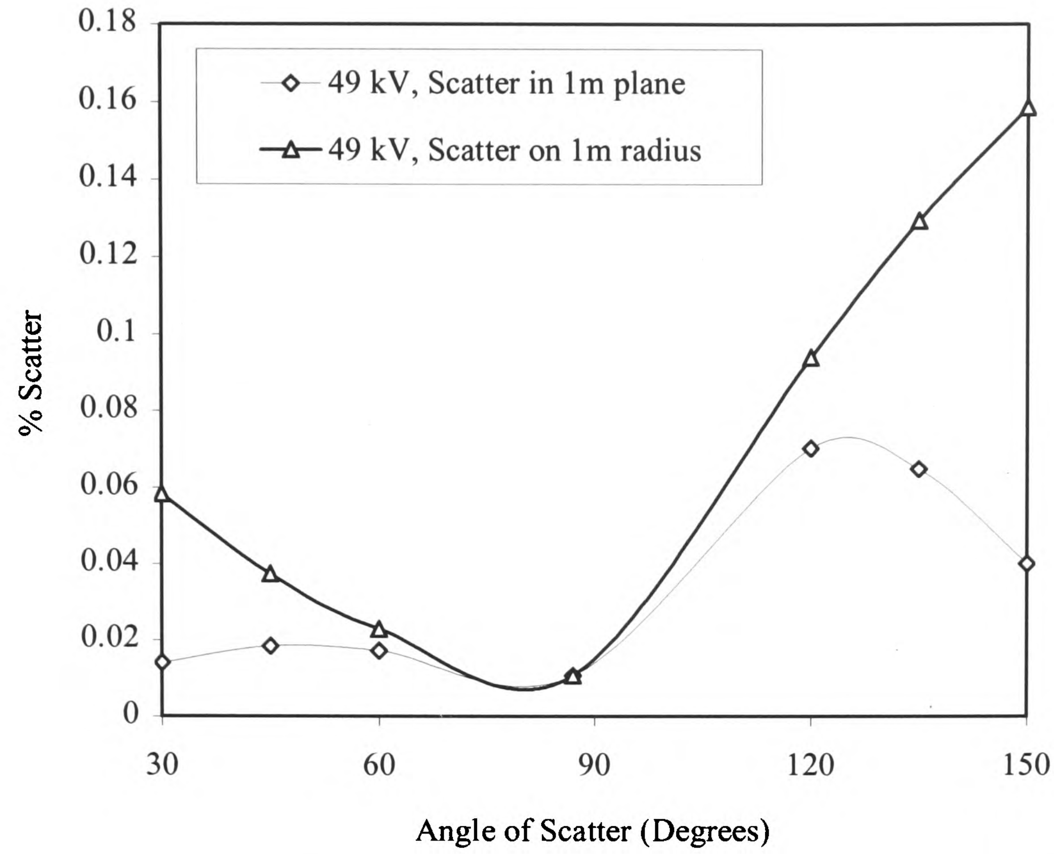

Figure 7.13*. The comparison of the percentage scatter calculated at positions on a radius of 1 m and in a plane 1 m from the phantom surface for 49 kV x-rays.*

7.2.2.7 Effect of Air Surrounding the Phantom on the Percentage Scatter Calculations

The XYZSCAT code used an air density of 1.205×10^{-6} kg/m^3 to compare percentage scatter calculations with the VOXSCAT code in sections 7.2.1.1 to 7.2.1.4. This ensured that no interactions occurred in the air surrounding the phantom. This section investigates the effect on the percentage scatter of using the actual air density of 1.205 kg/m^3 in the calculations with 49, 69, 100 and 121 kV x-rays.

Figure 7.14 compares the total percentage scatter with air present, the total percentage scatter without air present, the percentage scatter from the phantom only (with air present in the simulation) and the percentage scatter from the air only. The presence of air has the largest effect for 49 kV x-rays as its attenuation decreases for increasing tube potential. The total scatter with air present is 63% higher than the total scatter without air present for a scattering angle of 87°. For this scattering angle, the phantom scatter is lowest and therefore, its contribution to the total scatter is lowest. The phantom scatter contribution to the total scatter is 58% compared to the air scatter contribution of 42%. The difference between the total scatter without air present and the phantom scatter with air present is on average 5% for all tube potentials and scattering angles. This decrease is due to the air attenuating the scattered x-rays.

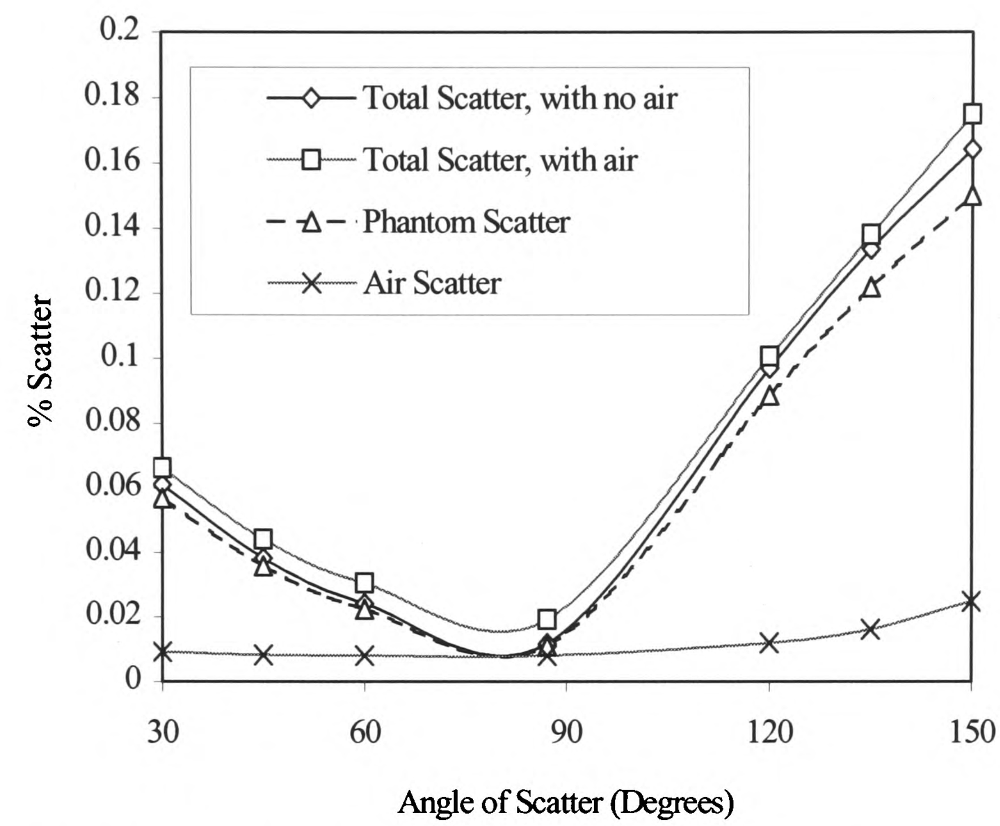

***Figure 7.14**. The comparison of the percentage scatter calculated using the XYZSCAT code with and without air surrounding the phantom. The percentage scatter from the phantom only and the air only is also shown.*

Figure 7.15 shows the percentage scatter produced by air for tube potentials between 49 and 121 kV. The uncertainty in the scatter values is less than ±2%. Each tube potential gives a similar value for each scattering angle with the values varying by less than ±10% of the mean value. The mean percentage scatter for air is approximately 0.01% between 30° and 87° and increases to 0.025% at 150°. This is similar to a measured value of 0.02% between 50 and 150 kV from Trout and Kelley (1965). These results show that it is important to include air in the model of an x-ray room. The results also indicate that the scatter contributions from materials surrounding the phantom may be large.

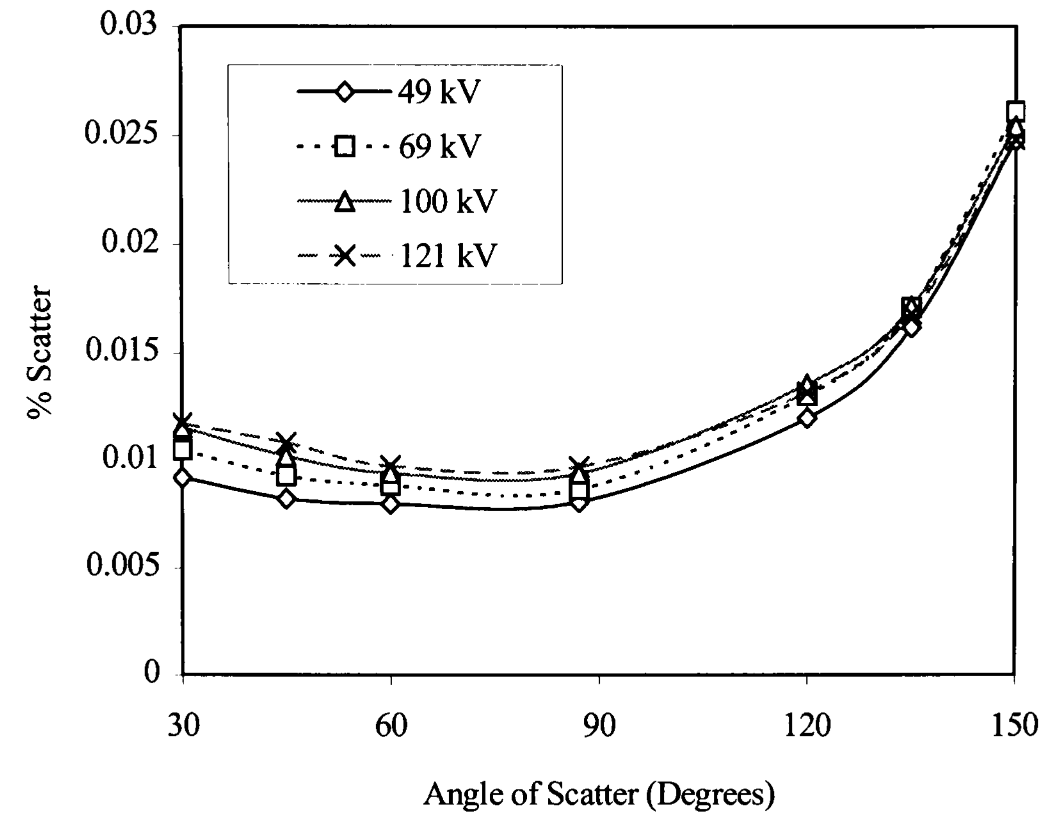

***Figure 7.15**. The percentage scatter from the air surrounding the phantom for 49 kV, 69 kV, 100 kV and 121 kV x-rays.*

7.2.3 Comparison of Calculations with Measurements in the Philips X-ray Room

Sections 7.2.3.1 and 7.2.3.2 show the comparison of XYZSCAT calculations with measurements of percentage scatter carried out in the Philips x-ray room (section 3.2). Phantoms of different materials (table 3.2) were supported against one of the x-ray room walls and irradiated at measured tube potentials between 49 and 121 kV. The results have also been used to study the variation of percentage scatter from slab phantoms with tube potential and field area. Section 7.2.3.3 investigates the scatter contributions from different materials in the x-ray room using the results of calculations and measurements. The phantom was positioned in the centre of the x-ray room to obtain the percentage scatter for scattering angles in both the forward and backward directions.

A brief description of the x-ray room is given here with a full description given in section 3.2. The XYZSCAT code models the x-ray room with dimensions: 6 m long, 6 m wide and 3 m high. The model includes the phantom, a DAP meter (section 3.2.7), the surrounding air and the x-ray room walls. The centre of the field incident on the phantom is 1.2 m above the floor. The closest wall to the side of the phantom is at a distance of 2 m (figure 3.2) with the phantom positioned against one of the walls. The walls are assumed to be constructed from 0.2 m thick concrete with a density of 2350 kg/m^3.

The XYZSCAT code used between 20×10^6 photons for WT1 material and 80×10^6 photons for copper to achieve a statistical uncertainty in the calculated percentage scatter of less than ±2%. A further uncertainty in the calculated percentage scatter has to be determined due to the uncertainty in the quality of the spectra, for the Philips X-ray unit, as discussed in section 4.4. This has been estimated by undertaking scatter calculations with spectra obtained using the BM model with its input parameters either increased or decreased. The uncertainty is then determined as the difference between the scatter calculated with the spectra using the varied input parameters and the scatter calculated with the spectra using the standard input parameters. These standard spectra were derived from HVL measurements on the exit side of the DAP meter whereas the spectra are simulated as being incident on the DAP meter. Therefore, an uncertainty of 0.2 mmAl was added in quadrature to the uncertainty of the tube filtration (section 4.4) to take into account the DAP meter's equivalent thickness. The estimated uncertainty was ±11.5% for forward directed scatter and ±6.4% for backward directed scatter. This compares to the percentage uncertainty in the measured scatter of ±10.4% (section 3.2.12).

7.2.3.1 Effect of Tube Potential on the Percentage Scatter

Table 7.6 compares the measured and calculated percentage scatter for a 400 cm^2 field size incident on the five different phantoms for a 135° scattering angle. The measured scatter tends to be greater than the calculated scatter which may be due to scatter from the x-ray collimators. The WT1 material produces the largest percentage scatter of all the materials studied as it has the lowest atomic number. The other materials all produce similar percentage scatter values. The phantoms produce less scatter with increasing atomic number but this is balanced by the scatter from the surroundings.

	Percentage Scatter from Different Materials					
	WT1 Material		**Concrete**		**Copper**	
kV	**Measured Values**	**Calculated Values**	**Measured Values**	**Calculated Values**	**Measured Values**	**Calculated Values**
49	0.176	0.144			0.127	0.125
69	0.229	0.181	0.088	0.084	0.136	0.121
100					0.124	0.111
121	0.288	0.235	0.114	0.118	0.104	0.106
	Brick		**Aluminium**			
kV	**Measured Values**	**Calculated Values**	**Measured Values**	**Calculated Values**		
49	0.063	0.065				
69	0.091	0.082	0.104	0.085		
100	0.108	0.102	0.129	0.107		
121	0.121	0.111				

Table 7.6. *Comparison of the measured and calculated percentage scatter at a scattering angle of 135 °for a 400 cm^2 field size.*

The measured percentage scatter in table 7.6 was compared to the values calculated with the XYZSCAT code using a paired t-test (Altman, 1991) by the method described in section 6.4.2.7. The t-test shows that the mean scatter estimates are significantly different (P = 0.005). The difference in the mean scatter values is 12.7% which is similar to the combined uncertainty from the calculations and measurements of ±12.4%. The limits of agreement, as derived from the t-test, at the 95% confidence level for individual scatter estimates are -0.019% to 0.049%. This corresponds to good agreement between the measured and calculated values (Bland and Altman, 1986).

Table 7.7 shows the measured and calculated scatter values in table 7.6 normalised to the values for 69 kV x-rays to demonstrate the variation of scatter with tube potential. There is a similar variation between the measured and the calculated scatter values for all materials. The percentage scatter increases with increasing tube potentials for the low atomic number materials: WT1, concrete, brick and aluminium. There is a slightly greater variation in the percentage scatter from concrete than WT1 material. The percentage scatter decreases with increasing tube potentials above 69 kV for copper. The scatter from the copper blocks decreases more rapidly than the scatter from the DAP and the surroundings increases. Thus, there is an overall decrease.

	Percentage Scatter Normalised to Percentage Scatter for 69 kV					
	WT1 Material		**Concrete**		**Copper**	
kV	**Measured Values**	**Calculated Values**	**Measured Values**	**Calculated Values**	**Measured Values**	**Calculated Values**
49	0.77	0.80			0.93	1.03
69	1.00	1.00	1.00	1.00	1.00	1.00
100					0.91	0.92
121	1.26	1.30	1.30	1.40	0.76	0.88
	Brick		**Aluminium**			
kV	**Measured Values**	**Calculated Values**	**Measured Values**	**Calculated Values**		
49	0.69	0.79				
69	1.00	1.00	1.00	1.00		
100	1.19	1.24	1.24	1.26		
121	1.33	1.35				

***Table** 7.7. Comparison of the measured and calculated percentage scatter (in table 7.6) normalised to the percentage scatter for 69 kV x-rays.*

7.2.3.2 Effect of Field Size on the Percentage Scatter

Table 7.8 compares the measured and calculated scatter values for field areas between 100 and 900 cm^2 for tube potentials of either 100 kV or 121 kV at a scattering angle of 135°. Again, the measured scatter tends to be greater than the calculated scatter. The measured percentage scatter in table 7.8 was compared to the values calculated with the XYZSCAT code using a paired t-test (Altman, 1991) by the method described in section 6.4.2.7. The t-test shows that the mean scatter estimates are not significantly different ($P = 0.092$). The difference in the mean scatter values is 11.8% which is less than the combined uncertainty from the calculations and measurements of ±12.4%. The limits of agreement, as derived from the t-test, at the 95% confidence level for individual scatter estimates are -0.037% to 0.077%. This corresponds to good agreement between the measured and calculated values (Bland and Altman, 1986).

	Percentage Scatter Values for Different Materials					
	WT1: 121 kV		**Concrete: 121 kV**		**Copper: 100 kV**	
Field Size (cm^2)	**Measured Values**	**Calculated Values**	**Measured Values**	**Calculated Values**	**Measured Values**	**Calculated Values**
100	0.074	0.060	0.032	0.028	0.037	0.028
400	0.288	0.235	0.114	0.118	0.124	0.111
900	0.593	0.517			0.248	0.253

***Table 7.8**. Comparison of the measured and calculated percentage scatter at a scattering angle of 135 ° for increasing field size.*

Table 7.9 shows the percentage scatter normalised to the values for the 100 cm^2 field area. NCRP (1976) assumes a linear relationship between percentage scatter and field area in order to calculate the percentage scatter semi-empirically. The results in table 7.9 can then be used to study this relationship for scatter from slab phantoms. All of the calculated values and most of the measured values show a linear relationship with increasing field area. Only the measured values for copper do not show this relationship. This is due to the relatively large measured percentage scatter for the 100 cm^2 field which in turn reduces the normalised values for the other fields. This reflects the difficulty of measuring small values. Trout and Kelley (1972) studied the variation of percentage scatter with field area. They found that the measured values were larger than expected for large fields and smaller than expected for small fields. This is possibly due to their use of a human torso shaped phantom (section 8.2.4). Bomford and Burlin (1963) found that the percentage scatter had a linear relationship with field area for scatter in the backward direction.

	Percentage Scatter Normalised to Percentage Scatter for a 100 cm^2 Field					
	WT1: 121 kV		**Concrete: 121 kV**		**Copper: 100 kV**	
Field Size (cm^2)	**Measured Values**	**Calculated Values**	**Measured Values**	**Calculated Values**	**Measured Values**	**Calculated Values**
100	1.0	1.0	1.0	1.0	1.0	1.0
400	3.9	3.9	3.6	4.2	3.4	4.0
900	8.0	8.6			6.7	9.0

Table 7.9. *Comparison of the measured and calculated percentage scatter (in table 7.8) normalised to the percentage scatter for a 100 cm^2 incident field area.*

7.2.3.3 Variation of Percentage Scatter from the X-ray Tube Head

Section 3.2.6 studied the effect of scatter from the x-ray tube head. A mobile protective screen was used to shield against scattered x-rays from the collimator and DAP meter reaching the measuring chamber. The WT1 phantom was positioned in the centre of the x-ray room. The closest wall behind the phantom was at a distance of 1 m. This experimental set up was simulated and the results are given here.

	Percentage Scatter			
kV	**Measured Values**	**Calculated Values**	**Measured Values With Mobile Shield**	**Calculated Values without DAP meter**
49	0.181	0.140	0.136	0.126
69	0.237	0.181	0.183	0.167
117	0.312	0.234	0.242	0.221

Table 7.10. *The first comparison is between the measured and calculated percentage scatter at a 135° scattering angle. The second comparison is between the percentage scatter measured with the mobile shield in position and the values calculated with the DAP meter not included in the computation.*

The first set of results in table 7.10 compares the measured and calculated percentage scatter for a 400 cm^2 field size at a scattering angle of 135°. The first set of results in table 7.11 compares the measured and calculated percentage scatter for a 400 cm^2 field size for 69 kV x-rays. The second set of results in tables 7.10 and 7.11 compares the measured scatter with the mobile shield in place (figure 3.4) and the calculations carried out without the DAP meter included in the simulation. There is reasonable agreement between the measured and calculated percentage scatter due to the large combined uncertainty. However in both tables 7.10 and 7.11, the measured scatter is nearly always larger than the calculated scatter. The differences between the measured and calculated scatter are decreased by shielding out the scatter from the x-ray tube head. However, there still remains a tendency for the measured scatter to be larger than the calculated scatter. The reason for this is unknown and requires further work.

	Percentage Scatter			
Scattering Angle (°)	**Measured Values**	**Calculated Values**	**Measured Values with Mobile Shield**	**Calculated Values without DAP Meter**
45	0.137	0.090	0.092	0.073
87	0.078	0.052	0.027	0.030
120	0.195	0.143	0.149	0.125
135	0.237	0.181	0.183	0.167
150	0.252	0.269	0.229	0.207

Table 7.11. *The first comparison is between the measured and calculated percentage scatter for 69 kV x-rays. The second comparison is between the percentage scatter measured with the mobile shield in position and the values calculated with the DAP meter not included in the computation.*

Unfortunately, the x-ray collimator system could not be readily modeled with the XYZSCAT code. Therefore, the percentage scatter produced by the collimator system was estimated by the difference between the measured percentage scatter without the shield and the percentage scatter calculated with the DAP meter included in the simulation. From table 7.10, the percentage scatter produced by the collimator is estimated to be 0.04%, 0.06% and 0.08% for 49 kV, 69 kV and 117 kV x-rays respectively. These values as a percentage of the measured scatter are 22%, 24% and 25% respectively. In table 7.11, the measured percentage scatter values are on average 31% smaller with the shield in place. Therefore, there is significant scatter produced in the x-ray tube head. The percentage scatter from the collimator system is estimated to be 0.05%, 0.03% and 0.05% for 45°, 87° and 120° scattering angles respectively. These values as a percentage of the measured scatter are 34%, 33% and 27% respectively. The estimated collimator scatter is similar to the value of 0.04% measured by Trout and Kelley (1965).

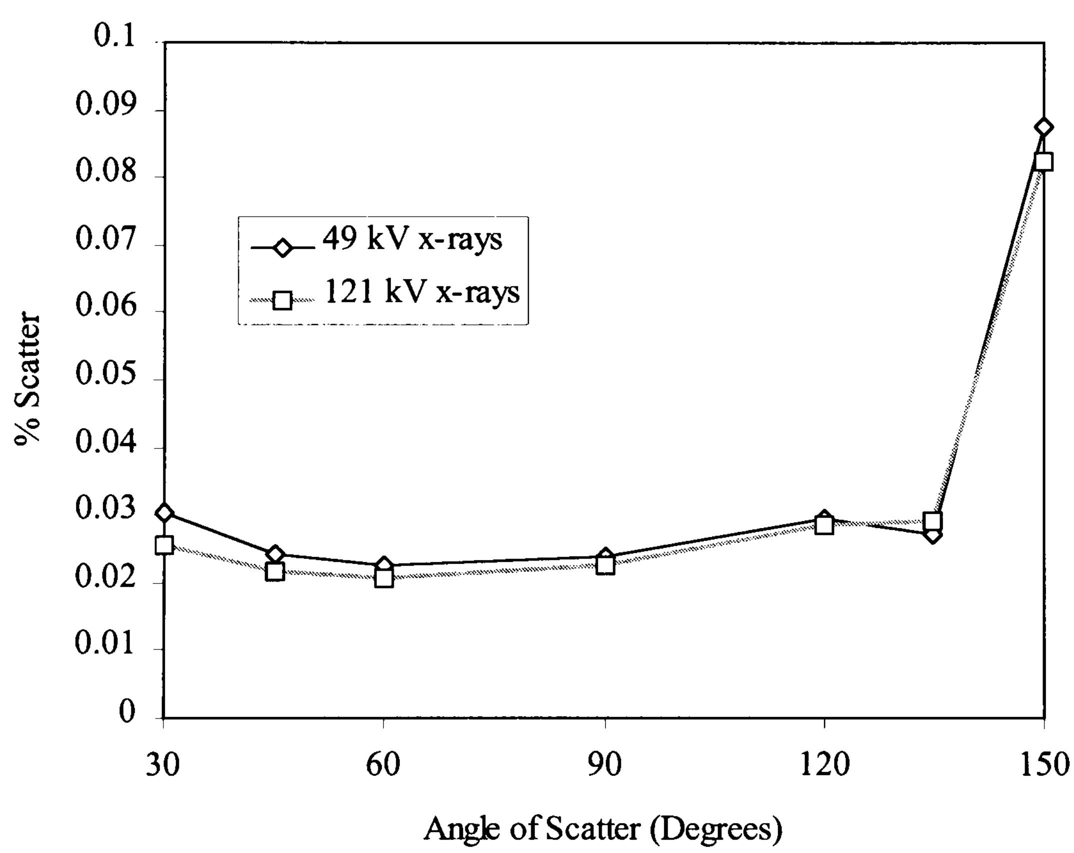

Figure 7.16*. The percentage scatter from the DAP meter for 49 kV and 121 kV x-rays calculated using the VOXSCAT code.*

Figure 7.16 shows the percentage scatter produced by the DAP meter for 49 kV and 121 kV x-rays calculated with the VOXSCAT code. The uncertainty in the percentage scatter values is less than ±1%. The percentage scatter is similar for each tube potential at each scattering angle and varies within ±10% of the mean value. The mean percentage scatter is approximately 0.025% of the incident x-ray beam between scattering angles of 30° and 135° and increases to 0.085% at 150°.

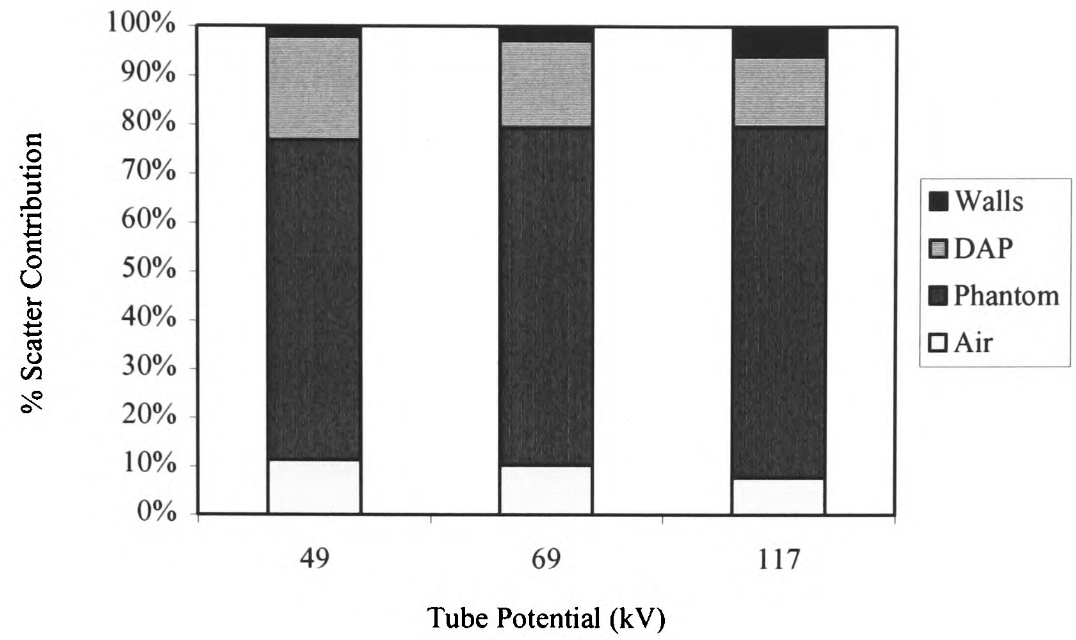

Figure 7.17. *The percentage contributions to the total scatter from the air, the WT1 phantom, the DAP meter and the concrete ceiling, floor and walls.*

Figure 7.17 shows the percentage scatter contributions from the air, WT1 phantom, the DAP meter and the concrete ceiling, floor and walls to the total calculated scatter at a 135° scattering angle for 49 kV, 69 kV and 117 kV x-rays. The results confirms that a slab phantom and hence, the patient is the primary source of scatter in an x-ray room. The average percentage contributions to the overall scatter are 68.9% by the slab phantom, 17.7% by the DAP meter, 9.7% by the air and 3.7% by the x-ray room walls. The calculated percentage contribution for the x-ray room walls agrees fairly well with the measured value of 6.7% (section 3.2.5). It also shows that the secondary sources of scatter (e.g. room walls) produce a small contribution to the total scatter compared to materials in the primary beam such as the phantom, collimator and DAP meter.

7.2.4 Measured Scatter Distributions in the Literature

Trout and Kelley (1972) and Williams (1996) measured the percentage scatter from contoured phantoms which simulate the curvature of the human body. Voxelised cylindrical phantoms were implemented in this work to approximate the contoured phantoms. The phantom's width and the thickness are defined as the major and minor axes of an ellipse. All voxels which lie within the boundary of the ellipse are specified with the phantom's material. All other voxels are specified as air. These voxelised cylindrical phantoms were used with the VOXSCAT code to calculate the percentage scatter and the quality of the scattered radiation in order to simulate the studies of Williams (1996) and Marshall et al. (1996) as shown in sections 7.2.4.1 and 7.2.4.2. Section 7.2.4.3 shows an overall comparison of the calculated and measured scatter values with those in the literature for tissue equivalent materials.

7.2.4.1 Comparison of Percentage Scatter from Williams (1996) with VOXSCAT Code Calculations

Williams (1996) measured the percentage scatter from the abdominal and pelvic sections of a RANDO phantom (ICRU, 1992b). A cylindrical phantom of dimensions 1.75 m long, 0.25 m wide and 0.215 m thick produced a mass of 74 kg. The total mass of the RANDO phantom stated by ICRU Report No. 48 (ICRU, 1992b) is 73 kg. The length of the abdominal and pelvic sections was assumed to be 0.50 m. The RANDO phantom is a dosimetric phantom constructed in the form of a human torso. It is manufactured with a natural skeleton embedded within Alderson Muscle A material. A voxelised cylinder of Alderson material was used to simulate the RANDO phantom with the composition and density obtained from ICRU Report No. 44 (ICRU, 1989).

Williams measured the scatter in terms of air kerma normalised to the DAP. Therefore, a DAP meter (section 3.2.7) and the air between it and phantom surface were also modeled. The DAP meter was assumed to be at a distance of 26.6 cm from the x-ray focus and the focus to surface distance was 80 cm. The incident field size at the RANDO phantom was 22 cm long and 17.5 cm wide. A Philips x-ray tube was simulated to produce scatter for tube potentials between 50 and 125 kV. The x-ray tube characteristics were 3.5 mmAl total filtration, a 13° target angle and a constant potential generator.

The distance to the measurement position is taken from the centre of the phantom in Williams' work and these were used as the scoring positions in the VOXSCAT code calculations. Williams' results are in terms of scattered air kerma normalised to DAP and were therefore converted to be normalised to incident air kerma. This enables the comparison with the percentage scatter calculated by the VOXSCAT code.

	Percentage Scatter					
	50 kV X-rays		**70 kV X-rays**		**85 kV X-rays**	
Scattering Angle(°)	**Williams' Values**	**Calculated Values**	**Williams' Values**	**Calculated Values**	**Williams' Values**	**Calculated Values**
30	0.068	0.056	0.081	0.078	0.093	0.093
60	0.070	0.064	0.082	0.088	0.092	0.103
90	0.115	0.094	0.132	0.123	0.146	0.137
120	0.213	0.153	0.243	0.190	0.263	0.210
150	0.302	0.306	0.345	0.352	0.372	0.374
	100 kV X-rays		**125 kV X-rays**			
Scattering Angle(°)	**Williams' Values**	**Calculated Values**	**Williams' Values**	**Calculated Values**		
30	0.104	0.106	0.122	0.127		
60	0.104	0.116	0.122	0.135		
90	0.157	0.151	0.176	0.169		
120	0.280	0.225	0.304	0.242		
150	0.397	0.387	0.428	0.400		

Table 7.12. *The comparison of the percentage scatter calculated with the VOXSCAT code and the values measured by Williams (1996).*

Table 7.12 shows that the percentage scatter measured by Williams (1996) tends to be larger than the values calculated by the VOXSCAT code. Williams' states that the uncertainty in his measurements as ±8%. The measured percentage scatter from Williams (1996) in table 7.12 was compared to the values calculated with the VOXSCAT code using a paired t-test (Altman, 1991) by the method described in section 6.4.2.7. The t-test shows that the mean scatter estimates are significantly different (P = 0.011). However, the difference in the mean scatter values is 7.4% which is similar to the uncertainty in the measurements of ±8%. The limits of agreement, as derived from the t-test, at the 95% confidence level for individual scatter estimates are -0.034% to 0.061%. This corresponds to good agreement between the measured and calculated values (Bland and Altman, 1986).

The average difference between the measured and calculated scatter values at a scattering angle of 120° is 22%. In Williams' experimental set up, the measurement position for this angle of scatter is close to the DAP meter and collimators. Hence, the average percentage scatter produced by the collimator system is estimated as 0.06% for this scattering angle. This compares well with the collimator percentage scatter of 0.04% which was measured by Trout and Kelley (1965) and the estimated values of collimator scatter in the Philips x-ray room (section 7.2.3.3).

7.2.4.2 Comparison of Scattered Spectra from Marshall et al. (1996) with VOXSCAT Code Calculations

Marshall et al. (1996) measured the x-ray spectra scattered from a 3M pelvic phantom using a Germanium crystal spectrometer. The VOXSCAT code has been used to calculate the scattered spectra for the experimental setup used by Marshall. The half value layers (HVLs) and mean photon energies of the calculated and measured scattered spectra are compared.

The 3M pelvic phantom is anthromorphic with a human skeleton embedded in a block of PMMA. However as the phantom dimensions were not reported by Marshall, they were chosen to be similar to that of the RANDO phantom (section 7.2.4.1) with the width set to the average pelvic width of an European Male (ICRU, 1992b). The phantom dimensions were then 50 cm long, 28 cm wide and 21.5 m thick. The scattered spectra were measured at 50 cm from the phantom at 90° and 135° scattering angles. The focus to phantom surface distance was 1 m. A Picker x-ray tube was simulated to produce scatter for tube potentials between 61 and 112 kV. The x-ray tube characteristics were 2.6 mmAl total filtration, a 15° target angle and a three phase 12 pulse generator.

		Half Value Layers (mmAl) of Scattered Spectra			
		90° Scattering Angle		135° Scatter Angle	
Tube Potential (kV)	**Incident Spectra HVL (mmAl)**	**Marshall's Values**	**Calculated Values**	**Marshall's Values**	**Calculated Values**
61	2.07	2.31	2.20	1.88	1.80
74	2.49	2.73	2.62	2.30	2.18
85	2.87	3.21	3.04	2.64	2.50
90	3.06	3.47	3.25	2.79	2.67
101	3.47	4.03	3.55	3.13	2.88
112	3.90	4.50	3.84	3.49	3.14

***Table 7.13**. The comparison of the HVLs of the measured and calculated scattered spectra.*

		Mean Photon Energies (keV) of Scattered Spectra			
		90° Scattering Angle		135° Scatter Angle	
Tube Potential (kV)	**Incident Mean Energy (keV)**	**Marshall's Values**	**Calculated Values**	**Marshall's Values**	**Calculated Values**
61	35.6	36.0	34.6	33.3	32.4
74	40.1	39.9	38.2	37.5	35.9
85	43.8	43.7	41.1	40.4	38.3
90	45.4	45.4	42.6	41.7	39.7
101	48.7	48.4	44.9	44.2	41.5
112	51.7	50.6	46.9	46.3	43.2

***Table 7.14**. The comparison of the mean photon energies of the measured and calculated scattered spectra.*

Table 7.13 compares the calculated and measured HVLs for 90° and 135° scattering angles. Table 7.14 compares the calculated and measured mean photon energies for 90° and 135° scattering angles. There are systematic differences between measured and calculated quality of the scattered radiation. The measured HVLs and mean energies are always larger than the calculated values. These differences may be because the exact phantom dimensions were not known and that the phantom is simulated as an homogeneous block of perspex whereas bone is embedded in the actual phantom. However, there is reasonable agreement in table 7.13 (differences within ±10%) between 61 and 90 kV at a 90° scattering angle. The calculated HVL is 15% lower than the measured HVL for 112 kV. There is also reasonable agreement between the calculated and measured HVLs for all tube potentials at the 135° scattering angle. Table 7.14 shows agreement within ±10% between the calculated and measured mean photon energies for all tube potentials at both scattering angles.

7.2.4.3 Summary of Percentage Scatter Values for Tissue Equivalent Materials

	Image Parameters			
Parameter Type	**Trout and Kelley (1972)**	**Bomford and Burlin (1963)**	**Measurements and XYZSCAT Calculations**	**Williams (1996) and VOXSCAT Calculations**
Tube Potentials (kV)	50, 70, 100	100	50, 70, 100(1)	50, 70, 100
Filtration (mmAl)	0.5, 1.5, 2.5	-	3.4	3.5
Generator Type	Self-rectified and single phase(2)	-	Medium frequency, 3% ripple	Constant Potential
Phantom Material	Torso-shaped masonite	MixD block	Solid Water block	RANDO phantom (Alderson A muscle)
Phantom Dimensions (cm×cm×cm)	72×30×20	30×30×22	30.5×30.5×10	50×25×21.5
Incident Field Size	20cm×20 cm	400 cm^2 (circle)	20cm×20cm	22cm×17.5 cm
FSD (cm)	100	100	100	80

Table 7.15. *The parameters used for measuring scatter in the different reports in the literature. Footnotes: (1) 100 kV for calculation only; (2) 50 kV and 70 kV were used with a self-rectified generator and 100 kV was used with a single phase generator.*

Table 7.15 shows a summary of the imaging parameters stated in the literature which were used to obtain the scatter values shown in table 7.16. Table 7.15 also summarises the imaging parameters used in the comparison of the measurements and XYZSCAT calculations (section 7.2.3). All the imaging parameters were selected to be as similar as possible for this comparison. The range of tube potentials studied was restricted to be from 50 to 100 kV. All scattering materials used are tissue equivalent. The phantoms used by Trout and Kelley (1972) and Williams (1996) have a human body contour. The VOXSCAT code modeled the experimental set up for Williams work (section 7.2.4.1).

Table 7.16 shows the scatter values for the different experiments. The values have been corrected where necessary to have them all in the same units of percentage scatter. Bomford and Burlin (1963) measured the percentage scatter for incident air kerma on the surface of the phantom. Thus, a backscatter factor of 1.3 (BIR, 1996) was used to give the values in table 7.16 as the ratio of scattered air kerma to incident air kerma without backscatter. Williams (1996) reports scattered air kerma divided by the DAP. Williams' values in table 7.16 were converted to be in terms of scattered air kerma divided by the incident air kerma without backscatter. These values have also been increased to be equivalent to a field area of 400 cm^2, which is the same field area as the other studies, instead of 385 cm^2 (table 7.15).

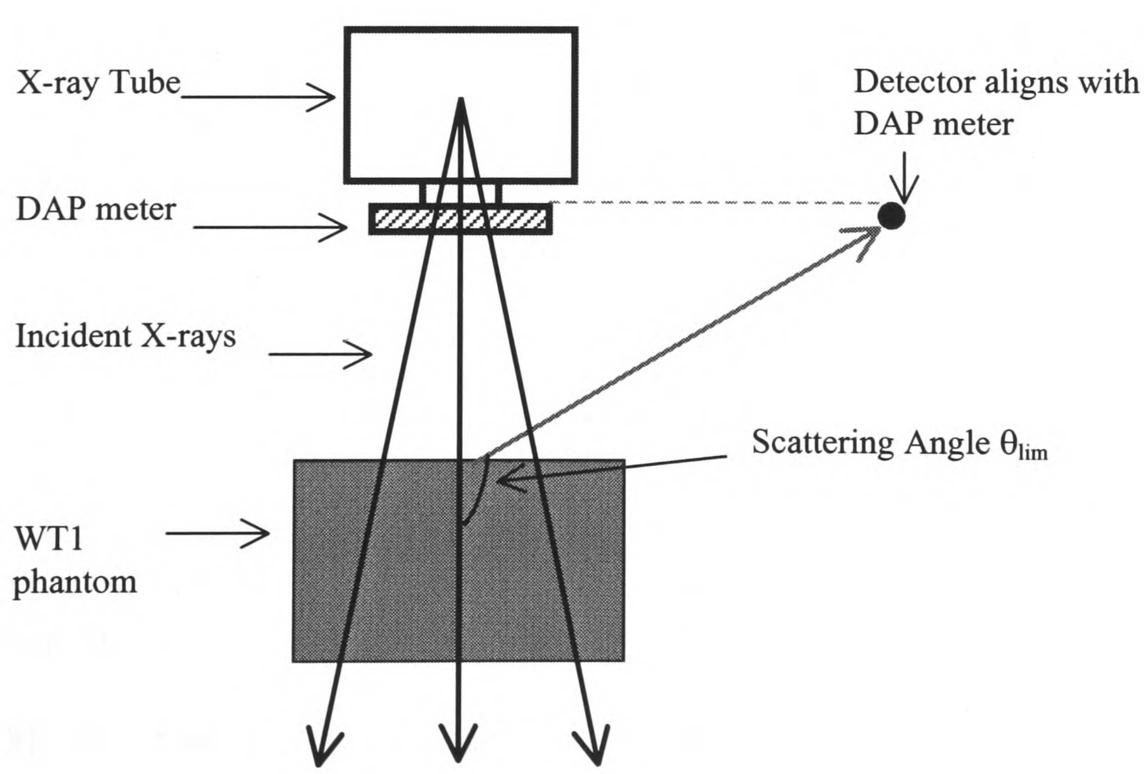

Figure 7.18*. The measuring position which produces a large increase in scatter from the DAP meter.*

Source of Data	Percentage Scatter Values for 50 kV x-rays						
	30°	45°	60°	90°	120°	135°	150°
Trout et al. (1972)	0.044	0.011	0.012	0.024	0.069	0.095	-
Measured Values	-	-	-	-	-	0.176	-
XYZSCAT Values	0.081	0.059	0.048	0.041	0.114	0.140	0.222
Williams (1996)	0.071	0.070	0.073	0.120	0.221	0.279	0.314
VOXSCAT Values	0.059	-	0.068	0.100	0.162	-	0.321
Source of Data	**Percentage Scatter Values for 70 kV x-rays**						
	30°	45°	60°	90°	120°	135°	150°
Trout et al. (1972)	0.052	0.021	0.020	0.035	0.091	0.120	-
Measured Values	-	0.137	-	0.078	0.195	0.237	0.252
XYZSCAT Values	0.123	0.090	0.068	0.052	0.143	0.181	0.269
Williams (1996)	0.084	0.083	0.086	0.137	0.253	0.322	0.358
VOXSCAT Values	0.080	-	0.090	0.126	0.196	-	0.363
Source of Data	**Percentage Scatter Values for 100 kV x-rays**						
	30°	45°	60°	90°	120°	135°	150°
Trout et al. (1972)	0.127	0.100	0.098	0.110	0.190	0.210	-
Bomford and Burlin (1963)	0.026	0.039	0.052	0.065	0.156	0.221	0.273
XYZSCAT Values	0.180	0.133	0.098	0.070	0.176	0.220	0.309
Williams (1996)	0.108	0.106	0.108	0.163	0.291	0.355	0.412
VOXSCAT Values	0.106	-	0.116	0.153	0.228	-	0.395

Table 7.16. *The comparison of the calculated and measured scatter values obtained in this thesis with the values stated in the literature for tissue equivalent materials.*

Table 7.16 shows that the scatter values are considerably different in the various reports. Bomford and Burlin's values in the forward direction are considerably smaller than Trout and Kelley's values. For example at a 30° scattering angle, Bomford and Burlin's values are 0.2 times smaller than Trout and Kelley's. It is difficult to understand the reason for the differences between Trout and Kelley's and Bomford and Burlin's results as their respective phantoms have similar thicknesses (table 7.15). Bomford and Burlin have corrected their values for scatter from the surroundings and leakage from the x-ray tube head. These contributions are a large proportion of the total reading as the scatter from the phantom is small in the forward direction. The scatter from the collimators, ceiling, floor and walls (section 7.2.3.3) varies between 0.03% and 0.05%. This accounts for some of the differences which are between 0.045% and 0.101% but also suggests that the masonite and MixD phantoms may have substantially different attenuating properties. VOXSCAT calculations imply that the masonite phantom density may lie between 600 kg/m^3 and 800 kg/m^3. The scatter values are similar in the backward direction for the two phantoms as the scatter is less dependent on the phantom thickness or density.

The VOXSCAT calculations show good agreement with Williams' data (section 7.2.4.1). Williams' values in the backward direction are larger than the measurements carried out in the Philips x-ray room and the XYZSCAT calculated values. This may be due to the differing position of the DAP meter in the two experiments. In Williams' work, the DAP meter is closer to the phantom surface and thus, there is considerable backscatter from the DAP for scattering angles greater than 130°. In our work, the DAP meter is further away and the backscatter increases at a scattering angle of 137° (figure 7.16). Marshall and Faulkner (1992) found that the percentage scatter was independent of FSD. Section 7.2.2.4 also shows the scatter to be independent of FSD but in this case, a DAP meter was not modeled. Figure 7.16 shows that the percentage scatter will increase greatly for scattering angles (θ_{lim}) which align with the DAP meter (figure 7.18) and stay nearly constant for scattering angles less than θ_{lim}. Marshall and Faulkner's results will not have been affected by scatter from the DAP as they undertook their measurements for a 90° scattering angle which is smaller than θ_{lim}. Therefore depending on the angle of scatter, the percentage scatter may or may not be independent of FSD if a DAP meter is present. This should be further investigated in the future. The XYZSCAT and measured values lie between Trout's and Williams' values for backward directed scatter and are greater than

Trout's and Williams' values for forward directed scatter due to the smaller phantom thickness.

7.3 Calculation of Scatter and Transmission for Shielding Barriers

7.3.1 Comparison of Transmission through Concrete and Lead Walls

The percentage transmission, through concrete and lead slabs, calculated with the XYZSCAT code is compared to the values shown in the literature in this section. The work of Simpkin (1989), Rossi et al. (1991) and Archer et al. (1994) has been employed and is detailed below.

Simpkin (1989) calculated the transmission through semi-infinite slabs of concrete and lead using the EGS4 Monte Carlo code. He simulated a plane parallel broad beam of x-rays produced by a General Electric x-ray tube for tube potentials between 70 and 140 kV produced by a constant potential generator. The unit had a target angle of 10° and 2.3 mmAl total filtration. Simpkin (1989) simulated a broad beam using an incident pencil beam with the transmitted exposure scored in a semi-infinite region immediately behind the slab.

Rossi et al. (1991) measured the percentage transmission through concrete slabs. The experiment consisted of a x-ray tube placed at 90 cm from the front surface of the concrete slab. A three phase 12 pulse x-ray generator was used to produce 100 kV and 125 kV x-rays. The transmitted exposure was measured at 10 cm from the exit surface of the slab. An incident field size of 3600 cm^2 was used for all measurements.

Archer et al. (1994) measured the percentage transmission through lead slabs. The experiment consisted of a x-ray tube placed at 1 m from the front surface of the slab. A three phase x-ray generator was used to produce 70 kV, 100 kV, 125 kV and 150 kV x-rays. The transmitted air kerma was measured at 10 cm from the exit surface of the slab. Broad beam conditions were found by increasing the field size until the transmitted air kerma did not increase. This occurred with a 900 cm^2 field size.

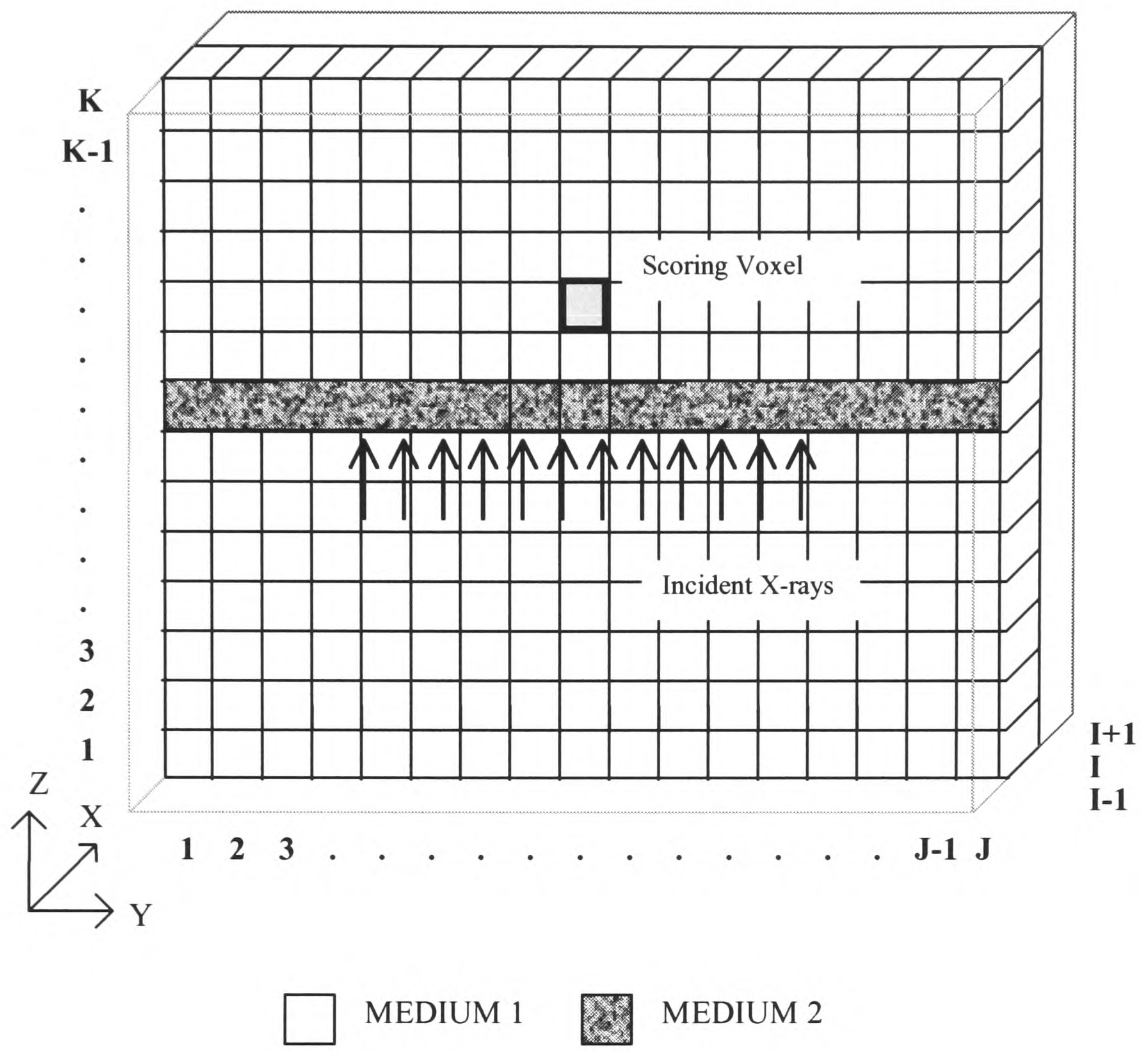

***Figure 7.19**. The voxels defining the XYZSCAT model for the transmission calculations (Media 1 and 2 are air and the concrete shielding barrier respectively).*

The XYZSCAT code was used to calculate the transmission behind concrete (2350 kg/m^3 density) and lead slabs. Figure 7.19 shows the voxels specified as either concrete or lead across the whole calculation geometry. Their thickness was incremented to obtain different transmissions. The transmitted air kerma was scored in a voxel with its centre 10 cm from the exit surface of the slab. The voxel's centre was positioned on the central axis of a plane parallel field incident on the slabs. The sizes of the voxel sides were 10 cm. Percentage transmission was calculated as the ratio of the transmitted air kerma in the voxel to the incident air kerma. The XYZSCAT calculations of transmission used typically 50×10^6 photons and this was increased to between 200×10^6 and 500×10^6 photons for concrete thicknesses greater than 10 cm and for lead thicknesses of 3 mm. This achieved a percentage uncertainty of less than ±3% for all thicknesses.

7.3.1.1 Investigation of Broad Beam Conditions

The field areas that provided broad beam conditions were investigated initially. The calculations used field areas between 4 and 3600 cm^2 for lead slabs and between 100 cm^2 and 1 m^2 for concrete slabs. The transmission through lead was calculated with a 1 mm thickness for 70 kV x-rays and with a 2 mm thickness for 140 kV x-rays. The transmission through concrete was calculated with a 10 cm thickness for 70 kV x-rays and with a 20 cm thickness for 140 kV x-rays. These thicknesses provided a similar percentage transmission at both tube potentials.

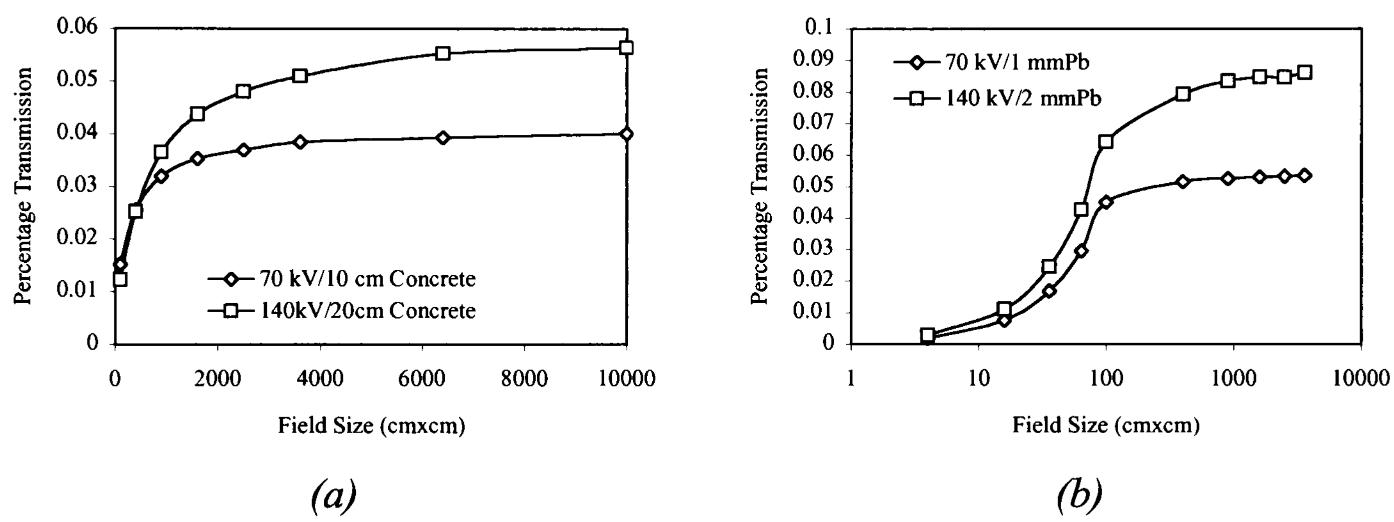

Figure 7.20. *The variation of percentage transmission for increasing field area with 70 kV and 140 kV x-rays incident on (a) concrete and (b) lead.*

Figures 7.20 shows the concrete and lead transmissions for increasing field area. The broad beam field size is found if the difference in the transmissions for each field area examined and the largest field area is less than their combined calculation uncertainties. Therefore, a field area of 900 cm^2 provided broad beam conditions for lead. This agrees with the field area found by Archer et al. (1994). It was found that a field area of 6400 cm^2 provided broad beam conditions for concrete. This is significantly larger than the field area of 3600 cm^2 used by Rossi et al. (1991) in their experiments.

7.3.1.2 Primary Beam Transmissions for Concrete and Lead

The broad beam field sizes are used to calculate the transmission through different thicknesses of lead and concrete. The maximum thicknesses of lead used in the calculations were 1.5 mm, 2.5 mm, 2.5 mm and 3.0 mm for 70 kV, 100 kV, 120 kV and 140 kV x-rays respectively. The maximum thicknesses of concrete used in the calculations were 15 cm, 20 cm, 20 cm and 20 cm for 70 kV, 100 kV, 120 kV and 140 kV x-rays respectively. Figures 7.21 shows the calculated percentage transmissions through concrete and lead.

Table 7.17 compares the XYZSCAT calculations of percentage transmission for lead with the values from Archer et al. (1994) and Simpkin (1989). Archer's percentage transmissions for 120 kV and 140 kV x-rays were found using linear interpolation of the appropriate data. Table 7.18 compares the XYZSCAT calculations of percentage transmissions for concrete with the values from Rossi et al. (1991) and Simpkin (1989). Rossi's percentage transmissions for 120 kV were found using linear interpolation of the appropriate data. Archer, Simpkin and Rossi report their percentage transmissions, T, for a thickness, x, using an interpolation formula (equation 7.1) developed by Archer (1983). The appropriate fitting coefficients (α, β, and Γ) given by Archer et al. (1994), Simpkin (1989) and Rossi et al. (1991) were used to calculate the percentage transmissions for comparison with this work. The transmissions are shown in tables 7.17 and 7.18.

$$T = 100\left[\left(1 + \beta/\alpha\right)\exp\left(\alpha\Gamma x\right) - \beta/\alpha\right]^{-1/\Gamma} \qquad (7.1)$$

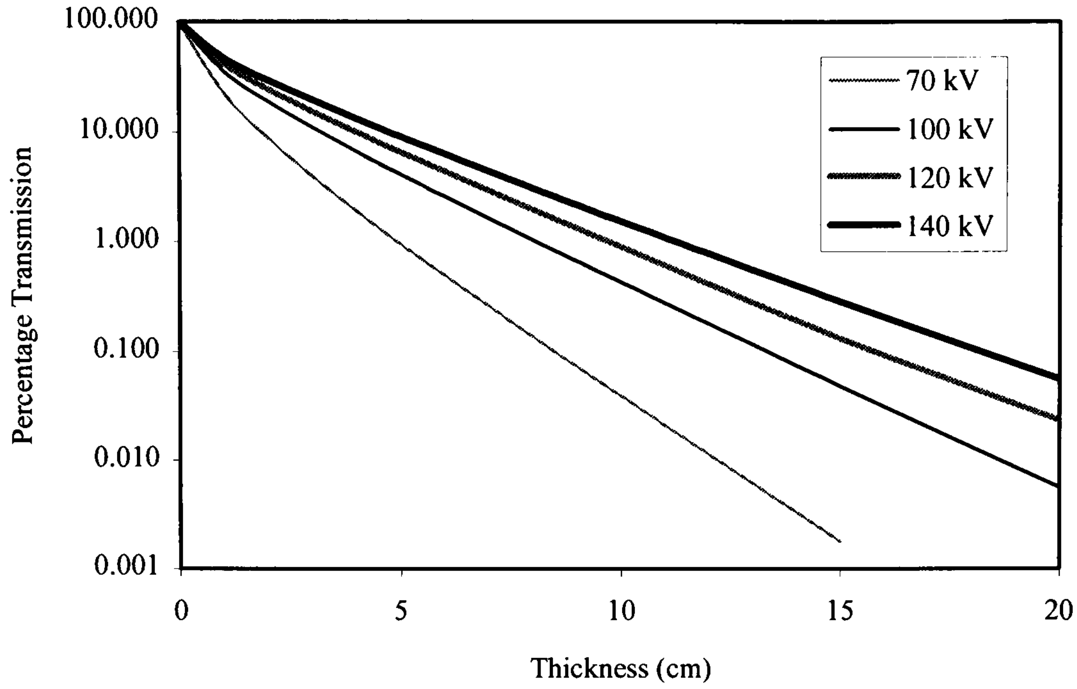

(a)

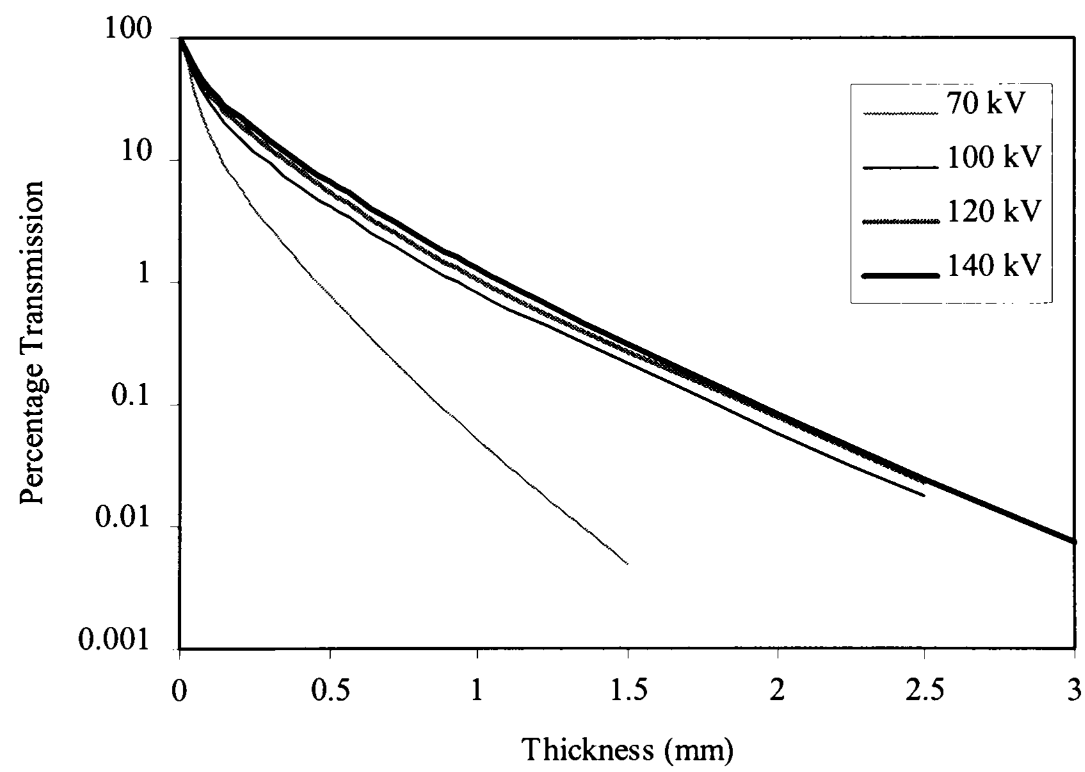

(b)

Figure 7.21*. The percentage transmission calculated by the XYZSCAT code through (a) concrete and (b) lead.*

Thickness (mm)	Percentage Transmissions for Lead					
	70 kV X-rays			100 kV X-rays		
	Archer Values	Simpkin Values	XYZSCAT Values	Archer Values	Simpkin Values	XYZSCAT Values
0.1	15.485	16.190	16.240	30.092	29.785	28.594
0.2	5.135	6.093	6.071	14.674	14.990	15.252
0.3	2.181	2.866	2.787	8.536	8.929	9.331
0.4	1.043	1.488	1.415	5.438	5.775	6.111
0.5	0.534	0.815	0.760	3.660	3.917	4.172
0.8	0.088	0.154	0.145	1.333	1.414	1.505
1.0	0.028	0.053	0.053	0.736	0.762	0.821
1.2	0.0094	0.019	0.020	0.420	0.420	0.470
1.5	0.0018	0.0039	0.0049	0.188	0.176	0.211
2.0	-	-	-	0.052	0.042	0.058
2.5	-	-	-	0.015	0.010	0.017

Thickness (mm)	120 kV X-rays			140 kV X-rays		
	Archer Values	Simpkin Values	XYZSCAT Values	Archer Values	Simpkin Values	XYZSCAT Values
0.1	40.223	34.630	33.820	48.654	39.188	38.150
0.2	20.918	18.368	19.062	26.976	21.867	22.384
0.3	12.300	11.287	12.009	16.177	13.848	14.400
0.4	7.791	7.465	7.945	10.243	9.346	9.642
0.5	5.187	5.155	5.436	6.753	6.547	6.627
0.8	1.832	1.938	1.963	2.283	2.521	2.406
1.0	1.001	1.067	1.068	1.215	1.397	1.293
1.5	0.259	0.258	0.269	0.303	0.338	0.312
2.0	0.075	0.065	0.076	0.089	0.084	0.083
2.5	0.023	0.016	0.023	0.028	0.021	0.024
3.0	-	-	-	0.0096	0.0053	0.0073

Table 7.17. *The comparison of the calculated percentage transmissions through lead with the values stated by Archer et al. (1994) and Simpkin (1989).*

The calculated lead transmissions in table 7.17 were compared to the values from Archer et al. and Simpkin using paired t-tests (Altman, 1991) by the method described in section 6.4.2.7. The t-tests show that the mean calculated transmission is not significantly different from the mean of Archer's measured values (P = 0.13) or the mean of Simpkin's calculated values (P=0.47). The differences in the mean transmissions are 0.6% between the calculations and Simpkin's work and 7.7% between the calculations and Archer's work. The limits of agreement, as derived from the t-tests, at the 95% confidence level for individual transmission estimates are:

-0.77% to 0.68% between the calculations and Simpkin's work; and –3.6% and 4.6% between the calculations and Archer's work. This corresponds to good agreement between the published and calculated transmissions (Bland and Altman, 1986).

Thickness (cm)	Percentage Transmissions for Concrete				
	70 kV X-rays		100 kV X-rays		
	Simpkin Values	XYZSCAT Values	Rossi Values	Simpkin Values	XYZSCAT Values
1	23.290	22.690	23.321	38.598	35.668
2	9.152	8.910	10.383	19.853	19.100
3	4.161	4.025	5.376	11.309	11.118
4	2.009	1.935	2.958	6.760	6.684
5	0.999	0.960	1.674	4.146	4.154
8	0.131	0.137	0.324	1.022	1.048
10	0.034	0.039	0.110	0.410	0.433
12	0.0090	0.011	0.038	0.165	0.182
15	0.0012	0.0018	0.007	0.042	0.048
20	-	-	0.00051	0.0044	0.0056

Thickness (cm)	120 kV X-rays			140 kV X-rays	
	Rossi Values	Simpkin Values	XYZSCAT Values	Simpkin Values	XYZSCAT Values
1	31.070	45.718	42.095	51.809	47.281
2	15.939	25.878	24.687	31.332	29.549
3	9.223	15.902	15.513	20.276	19.537
4	5.602	10.174	10.026	13.601	13.182
5	3.482	6.655	6.599	9.316	9.080
8	0.881	1.974	1.983	3.178	3.094
10	0.358	0.895	0.904	1.585	1.537
15	0.038	0.126	0.131	0.284	0.284
20	0.0041	0.018	0.023	0.051	0.055

Table 7.18*. The percentage transmissions through concrete calculated with the XYZSCAT code compared to the values stated by Rossi et al. (1991) and Simpkin (1989).*

The differences between the percentage transmissions for lead calculated by the XYZSCAT code and the measured values of Archer et al. are larger than the differences between the calculated transmissions and Simpkin's values. The differences with Archer's work are largest for lead thicknesses above 0.2 mm with 70 kV x-rays and the differences increase for increasing thickness. This may be due to the calculations being undertaken for a constant potential x-ray unit whereas Archer's measurements were undertaken for a three phase x-ray unit. There is good agreement for the other tube potentials investigated. It would be expected that differences in the quality of the x-ray spectra will have the greatest effect on the transmission for low tube potentials.

The calculated concrete transmissions in table 7.18 were compared to the values from Rossi et al. and Simpkin using paired t-tests (Altman, 1991) by the method described in section 6.4.2.7. The t-tests show that the mean calculated transmission is significantly different from the mean of Rossi et al.'s measured values ($P = 0.002$) and the mean of Simpkin's calculated values ($P=0.008$). The differences in the mean transmissions are 5.3% between the calculations and Simpkin's work and 44.8% between the calculations and Rossi's work. However, the 5.3% difference is reasonable considering that Simpkin's calculation uncertainty is less than or equal to ±10% (Simpkin, 1989). The difference between the calculated and Rossi's mean transmissions is large. The limits of agreement, as derived from the t-tests, at the 95% confidence level for individual transmission estimates are: -1.6% to 2.6% between the calculations and Simpkin's work; and –5.6% and 13.9% between the calculations and Rossi's work. This corresponds to good agreement between Simpkin's values and the calculated values (Bland and Altman, 1986). The difference in the means and the limits of agreement suggest that there is poor agreement between Rossi's transmissions and the calculated values.

Table 7.18 shows that Rossi's measured transmissions are consistently lower than either the calculations or Simpkin's values. This may be due to the low beam quality of the x-ray tube employed. There are further sources of uncertainty in Rossi's work: the composition of the concrete was not known; the concrete slab density varied between 1800 and 2500 kg/m^3; the field size was smaller than that used in the calculations; and the measurements were undertaken with only six slab thicknesses which may result in a poor fit to the interpolation formula (equation 7.1). These factors may account for the large differences from the calculated values.

The best agreement for the percentage transmissions calculated with the XYZSCAT code is with the values from Simpkin (1989). This is to be expected as both calculations use the EGS4 Monte Carlo code although with different user codes. The percentage transmissions calculated by the XYZSCAT code are also representative of the values of Archer et al. (1994) but not of Rossi et al. (1991). Therefore, the XYZSCAT code can be used to provide shielding data for primary x-rays which is similar to that found in the literature. In the future, the XYZSCAT code could be used to extend this data if necessary.

7.3.1.3 Leakage Beam Half Value Layers for Concrete and Lead

The transmission curves can be used to find the 'high attenuation' half value layers to shield against leakage radiation. The leakage x-rays are assumed to be of high quality as they have been transmitted through the x-ray tube head. Therefore, the 'high attenuation' half value layers HVL_n are found from the transmission given by $1/2^n$ where n is large. A number of HVLs, n, are therefore required to provide adequate shielding. Equation 7.2 shows equation 7.1 re-arranged by Archer, Simpkin and Rossi to obtain the nth half value layer, HVL_n which is typically the 10th HVL (Archer et al., 1994)

$$HVL_n = \frac{1}{\alpha\Gamma}\ln\left\{\frac{\left[\left(2^n\right)^\Gamma + \beta/\alpha\right]}{\left[1+\beta/\alpha\right]}\right\} - \sum_{i=1}^{n-1} HVL_i \qquad (7.2)$$

Equation 7.2 was used to provide the high attenuation HVLs shown in table 7.19 using the appropriate coefficients α, β, and Γ from Archer et al. (1994), Rossi et al.

(1991) and Simpkin (1989). The percentage transmissions calculated by the XYZSCAT code were not fit to equation 7.1. Instead, the 'high attenuation' HVLs in table 7.19 were found by logarithmic interpolation of the percentage transmissions.

	'High Attenuation' Half Value Layers (mm)					
	Concrete Barrier			Lead Barrier		
Tube Potential (kV)	**Rossi's Values**	**Simpkin's Values**	**Calculated Values**	**Archer's Values**	**Simpkin's Values**	**Calculated Values**
70		10.4	11.0	0.120	0.134	0.138
100	12.9	15.3	15.9	0.270	0.245	0.273
120	15.1	17.7	19.1	0.278	0.253	0.276
140		20.3	21.0	0.286	0.250	0.270

***Table 7.19**. The comparison of the 'high attenuation' HVLs for concrete and lead from XYZSCAT calculations with the values stated in Archer et al. (1994), Rossi et al. (1991) and Simpkin (1989).*

Table 7.19 shows the comparison between the calculated HVLs with those stated in the literature. The HVLs derived from the XYZSCAT calculations show good agreement (mostly within ±10%) with Simpkin's and Archer's HVLs and reasonable agreement (within ±20%) with Rossi's HVLs. Therefore, the XYZSCAT code can be used to provide shielding data for leakage x-rays which is representative of that found in the literature. Again, in the future, the XYZSCAT code could be used to extend this data.

7.3.2 Calculation of Scatter from Concrete Shielding Barriers

The relationship between percentage scatter and field area from slab phantoms was examined in section 7.2.3.2. A linear variation was found but this study was carried out for field areas less than 900 cm^2. Primary beams incident on shielding barriers can have large field sizes if the x-ray focus to barrier distance is large. The scatter from the patient or phantom will also irradiate the whole shielding barrier and it is therefore important to know the amount of secondary scatter produced by the barrier (section

8.3.2.3). Hence, the variation of percentage scatter with large field sizes has been studied using XYZSCAT calculations with field areas varied up to 40000 cm^2. The XYZSCAT code calculations were carried with the same parameters used in section 7.3.1. The simulations used between 50×10^6 and 500×10^6 photons to give a percentage uncertainty of less than ±2% in the scatter values.

7.3.2.1 Comparison with Percentage Scatter from Concrete Barriers in the Literature

Source	kV or kV range	Percentage Scatter from Concrete Barriers 120° Scattering Angle	135° Scattering Angle	150° Scattering Angle
HMSO (1972)	100 to 300 kV	0.044	0.052	0.066
XYZSCAT Calculations	140 kV	0.014	0.020	0.025
Source	**kV or kV range**	**Percentage Scatter from Concrete Blocks 120° Scattering Angle**	**135° Scattering Angle**	**150° Scattering Angle**
Measurements (section 7.2.3.1)	121 kV	-	0.032	-
XYZSCAT Calculations (section 7.2.3.1)	121 kV	0.024	0.028	0.046

Table 7.20. *The comparison of the percentage scatter from concrete blocks or walls with a 100 cm^2 field area.*

Initially, the calculated percentage scatter from shielding barriers is compared to the values in the literature. Table 7.20 shows the calculated scatter values for 120°, 135° and 150° scattering angles for 140 kV x-rays incident on 20 cm thick concrete. A field size of 100 cm^2 was used in the calculations. Table 7.20 compares the scatter values for concrete from the 'Handbook of Radiological Protection' (HMSO, 1971) with the calculated values for x-rays incident on concrete barriers and the calculated and measured values for x-rays incident on concrete blocks (section 7.2.3.1). The HMSO values are considerably larger than the other values due to their values representing a large range in tube potentials between 100 and 300 kV. The measured HMSO values will also include scatter from the surroundings not taken into account in the calculations. The XYZSCAT calculations with the concrete barrier are smaller than the calculations and measurements for the concrete blocks because the latter values include scatter from the DAP meter and the surrounding walls. The calculated value for concrete blocks increases rapidly at a 150° scattering angle due to scatter from the DAP meter (figure 7.16).

7.3.2.2 Variation of Percentage Scatter with Field Size

Figures 7.22 shows the percentage scatter for field areas between 4 and 40000 cm^2 normalised to the percentage scatter calculated for 100 cm^2 (table 7.20). The calculations were carried out for a plane parallel beam of 140 kV x-rays incident on a concrete barrier with a thickness of 20 cm and the ratios are shown for 120°, 135° and 150° scattering angles.

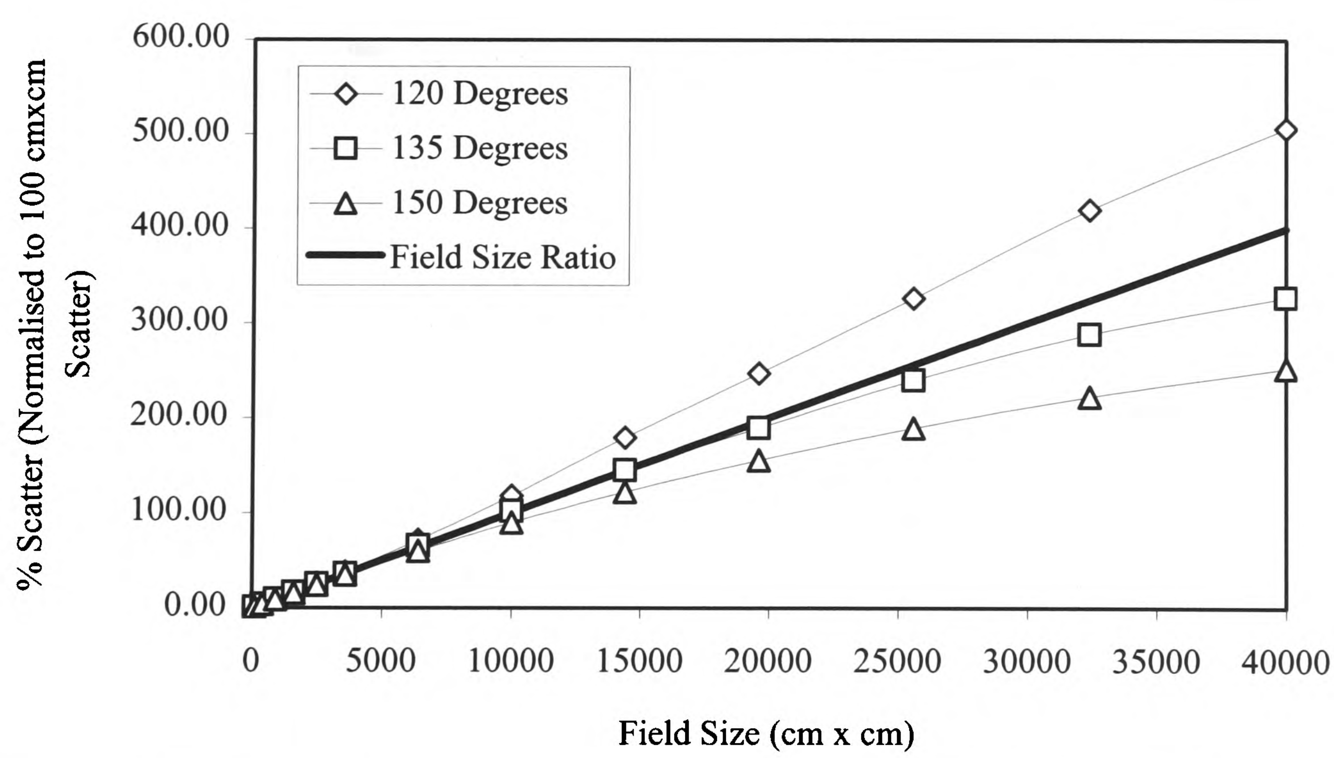

Figure 7.22. *The variation of the percentage scatter (normalised to the percentage scatter for a 100 cm^2 field size) with field size for 140 kV x-rays incident on a concrete barrier.*

There is a linear relationship between the percentage scatter and the field area for areas less than 2500 cm^2 for 120° and 150° scattering angles and for areas less than

14400 cm^2 for the 135° scattering angle. The scatter values for the 120° scattering angle increase more rapidly than a linear relationship for field areas greater than 2500 cm^2. This is because the field borders are closer to the scoring position with increasing field size as shown in figure 7.23. For example by increasing the field area from 10000 cm^2 to 25600 cm^2, the distance from the field centre to the field border increases from 50 to 80 cm. Therefore, the field borders are significantly closer to the scoring position which is 87 cm from the field centre at the 120° scattering angle. The rapid increase in scatter cannot be an artefact due to primary x-rays traversing the scoring voxel as the transport of the incident photons was initiated 1 cm in front of the barrier's surface. The variation of percentage scatter with field size for the other scattering angles will also be due to the scoring position in relation to the field borders.

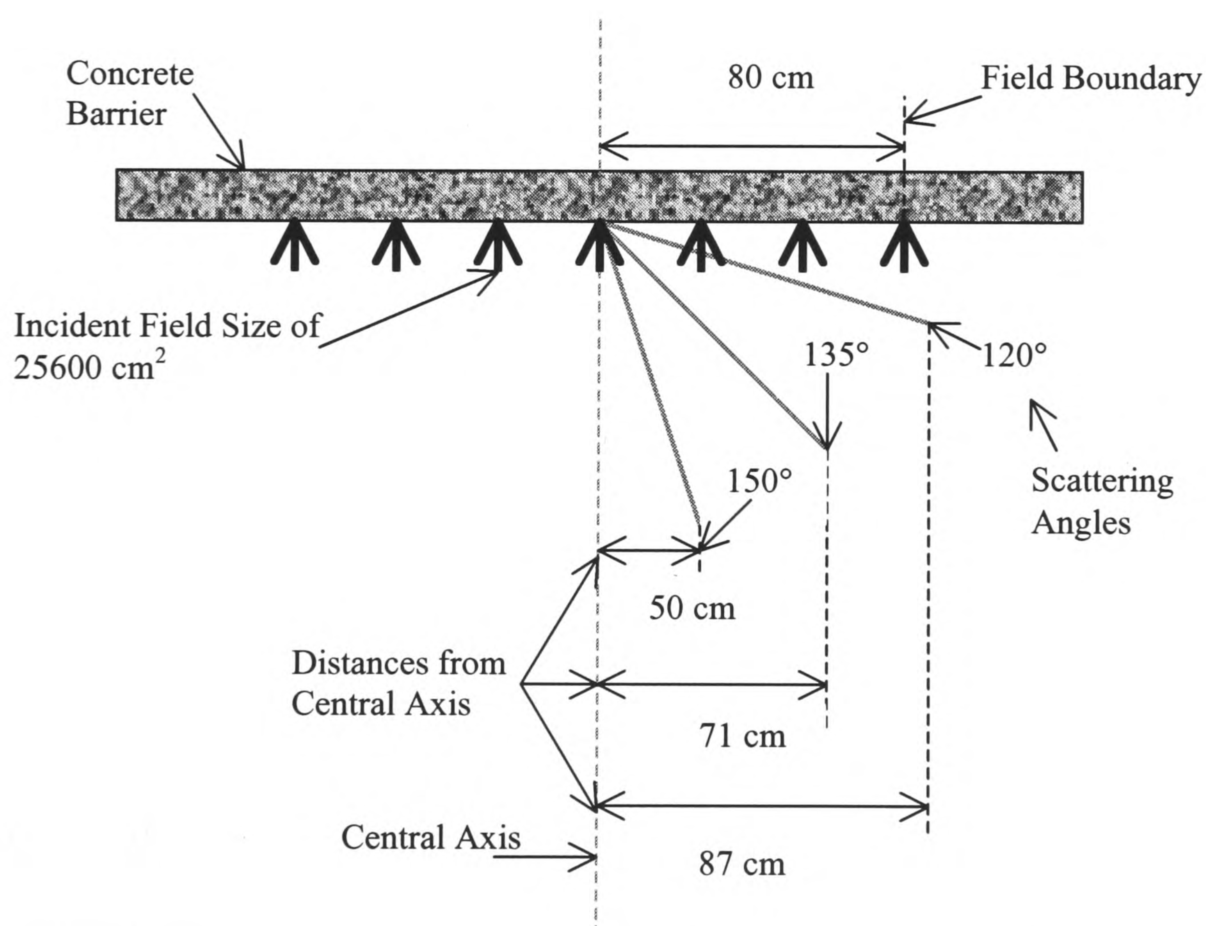

***Figure 7.23**. The scoring positions in relation to the field size.*

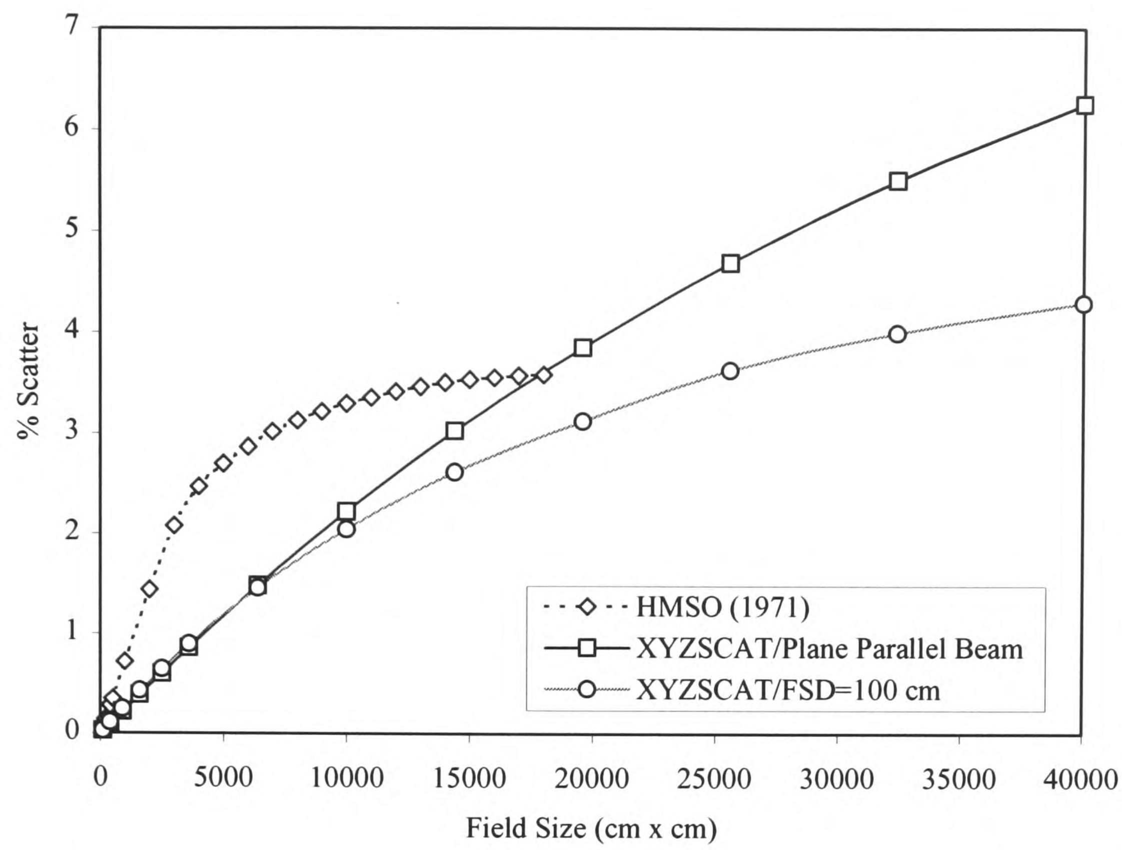

***Figure 7.24**. Comparison of the percentage scatter with increasing field size from the 'Handbook of Radiological Protection' (HMSO, 1971) with the XYZSCAT calculated values for a plane parallel beam and a divergent beam with a FSD of 100 cm.*

Figure 7.24 compares the variation of the HMSO (1971) percentage scatter and the XYZSCAT calculated values with field size for a plane parallel beam and a divergent beam with a FSD of 100 cm. The HMSO data was measured at a 160° scattering angle for 100 to 300 kV x-rays with normal incidence on concrete. The XYZSCAT code calculated values with 140 kV x-rays incident on a concrete barrier at a 150° scattering angle. Figure 7.24 shows that the shape of the measured and calculated curves are very different. The maximum calculated scatter values are 6.3% and 4.3% for the plane parallel beam and the divergent beam respectively at a field size of 4 m^2. The FSD clearly has a large effect on the calculated scatter due to the greater attenuation of the scattered photons which have oblique incidence. The HMSO values show a linear variation with field area below field areas of 4000 cm^2 and the scatter increases to reach a maximum value of 3.6% for a field area of 1.8 m^2. It is difficult to know the reason for the large difference in the shape of the calculated and published curves as the HMSO report gives very little information on the experimental arrangement used to measure the scatter. Although the HMSO states that the scattering material is concrete, the difference may be due to the composition and density of the scattering material employed in the experiments. The same composition and density of concrete was used in the scatter calculations as was used in the transmission calculations (section 7.3.1.2).

7.3.2.3 Variation of Percentage Scatter with Barrier Thickness

Figures 7.25 shows the variation of percentage scatter for 120°, 135° and 150° scattering angles with different thicknesses of concrete. The percentage scatter was calculated for 140 kV x-rays incident with a field size of 6400 cm^2 on concrete barriers with their thicknesses varied from 1 cm to 20 cm. The percentage scatter does not increase for increasing concrete thicknesses above 4 cm for all three scattering angles. Martin et al. (1961) has studied the variation of percentage scatter with the thickness of different scattering blocks. Martin found that for aluminium (which has a similar atomic number to that of concrete) there is full build up of scatter for barrier thicknesses above 25% of the total thickness. This approximately agrees with the calculated variation of percentage scatter with barrier thickness. In practice, barriers that are thick enough to protect from primary and secondary radiation will produce full scatter in the x-ray room.

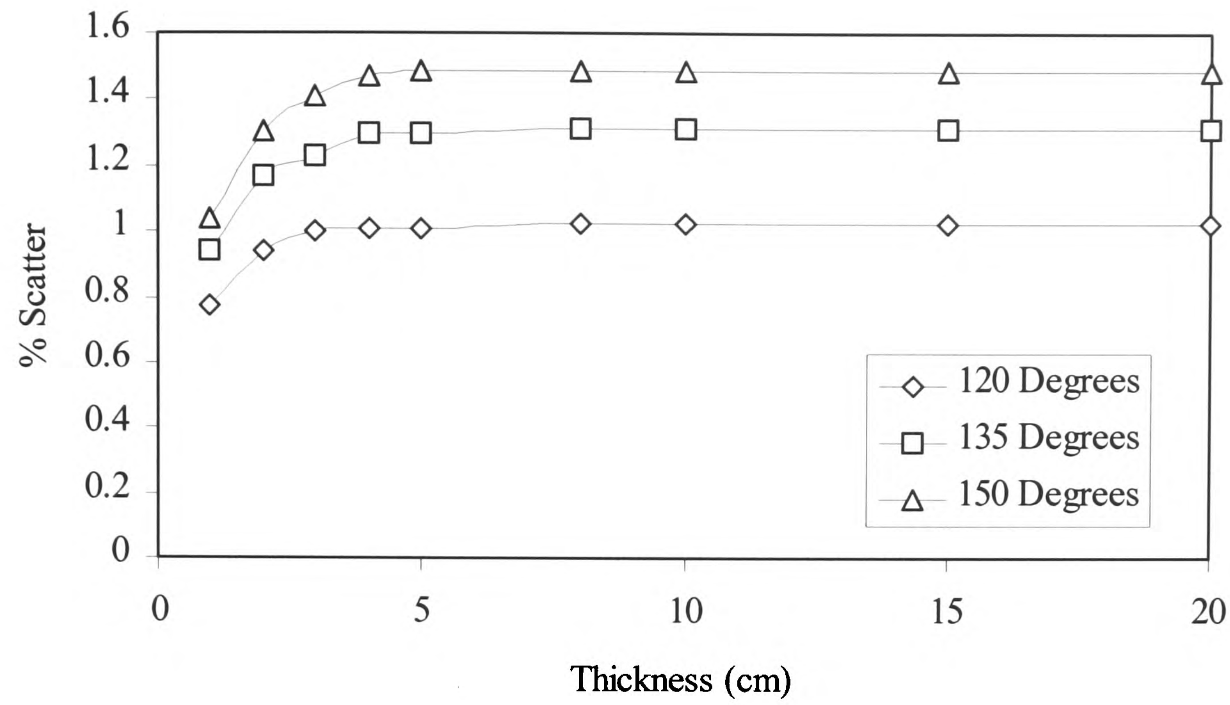

Figure 7.25*. The variation of the percentage scatter with concrete barrier thickness for 140 kV x-rays.*

7.4 Calculation of Transmission through Slab Phantoms in the Linköping Physics Laboratory

The VOXSCAT code calculates entrance air kerma (without backscatter), air kerma transmitted through the phantom and air kerma transmitted through the anti-scatter device and the cassette front. These quantities can be used to estimate the transmission through a PMMA slab phantom in the Linköping Physics Laboratory and through the table top and table top and grid in the Linköping lumbar spine Laboratory. This work provides a validation of the computation method used in the VOXSCAT code. All quantities were estimated with a statistical precision of 3% or better.

The measurements in this laboratory (Sandborg and Persliden, private communication) were made with an X-ray tube with a target angle of 12°. The added filtration was estimated as 3.2 mm aluminium using HVL measurements at nominal tube potentials of 70 and 100 kV.

Measured or Estimated kV	Measured HVL (mmAl)	PMMA Thickness (cm)	Measured Transmission	Calculated Transmission	% Difference
53.0		3.93	0.108	0.106	-0.9
73.2		3.93	0.125	0.124	-0.8
73.2		3.93	0.126	0.124	-1.8
73.2	2.90	3.93	0.128	0.124	-2.8
105.1		3.93	0.143	0.145	1.4
103.3		3.93	0.146	0.145	-0.5
103.3		3.93	0.146	0.145	-0.3
53.0		11.77	0.00922	0.00913	-1.0
73.2		11.77	0.0138	0.0144	5.1
73.2		11.77	0.0135	0.0144	6.8
73.2		11.77	0.0139	0.0144	3.5
105.1		11.77	0.0190	0.0208	8.9
103.3	4.00	11.77	0.0200	0.0208	3.7
103.3		11.77	0.0201	0.0208	2.9

***Table 7.21**. Comparison of measured and calculated transmissions through slabs of PMMA.*

Table 7.21 shows the results of measurements and calculations for the transmission estimation. The experimental results are from two series of measurements detailed in section 3.4. The experimental arrangement is given in table 3.5.

Good agreement (within ±9%) is achieved in the comparison of measured and calculated ratios of transmitted air kerma to incident air kerma. Hubbell (1982) estimates that the uncertainty in mass attenuation coefficients is ±2% in the energy range of 5 keV to 10 MeV. A change of 2% in the cross sections produces an estimated change in transmission of 7.5 % for 11.77 cm thick PMMA.

7.5 Calculation of Optical Density behind Slab Phantoms

7.5.1 Linköping Physics Laboratory

Table 7.22 shows the results of measurements and calculations for the film exposures with and without the grid. The experimental results are from two series of measurements (Sandborg and Persliden, private communication) detailed in section 3.4. The experimental arrangement is given in table 3.5. The agreement of the calculated and measured optical densities is good.

Measured or Estimated kV	Measured HVL (mmAl)	PMMA Thickness (cm)	Measured OD	Calculated OD	% Difference
61.7		15.70	1.53	1.48	-3.3
103.3	4.00	15.70	1.53	1.31	-14.4

***Table** 7.22. Comparison of the measured and calculated optical densities through a 15.7 cm thick slab of PMMA in a grid and receptor geometry.*

7.5.2 Norrköping Chest Laboratory

The measurements in this laboratory were made with an X-ray tube with a target angle of 13.5°. The tube had added filtration of 0.1 mm copper for the optical density measurements and the added aluminium filtration was estimated as 2.7 mm using HVL measurements at nominal tube potentials of 90 and 140 kV.

The screen/film combination was Agfa Curix Ortho Med / Fuji Super HRL. The screen had a thickness of 120 mg/cm^2 Gd_2O_2S. The H and D curve was measured at 140 kV using a 20 mm thick aluminium block to simulate the phantom, but with no copper filter in the beam. The geometrical arrangements for the optical density measurements are given in table 3.6. Measurements were made both in front of and behind the chest stand/grid assembly.

Nominal kV	Measured HVL (mmAl)	PMMA Thickness (cm)	Grid	Chest Stand	Measured OD	Calculated OD	% Difference
90.0	5.25	11.77	No	No	1.11	0.97	-12.6
140.0	7.40	11.77	No	No	1.19	1.15	-3.4
90.0	5.25	11.77	Yes	Yes	1.22	1.19	-2.5
140.0	7.40	11.77	Yes	Yes	1.39	1.38	-0.7

***Table** 7.23. Comparison of the measured and calculated optical densities through an 11.77cm thick slab of PMMA in geometries with and without the grid and chest stand.*

The chest stand thickness was 4 mm of PMMA. The detailed composition of the front face of the Agfa Curix cassette was not known, so calculations were made for both 2.5 mm of polystyrene and 1.74 mm aluminium (Dance et al., 1997). The results for the two choices were quite similar and those presented here are for aluminium. It is believed that the grid was manufactured by Mitaya with parameters: strip density N =

40 cm^{-1}, grid ratio r = 12, strip width d = 50 μm, interspace width D = 200 μm, aluminium interspace and grid covers of 2×0.15 mm aluminium.

Table 7.23 shows the results of the measurements and calculations for the film exposures with and without the grid. The results presented are from two series of measurements (Sandborg and Persliden, private communication) detailed in section 3.4. Good agreement is achieved (within ±13%) in the comparison of measured and calculated values of the optical density both with and without the chest stand and grid. This agreement is regarded as satisfactory considering the day-to-day fluctuations in film processing and the strong dependence of optical density on tube potential.

7.5.3 Linköping Lumbar Spine Laboratory

Measured kV	Measured HVL (mmAl)	Grid	Couch Top	Measured Transmission	Calculated Transmission	% Difference
70.8	2.80	No	Yes	0.822	0.948	15.3
72.4	2.90	Yes	Yes	0.292	0.378	29.5
98.0	3.90	Yes	Yes	0.347	0.438	26.3

***Table 7.24**. Comparison of the measured and calculated transmissions through the couch top and the couch top plus grid. Note that the couch top only measurement was carried out with a different x-ray tube.*

Measured kV	Measured HVL (mmAl)	PMMA Thickness (cm)	Grid	Couch Top	Measured OD	Calculated OD	% Difference
50.0		11.77	No	No	1.37	1.20	-12.4
71.6	3.00	11.77	No	No	1.06	1.06	0.0
72.4	2.90	18.22	No	No	1.58	1.63	3.2
85.8		15.70	No	No	1.39	1.47	5.8
98.0	3.90	18.22	No	No	1.45	1.48	2.1
50.0		11.77	Yes	Yes	1.14	1.12	-1.8
71.6	3.00	11.77	Yes	Yes	1.02	1.01	-1.0
72.4	2.90	18.22	Yes	Yes	1.21	1.20	-0.8
85.8		15.70	Yes	Yes	1.18	1.06	-10.2
98.0	3.90	18.22	Yes	Yes	1.15	1.06	-7.8

***Table 7.25**. Comparison of the measured and calculated optical densities through slabs of PMMA in geometries with and without the grid and couch top.*

The measurements in this laboratory were made with an X-ray tube with a target angle of 12°. The added aluminium filtration was estimated as 3.1 mm using HVL measurements at nominal tube potentials of 70 kV and 99 kV.

The screen/film combination was Lanex medium / Fuji HRE. The medium screen had a thickness of 118.4 mg/cm^2 Gd_2O_2S. The H and D curve was measured at 90 kV using a 13 mm thick aluminium block to simulate the phantom.

The transmissions through the couch top and the couch top and grid were measured in geometries which included some scatter from the couch. The geometrical arrangements for the optical density measurements are given in table 3.7. Measurements were made both in front of and behind the couch top/grid assembly.

The couch top thickness was understood to be 6 mm of PMMA, but subsequent measurements proved this information to be unreliable (table 7.24). The thickness of the front face of the X-omatic cassette front was 1.74 mm aluminium. The grid was manufactured by Lysholm with parameters: strip density N = 70 cm^{-1}, grid ratio r = 16, strip width d = 36 μm, interspace width D = 90 μm, aluminium interspace, and grid covers of 2×0.2 mm aluminium.

Table 7.24 shows the results of the measurements and calculations for transmissions through the couch top and couch top plus grid. It can be seen that there is an important difference between the measurements and calculations. This can be corrected by increasing the thickness of the couch top. Calculations show that the results for the couch top transmission at both tube potentials can be explained by increasing the couch top thickness to 2.124 g/cm^2. The results for the couch top plus grid transmission can be explained by increasing the couch top thickness to 1.770 g/cm^2. These two results agree within experimental error of the transmission measurements and a couch top thickness of 1.947 g/cm^2 is used in all subsequent calculations. It is likely that the true explanation is that the couch top contains some metal reinforcement.

Table 7.25 shows the results of the measurements and calculations for the film exposures with and without the grid and couch top. The results presented are from two series of measurements detailed in section 3.4. Good agreement (within 12%) is achieved in the comparison of the measured and calculated values of the optical density both with and without the grid and couch top. This agreement is regarded as satisfactory considering the day-to-day fluctuations in film processing and the strong dependence of optical density on tube potential.

7.6 Comparison of VOXSCAT Calculations with Patient Image Measurements

7.6.1 Preliminary Studies with the Voxel Phantom

This section describes initial studies carried out to ascertain appropriate values of various model parameters for each of the four projections considered in this study.

7.6.1.1 Patient Thickness

The effect of changing patient thickness on the entrance air kerma was studied for the chest PA images. For six male patient radiographs selected, three patients had a thickness of 20 cm and another three had a thickness of 26 cm.

The median optical densities and the measured entrance doses were obtained for each of the images. The average of the median optical densities was found for the patients with a 20 cm chest thickness and for the patients with a 26 cm chest thickness. The corresponding values of the entrance air kerma (without backscatter) were calculated with the VOXSCAT code using the appropriate median optical densities for each patient group and equation 6.31.

The resulting entrance air kerma values were 0.16 mGy for the 20 cm thick phantom and 0.31 mGy for the 26 cm thick phantom. The range of measured entrance doses for the three 20 cm thick male patients was 0.11 - 0.13 mGy and for the three 26 cm thick patients was 0.13 - 0.17 mGy. The range of entrance doses for all male patients was 0.11 - 0.21 mGy and for all patients was 0.11 - 0.30 mGy. On the basis of these results, the 20 cm thick voxel phantom is representative of patients of both sizes.

7.6.1.2 Field Size and Tissue Density

Calculations of entrance air kerma were carried out for three field sizes (section 6.5.1.1) with the 20 cm thick voxel phantom. The calculated values were compared to measurements on the six selected chest PA images. It was found that all three values of the calculated entrance air kerma fell within the range of the measured values. The large field size, covering the lungs and soft tissue close to the bottom of the rib cage, was chosen as it was the most physically realistic.

Calculations of entrance air kerma were also carried out for different densities for soft tissue and lung tissue in the chest PA examination and different densities for soft tissue and bone in the lumbar spine PA examination. It was decided to use the standard tissue densities as given in table 6.4 for simplicity and compatibility reasons.

7.6.1.3 Calculation of the Factor $r_{2,50}$

The precision of the Monte Carlo estimates of entrance air kerma and dynamic range parameters P70:P30, P80:P20 and P90:P10 depends on the number of image points used for the calculation. Figure 7.26 shows this dependence for entrance air kerma and dynamic range for chest PA and lumbar spine PA. Similar results were obtained for the lateral projections. It can be seen that after an initial oscillation occurring for a small grid of data points, a plateau value is reached. The oscillations are largest for P90:P10. This is expected as this dynamic range measure is determined by sparser data close to the edges of the grey scale distribution. On the basis of these results, the program used grids of at least 200, 150, 200, 150 points for the chest PA, chest lateral, lumbar spine PA/AP and lumbar spine lateral projections respectively.

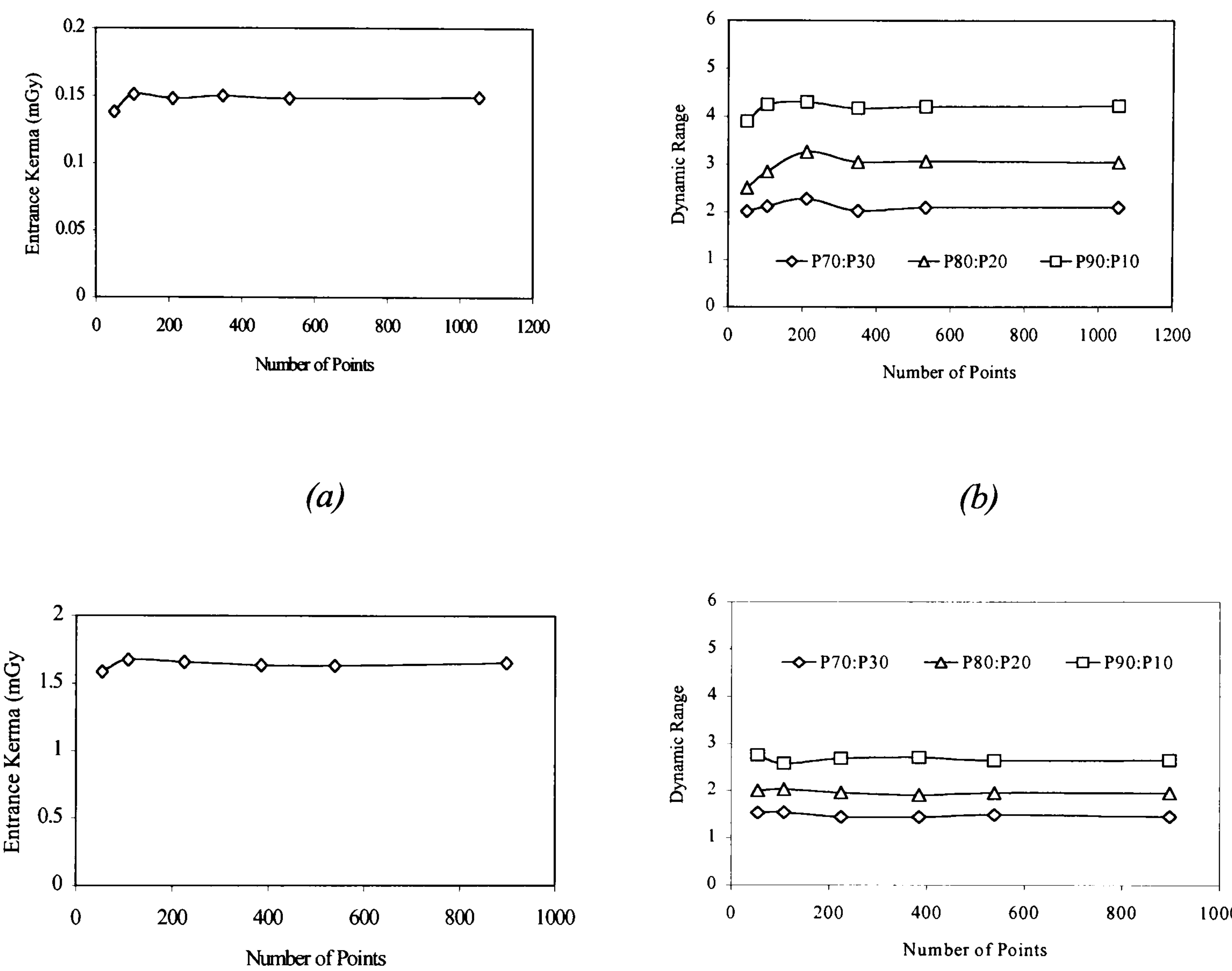

(a) (b)

(c) (d)

Figure 7.26. *The dependence of the calculated entrance air kerma (without backscatter) on the number of image points simulating (a) the chest PA projection and (c) the lumbar spine AP/PA projection. The dependence of the calculated dynamic range parameters P70:P30, P80:P20 and P90:P10 on the number of image points simulating (b) the chest PA projection and (d) the lumbar spine AP/PA projection.*

7.6.2 Validation of the Voxel Phantom

7.6.2.1 Entrance Air Kerma

Table 7.26 shows the calculated and measured entrance air kerma for the four radiographic projections. The calculated dose has been obtained following the method outlined in section 6.5.3.1 and using the final parameters set out in section 7.6.1. The entrance air kerma values calculated using the VOXSCAT code for the chest PA, chest LAT and the lumbar spine LAT projections lie within the range of measured values for male patients. They are thus representative of clinical practice.

For the lumbar spine PA projection, the calculated entrance air kerma is 30% less than the lowest value encountered in the surveys for all male patients and 20% less than the lowest value encountered in the surveys for all patients. The small calculated value may be related to the density assumed for bone and/or soft tissue, the external dimension of the phantom or the size of the vertebrae within the phantom.

In view of the good agreement obtained for the other three projections, no attempt was made to adjust the phantom parameters to improve this result. It was felt that the calculated and measured values of entrance air kerma for this lumbar spine PA projection were sufficiently close to validate the model for this projection as well.

Examination	Calculated Entrance Air Kerma (mGy)	Range of Measured Entrance Air Kerma (mGy)
Chest PA	0.15	0.11 – 0.30
Chest LAT	0.61	0.18 – 1.5
LS PA	1.7	2.1 – 5.5
LS LAT	8.7	7.5 – 21.5

Table 7.26*. Comparison of the calculated entrance air kerma using the VOXSCAT code with the range of the measured entrance air kerma values for all patient images for each projection.*

As noted in section 6.5.3.1, the entrance air kerma for the chest PA projection was also calculated by normalising to the optical density measured in the central right lung and left lung apex in patient chest images. The resulting calculated entrance air kerma values were 0.15 mGy and 0.16 mGy respectively. This excellent agreement with the result for the standard approach (which uses the median optical density from a grid of points across the whole image) is encouraging. It shows the robustness of the method and further demonstrates the realism of the voxel phantom model.

7.6.2.2 Dynamic Range

Table 7.27 shows the comparison of the calculated and measured dynamic range for the four projections. The agreement between measurement and calculation can be regarded as moderate to good, depending on the choice of parameter and projection. This is the expected level of agreement and is adequate for the purpose of the thesis. The voxel phantom is a simplification of the real situation. It uses only four different tissue densities and was obtained with a supine patient whereas the chest X-rays were obtained with a standing patient at full inspiration. Therefore, it is not likely that it will give a very close representation of the dynamic range that is obtained in practice.

Exam	Calculated P70:P30	Measured Range of P70:P30	Calculated P80:P20	Measured Range of P80:P20	Calculated P90:P10	Measured Range of P90:P10
Chest PA	2.09	2.10 – 3.08	3.04	3.25 – 4.90	4.22	5.04 – 8.36
Chest LAT	2.17	1.67 – 2.19	2.94	2.54 – 3.24	4.84	4.50 – 6.45
LS PA	1.45	1.39 – 1.63	1.95	1.73 – 2.33	2.64	2.57 – 4.16
LS LAT	1.42	1.89 – 3.69	1.71	2.92 – 8.48	3.52	5.57 – 17.6

***Table** 7.27. Comparison of the calculated dynamic range using the VOXSCAT code with the range of measured dynamic range for all patient images for each projection.*

7.7 Summary of Work

7.7.1 Validation of the Monte Carlo Codes

1. The VOXSCAT and XYZSCAT codes were rigorously validated by comparison of their calculated scatter values. There were no significant differences between the scatter values calculated with the two Monte Carlo codes.
2. The measured percentage scatter tended to be larger than the XYZSCAT calculated values. This comparison was more problematic than comparing the calculations due to the large measurement uncertainty and the contributions of scatter from materials other than the phantom in the x-ray room. Despite these difficulties, there were no significant differences between the measured and

calculated scatter values for all materials. This work shows that the scatter values calculated by the Monte Carlo codes are therefore representative of the scatter found in clinical x-ray rooms.

3. The comparison of the calculated scatter values with the data in the literature was generally good. The work of Williams (1996) and Marshall et al. (1996) were selected for detailed comparison as they are recent work and use modern equipment. The percentage scatter measured by Williams (1996) tends to be larger than the values calculated by the VOXSCAT code. This may be due to scatter from x-ray collimators particularly for the 120° scattering angle. However, there was good overall agreement with the values from Williams (1996). The quality of scattered radiation measured by Marshall et al. (1996) tended to be higher than the calculated spectra. This was due to the experimental arrangement not being known in detail. However, there was reasonable agreement between the calculated and measured quality of the scattered radiation.
4. The XYZSCAT calculated percentage transmissions for concrete and lead were compared with the values from recent work of Archer et al. (1994), Rossi et al. (1991) and Simpkin (1989). Good agreement was achieved for primary beam transmissions and 'high attenuation' HVLs for the leakage beam between the XYZSCAT calculations and Archer's and Simpkin's values. Poor agreement was found for the comparison of the XYZSCAT calculations with the data from Rossi et al..
5. The VOXSCAT code calculations of transmission behind a PMMA block agreed with the measured values.
6. The VOXSCAT code calculations of optical density behind a PMMA block agreed with the measured values. This work, together with part 5, validated the

computational method used in the VOXSCAT code with homogeneous blocks of material.

7. The VOXSCAT calculations of entrance air kerma agreed within the range of measured values from patient image studies. This work validated that the voxel phantom (Zubal et al., 1994) was representative of a patient.

7.7.2 Results from Initial Investigations of Scatter

1. Using monoenergetic photons with the mean energies of clinical x-ray spectra to calculate the percentage scatter results in an overestimate of the percentage scatter for clinical x-ray beams by on average 42%.
2. All orders of Compton and coherent scatter are required to accurately calculate the percentage scatter. The percentage of the first order Compton scatter to the total scatter varies between 32% and 59% depending on tube potential and scattering angle. The percentage of the total coherent scatter to the total scatter varies between 8% and 22% depending on tube potential and scattering angle. The first four orders of scatter produce the majority of the total scatter.
3. There was little difference in the percentage scatter calculated with different tabulations of cross sections. The largest difference was 8% between the percentage scatter calculated with Berger and Hubbell (1987) cross sections (with incoherent scattering) and Storm and Israel (1970) cross sections (with Compton scattering).
4. The focus to surface distance (FSD) had little or no effect on the percentage scatter values calculated. Marshall and Faulkner (1992) found the same result. This result applies where there is no DAP meter or where the scattering angle is less than the angle with which the measurement position aligns with the DAP meter.

5. The inverse square law may be used to estimate the percentage scatter at different distances from the scatterer. If one value is known for example at a distance of 1 m from the scatterer then there will be at most an error of ±14% in the estimated values.
6. There are two maximum values of percentage scatter in the plane 1 m from the phantom which is parallel to the direction of the x-ray beam. The smaller of the two values is at a scattering angle between 45° and 60°. The larger of the two maximum values is at a scattering angle between 120° and 135°. Thus, under couch x-ray tubes will reduce the scatter dose received by staff who are performing interventional procedures on patients. Tube orientation is thus an important factor with the ratio of the over couch and under couch doses being 4 (Faulkner and Moores, 1982).

7.7.3 Factors Affecting the Percentage Scatter

1. Measurements and calculations show that the percentage scatter is dependent on material. There are more Compton scatters and less photoelectric interactions with lower atomic number materials. Thus, the calculated percentage scatter values for WT1 material are larger than for the other materials.
2. Measurements and calculations show that the percentage scatter increases with increasing tube potential for x-rays incident on low atomic number materials. For higher atomic number materials, there is less variation for increasing tube potential and in the case of copper, the percentage scatter decreases.
3. Measurements and calculations show that percentage scatter varies linearly with small field areas. However, the variation of percentage scatter becomes non-linear as the field area increases above 2500 cm^2 for a concrete barrier. There is more

rapid than linear increase in percentage scatter for a 120° scattering angle and a slower than linear increase in percentage scatter for a 150° scattering angle.

4. Calculations show that a WT1 phantom produces the largest contribution (68.9%) to the total scatter at a scattering angle of 135°. However, there are significant contributions to the total scatter from other materials particularly those which lie within the primary beam. Thus, the DAP contributes 17.7%, the air surrounding phantom contributes 9.7% and the room walls, ceiling and floor contribute 3.7% to the total scatter at a scattering angle of 135°.
5. Calculations show that the air surrounding a WT1 phantom has a considerable contribution (42%) to the total scatter compared to the contribution from the phantom (58%) at an 87° scattering angle.
6. Trout and Kelley (1965) showed that there was a significant amount of scatter from the x-ray collimator system. The collimators are not included in the XYZSCAT calculation model. Therefore, the collimator scatter was estimated as the difference between the measured and calculated percentage scatter. Thus, the contribution to the total measured scatter from the collimators was approximately 24%. A similar estimate of collimator scatter was found by comparing calculations with Williams' (1996) measurements.

Chapter 8: Applications of the Monte Carlo Models

8.1 Introduction

Two applications of the Monte Carlo codes are studied in this chapter. Firstly, the VOXSCAT code is used to calculate scatter from a patient. This code is thus a valuable tool as different experimental configurations can be investigated which would not be possible in the clinic. Secondly, the XYZSCAT code is used to calculate scatter behind a protective screen at the radiographers console. Instantaneous doses are difficult to measure at this position in the x-ray room.

8.1.1 Applications of the VOXSCAT Code

The VOXSCAT code is used to calculate the scatter produced by a patient undergoing chest PA, lumbar spine AP and lumbar spine LAT radiographic examinations. Three different studies have been undertaken for these three examinations and are detailed below:

Study 1: the VOXSCAT code is used to calculate the scatter for four different patient models. The first model is a thick slab phantom. The second model is a slab phantom specified by the average dimensions of the Yale voxel phantom. The third model is a homogeneous phantom whose outline corresponds to that of the human body. The fourth model is the Yale voxel phantom. The effect of the obliquity of the human body and the effect of the tissue inhomogeneities are studied.

Study 2: the VOXSCAT code is used to calculate the effect on the patient scatter of varying the imaging parameters: tube potential, filtration and voltage ripple.

Study 3: the VOXSCAT code is used to calculate the effect on the patient scatter of varying the field size.

8.1.2 Applications of the XYZSCAT Code

Sutton and Williams (2000) provide worked examples for a wide variety of shielding problems which may be encountered in practice. However, they only give limited advice on the common shielding problem of how to estimate the dose behind the protective screen at the radiographer's console produced by scatter from the ceiling. Instantaneous dose is difficult to measure and the dose is usually monitored by film badges and/or thermoluminesence detectors (TLDs) over a period of time (e.g. a month). Therefore, it is difficult to determine the contributions to the total dose from different individual examinations undertaken in the x-ray room (Faulkner and Moores, 1982). Hence, a benefit of Monte Carlo modeling is that they can provide data in these situations. The doses calculated by the XYZSCAT code are compared to the doses calculated by a frequently used 'rule of thumb' method (BSI, 1971). Furthermore, as an example of the practical benefit of Monte Carlo modeling, it is determined whether an entrance to the x-ray room behind the protective screen (acting as a secondary radiation barrier) is required to be further protected with a lead lined door.

8.2 Scatter from a Patient

8.2.1 X-ray Imaging Systems

X-ray examinations are used to aid the diagnosis of disease in a patient. The radiographic technique determines the physical image quality and dose to the patient. The CEC Quality Criteria Document (Carmichael et al., 1996) provides a list of good radiographic techniques for common x-ray examinations, for example using a tube potential of 125 kV in chest radiography. If the tube potential is increased then the patient dose is reduced but so too is the image quality. The physical contrast and signal-to-noise ratio (SNR) of features in the image will decrease for increasing tube potential. In this case, a higher tube potential may not be advantageous. Therefore, optimisation is required to obtain the technique factors that provide the best combination of high image quality with low dose.

Although it is worthwhile to optimise technique factors, radiographic practice varies from centre to centre and thus, in order to provide comprehensive data for protecting against scattered radiation, a large range of different technique factors have to be investigated. The scatter has therefore been calculated for different tube potentials, x-ray tube filtrations, voltage ripples and field sizes for chest and lumbar spine examinations.

	Imaging System Parameters	
Parameter Type	**Chest**	**Lumbar Spine**
Tube Potential (kV)	141	72 (for AP projection), 77 (for LAT projection)
Filtration (mmAl)	5.7	4.7
Target Angle (°)	15	12
Voltage Ripple (%)	0	0
Focus Film Distance (m)	1.50	1.46
Focus Surface Distance (m)	1.27	1.12 (for AP projection) 0.98 (for LAT projection)
Field Size at FSD (mm × mm)	306 × 212	275 × 109 (for AP projection) 234 × 92 (for LAT projection)
Chest Stand/Couch Top	6.0 mm of wood	1.2 mm Al

***Table 8.1**. The parameters for the chest and lumbar spine imaging systems.*

Figure 8.1 shows the model for the calculation of scatter which is simpler than the one described in section 6.5. It includes the x-ray spectrum from the x-ray tube, the patient and the couch top or chest stand. The grid and the imaging system are not included in the model. This has two effects which should be noted. Firstly, the scatter from the grid and cassette are assumed to be negligible. The patient and the chest stand or couch top attenuate the x-ray beam. Monte Carlo calculations show that their primary transmission is less than 10% for the chest PA view and approximately 1% for the lumbar spine AP view. Therefore, there will be few photons incident on the grid and cassette front and thus, these devices will produce only a small contribution to the total scatter. Secondly and more importantly, the grid and cassette front significantly attenuate the forward directed scatter produced by the patient. Therefore as they are not included in the model, the percentage scatter calculated is a conservative estimate of the clinical situation.

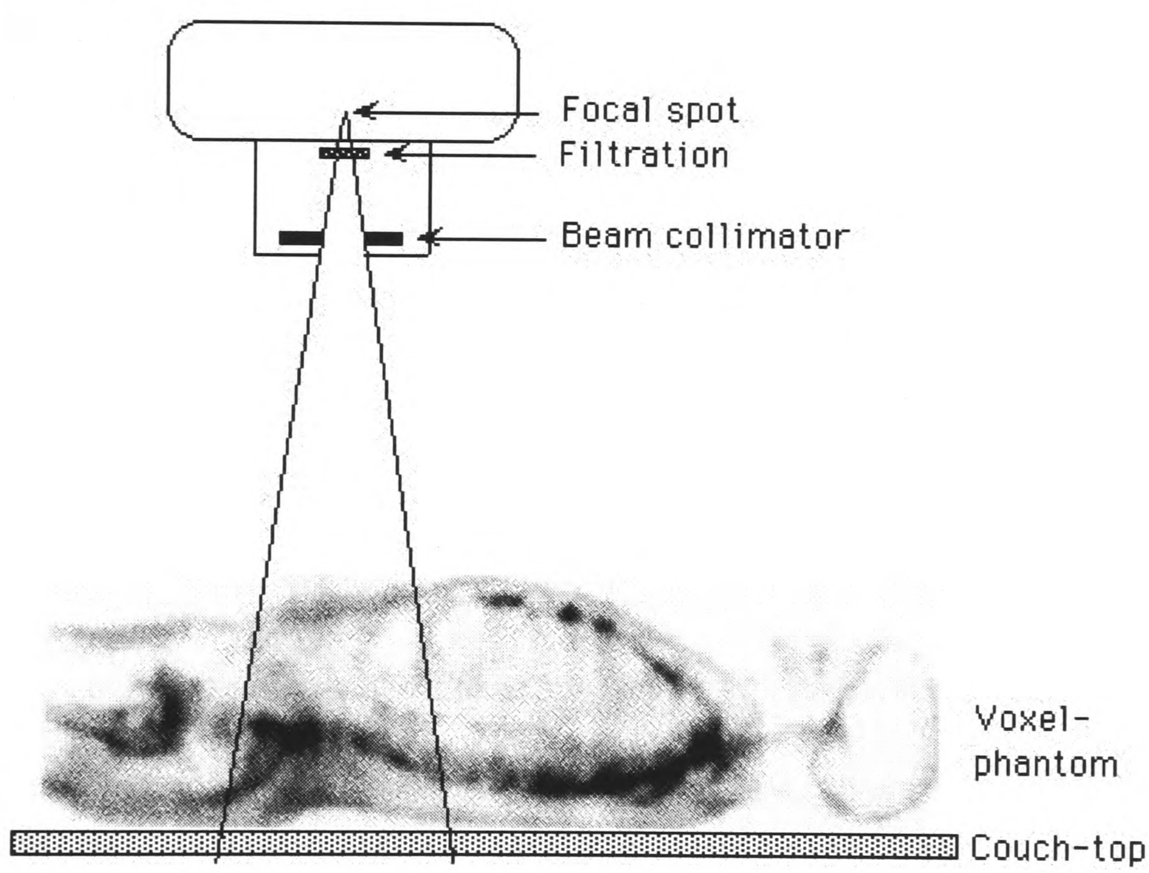

Figure 8.1*. The Monte Carlo model used in the VOXSCAT code for the calculation of patient scatter.*

The imaging system parameters for this study are given in table 8.1. These imaging parameters are those which were found to provide good image quality in a recent EU clinical trial (Almén et al., 2000; Lanhede et al., 2000) and are thus used as a reference system to observe the differences in patient scatter when the imaging parameters are varied. The scatter is calculated at 45° and 120° scattering angles as these angles are representative of forward and backward directed scatter (section 7.2.2.6).

8.2.2 Influence of the Phantom Type

	Slab Phantom Dimensions for Different Examinations		
Examination	**Length (mm)**	**Width (mm)**	**Thickness (mm)**
Chest PA	899	220	160
Lumbar Spine AP	899	240	180
Lumbar Spine LAT	899	180	244

Table 8.2. *The dimensions of the slab phantom with the average dimensions of the patient model. The phantom thickness includes the chest stand or couch top.*

Homogeneous slab phantoms are frequently used to represent the patient in either measurements or calculations (Chapter 7). However, a patient is heterogeneous and has a variable contour. Hence, the differences in scatter from slab phantoms and the patient have been studied. This was carried out in three steps. In the first step, the scatter was calculated for a thick slab phantom defined with all voxels apart from the chest stand or couch top set to be average soft tissue. The phantom dimensions are 899 mm long, 356 mm wide and 200 mm thick (section 6.5.1). In the second step, the scatter was calculated for a homogeneous contoured phantom which was defined with all the voxels inside the patient's surface boundary set to average soft tissue and those outside the boundary set to air. In the third step, the scatter was calculated with the heterogeneous patient model. A further scatter calculation used a slab phantom with the dimensions defined by the average thickness (z direction) and width (y direction) of the patient model within the field size for each projection as given in table 8.2. These calculations were undertaken as the shoulder width is considerably larger than the width further down the human body. Thus, the phantom's width and thickness are smaller than those used in step 1.

8.2.2.1 Results for the Different Phantoms

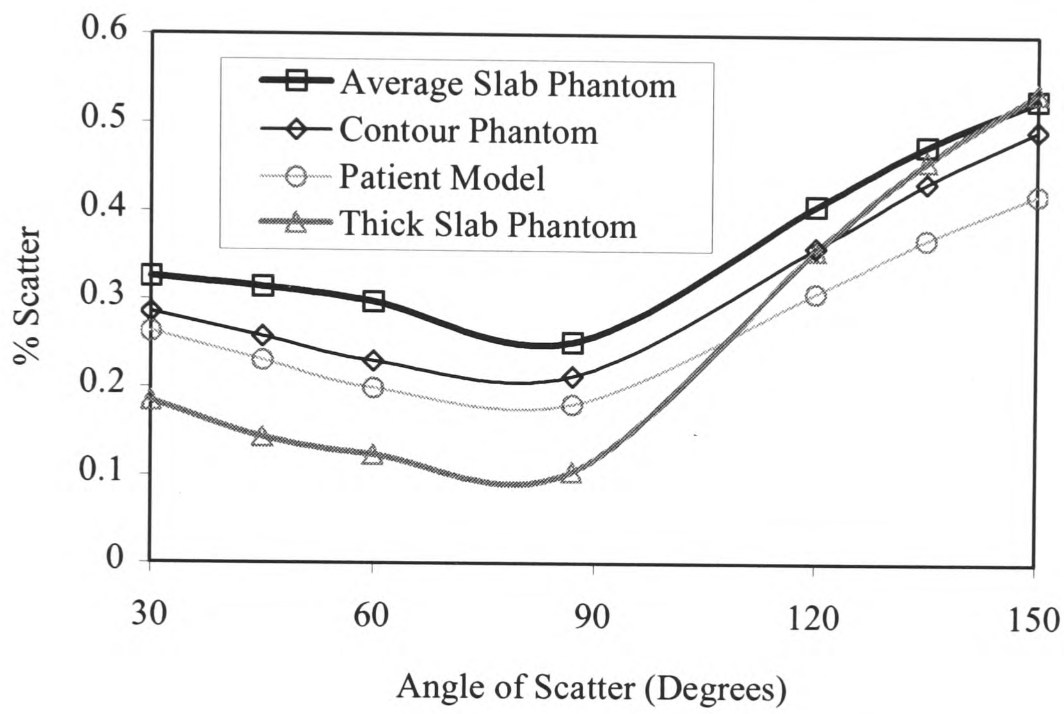

A

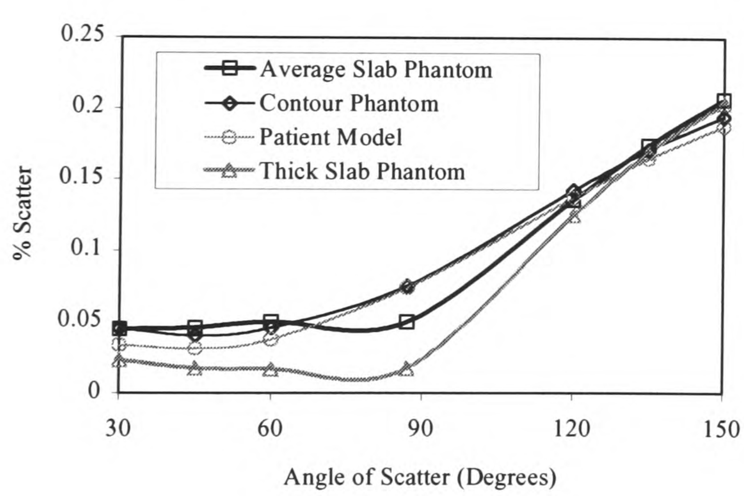

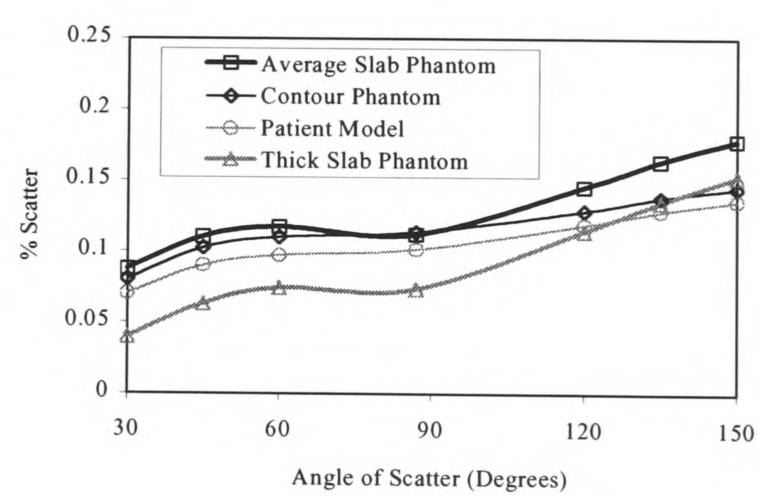

B *C*

***Figure 8.2**. The variation of the percentage scatter with different phantoms for (A) the chest PA projection, (B) the lumbar spine AP projection and (C) the lumbar spine LAT projection.*

Figure 8.2 shows the percentage scatter calculated with the four phantoms for the three examinations. For the chest PA projection, the scatter from the patient and the contoured phantom lie between the values for the two slab phantoms for scattering angles below 120°. This occurs only for angles of scatter below 60° for the lumbar spine AP projection and between 30° and 120° scattering angles (except for 87°) for the lumbar spine LAT projection. Therefore, the phantoms with the average dimensions (table 8.2) can provide a conservative estimate of the scatter from a patient for most angles of scatter.

Phantom Type	Percentage Scatter for a 45° Scattering Angle		
	Chest PA Exam	**Lumbar Spine AP Exam**	**Lumbar Spine LAT Exam**
Thick Slab Phantom	0.62	0.56	0.70
Contoured Phantom	1.12	1.29	1.14
Patient Model	1.00	1.00	1.00
Slab Phantom with Average Dimensions	1.36	1.46	1.22
Phantom Type	**Percentage Scatter for a 120° Scattering Angle**		
	Chest PA Exam	**Lumbar Spine AP Exam**	**Lumbar Spine LAT Exam**
Thick Slab Phantom	1.16	0.91	0.96
Contoured Phantom	1.17	1.04	1.08
Patient Model	1.00	1.00	1.00
Slab Phantom with Average Dimensions	1.32	0.99	1.22

***Table 8.3**. Percentage scatter for different phantom types relative to the percentage scatter for the patient for the three examinations.*

Table 8.3 shows that the scatter from the different phantom types varies the greatest in the forward direction. The largest variations are for the lumbar spine AP projection due to it having the lowest tube potential. The thick slab phantom produces the least scatter as it attenuates the scattered x-rays the most. The contoured phantom produces more scatter than the thick slab phantom in the forward direction as the phantom's obliquity attenuates the scattered x-rays less. The slab phantom with average dimensions produces more scatter due to its smaller dimensions. The patient produces less scatter than the contoured phantom in the forward direction. Bone attenuates the scattered x-rays more than soft tissue. In the chest projection, the lung produces less scatter and also attenuates scatter less than soft tissue due to its lower density. For the lumbar spine LAT projection, the differences are not as large as would be expected for the large thickness of the patient. This is due to the edge of the radiation field being closer to the phantom boundary and thus, the scattered x-rays are not greatly attenuated.

Table 8.3 shows that the phantom dimensions have less effect on the variation of scatter in the backward direction than in the forward direction. A large percentage of the total scatter is produced near the entrance surface of the phantoms (section 5.8.1). The effect of the tissue inhomogeneities in the backward direction is similar to their effect in the forward direction.

Figure 8.2 shows that the chest PA projection produces more patient scatter than the other two projections. This technique has the highest tube potential and largest field size with the lungs attenuating scatter less than soft tissue. The lumbar spine AP projection produces the least patient scatter in the forward direction as it has the lowest tube potential. The lumbar spine AP projection produces more scatter in the backward direction than the LAT projection as it has a larger field size.

8.2.3 Influence of Technique Factors

8.2.3.1 Effect of Tube Potential

Table 8.4 shows the variation of percentage scatter normalised to the reference system values for x-ray tube potentials between 60 and 150 kV for the different examinations.

kV	Percentage Scatter Relative to the Reference Imaging System Values					
	45° Scattering Angle			120° Scattering Angle		
	Chest PA Projection	Lumbar Spine AP Projection	Lumbar Spine LAT Projection	Chest PA Projection	Lumbar Spine AP Projection	Lumbar Spine LAT Projection
60		0.64			0.87	
70		0.91	0.90		0.97	0.94
72		1.00			1.00	
77			1.00			1.00
80		1.23	1.05		1.06	1.04
90	0.68	1.51	1.17	0.89	1.15	1.10
95			1.22			1.12
102	0.76			0.92		
110	0.83	1.97	1.36	0.94	1.23	1.18
130	0.95			0.99		
141	1.00			1.00		
150	1.03			1.01		

***Table 8.4**. The variation of percentage scatter from the patient for different tube potentials normalised to the scatter values for the reference imaging systems.*

The largest variation with tube potential is for forward directed scatter in all projections. The forward directed scatter becomes more penetrating with increasing tube potential. There is less variation of scatter in the backward direction as most of the scatter is produced close to the entrance surface (section 5.8.1). The scatter for the lumbar spine AP projection has the largest variation of all the projections studied as the reference system has the lowest tube potential of 72 kV. The forward directed scatter increases by a factor of 2 for an increase in tube potential of 38 kV. The scatter for the LAT projection varies less than the scatter for the AP projection. The LAT reference system uses a higher tube potential (77 kV) and its field is positioned close to the patient's edge. The scatter for chest PA projection varies by less than both the lumbar spine projections. The chest reference system uses the highest tube potential (141 kV) and the lung tissue attenuates the scatter less than the soft tissue. If the scatter for both the lumbar spine examinations is normalised to the scatter value for 70 kV, then their variation with tube potential is similar to that observed with the WT1 slab phantoms for backward directed scatter (section 7.2.3.1).

8.2.3.2 Effect of Filtration and Voltage Ripple

	Percentage Scatter Normalised to Reference Values for a 45° Scattering Angle								
	Chest PA Exam			**Lumbar Spine AP Exam**			**Lumbar Spine LAT Exam**		
Filtration (mmAl)	**2.5**	**5.7**	**7.0**	**2.5**	**3.5**	**4.7**	**2.5**	**3.5**	**4.7**
% Voltage Ripple									
0	0.80	1.00	1.06	0.70	0.84	1.00	0.80	0.92	1.00
5	-	0.99	-	-	-	0.94	-	-	0.98
20	-	0.96	-	-	-	0.85	-	-	0.94
50	-	0.90	-	-	-	0.78	-	-	0.90
	Percentage Scatter Normalised to Reference Values for a 120° Scattering Angle								
	Chest PA Exam			**Lumbar Spine AP Exam**			**Lumbar Spine LAT Exam**		
Filtration (mmAl)	**2.5**	**5.7**	**7.0**	**2.5**	**3.5**	**4.7**	**2.5**	**3.5**	**4.7**
% Voltage Ripple									
0	0.89	1.00	1.03	0.83	0.91	1.00	0.84	0.93	1.00
5	-	1.00	-	-	-	0.98	-	-	0.99
20	-	0.99	-	-	-	0.94	-	-	0.97
50	-	0.98	-	-	-	0.91	-	-	0.94

Table 8.5. *The variation of percentage scatter from the patient for different filtrations and voltage ripples normalised to the reference system scatter values.*

Table 8.5 shows the variation of scatter for different filtrations and different peak voltage ripples. The filtrations were varied between 2.5 mmAl and 7.0 mmAl for the chest PA examination and between 2.5 mmAl and 4.7 mmAl for the lumbar spine examinations. The voltage rectifications were varied between 0% and 50% ripple. The variation of scatter is smaller for changing the tube filtration than for changing the tube potential. There is a similar effect on the scatter of changing the voltage ripple as for the tube filtration. The scatter increases for decreasing voltage ripple as the x-rays become more penetrating. However, replacing an old x-ray generator with significant voltage ripple with a new medium frequency x-ray generator will not produce a significantly more scatter.

The percentage scatter for the lumbar spine AP projection has the largest variation with filtration and voltage ripple. The percentage scatter in the forward direction decreases by 15% if the filtration decreased by 1.2 mmAl or the voltage ripple is decreased by 20%. The variations in percentage scatter for the lumbar spine LAT and chest PA projections are less due to their higher beam qualities. Similar variations in the percentage scatter are observed with changing the filtration and voltage ripple at tube potentials of 102 kV, 90 kV and 95 kV for the chest PA, lumbar spine AP and lumbar spine LAT projections respectively. Hence, the variations shown in table 8.5 are applicable over a large range of tube potentials.

8.2.4 Effect of Field Size

8.2.4.1 Square Field Sizes

	Percentage Scatter for a 10cm × 10cm Field Size	
Examination	**45° Scattering Angle**	**120° Scattering Angle**
Chest PA	0.035	0.049
Lumbar Spine AP	0.011	0.048

Table 8.6. *The percentage scatter for the chest PA and lumbar spine AP reference imaging systems with 100 cm^2 field sizes.*

The percentage scatter from slab phantoms varies linearly with incident field area (section 7.2.3.2). Therefore, it is of interest to study the variation of scatter from the patient and to observe if it also varies linearly with field area. Table 8.6 shows the scatter values for a 100 cm^2 field area which are used to normalise the scatter values for the different field areas. All the reference system parameters for each projection as shown in table 8.1 have been employed except for the field size.

		Percentage Scatter Normalised to the Value for a 10cm × 10cm Field Size at a 45° Scattering Angle	
Field Size (cm × cm)	**Expected Values**	**Chest PA Projection**	**Lumbar Spine AP Projection**
5×5	0.25	0.25	0.21
10×10	1.00	1.00	1.00
15×15	2.25	2.20	2.86
20×20	4.00	4.07	7.55
25×25	6.25	6.90	11.92
30×30	9.00	9.45	14.52
35×35	12.25	11.64	17.38
		Percentage Scatter Normalised to the Value for a 10cm × 10cm Field Size at a 120° Scattering Angle	
Field Size (cm × cm)	**Expected Values**	**Chest PA Projection**	**Lumbar Spine AP Projection**
5×5	0.25	0.26	0.25
10×10	1.00	1.00	1.00
15×15	2.25	2.22	2.25
20×20	4.00	3.94	3.86
25×25	6.25	6.01	5.19
30×30	9.00	7.78	6.13
35×35	12.25	9.34	7.16

Table 8.7. *Percentage scatter for different square field sizes relative to the percentage scatter for a 100 cm^2 field size.*

Table 8.7 shows the variation of the normalised percentage scatter with square field areas between 25 and 1225 cm^2 for tube potentials of 141 kV and 72 kV for the chest PA and lumbar spine AP projections. The expected values show the linear relationship of scatter with field area. It can be seen that the linear relationship between the percentage scatter and field area does not always hold for scatter from the patient. For the chest PA projection, the normalised scatter values for a 625 cm^2 field area are 10.5% higher than the expected values for a scattering angle of 45°. The differences between the normalised percentage scatter and the expected values are even larger for the lumbar spine due to the low tube potential used. For a 625 cm^2 field area, the normalised scatter values are 90.7% higher and 17.0% lower than their expected values at scattering angles of 45° and 120° respectively. For the lumbar spine AP projection, the forward directed scatter increases more rapidly than expected for increasing field area because of the lower attenuation at the patient obliquities. There is less effect on the forward directed scatter for the chest PA projection due to the higher tube potential. The backward directed scatter is lower than expected due to the lack of tissue at the patient obliquities.

Figure 8.3 compares the normalised scatter values at a 45° scattering angle calculated by the VOXSCAT code for the chest PA (141 kV) and lumbar spine AP (72 kV) projections to the values given by Trout and Kelley (1972). There is a similar increase in the scatter for the calculated values at 141 kV and for Trout's values between 100 and 150 kV. Trout and Kelley's values for 70 kV x-rays are significantly larger than the calculated values for 72 kV. Trout's scatter data for the low tube voltage x-rays was produced with a self-rectified generator. These x-rays have a significantly lower penetrating power than the simulated x-rays and thus, are more affected by the patient obliquity. The rate of increase in the calculated scatter is lower than Trout and Kelley's above a field size of 25 cm × 25 cm as the patient simulated is approximately 25 cm wide in the lumbar region whereas the phantom used in Trout and Kelley's work was 30 cm wide (table 7.15).

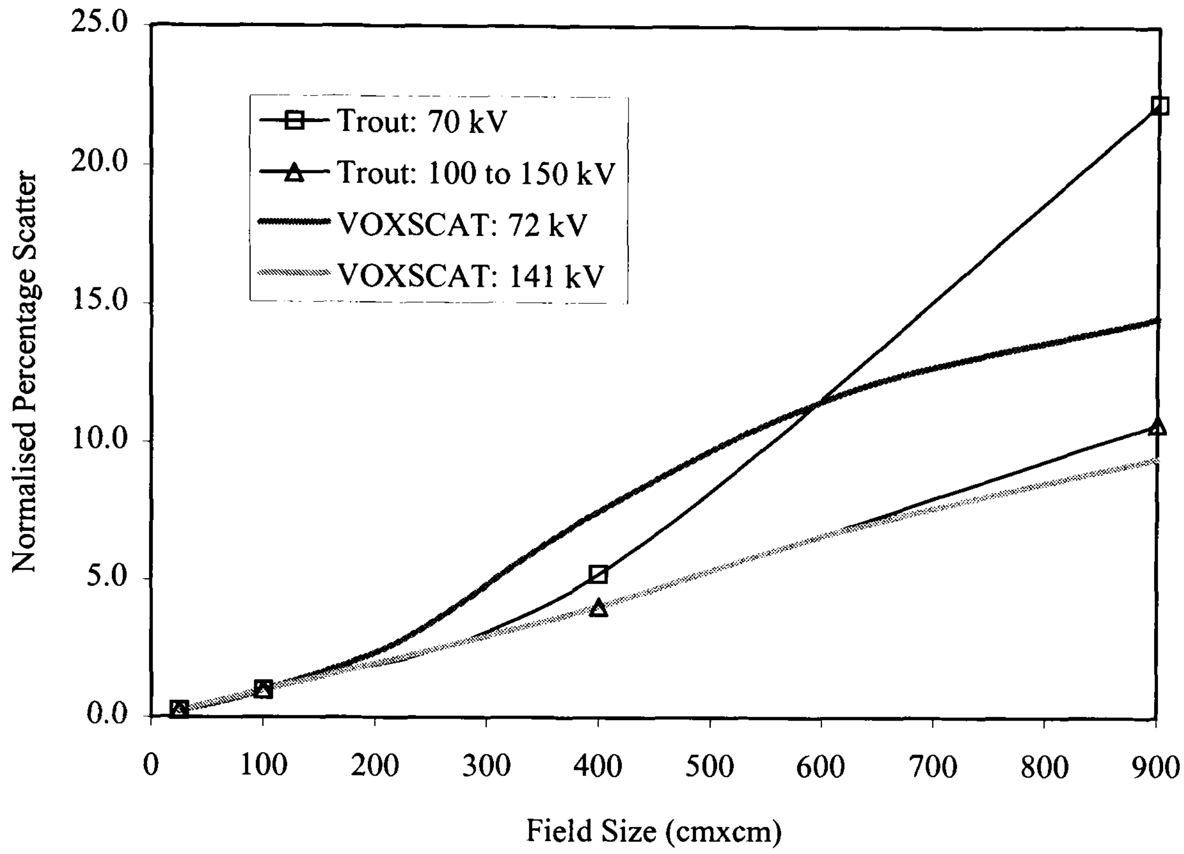

Figure 8.3. *The comparison of the percentage scatter, normalised to the value for a field size of 100 cm^2, at a 45° scattering angle calculated by the VOXSCAT code with the values given by Trout and Kelley (1972).*

8.2.4.2 Rectangular Field Sizes

Figure 8.4 shows the variation of the normalised percentage scatter at a 45° scattering angle with square and rectangular field sizes between 25 and 900 cm^2 for the chest PA projection. The field length was kept constant at 30 cm and the width increased from 5 to 30 cm.

The rectangular field produces less scatter than the square field for the same field area. For example, the difference in the percentage scatter is 13.1% between the rectangular and square fields with areas of 300 cm^2. For the rectangular field, the scattered x-rays are more attenuated as the smaller width covers thicker parts of the patient model. For the square field, the scattered x-rays are less attenuated as the field edge is closer to the patient obliquity. The variation of scatter with increasing field size is similar for both the square and rectangular field sizes in the backward direction.

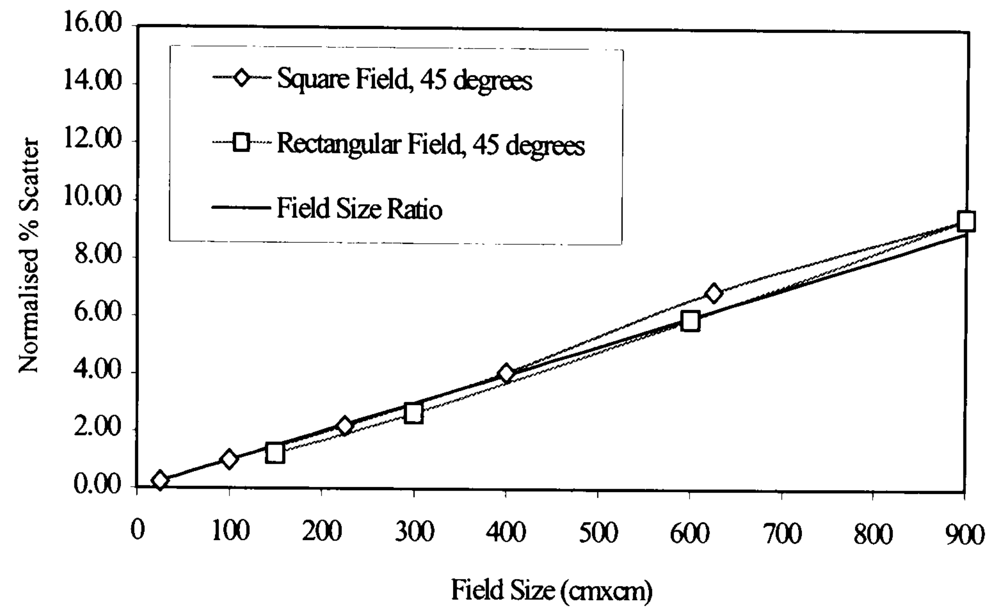

Figure 8.4. *The variation of the normalised percentage scatter at a 45° scattering angle with square and rectangular field sizes between 25 and 900 cm² for the chest PA projection.*

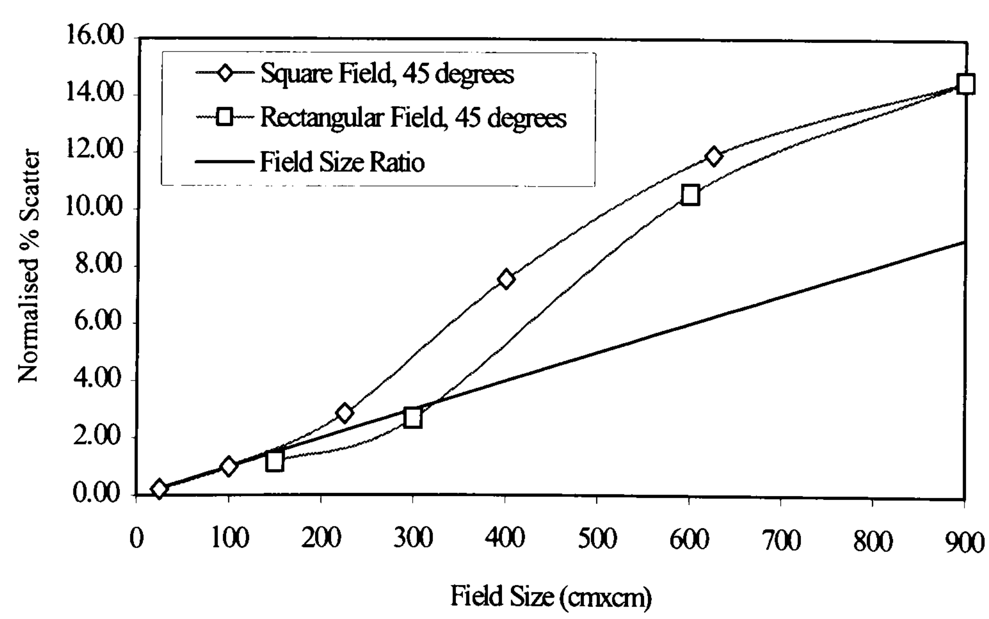

Figure 8.5. *The variation of the normalised percentage scatter at a 45° scattering angle with square and rectangular field sizes between 25 and 900 cm² for the lumbar spine AP projection.*

Figure 8.5 shows there is a greater difference in the normalised percentage scatter between rectangular and square fields for the lumbar spine AP projection than for the chest PA projection. For example, the difference is 82% between the rectangular and square fields with areas of 300 cm^2. The difference is larger as the scatter is more attenuated due to the low tube potential used for the lumbar spine AP projection.

8.2.4.3 Effect of Field Position on the Patient

Table 8.8 shows the percentage scatter for the lumbar spine LAT projection with the field centre positioned at the same place as the reference system (close to the patient's lateral boundary) and with the field centre positioned at the centre of the patient's width. The position of the field centre has a considerable effect on the scatter values. The scatter at the 45° scattering angle is 2.3 times larger with the field centred on the patient's obliquity as there is less tissue to attenuate the scattered radiation than the field centred on a thicker part of the patient. Trout and Kelley (1972) found that the scatter for the field centred at the phantom's edge was between 6.5 and 1.8 times larger than the scatter for the field positioned at the centre of the phantom's width for tube potentials between 50 and 150 kV at a 45° scattering angle.

	Percentage Scatter for a 10cm × 10cm Field Size	
Field Centre Position	**45° Scattering Angle**	**120° Scattering Angle**
Reference System Position	0.048	0.058
Centre of Patient's Width	0.021	0.041

Table 8.8. *The percentage scatter for the lumbar spine LAT imaging system centred at the reference system position and at the centre of the patient's width with 100 cm^2 field sizes.*

Table 8.9 shows the variation of scatter with square field sizes between 25 and 225 cm^2 for a tube potential of 77 kV with the field centred at the same position as for the lumbar spine LAT reference system and with the field centred at the centre of the patient's width.

		Percentage Scatter Normalised to the Value for a 10cm × 10cm Field Size at a 45° Scattering Angle	
Field Size (cm × cm)	**Expected Values**	**Reference System Position**	**Centre of Patient's Width**
5×5	0.25	0.20	0.20
10×10	1.00	1.00	1.00
15×15	2.25	1.61	3.38
		Percentage Scatter Normalised to the Value for a 10cm × 10cm Field Size at a 120° Scattering Angle	
Field Size (cm × cm)	**Expected Values**	**Reference System Position**	**Centre of Patient's Width**
5×5	0.25	0.26	0.26
10×10	1.00	1.00	1.00
15×15	2.25	1.63	2.29

Table 8.9. *The percentage scatter for different square field sizes relative to the percentage scatter for a 100 cm² field size for the lumbar spine LAT projection. The first set of results has the field size centred at the reference system position. The second set of results has the field size centred at the centre of the patient's width.*

Table 8.9 shows that the normalised scatter values for a field area of 225 cm² are 28.5% and 27.4% lower than the expected values at scattering angles of 45° and 120° respectively for the field centred at the reference system position. The scatter values are lower than expected as the field edge is over the patient's obliquity. For the field positioned at the centre of the patient's width, the scatter values for a field area of 225 cm² are 50.2% higher and 1.6% higher than the expected values at scattering angles of 45° and 120° respectively. There is a larger than expected variation of scatter at the 45° scattering angle as the field is centred on a thick part of the patient and as the field area increases the field edge gets closer to the patient obliquity. There is the expected variation of scatter with field size for the 120° scattering angle as the field is centred on the thick part of the patient.

8.3 Scatter behind a Protective Screen at a Radiographer's Console

8.3.1 Model of the X-ray Room

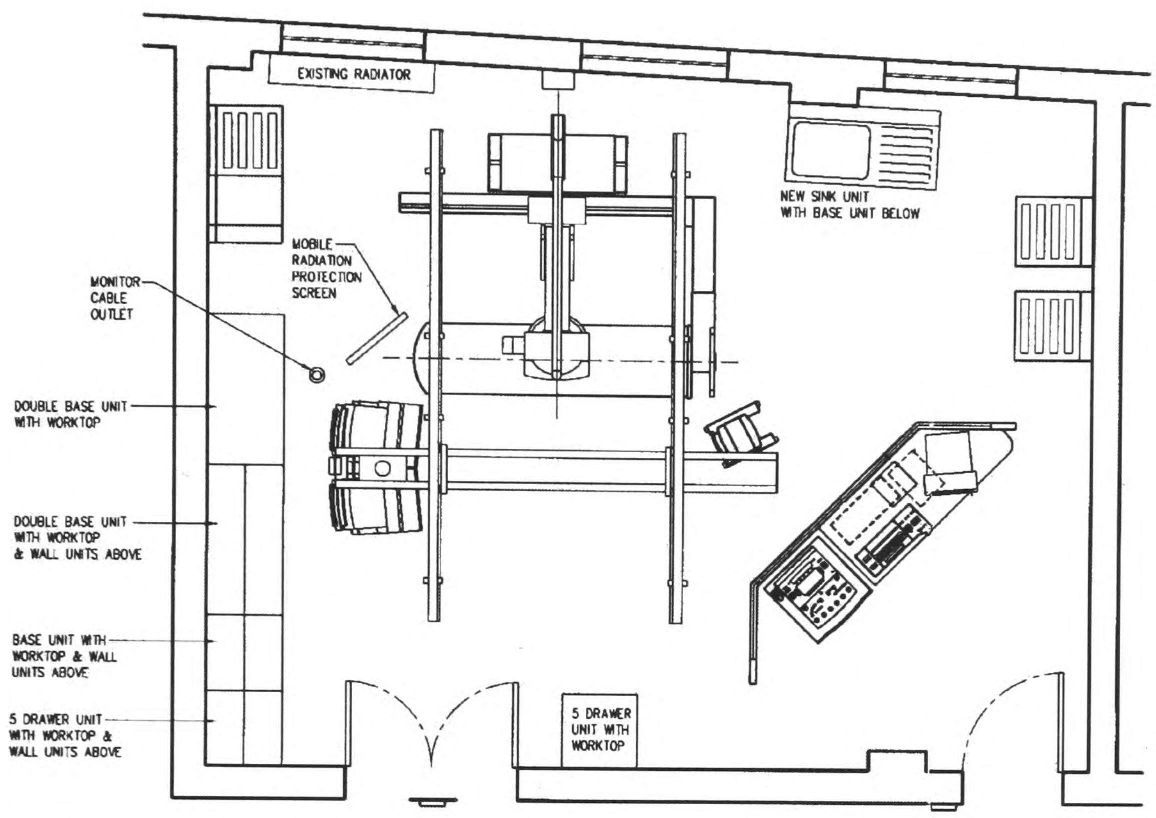

Figure 8.6*. The fluoroscopy room layout containing a Philips C-arm x-ray set at the Royal Marsden Hospital, London.*

A fluoroscopy room at the Royal Marsden Hospital, London was modeled with the XYZSCAT code and the dose calculated at an x-ray room entrance behind the protective screen at the radiographer's console. Figure 8.6 shows the fluoroscopy room containing a Philips C-arm x-ray set. Figure 8.7 shows the model of the room design used with the XYZSCAT code and shows two modifications to the original design. The first modification was that the screen was extended to be in contact with the right hand wall. This was changed after the plan shown in figure 8.7 was drawn due to concerns about the amount of scattered radiation reaching behind the radiographer's console from the right hand wall. The second modification was due to the rigid voxel geometry used with the XYZSCAT code. The diagonal section of the protective screen cannot be modeled and therefore, the screen was modeled as rectangular slabs. In order to study the effect of the second modification on the room design, the scatter at the x-ray room entrance was calculated for varying the position of the protective screen (section 8.3.2.1).

The patient's torso was modeled as a slab of average soft tissue (90 cm long, 22 cm wide and 18 cm thick). The patient's dimensions were chosen to be similar to the slab phantoms shown in table 8.2. The patient is supported on a carbon fibre couch top (220 cm long, 56 cm wide and 1 cm thick). The centre of the phantom is 110 cm above the floor and 278 cm from the left hand wall (figure 8.7). The calculation model includes a DAP meter (PTW type B) as it is used to monitor the patient dose. It is positioned 27 cm in front of the x-ray tube focus. The walls, ceiling and floor of the x-ray room are assumed to be constructed of concrete with a density of 2.35 g/cm^3 and are 20 cm thick. The false ceiling is constructed of 1.3 cm thick plywood with a density of 0.3 g/cm^3 and is suspended 52 cm below the actual concrete ceiling. The screen in front of the radiographer's console is 2 mm lead equivalent and has a height of 200 cm (Sutton and Williams, 2000) which is the same height as the x-ray room entrance. No door was modeled at the room entrance because a wooden door would not significantly attenuate the scattered x-rays and would only produce a small amount of back scatter to positions behind the protective screen. The dimensions of the x-ray room were 533 cm long, 705 cm wide and 341 cm high (including above the false ceiling).

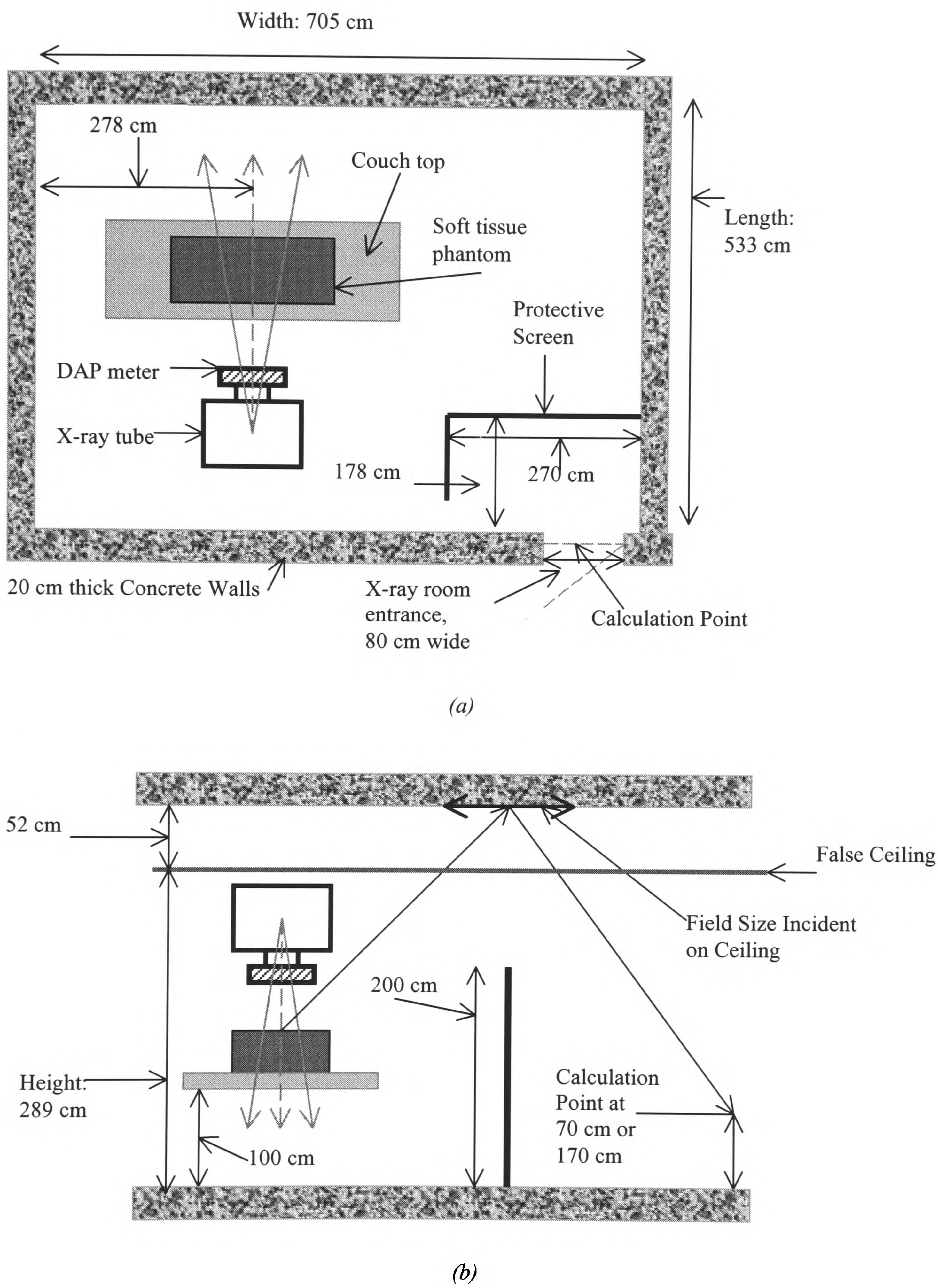

***Figure 8.7**. The XYZSCAT model of the Philips fluoroscopy room in (a) the over head view with the x-ray tube in a lateral orientation and (b) the lateral view with the x-ray tube in the over couch orientation. The patient access to the x-ray room is not included in the model.*

Material	Density (gcm^{-3})	Elemental Composition (Percentage by mass)												
		H	C	N	O	Na	Mg	Al	Si	S	Ar	K	Ca	Fe
Air	0.1205	0	0	78.0	21.0	0	0	0	0	0	0.9	0	0	0
Soft Tissue	1.00	10.1	11.1	2.6	76.2	0	0	0	0	0	0	0	0	0
Concrete	2.35	0.6	0	0	49.8	1.7	0.4	4.6	31.6	0.1	0	1.9	8.3	1.2
Perspex	0.319	8.0	60.0	0	32.0	0	0	0	0	0	0	0	0	0
Carbon Fibre or Wood	0.50 or 0.30	6.2	44.4	0	49.3	0	0	0	0	0	0	0	0	0

Table 8.10*. The compositions and densities of materials used in the XYZSCAT model of the Fluoroscopy room at the Royal Marsden Hospital, London.*

The composition and density of the materials used in the XYZSCAT model are shown in table 8.10. The data for average soft tissue was obtained from ICRU (1992a) and the data for wood and carbon fibre were obtained from NPL (1993). Under couch, over couch and lateral orientations of the x-ray tube were simulated for the barium enema, barium swallow and other interventional procedures. Each examination constituted a third of the total examinations performed in the x-ray room. The frontal views are obtained with the x-ray tube underneath the couch top. The x-ray tube would not normally be used in an over couch orientation but it has been included for completeness. The imaging parameters for the different examinations and orientations are given in table 8.11 and were obtained from the manufacturer, Philips. The Philips x-ray tube is assumed to have a 13° target angle and 3.4 mmAl total filtration (section 3.2.1). Table 8.11 shows the entrance dose rates to the patient for continuous fluoroscopy as specified by the manufacturer and the annual total dose to the patient. The total dose has been estimated by summing fluoroscopy times for all patients undergoing fluoroscopy in one year. Large field sizes were used in the

XYZSCAT calculations to produce a large amount of scatter and hence provide a conservative estimate of the dose at the x-ray room entrance. For a C-arm x-ray set, there is an image intensifier present behind the phantom which has 2 mm lead equivalence in order to absorb primary radiation. The intensifier has not been modeled so that the results of the scatter calculations are also applicable to radiographic rooms.

Parameter Type	Image System Parameters		
	Barium Enema	Barium Swallow	Other Interventional Procedures
Tube Potential (kV)	100	85	90
FSD (cm)	82	87	82
Field Size (cm×cm)	25×25 (Frontal) 25×18 (Lateral)	15×6 (Frontal and Lateral)	25×25 (Frontal) 25×18 (Lateral)
Dose Rate (mGy/min)	90	50	75
Annual Dose (mGy/year)	38360	13560	25310

***Table 8.11**. The imaging parameters for the different examinations.*

8.3.2 Results

The number of photon histories used to calculate the percentage scatter behind the protective screen with the XYZSCAT code was 240×10^6. This achieved a calculation uncertainty of less than ±3% at all positions behind the protective screen.

8.3.2.1 Variation of Percentage Scatter with Distance from the Protective Screen

Figure 8.8 shows a close up of figure 8.6 to demonstrate the layout of the radiographer's console. The solid line is the position of the simulated protective screen as shown in figure 8.7. The depth of the simulated console from the wall with the x-ray room entrance was determined as 178 cm by the position where the actual protective screen intercepted the line between the central axis of the x-ray beam and the centre of the x-ray room entrance. This depth includes the access to the console between the wall and the protective screen of 68 cm. The width of the simulated console area from the right hand wall used the same width of the actual console of 270 cm. As the simulated console is a simplified model of the actual console, the effect of varying the position of the protective screen on the percentage scatter at the x-ray room entrance was studied to ensure that the simulated depth and width of the console area were suitable.

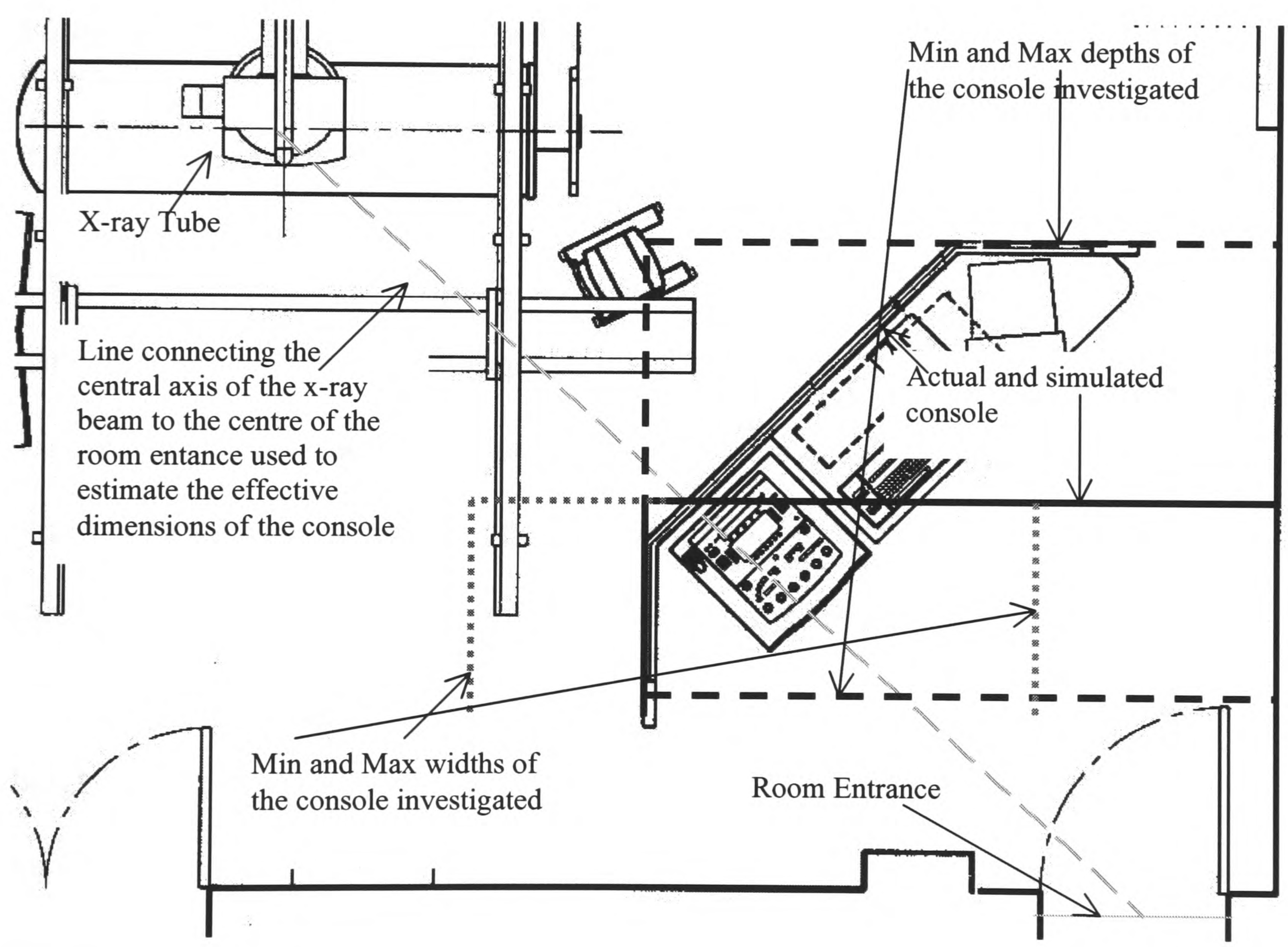

***Figure 8.8**. The planned and simulated positions of the protective screen at the radiographer's console. The minimum and maximum distances of the simulated protective screen from the x-ray room entrance are shown.*

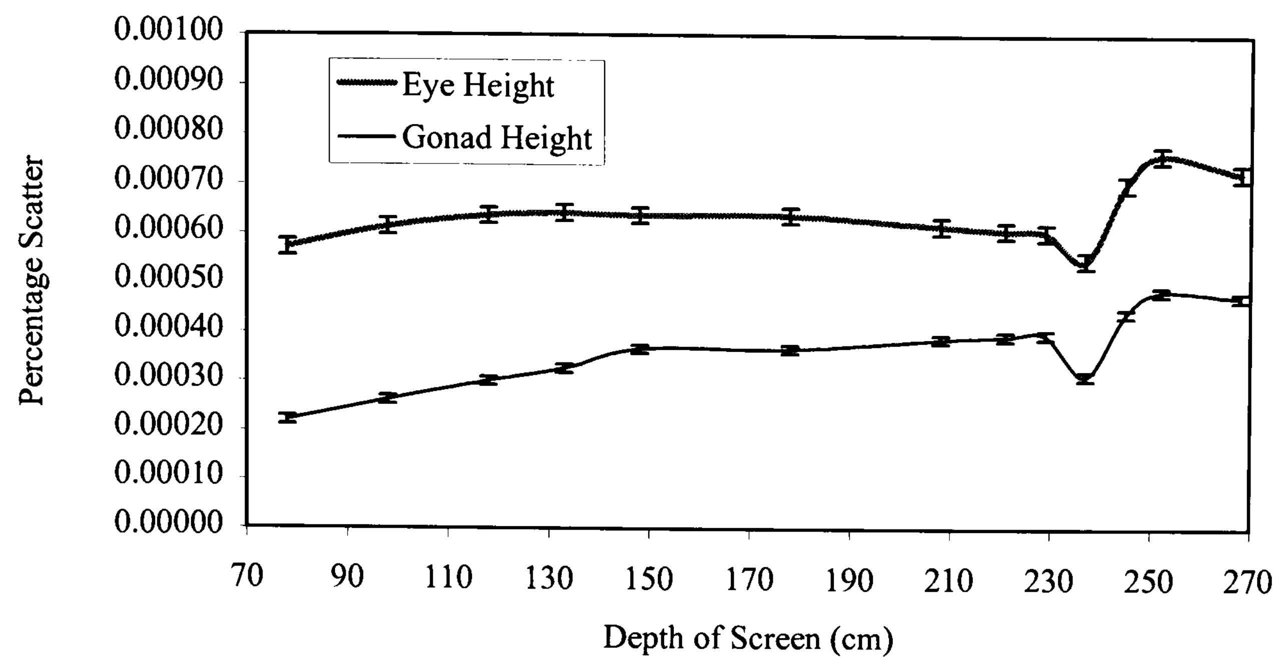

***Figure 8.9**. The variation of percentage scatter at the x-ray room entrance behind the radiographer's console for increasing depth of the protective screen from the wall with the x-ray room entrance. The calculation uncertainties on the individual scatter values are also shown.*

Figure 8.9 shows the variation of the percentage scatter at the x-ray room entrance with the depth of the protective screen from the wall. A barium enema examination was simulated with the x-ray tube in a lateral orientation to the patient. The scatter was calculated at eye height and gonad height for an individual standing in the centre of the x-ray room entrance. The radiosensitive organs in the human body all lie within this range of heights. At the minimum depth investigated of 78 cm, the scatter at eye height is 10% lower and the scatter at gonad height is 40% lower than the scatter values for the screen at a depth of 178 cm. At the maximum depth investigated of 268 cm which is equivalent to the maximum depth of the actual console, the scatter at eye height is 14% higher and the scatter at gonad height is 29% higher than the scatter values for the screen at a depth of 178 cm.

The diagonal section of the actual screen is between depths of 152 cm and 268 cm The scatter at gonad height for the screen at these depths varies between 1 and 1.3

times the scatter for the screen at a depth of 178 cm. Therefore, the simulated screen depth of 178 cm seems to be reasonably representative of the clinical situation. The console area behind the rectangular screen with a depth of 268 cm is larger than the actual console area and hence the scatter reaching the x-ray room entrance may not be as large if a diagonal screen was in place.

Figure 8.9 shows that there are some oscillations of the percentage scatter for the screen at depths between 229 and 245 cm. This is possibly due to the scatter from the DAP meter as it is at a distance of 236 cm from the wall with the x-ray room entrance for the x-ray tube in a lateral orientation. The overall increase in the percentage scatter for increasing depth is probably due to the screen getting closer to the patient which is the primary source of scatter.

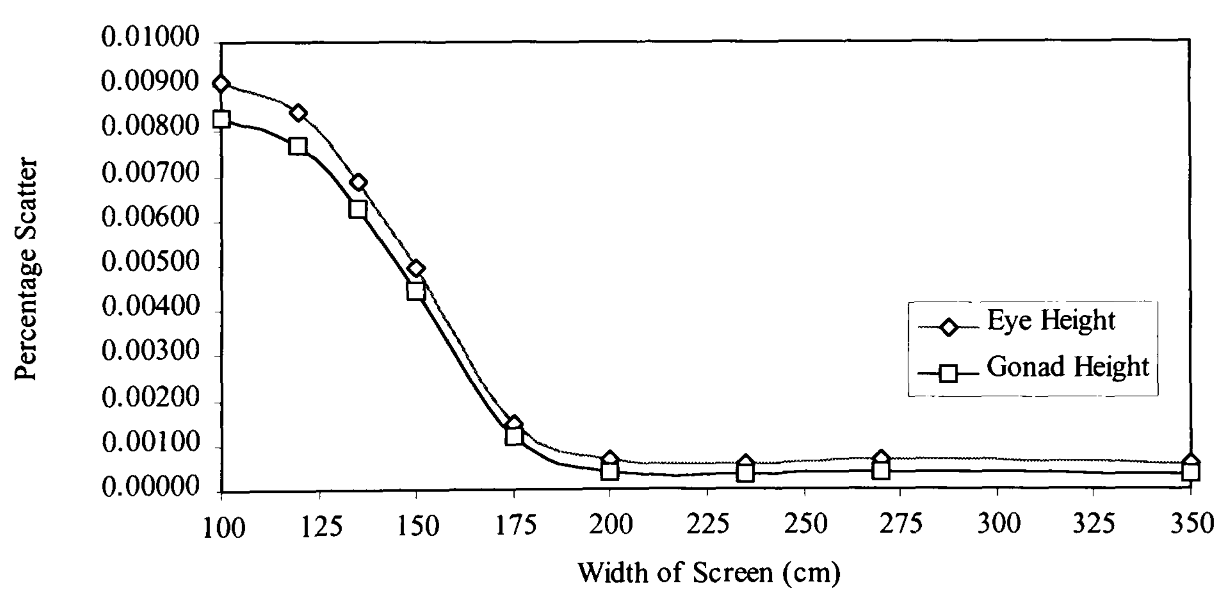

Figure 8.10. *The variation of percentage scatter at the x-ray room entrance behind the radiographer's console for increasing width of the protective screen from the right hand wall.*

Figure 8.10 shows the variation of the percentage scatter at the x-ray room entrance with the width of the protective screen from the right hand wall. A barium enema examination was simulated with the x-ray tube in a lateral orientation to the patient.

The scatter was calculated at eye height and gonad height. At the minimum width investigated of 100 cm, the scatter at eye height is 14.3 times higher and the scatter at gonad height is 22.6 times higher than the scatter values for the screen with a width of 270 cm. At the maximum width investigated of 350 cm, the scatter at eye height is 0.92 times lower and the scatter at gonad height is 0.95 times lower than the scatter values for the screen with a width of 270 cm. Figure 8.10 shows that widths of the screen greater than 200 cm provide adequate protection of the x-ray room entrance and as the width of screen decreases then it will no longer be adequate.

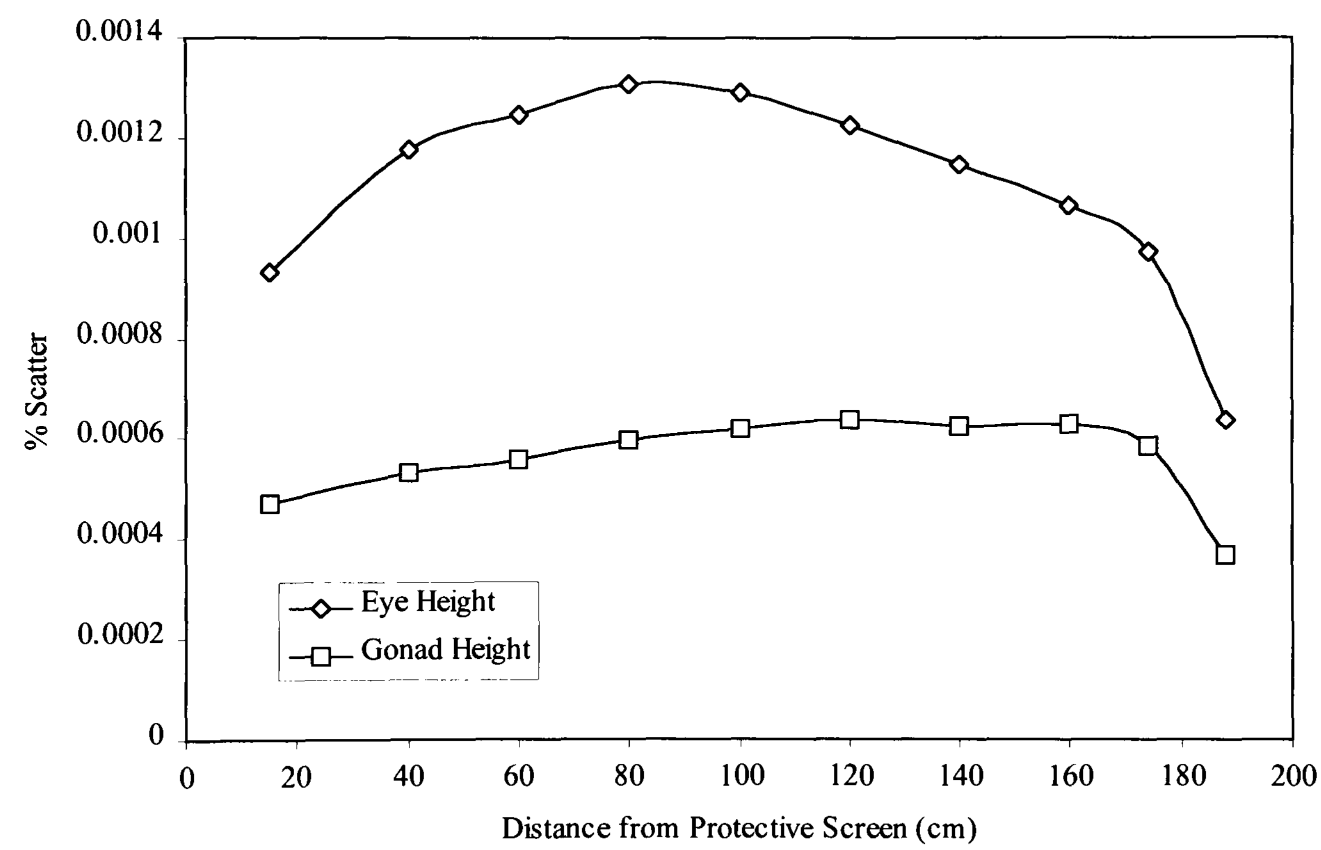

Figure 8.11. *The variation of percentage scatter with distance from the protective screen at the radiographer's console of dimensions: 178 cm deep and 270 cm wide.*

If a door of 2 mm lead equivalent material was placed at the access to the console area from the x-ray room, then the percentage scatter at the x-ray room entrance would be reduced by on average 16.8% at gonad height and and 6.7% at eye height for all examinations and all tube potentials. Therefore, there is only a small reduction in scatter achievable by extending the protective screen around the console area. This result shows that the majority of the scatter is produced by secondary scattering from the ceiling.

Figure 8.11 shows the variation of the percentage scatter with distance from the protective screen in front of the x-ray room entrance. A barium enema examination was simulated with the x-ray tube in a lateral orientation to the patient. The scatter was calculated at eye height and gonad height. The minimum scatter values at eye height and gonad height are both at the centre of the x-ray room entrance, at a distance of 188 cm from the protective screen. This is due to the x-ray room walls, surrounding the entrance, providing some protection from scatter. The scatter increases at positions closer to the protective screen due to the scatter contributions from the surrounding ceiling, floor and walls. The maximum scatter at eye height is 2.03 times the value at the x-ray room entrance and is at a distance of 80 cm from the protective screen. The maximum scatter at gonad height is 1.74 times the value at the x-ray room entrance and is at a distance of 120 cm from the protective screen. At positions closest to the protective screen, the scatter is 1.46 and 1.26 times the values at the x-ray room entrance at eye height and gonad height respectively. The scatter is less here than in the centre of the console area as the solid angle into which the scatter from the ceiling can reach this position is smaller.

8.3.2.2 Variation of Scatter at the X-ray Room Entrance with Height Above the Floor

Figure 8.12 shows the variation of scatter with height above the floor at the x-ray room entrance for all lateral examinations. There is a significant reduction in the scatter with increasing distance from the ceiling. This also suggests that the majority of the scatter reaching the x-ray room entrance was scattered from the ceiling. This is expected as the distance between the top of the protective screen and the ceiling is larger than the access between the protective screen and the wall. The slight reduction in the scatter at the top of the x-ray room entrance (190 cm) may be due to oblique scatter from further along the ceiling. The scatter for the barium swallow examination is considerably lower than the values for the other examinations due to the smaller field size.

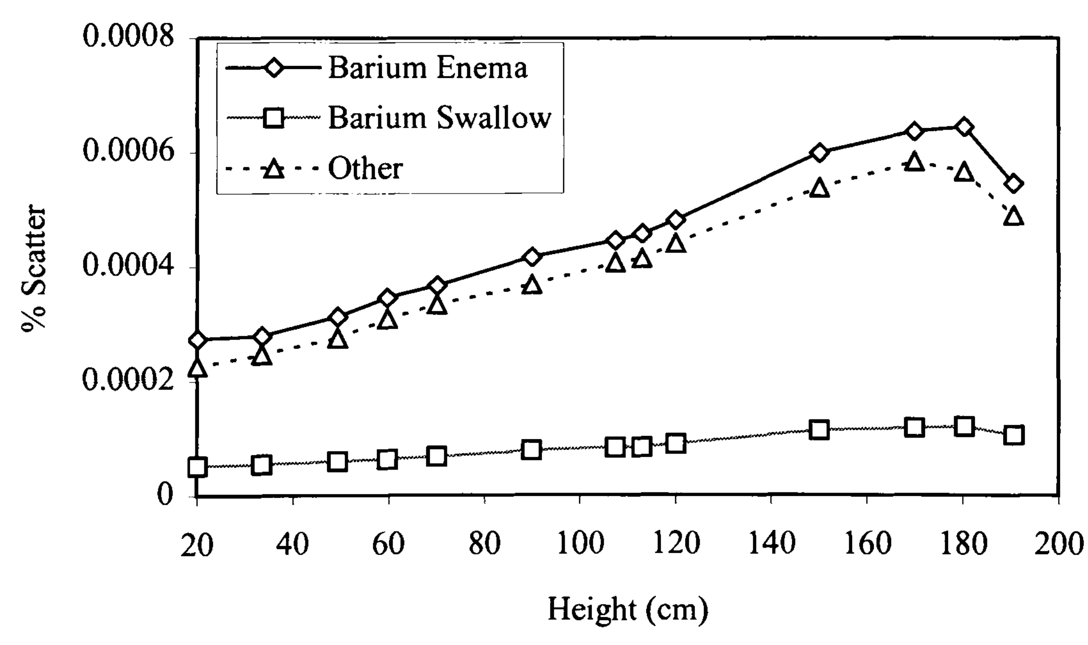

Figure 8.12. *The percentage scatter at the x-ray room entrance behind the radiographer's console for increasing height above the floor.*

Table 8.12 shows the scatter values at gonad height and at eye height calculated with the XYZSCAT code. The largest scatter values are for the barium enema examination with the x-ray tube in the over couch position. This is due to the high tube potential, the large field size and that more scatter is directed towards the ceiling for this tube orientation.

The barium enema and other interventional examinations carried out with the x-ray tube in the lateral and under couch orientations produce similar scatter values. The scatter directed towards the ceiling is similar for both orientations. The smallest scatter value at the entrance is for the barium swallow examination with the x-ray tube under the couch. This is due to the low tube voltage, the small field size and that there is less scatter directed towards the ceiling.

8.3.2.3 Comparison of Monte Carlo and 'Rule of Thumb' Calculations

In the past, a 'rule of thumb' calculation has been used to estimate the scatter behind the protective screen at the radiographer's console. Therefore, 'rule of thumb' calculations using equation 8.1 (BSI, 1971) have been compared to the XYZSCAT calculations of scatter.

$$S = 100\left(\frac{A_{patient}}{100}\frac{0.0005}{d_{ceiling}^{2}}\right)\left(\frac{A_{ceiling}}{100}\frac{0.0005}{d_{entrance}^{2}}\right) \tag{8.1}$$

Equation 8.1 calculates the percentage scatter, S, in two parts. In the first bracket, the amount of scatter from the patient incident on the ceiling above the protective screen is calculated. The scatter factor is 0.0005 at 1.0 m from a patient for a field size of 100 cm^2. Table 8.11 shows the field sizes incident on the patient, A_{patient}, for each examination and tube orientation. The distance from the patient to a position on the ceiling above the protective screen d_{ceiling} is 2.96 m. In the second brackets, the scatter from the ceiling reaching the x-ray room entrance is calculated for two positions. The first position is at gonad height which is 0.7 m above the floor and the distance from the ceiling to the entrance is $d_{entrance}$ = 3.66 m. The second position is at eye height which is 1.7 m above the floor and 3.05 m from the ceiling. For simplicity, the same scatter factor of 0.0005 at 1 m is used for a field size of 100 cm^2 (HMSO, 1971).

The problem with using this 'rule of thumb' calculation is that the area on the concrete ceiling $A_{ceiling}$ has to be chosen. If the whole area of the ceiling was used then the percentage scatter reaching the entrance may be unrealistically large. Therefore in the past, a field size of 10000 cm^2 (HMSO, 1971) was chosen which corresponds to a scatter value of 5% at 1 m (Sutton and Williams, 2000). This field size was chosen as the scatter values given by the HMSO (1971) did not increase for field sizes above 10000 cm^2 (figure 7.24). However, the XYZSCAT calculated values increase for field sizes above 10000 cm^2 (figure 7.24) and therefore, a field size of 35000 cm^2 was chosen for use in a new 'rule of thumb' calculation. Thus, the scatter calculated with the XYZSCAT code is compared to the old and new 'rule of thumb' models.

Table 8.12 compares the results of the 'rule of thumb' calculations with the XYZSCAT calculated values. The scatter values from Monte Carlo calculations are between 1.8 and 5.2 times greater than the values calculated using the old 'rule of thumb' method and between 0.4 times lower and 1.5 times greater than the values calculated using the new 'rule of thumb' method. Hence, the larger field size used in the new 'rule of thumb' model significantly improves the agreement with the Monte Carlo calculated values.

It is of interest to compare the scatter values for the barium swallow examination with the x-ray tube under the couch. For this examination, the Monte Carlo values agree best with the old 'rule of the thumb' model and agree least with the new 'rule of thumb' model. This may be due to the small field size, the low tube potential and the small amount of scatter from the patient and the other materials in the x-ray room.

	Percentage Scatter (×10^{-4}) at the X-ray Room Entrance For the X-ray Tube in a Lateral Orientation					
	Gonad Height			Eye Height		
Exam	**XYZSCAT Values**	**Old Model Values**	**New Model Values**	**XYZSCAT Values**	**Old Model Values**	**New Model Values**
Enema	3.67	0.959	3.36	6.37	1.38	4.83
Swallow	0.680	0.192	0.671	1.18	0.276	0.966
Other	3.34	0.959	3.36	5.84	1.38	4.83
	Percentage Scatter (×10^{-4}) at the X-ray Room Entrance for the X-ray Tube in a Under couch Orientation					
	Gonad Height			**Eye Height**		
Exam	**XYZSCAT Values**	**Old Model Values**	**New Model Values**	**XYZSCAT Values**	**Old Model Values**	**New Model Values**
Enema	3.94	1.33	4.66	6.55	1.92	6.71
Swallow	0.291	0.192	0.671	0.502	0.276	0.966
Other	3.47	1.33	4.66	5.90	1.92	6.71
	Percentage Scatter (×10^{-4}) at the X-ray Room Entrance for the X-ray Tube in a Over couch Orientation					
	Gonad Height			**Eye Height**		
Exam	**XYZSCAT Values**	**Old Model Values**	**New Model Values**	**XYZSCAT Values**	**Old Model Values**	**New Model Values**
Enema	5.01	1.33	4.66	9.98	1.92	6.71
Swallow	0.606	0.192	0.671	1.33	0.276	0.966
Other	4.54	1.33	4.66	9.01	1.92	6.71

***Table 8.12**. The percentage scatter at the x-ray room entrance behind the protective screen at the radiographer's console calculated using the XYZSCAT code and the old and new 'rule of thumb' calculations. The values in the table have to be multiplied by a factor of 10^{-4} to obtain the percentage scatter.*

8.3.2.4 Comparison of Total Annual Dose Calculations

Table 8.13 shows the total annual dose at the x-ray room entrance estimated from the scatter calculated by the XYZSCAT code and the old and new 'rule of thumb' calculations. The amount of leakage radiation depends on the design of the x-ray tube assembly and thus, the leakage dose may or may not be negligible. Therefore, the amount of leakage radiation reaching the x-ray room entrance behind the protective screen has to be estimated. The annual leakage dose was calculated as 0.026 mGy using the maximum leakage dose rate of 1 $mGyhr^{-1}$ at 1 m (NRPB, 1988) and the new 'rule of thumb' method employed to calculate the leakage x-rays scattered from the ceiling. Thus, the dose due to the scatter is significantly larger than that due to leakage radiation.

Tube Orientation	**Height**	**XYZSCAT Calculated Values**	**Total Annual Dose (mGy/yr)**	
			Old 'Rule of Thumb' Model Values	**New 'Rule of Thumb' Model Values**
Lateral	Gonad	0.23	0.064	0.22
	Eye	0.41	0.092	0.32
Undercouch	Gonad	0.24	0.087	0.31
	Eye	0.41	0.13	0.44
Overcouch	Gonad	0.32	0.087	0.31
	Eye	0.63	0.13	0.44

***Table 8.13**. The total annual dose for all examinations at the x-ray room entrance for different orientations of the x-ray tube.*

Table 8.13 shows there are large differences between the XYZSCAT calculated values and the old 'rule of thumb' calculation. The Monte Carlo code calculates the dose up to 5.0 times greater than the value estimated with the old 'rule of thumb' method whereas the Monte Carlo calculated dose is less than 1.4 times the value estimated by the new 'rule of thumb' method. Therefore, a reasonable 'rule of thumb' can estimate the dose at the entrance similar to that calculated by the Monte Carlo method if the protective screen is assumed to be a secondary barrier.

The public annual dose limit is 1 mSv per year (IRR, 1999). The annual dose including leakage and scatter at the x-ray room entrance at the gonad height is less than or approximately equal to 3/10 of the dose limit (NRPB, 1993) for all orientations of the x-ray tube. Therefore, a door in the x-ray room entrance is not required to be lead lined. Figure 8.11 shows that the dose to staff behind the protective screen reaches a maximum value of 2 times the dose at the x-ray room entrance. The annual dose limit for an employee is 20 mSv (IRR, 1999). The maximum dose to staff, estimated as 2 times the values in table 8.13, is a lot smaller than 3/10 of this dose limit (NRPB, 1993) for all orientations of the x-ray tube. Therefore, the protective screen provides adequate protection of staff in the console area.

8.4 Summary of Work

8.4.1 Scatter from a Patient

1. The slab phantom with average dimensions of the patient and the homogeneous contoured phantom produce more scatter than the patient and the slab phantom with the actual patient dimensions produces less scatter than the patient.
2. The patient scatter is less than the scatter from the homogeneous contoured phantom due to the greater attenuation of bone.
3. The largest differences in the scatter produced by the different phantoms are for the lumbar spine AP projection at scattering angles less than 90° due to the low tube potential.
4. The largest variations in patient scatter with varying the imaging parameters (tube voltage, tube filtration, voltage ripple and field size) are for the lumbar spine AP projection and at scattering angles less than 90°.

5. The patient scatter increases by 97% for increasing the tube voltage from 72 to 110 kV.
6. The patient scatter decreases by 30% for decreasing the tube filtration from 4.7 to 2.5 mmAl.
7. The patient scatter increases by 22% if an x-ray generator with a peak voltage ripple of 50% is replaced by a constant potential x-ray generator. Therefore, replacing single phase x-ray generators with medium frequency units would not produce sufficiently more scatter to warrant a change to the x-ray room design.
8. There is no linear relationship between patient scatter and field area.
9. The patient scatter is 91% larger than the expected value for increasing the field area from 100 to 625 cm^2.
10. The patient scatter is dependent on the position of the field edge in relationship to the patient obliquities. Thus, the patient scatter is dependent on field width and the position of the field centre. The lack of tissue at the obliquities increases the forward directed scatter due to lower attenuation and decreases the backward directed scatter due to the smaller scattering volume.
11. The patient scatter in the lumbar spine LAT projection increased by 2.3 times for the centre of the field being moved from the centre of patient's width closer to the patient's obliquity.
12. This work can also be applied to the protection of staff who undertake fluoroscopic produces. If large field sizes are generally used in fluoroscopic procedures then doses to staff can be greatly reduced by decreasing the field size.

8.4.2 Scatter behind a Protective Screen at a Radiographer's Console

1. The scatter at the x-ray room entrance varied mostly within ±20% for differing depths of the radiographer's console behind the protective screen. Therefore, the shape of the protective screen may not matter.
2. The scatter at the x-ray room entrance was largest at heights close to the ceiling.
3. The scatter at the x-ray room entrance was largest for the x-ray tube in an over couch orientation as the patient scatter is largest in the direction towards the ceiling.
4. The old 'rule of thumb' calculation underestimated the Monte Carlo calculated dose at the x-ray room entrance by up to 5.0 times.
5. The new 'rule of thumb' calculation showed reasonable agreement with the Monte Carlo calculated dose at the x-ray room entrance. Therefore, this 'rule of thumb' calculation will be useful in providing a quick calculation of the scattered dose at the x-ray room entrance.
6. The doses at the x-ray entrance were low enough not to require a lead lined door if the protective screen was used as a secondary barrier.
7. The maximum estimated doses at the radiographer's console showed that the protective screen provided adequate protection of staff.

Chapter 9: Summary and Conclusions

9.1 Introduction

The doses at points outside the protective barriers have to be calculated in order to design an x-ray room. This design takes into account the appropriate data for the primary, scatter and leakage radiation which is obtained from reports such as the 'Handbook of Radiological Protection' (HMSO, 1971), NCRP Report No. 49 (NCRP, 1976), ICRP Report No. 33 (ICRP, 1982) and 'Radiation Shielding for Diagnostic X-rays' (Sutton and Williams, 2000). The older reports give scatter and transmission data which were measured with x-ray units using single phase generators. This data has to be updated as modern x-ray units with medium frequency generators are becoming increasingly common. The differences in the penetrating power of the x-rays produced by the different generators prompted Archer et al. (1994) and Simpkin (1989) to produce new transmission data for primary and leakage radiation and this data has been assessed in this thesis. Similarly, Sutton and Williams (2000) found that there is not enough current data for determining the amount of scatter. Thus this thesis has concentrated on providing new scatter data and studying the variation of scatter in different situations. The new scatter data has been compared to older and more recent data where appropriate.

9.2 Code Development

The XYZSCAT and VOXSCAT codes have been developed as the tools with which to consolidate and extend the radiation protection data as required. The XYZSCAT code uses the EGS4 Monte Carlo code (Nelson et al., 1985) and can calculate the scatter at points inside an x-ray room and the transmission behind protective barriers.

The VOXSCAT code calculates the scatter from a patient simulated by a voxel phantom (Zubal et al., 1994). This code was developed from a program to study image quality and patient dose (Dance et al., 2000; Sandborg et al. 2001). An analytical program was also developed but it could only be used to calculate the first order Compton scatter. Monte Carlo calculations had to be used as the first order Compton scatter is less than 59% of the total scatter. However, the analytical program still proved useful as it provided insights into the Compton scattering process.

9.3 Primary and Leakage Transmission

The primary and leakage transmission data was assessed by comparison of the XYZSCAT calculated transmissions for concrete and lead with the values of Archer et al. (1994), Rossi et al. (1991) and Simpkin (1989). The best agreement was between Simpkin's and the XYZSCAT calculated primary beam transmissions. The good agreement was due to both sets of data being calculated with the EGS4 code. The results of the XYZSCAT calculations were also representative of Archer's measured values but not of Rossi's measured values. Therefore, the primary radiation data can be considered as updated because the new data are mostly consistent with each other. There was good agreement between the 'high attenuation' HVLs for the leakage beam derived from XYZSCAT calculations and the values from Archer et al., Simpkin and Rossi et al.. The amount of leakage radiation depends on the design of the x-ray tube assembly. It was measured to be negligible for tube potentials less than 100 kV in the Philips fluoroscopy room at the Churchill Hospital which agrees with the data given by Sutton and Williams (2000). However, the amount of leakage radiation is often conservatively estimated in the room design as 1mGyhr^{-1} at 1 m (NRPB, 1988).

9.4 Amount of Scatter

The XYZSCAT and VOXSCAT codes were rigorously validated by intercomparison of their scatter values before they were used to study the scatter in diagnostic x-ray rooms. The scatter calculated by the XYZSCAT code was compared to the measured scatter from a block of WT1 material and the calculated scatter was thus determined to be representative of the scatter in clinical x-ray rooms. However, this comparison was problematic because the materials surrounding the phantom contributed significant amounts of scatter to the measurements. The DAP meter produced scatter between 0.02% and 0.09%, the surrounding air produced scatter between 0.01% and 0.03%, the x-ray room walls, ceiling and floor produced scatter of 0.007% and the x-ray tube collimators produced scatter between 0.03% and 0.08%. These values were calculated for a 400 cm^2 field size at 1 m from the x-ray focus and are similar to those estimated from data given by Trout and Kelley (1965).

The measured and calculated scatter values are larger than the values given by Trout and Kelley (1972) and Bomford and Burlin (1963) and smaller than the values given by Williams (1996). The scatter calculated by the VOXSCAT code simulating Williams' (1996) experimental set up showed good agreement his values. Thus, the new measured and calculated scatter values, given in table 7.16, are recommended for use in x-ray room design if the FSD is 100 cm and the values from Williams (1996) are recommended if the FSD is 80 cm. The scatter from the patient given in figure 8.2 could also be used. However, these scatter values do not include the significant scatter from the surroundings. Therefore, the amount of scatter produced when an x-ray room is in clinical use can be estimated by adding the scatter from the surroundings to the patient scatter. For changing beam quality, the patient scatter can be modified by the ratios in tables 8.4 and 8.5.

The values given by Trout and Kelley (1972) and Bomford and Burlin (1963) are not recommended for use even for x-ray units which have significant voltage ripple. In this case, the scatter data from this work or that of Williams' should be used and modified by the ratios given in table 8.5 depending on the amount of voltage ripple. This modification of the scatter may only be necessary for low tube voltages.

The Monte Carlo codes have been successful in calculating the scatter in diagnostic x-ray rooms. However, the codes themselves are not easy to use and work will be undertaken to adapt them for use in the clinical environment. Therefore as a user friendly version of the programs is some time away, work has been undertaken to verify straightforward methods of estimating the scatter. The 'rules of thumb' investigated include: (1) the estimation of scatter for varying distances from the phantom; (2) the estimation of scatter for varying the field size incident on tissue equivalent phantoms or patients; and (3) the estimation of scatter for varying the field size incident on shielding barriers. The results of comparing each 'rule of thumb' with Monte Carlo calculations are detailed below:

1. The scatter is typically measured or calculated at a distance of 1 m from the phantom. In order to obtain the scatter at different distances, an inverse square law correction is usually applied to the scatter values (NCRP, 1976). Monte Carlo calculations have shown that the scatter can be estimated by this method without

large errors. The largest difference between the Monte Carlo calculated values and the estimated values was ±14%.

2. The scatter is typically calculated or measured at a field size of 400 cm^2. Calculations and measurements with slab phantoms show that they can be scaled by their area which agrees with the work of Bomford and Burlin (1963). However, it was observed there is no linear relationship between patient scatter and field area. The patient scatter could be up to 91% larger than the expected value for increasing the field area from 100 to 625 cm^2 for a patient undergoing a x-ray examination in the lumbar spine region. Similar or even larger differences between the scatter and the expected values were observed by Trout and Kelley (1972) for increasing the field area incident on homogeneous contoured phantoms. The position of the field on the patient also has an effect. The scatter from a patient undergoing a lumbar spine LAT exam increased by 2.3 times for the centre of the field being moved from the centre of patient's width closer to the patient's obliquity. Again, similar results were shown by Trout and Kelley (1972).
3. The field sizes incident on the x-ray room walls, ceiling or floor are generally significantly larger than the field sizes incident on the patient as they may be considerably further away. Monte Carlo calculations have shown that the scatter varies linearly with field size for areas up to 2500 cm^2 incident on concrete barriers. The 'Handbook of Radiological Protection' (HMSO, 1971) shows that the scatter reaches a maximum value at a field area of 10000 cm^2. However, Monte Carlo calculations show that the scatter continues to increase for field areas above 10000 cm^2.

Monte Carlo calculations are a good means of undertaking theoretical experiments which would be impossible in the clinical environment for example, estimating the scatter for monoenergetic photons. It would be difficult to extract the variation of scatter with photon energy from measured scatter involving x-ray spectra. Calculations show that there are maximum values of the scatter at 80 keV in the forward direction and at 60 keV in the backward direction. Conversely if the scatter for monoenergetic photons were used to estimate the scatter from x-ray spectra then the scatter would be overestimated by on average 42%.

9.5 Estimation of the Dose behind the Protective Screen at the Radiographer's Console

Sutton and Williams (2000) provide worked examples for a wide variety of shielding problems which may be encountered. However, they only give limited advice on the common shielding problem of how to estimate the dose behind the protective screen at the radiographer's console produced by scatter from the ceiling. A fluoroscopy room at the Royal Marsden Hospital, London was modeled and the dose calculated at an x-ray room entrance behind a protective screen at the radiographer's console. The XYZSCAT calculations showed the scatter at the x-ray room entrance was largest at heights close to the ceiling implying that the ceiling was the primary source of this secondary scatter. The scatter was also found to be largest for the x-ray tube in an over couch orientation as the patient scatter is largest in the direction towards the ceiling. The scatter behind the protective screen was 1.6 times larger for the x-ray tube in the over couch position than for the tube in the under couch position.

In the past, a 'rule of thumb' calculation has been the only method to estimate the scatter behind the protective screen. This method estimates the scatter from the concrete ceiling as 5% at 1 m (Sutton and Williams, 2000) using a 10000 cm^2 field size (HMSO, 1971). The XYZSCAT code was used to provide new data for the variation of scatter from concrete with field size. It was found that a more appropriate field size was 35000 cm^2. Hence, this new 'rule of thumb' estimate provides reasonable agreement with the Monte Carlo calculations whereas the Monte Carlo calculations were up to 5.0 times greater than the old estimate. However, this new 'rule of thumb' has not been tested for situations other than those modeled, for example, for different heights of the screen or ceiling. Therefore, further work is required to determine the range of these parameters over which the new 'rule of thumb' may be employed. The doses at the x-ray room entrance were low enough not to require a lead lined door if the protective screen was a secondary barrier.

9.6 Overall Conclusions

It has been shown in this thesis that Archer et al. (1994), Simpkin (1989) and the XYZSCAT code give consistent transmission data for determining the dose outside the shielding barriers for primary and leakage radiation. Therefore, any these data may be applied to x-ray room design.

The VOXSCAT code and Williams (1996) give consistent scatter values for an FSD of 80 cm. Good agreement was obtained between the XYZSCAT calculated and the measured values for an FSD of 100 cm. Thus, both sets of data may be used in x-ray room design. However, the values of Trout and Kelley (1972) and Bomford and

Burlin (1972) which appear in NCRP Report No. 49 (NCRP, 1976) and ICRP Report No. 33 (1982) respectively are not recommended for x-ray room design.

'Rules of thumb' are convenient methods for estimating the scatter in different situations as powerful simulation tools such as the Monte Carlo programs developed in this thesis are not currently in routine use. Therefore, the estimates of a number of 'rules of thumb' have been compared to the results of Monte Carlo calculations. Some of the results have been consistent and some of the results have highlighted important differences. A new 'rule of thumb' has been proposed for estimating the dose behind a protective screen which has given good comparisons with a complicated Monte Carlo simulation. This work shows that reasonably realistic simulations can be undertaken with the Monte Carlo programs developed in this thesis. Thus, Monte Carlo programs are available to aid the design of x-ray rooms now without having to rely on 'rule of thumb' estimates.

9.7 Future Work

The XYZSCAT code developed employs an analogue Monte Carlo method. Variance reduction techniques will have to be used to make it a more efficient computational tool. Chapter 7 shows the calculation of the primary beam transmission using the XYZSCAT code. It is of interest to study the difference in the transmission of scattered radiation compared to that of the primary beam. This has not been calculated at present due to the excessive calculation time required to obtain a low statistical uncertainty in the results. Metzger et al. (1993) showed that even for Monte Carlo calculations using variance reduction techniques the uncertainty in the scatter dose is high behind a shielding barrier in an x-ray room.

Currently, both the XYZSCAT and VOXSCAT Monte Carlo codes calculate the scattered air kerma relative to the incident air kerma. It is of interest to calculate the effective dose for a member of staff wearing a lead apron in an x-ray room. This is possible with the VOXSCAT code as it uses a voxel phantom segmented into different organs.

The Monte Carlo codes developed provide the basis for incorporating more realistic features of x-ray rooms into the models and for studying their effect on the dose received by staff and the general population. The validation of the programs will continue as more features are added to the codes.

References

A. Ahnesjö, 1995, '**Collimator Scatter in Photon Therapy Beams**', *Medical Physics*, Vol. 22, No. 3, 267-278.

G. Alm Carlsson, 1981, '**Effective Use of Monte Carlo Methods for Simulating Photon Transport with Special Reference to Slab Penetration Problems in X-ray Diagnostics**', Uli-RAD-R-49, Report Series, ISSN 0348-7679, Department of Radiation Physics, Linköping, Sweden.

A. Almén, A. Tingberg, S. Mattsson, J. Besjakov, S. Kheddache, B. Lanhede, L. G. Månsson and M. Zankl, 2000, '**The Influence of Different Technique Factors on Image Quality of Lumbar Spine Radiographs as Evaluated by Established CEC Image Criteria**', *British Journal of Radiology*, 73, 1192-1199.

P. R. Almond, 1993, '**The X-ray Centennial - Thompsons and Thomsons**', *Medical Physics*, Vol. 20, No. 2, Pt. 1, 275-281.

D. G. Altman, '**Practical Statistics for Medical Research**', 1st Edition, Chapman and Hall, London, 1991.

P. Andreo, 1991, '**Monte Carlo Techniques in Medical Radiation Physics**', *Phys. Med. Biol.*, Vol. 36, No. 7, 861-920.

B. R. Archer and L. K. Wagner, 1982, '**A Laplace Transform Pair Model for Spectral Reconstruction**', *Medical Physics*, Vol. 9, No. 6, 844-847.

B. R. Archer, J. I Thornby and S. C. Bushong, 1983, '**Diagnostic X-ray Shielding Design based on an Empirical Model of Photon Attenuation**', *Health Physics*, Vol. 44, No. 5, 507-517.

B. R. Archer, T. R. Fewell, B. J. Conway and P. W. Quinn, 1994, '**Attenuation Properties of Diagnostic X-ray Shielding Materials**', *Medical Physics*, Vol. 21, No. 9, 1499-1507.

B. R. Archer, 1995, '**History of the Shielding of Diagnostic X-ray Facilities**', *Health Physics*, Vol. 69, No. 5, 750-758.

F. H. Attix, '**Introduction to Radiological Physics and Radiation Dosimetry**', Wiley, USA, 1986.

M. J. Berger and J. H. Hubbell, 1987, '**XCOM: Photon Cross Sections on a Personal Computer**', NBSIR 87-3597, U.S. Department of Commerce, National Bureau of Standards, Office of Standard Reference Data, Gaithersburg, MD.

A. F. Bielajew and D. W. O. Rogers, 1992, '**A Standard Timing Benchmark for EGS4 Monte Carlo Calculations**', *Medical Physics*, Vol. 19, 303 – 304.

BIR, '**Central Axis Depth Dose Data for Use in Radiotherapy: 1996**', BJR Supplement 25, British Institute of Radiology, London, 1996.

R. Birch and M. Marshall, 1979, '**Computation of Bremsstrahlung X-ray Spectra and Comparison with Spectra Measured with a Ge(Li) Detector**', *Phys. Med. Biol.*, Vol. 24, No. 3, 505-517.

R. Birch, M. Marshall and G. M. Ardan, 1979, '**A Catalogue of Spectral Data for Diagnostic X-rays**', HPA.

J. M. Bland and D. G. Altman, 1986, '**Statistical Methods for Assessing Agreement between Two Methods of Clinical Measurement**', The Lancet, I, 307-310.

C. K. Bomford and T. E. Burlin, 1963, '**The Angular Distribution of Radiation Scattered from a Phantom Exposed to 100 - 300 kVp X-rays**', *British Journal of Radiology*, Vol. 36, 426-439.

J. M. Boone, 1988, '**The Three Parameter Equivalent Spectra as an Index of Beam Quality**', *Medical Physics*, Vol. 15, No. 3, 304-310.

J. M. Boone and J. A. Seibert, 1997, '**An Accurate Method for Computer-Generating Tungsten Anode X-ray Spectra from 30 to 140 kV**', *Medical Physics*, Vol. 24, No. 11, 1661-1670.

J. M. Briesmeister, 1994, '**MCNP – A General Monte Carlo N-Particle Transport Code**', MCNP Version 4A Manual, LA-12625-M, Los Alamos, New Mexico.

BSI, '**Recommendations for Data on Shielding from Ionizing Radiation: Part 2. Shielding from X-radiation**', British Standard 4094, Part 2, British Standards Institution, 1971.

F. Buchmann, H. W. G. Kleine Schaars and W. F. Koster, 1990, '**X-ray Tubes: the Clinical Requirements**', *MedicaMundi*, Vol. 35, 38-48.

J. H. Carmichael, C. Maccia, B. M. Moores, J. W. Oestmann, H. Schibilla, R. Van Tiggelen and B. Wall (eds), 1996, '**European Guidelines on Quality Criteria for Diagnostic Images**' Report EUR 16260 EN, European Commission, Luxembourg.

A. B. Chilton, 1978, '**A Note on the Fluence Concept**', *Health Physics*, Vol. 34, 715.

A. B. Chilton, 1979, '**Further Comments on an Alternative Definition of Fluence**', *Health Physics*, Vol. 36, 637.

W. A. Coleman, 1968, '**Mathematical Verification of a Certain Monte Carlo Sampling Technique and Applications of the Technique to Radiation Transport Problems**', *Nuclear Science and Engineering*, 32, 76 – 81.

K. Cranley, B. J. Gilmore and G. W. A. Fogarty, 1991, '**Data for Estimating X-ray Tube Total Filtration**', IPSM Report No. 64, Institute of Physical Sciences in Medicine, York.

K. Cranley, 1995, '**Measurement of the Performance Characteristics of Diagnostic X-ray Systems Used in Medicine: Part 1 X-ray Tubes and Generators**', 2nd Edition, IPEM Report No. 32, IPEM, York.

J. R. Cunningham and R. J. Schultz, 1984, '**On the Selection of Stopping Power and Mass Energy-Absorption Coefficient Ratios for High Energy X-ray Dosimetry**', *Medical Physics*, Vol. 11, No. 5, 618-623.

D. R. Dance, S. A. Lester, G. Alm Carlsson, M. Sandborg and J. Persliden, 1997, '**The Use of Carbon Fibre Material in Radiographic Cassettes: Estimation of the Dose and Contrast Advantages**', *British Journal of Radiology*, 70, 383 - 390.

D. R. Dance, G. McVey, M. Sandborg, J. Persliden and G. Alm Carlsson, 1999, '**Calibration and Validation of a Voxel Phantom for Use in the Monte Carlo Modeling and Optimization of X-ray Imaging Systems**', Proc. SPIE Medical Imaging 3659, 548-559.

D. R. Dance, G. McVey, M. Sandborg and G. Alm Carlsson, 2000, '**The Optimisation of Lumbar Spine Radiography using a Realistic Computer Model**', *Radiation Protection Dosimetry*, Vol. 90, Nos 1-2, 207-210.

R. L. Dixon, 1994, '**On the Primary Barrier in Diagnostic X-ray Shielding**', *Medical Physics*, Vol. 21, No. 11, 1785-1793.

K. Faulkner and B. M. Moores, 1982, '**An Assessment of the Radiation Dose Received by Staff using Fluoroscopic Equipment**', *British Journal of Radiology*, Vol. 55, 272-276.

T. R. Fewell, R. E. Shuping and K. E. Healy, 1981, '**Handbook of Computed Tomography X-ray Spectra**', HHS Publication (FDA) 81-8162, Rockville, MD.

B. J. Gilmore and K. Cranley, 1990, '**Errors in the Determination of Total Filtration of Diagnostic X-ray Tubes by the HVL Method**', *Phys. Med. Biol.*, Vol. 35, No. 7, 999-1015.

W. R. Hendee, 1993, '**History, Current Status, and Trends of Radiation Protection Standards**', *Medical Physics*, Vol. 20, No. 5, 1303-1314.

HMSO, 1971, '**Handbook of Radiological Protection**', Part 1: Data, HMSO, London.

HPA, 1976, '**The Physics of Radiodiagnosis**', 2nd Edition, HPA, London.

J. H. Hubbell, 1969, '**Photon Cross Sections, Attenuation Coefficients, and Energy Absorption Coefficients from 10 keV to 100 GeV**', National Standard Reference Data Series, NSRDS-NBS 29.

J. H. Hubbell, W. J. Veigele, E. A. Briggs, R. T. Brown, D. T. Cromer and R. J. Howerton, 1975, '**Atomic Form Factors, Incoherent Scattering Functions and Photon Scattering Cross Sections**', *J. Phys. Chem. Ref. Data*, Vol. 4, No. 3, 471-537.

J. H. Hubbell and I. Øverbø, 1979, '**Relativistic Atomic Form Factors and Photon Coherent Scattering Cross Sections**', *J. Phys. Chem. Ref. Data*, Vol. 4, 71 – 538.

J. H. Hubbell, 1982, '**Photon Mass Attenuation and Energy Absorption Coefficients from 1 keV to 20 MeV**', *Int. J. Appl. Radiat. Isot.*, Vol. 33, 1269-1290.

J. S. Hughes, 1999, '**Ionising Radiation Exposure of the UK Population: 1999 Review**', NRPB-R311, NRPB, Didcot, Oxon.

ICRP, 1975, '**Reference Man: Anatomical, Physiological and Metabolic Characteristics**', ICRP Publication 23, Pergamon Press, Oxford.

ICRP, 1982, '**Protection Against Ionising Radiation from External Sources Used in Medicine**', ICRP Report No. 33, Pergamon Press, Oxford.

ICRP, 1991, '**1990 Recommendations of the International Commission on Radiological Protection**', ICRP Publication 60, Annals of the ICRP 21, Nos 1-3.

ICRU, 1989, '**Tissue Substitutes in Radiation Dosimetry and Measurement**', ICRU Report No. 44, Bethesda, MD.

ICRU, 1992a. '**Photon, Electron, Proton and Neutron Interaction Data for Body Tissues**', ICRU Report No. 46, Bethesda, MD.

ICRU, 1992b, '**Phantoms and Computational Models in Therapy, Diagnosis and Protection**', ICRU Report No. 48, Bethesda, MD.

ICRU, 1998, '**Fundamental Quantities and Units for Ionizing Radiation**', ICRU Report No. 60, Bethesda, MD.

IPSM, 1986, '**Radiation Protection in Radiotherapy**', IPSM Report No. 46, IPSM, York.

IRR, 1985, **The Ionising Radiation Regulations 1985**, Statutory Instrument No. 1333, HMSO, London.

IRR, 1999, **The Ionising Radiation Regulations 1999**, Statutory Instrument No. 3232, HMSO, London.

IR(ME)R, 2000, **The Ionising Radiation (Medical Exposure) Regulations 2000**, Statutory Instrument No. 1059, HMSO, London.

H. E. Johns and J. R. Cunningham, '**The Physics of Radiology**', 4th Edition, Thomas, Springfield, IL, 1983.

D. G. Jones and B. F. Wall, 1985, '**Organ Doses from Medical X-ray Examinations Calculated using Monte Carlo Techniques**', Report NRPB-R186, NRPB, Didcot, Oxfordshire.

R. T. Knight, 1996, '**Generation and Quality Control of Kilovoltage X-rays**' in 'A Practical and Theoretical Course in Radiotherapy Physics Part II', The Institute of Cancer Research and The Royal Marsden NHS Trust, Course Notes.

R. Kramer, 1979, '**Determination of Conversion Factors between Body Dose and Relevant Radiation Quantities for External X and γ Irradiation**', GSF Bericht-S-556, GSF, Neuherberg.

B. Lanhede, A. Tingberg, L.G. Månsson, S. Kheddache, M. Widell, L. Björneld, P. Sund, A. Almén, J. Besjakov, S. Mattsson, M. Zankl, W. Panzer and C. Herrmann, 2000, '**The Influence of Different Technique Factors on Image Quality for Chest Radiographs: Application of the Recent CEC Image Quality Criteria**', *Radiation Protection Dosimetry*, 90, No 1-2, 203-206.

J. M. Légaré, P. E. Carrières, A. Manseau, C. Bibeau, J. Robert, N. Robidoux, 1977, '**Blindage Contre les Grand Champs de Rayons X Primaires et Diffusés des Appareils Triphasés au Moyen de Panneaux de Verre, de Gypse et de Plomb Acoustique**', *Radioprotection*, Vol. 13, 77-95 (in French).

S. A. Lester, '**A Study of Scattered Radiation in Diagnostic Radiology**', Ph.D Thesis, University of London, 1998.

P. A. Love, D. G. Lewis, I. A. M. Al-Affan and C. W. Smith, 1998, '**Comparison of EGS4 and MCNP Monte Carlo Codes when Calculating Radiotherapy Depth Doses**', *Phys. Med. Biol.*, 43, 1351-1357.

N. W. Marshall and K. Faulkner, 1992, '**The Dependence of the Scattered Radiation Dose to Personnel on Technique Factors in Diagnostic Radiology**', *British Journal of Radiology*, Vol. 65, 44-49.

N. W. Marshall, K. Faulkner and H. Warren, 1996, '**Measured Scattered X-ray Energy Spectra for Simulated Irradiation Geometries in Diagnostic Radiology**', *Medical Physics*, Vol. 23, No. 7, 1271-1276.

J. H. Martin and G. M. Muller, 1961, '**Quantity and Quality of Scattered X-rays**', *British Journal of Radiology*, Vol. 34, No. 400, 227-235.

G. Matscheko and R. Ribberfors, 1987, '**A Compton Scattering Spectrometer for Determining X-ray Photon Energy Spectra**', *Phys. Med. Biol.*, Vol. 32, No. 5, 577-594.

N. Matsumoto, H. Kubota, H. Hayashi and H. Kanamori, 1991, '**Effects of Voltage Ripple and Current Mode on Diagnostic X-ray Spectra and Exposures**', *Medical Physics*, Vol. 18, No. 5, 921-927.

R. Metzger, R. Richardson and K. A. Van Riper, 1993, '**A Monte Carlo Model for Retrospective Analysis of Shield Design in a Diagnostic X-ray Room**', *Health Physics*, Vol. 65, No. 2, 164-171.

R. L. Morin (ed.), '**Monte Carlo Simulation in the Radiological Sciences**', CRC Press Inc., Boca Raton, FL, 1988.

H. D. Nagel, 1988, '**Limitations in the Determination of Total Filtration of X-ray Tube Assemblies**', *Phys. Med. Biol.*, Vol. 33, 271-289.

NCRP, 1976, '**Structural Shielding Design and Evaluation for Medical Use of X-rays and Gamma Rays of Energies Up to 10 MeV**', NCRP Report No. 49, Bethesda, MD.

W. R. Nelson, H. Hirayama and D. W. O. Rogers, 1985, '**The EGS4 Code System**', SLAC Report No. 265.

NPL, 1993, '**Radiation Transport Calculations Using the EGS4 Monte Carlo System**', NPL Course Notes, NPL, Middlesex.

NRPB, 1988, '**Guidance Notes for the Protection of Persons Against Ionising Radiations Arising from Medical and Dental Use**', NRPB, Didcot, Oxfordshire.

NRPB, 1993, '**Occupational, Public and Medical Exposure**', Doc. NRPB, Vol. 4, No. 2, NRPB, Didcot, Oxfordshire.

H. J. Patrocino, J.-P. Bissonette, M.R. Bussière and L.J. Schreiner, 1996, '**Limiting Values of Backscatter Factors for Low Energy X-ray Beams**', *Phys. Med. Biol.*, Vol. 41, 239-253.

J. Persliden and G. Alm Carlsson, 1986, '**Calculation of the Small-Angle Distribution of Scattered Photons in Diagnostic Radiology using a Monte Carlo Collision Density Estimator**', *Medical Physics*, Vol. 13, 13-24.

W. H. Press, S. A. Teukolsky, W. T. Vetterling and B. P Flannery, '**Numerical Recipes in C. The Art of Scientific Computing**', 2nd Edition, Cambridge University Press, Cambridge, 1992.

D. W. O. Rogers, 1984a, '**Low Energy Electron Transport with EGS**', *Nuc. Instr. Meth.*, 227, 535-548.

D. W. O. Rogers, 1984b, '**Fluence to Dose Equivalent Conversion Factors Calculated using EGS3 for Electrons from 100 keV to 20 GeV and Photons from 11 keV to 20 GeV**', *Health Physics*, Vol. 46, No. 4, 891-914.

R. P. Rossi, R. Ritenour, and E. Christodoulou, 1991, '**Broad Beam Transmission of Some Common Shielding Materials for Use in Diagnostic Radiology**', *Health Physics*, Vol. 61, No. 5, 601-608.

M. Sandborg, D. R. Dance, J. Persliden and G. Alm Carlsson, 1994, '**A Monte Carlo Program for the Calculation of Contrast, Noise and Absorbed Dose in Diagnostic Radiology**', *Comp. Meth. Prog. in Biomed.*, 42, 167-180.

M. Sandborg, G. McVey, D. R. Dance, G. Alm Carlsson and J. Persliden, 1997, '**Collection and Analysis of Patient and Image Data for Calibration of a Voxel-Phantom Based Monte Carlo Code and for the Modeling of Important Structures**', Department of Radiation Physics, Linköping University, Report No. 85, ISRN ULI-RAD-R—85—SE.

M. Sandborg, G. McVey, D. R. Dance, J. Persliden and G. Alm Carlsson, 2000, '**A Voxel Phantom Based Monte Carlo Computer Program for Optimisation of Chest and Lumbar Spine X-ray Imaging**', *Radiation Protection Dosimetry*, 90(1-2), 105-108.

M. Sandborg, G. McVey, D. R. Dance and G. Alm Carlsson, 2001, '**Schemes for the Optimization of Chest Radiography using a Computer Model of the Patient and X-ray Imaging System**', *Medical Physics*, Vol. 28(10), 2007-2019.

A. P. Sanders, C. W. Chui, K. W. Sharpe, R. I. Reeves and C. J. Baylin, 1960, '**Right Angle Scatter for X-ray Beams of 0.14 mm to 2.5 mm Copper H.V.L.**', *Radiology*, Vol. 75, 595-598.

R. L. Siddon, 1985, '**Fast Calculation of the Exact Radiological Path for a Three-Dimensional CT Array**', *Medical Physics*, Vol. 12, No. 2, 252-255.

D. J. Simpkin, 1989, '**Shielding Requirements for Constant Potential Diagnostic X-ray Beams Determined by a Monte Carlo Calculation**', *Health Physics*, Vol. 56, 151-164.

D. J. Simpkin, 1995, '**Transmission Data for Shielding Diagnostic X-ray Facilities**', *Health Physics*, Vol. 68, Vol. 5, 704-709.

D. J. Simpkin and R. L. Dixon, 1998, '**Secondary Shielding Barriers for Diagnostic X-ray Facilites: Scatter and Leakage Revisited**', *Health Physics*, Vol. 74, No. 3, 350-365.

E. Storm and H. I. Israel, 1970, '**Photon Cross Sections from 1 keV to 100 MeV, for elements Z=1 to Z=100**', Nuclear Data Tables A 7, 565-681.

D. G. Sutton and J. R. Williams, '**Radiation Shielding for Diagnostic X-rays**', Joint Report of the BIR/IPEM Working Party, 2000.

E. D. Trout and J. P. Kelley, 1965, '**Scattered Radiation in a Phantom from Diagnostic Quality Radiation**', *Radiology*, Vol. 85, 546-554.

E. D. Trout and J. P. Kelley, 1972, '**Scattered Radiation from a Tissue Equivalent Phantom for X-rays from 50 to 300 kVp**', *Radiology*, Vol. 104, 161-169.

I. A. Tsalafoutas, E. Yakoumakis, A. Manetou and A. Flioni-Vyza, 1998, '**The Diagnostic X-ray Protection Characterisitcs of Ytong, an Aerated Concrete Based Building Material**', *British Journal of Radiology*, Vol. 71, 944 – 949.

R. Veit, M. Zankl, N. Petoussi, E. Mannweiler, G. Williams and G. Drexler, 1989, '**Tomographic Anthromorphic Models Part 1: Construction Techniques and Description of Models of an 8 week Old Baby amd a 7 Year Old Child**', GSF-Bericht 3/89, GSF, Germany.

D. R. White, R.J. Martin and R. Darlison, 1977, '**Epoxy Resin-Based Tissue Substitutes**', *British. Journal of Radiology*, Vol. 50, 814.

J. R. Williams, 1996, '**Scatter Dose Estimation Based on Dose Area Product and the Specification of Radiation Barriers**', *British Journal of Radiology*, 69, 1032-1037.

J. W. Wong, R.M. Henkelman, A. Fenster and H.E. Johns, 1981a, '**Second Scatter Contribution to Dose in a Cobalt-60 Beam**', *Medical. Physics*, Vol. 8, No. 6, 775-782.

J. W. Wong, R. M. Henkelman, J. W. Andrew, J. Van Dyk, and H.E. Johns, 1981b, '**Effect of Small Inhomogeneities on Dose in a Cobalt-60 Beam**', *Medical Physics*, Vol. 8, No. 6, 783-791.

G. Zubal and C. R. Harrell, 1992, '**Voxel Based Monte Carlo Calculations of Nuclear Medicine Images and Applied Variance Reduction Techniques**', *Image and Vision Computing*, 10, 342-348.

G. Zubal, C. R. Harrell, E. O. Smith, Z. Rattner, G. Gindi and P. B. Hoffer, 1994, '**Computerised Three Dimensional Segmented Human Anatomy**', *Medical Physics*, 21, 299-302.